ROTARY LIP SEAL OPERATION WITH ENVIRONMENTALLY ACCEPTABLE LUBRICANTS

F. Xavier Borras

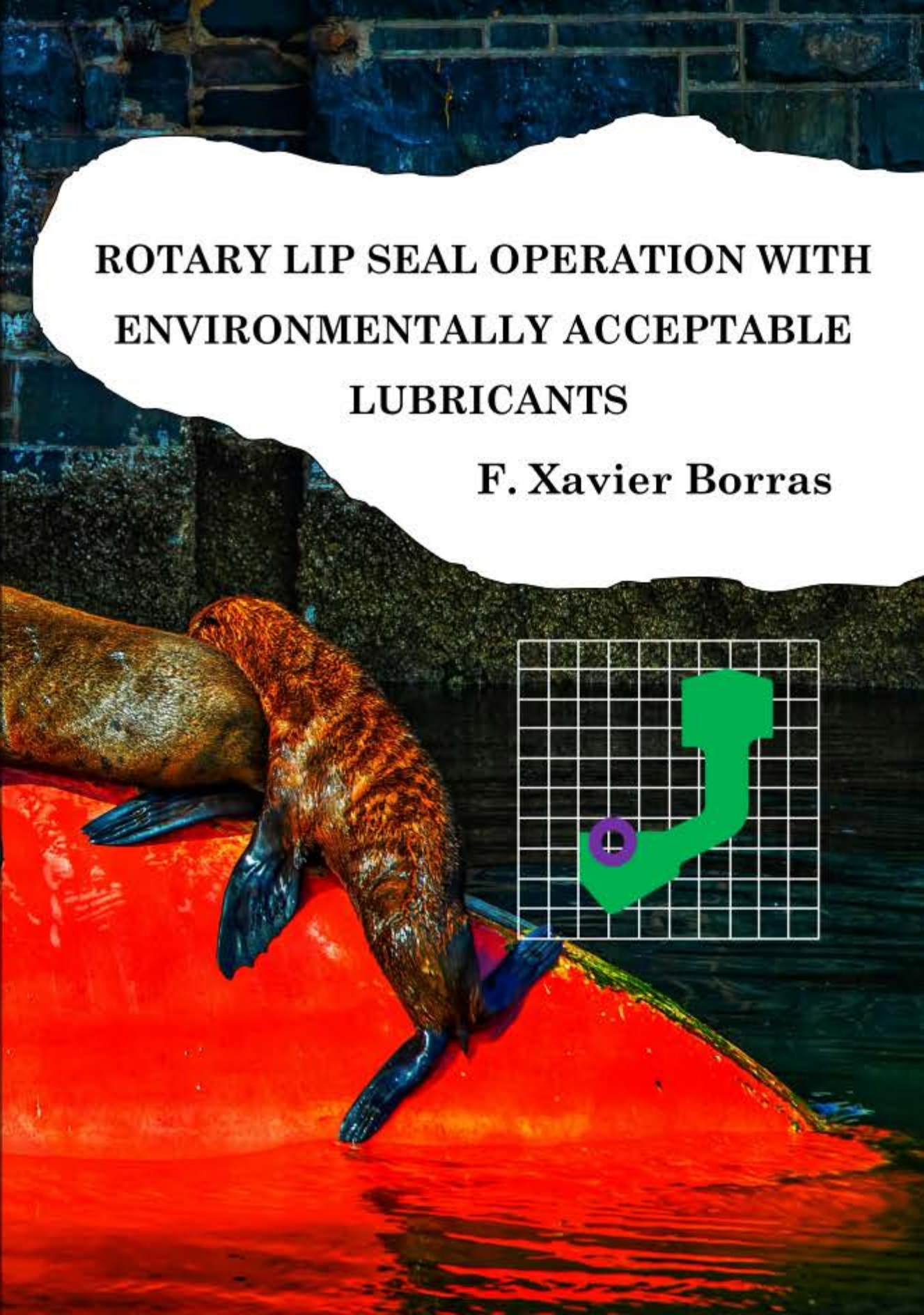

ROTARY LIP SEAL OPERATION WITH ENVIRONMENTALLY ACCEPTABLE LUBRICANTS

Francesc-Xavier Borras Subirana

(This page is intentionally left blank)

ROTARY LIP SEAL OPERATION WITH ENVIRONMENTALLY ACCEPTABLE LUBRICANTS

DISSERTATION

to obtain
the degree of doctor at the University of Twente,
on the authority of the rector magnificus,
Prof. Dr. T.T.M. Palstra,
on account of the decision of the Doctorate Board,
to be publicly defended
on Thursday the 3rd of September 2020 at 12.45 hours

by

Francesc-Xavier Borras Subirana

born on the 4th of April 1988

in Barcelona, Spain

This dissertation has been approved by:

Supervisor: Prof. Dr. Ir. M.B. de Rooij

Co-supervisor: Prof. Dr. Ir. D.J. Schipper

Printed by: Gildeprint Drukkerijen

ISBN: 978-90-365-5044-4

DOI: 10.3990/1.9789036550444

Graduation Committee

Chairman/secretary	Prof. Dr. Ir. H.F.J.M. Koopman, University of Twente
Supervisor	Prof. Dr. Ir. M.B. de Rooij, University of Twente
Co-supervisor	Prof. Dr. Ir. D.J. Schipper, University of Twente

Committee Members

Prof. Dr. A. Almqvist, Luleå University of Technology

Prof. Dr. R. Dwyer-Joyce, University of Sheffield

Prof. Dr. Ir. J.W.M. Noordermeer, University of Twente

Prof. Dr. Ir. T. Tinga, University of Twente

F. Xavier Borras Subirana
Rotary Lip Seal Operation with Environmentally Acceptable Lubricants
Ph.D. Thesis, University of Twente, The Netherlands, September 2020

(This page is intentionally left blank)

Summary

Stern tube seals are a type of rotary lip seals used in the propulsion system of ships. These large-sized elastomeric components are placed at both ends of the stern tube of a ship preventing the lubricant spillage to the environment while, at the same time, avoiding the entrainment of seawater to the stern tube. The ideal leakless situation does not occur and, in reality, a continuous amount of lubricant is discharged to the ocean. The continuous spillage of lubricant is normalized in the marine industry and it is typically referred as the stern tube consumption. To limit the environmental impact of the oil, new legislations replaced the traditionally-used mineral oil-based lubricants for less environmentally harmful products, i.e. the Environmentally Acceptable Lubricants (EALs). However, these lubricants have brought all sorts of issues with the already existing stern tube system of a ship, especially the stern tube seals. The investigation conducted aimed to shed some light on the operation of the stern tube seals in combination with these greener lubricants. This project was divided in three parts: the data collection, the modelling and the validation.

The first part consisted in obtaining the necessary information for developing the computational models. The characteristics of the tribo-system and the window of operation were investigated. The knowledge on Environmentally Acceptable Lubricants is limited and hence especial attention was paid to comparing the common mineral oil-based lubricants to the EALs. Additionally, the seal and shaft materials, the garter spring and the surface roughness were analysed.

The modelling part began by building a robust axisymmetric static model of the stern tube seal, i.e. when the shaft is not rotating. This thermomechanical model served as base on which to build more complex models of the seal. Next, the dynamic operation of the seal was modelled. Due to the complex alignment between the propulsion shaft and the stern tube seals, it is likely that the seals operate under non-concentric conditions. The focus of the research is placed on the lubrication mechanisms that develop as a consequence of such a misalignment. Two misalignment-induced hydrodynamic pressure build-up mechanisms are presented complementing the primary lubrication mechanism theory governing the operation of rotary lip seals.

Validation has been done on many aspects of the models developed. The unavailability of data on stern tube seals required from specialized setups for the validation of the models. Three specialized setups has been developed and used in this research: a split-shaft setup, a static glass shaft setup and a dynamic setup. The radial force between the shaft and the seal was measured via a large-sized split-shaft setup. The width of the contact and the percolation threshold of the seal was measured using the glass shaft test rig. Ultimately, the third setup made it possible to study the behaviour of stern tube seals under real operating conditions.

With the knowledge gained on the EALs, the models developed can be used to significantly shorten the effort required to develop a EAL-suitable seal design. On the longer term, the work presented will give the seals and lubricants manufacturers the opportunity to redesign their products resulting in a less contaminant sailing while extending the service time of stern tube seals.

Samenvatting

Schroefasafdichtingen zijn roterende lipafdichtingen die worden gebruikt in het voortstuwingssysteem van schepen. Deze grote componenten, gemaakt van elastomeren, worden aan beide uiteinden van de om de schroefas van een schip geplaatst om te voorkomen dat het smeermiddel naar de omgeving lekt en tegelijkertijd om te voorkomen dat zeewater wordt meegevoerd naar binnen. De ideale lekvrije situatie doet zich niet voor, in werkelijkheid wordt een continue hoeveelheid smeermiddel afgevoerd naar de oceaan. Dit voortdurend lekken van smeermiddel wordt meestal acceptabel gevonden. Om de milieugevolgen van de olie te beperken, worden smeermiddelen op basis van minerale olie vervangen door minder milieubelastende producten, d.w.z. de Environmentally Acceptable Lubricants (EALs). Deze smeermiddelen hebben echter voor allerlei problemen gezorgd met het reeds bestaande voortstuwingssysteem van een schip, met name met de schroefasafdichtingen. Het uitgevoerde onderzoek was gericht op het verkrijgen van kennis over de werking van de schroefasafdichtingen in combinatie met deze meer milieuvriendelijke smeermiddelen. Dit project was opgedeeld in drie delen: de bepaling van eigenschappen van vooral de smeermiddelen en de elastomeren, de modellering van het functioneel gedrag van deze schroefasafdichtingen en de validatie van deze modellen via experimenten.

Het eerste deel bestond uit het verkrijgen van de nodige parameters voor de input en de ontwikkeling van de rekenmodellen. De kenmerken van het tribo-systeem en de operationele omstandigheden werden onderzocht. De kennis over milieuvriendelijke smeermiddelen is beperkt en daarom is er speciale aandacht besteed aan het vergelijken van de gangbare smeermiddelen op basis van minerale olie met de EALs. Daarnaast werden de materiaaleigenschappen van de afdichting en de as, de in de afdichting aanwezige veer en de oppervlakteruwheid van de as en de afdichting geanalyseerd.

Het modelleergedeelte begon met het bouwen van een robuust symmetrisch statisch model van de schroefasafdichtingen, d.w.z. wanneer de as niet draait. Dit thermo-mechanische model diende als basis om meer complexe modellen van het functionele gedrag van afdichting te bouwen. Vervolgens werd de dynamische werking van de afdichting gemodelleerd. Vanwege de complexe uitlijning van de

schroefas ten opzichte van de afdichtingen, is het waarschijnlijk dat de afdichtingen werken onder niet-concentrische omstandigheden. De nadruk van het onderzoek ligt op de smeringsmechanismen die ontstaan als gevolg van een dergelijke niet gecentreerde opstelling. Dit onderzoek presenteert twee hydrodynamische mechanismen die verantwoordelijk zijn drukopbouw in een niet gecentreerde opstelling, als aanvulling op de theorie van het primaire smeringsmechanisme dat de werking van roterende lipafdichtingen bepaalt.

De ontwikkelde modellen zijn gevalideerd op verschillende aspecten. Gegevens over schroefasafdichtingen waren niet beschikbaar en daarom waren er gespecialiseerde opstellingen nodig voor de validatie van de modellen. In dit onderzoek zijn drie gespecialiseerde proefopstellingen ontwikkeld en gebruikt. De eerste was een radiale kracht opstelling, die de kracht tussen de as en de afdichting meet. Ten tweede werd een opstelling met een glazen holle as ontwikkeld om de breedte van het contact van de afdichting te meten. Uiteindelijk heeft de derde opstelling het mogelijk gemaakt om het gedrag van schroefasafdichtingen onder reële werkomstandigheden te bestuderen.

Met deze kennis, opgedaan met de EALs en de afdichtingen, kunnen de ontwikkelde modellen worden gebruikt om een efficiënte afdichting te ontwerpen welke geschikt is voor EALs. Op de langere termijn zal het gepresenteerde werk de fabrikanten van afdichtingen en smeermiddelen de mogelijkheid bieden om hun producten te verbeteren, wat leidt tot een minder vervuilende scheepvaarten een verlenging van de levensduur van schroefasafdichtingen.

Resum

Els segells de tub de botzina o tub de popa són un tipus de juntes rotacionals de llavi emprades en el sistema de propulsió dels vaixells. Aquestes juntes de goma de grans dimensions s'instal·len a ambdós extrems del tub de botzina impedint que l'aigua del mar entri al vaixell i, alhora, evitant que el lubricant de l'eix acabi a la sala de màquines del vaixell o vessant al mar. Malauradament sempre hi ha fuites de lubricant a través dels segells de tub de popa representant una important font de contaminació. Per minimitzar les conseqüències del vessament de lubricant al mar, el tipus de lubricant permès per a l'eix de propulsió s'està restringint als anomenats *Environmentally Acceptable Lubricants* (EALs). Desafortunadament, els EALs presenten incompatibilitats amb els components de l'eix de propulsió, principalment amb les juntes de goma. Això comporta un pitjor funcionament del sistema de propulsió i reparacions més freqüents. L'objectiu d'aquesta investigació és entendre el funcionament de les juntes en combinació amb els EALs. El projecte s'ha dividit en tres parts: la recopilació de dades, la simulació del sistema tribològic i la validació experimental del model.

La primera part consisteix en obtenir la informació necessària per desenvolupar els models matemàtics. S'han investigat les característiques del sistema juntament amb les condicions de funcionament de les juntes de tub de botzina. La reologia dels lubricants, els materials de l'eix i la junta, la molla de compressió i els acabats superficials també han estat analitzats.

La part de simulació comença per desenvolupar un model estàtic de la junta assumint simetria axial. Aquest model termo-mecànic s'utilitza com a punt de partida per desenvolupar models més complexes. El següent pas es incloure la rotació de l'eix en el model. Es complicat aconseguir que tant les juntes com l'eix estiguin perfectament alineades pel que la condició de simetria axial per aquest tipus de juntes és qüestionable. Una gran part de la recerca s'ha concentrat en estimar les conseqüències hidrodinàmiques que suposa navegar amb una junta descentrada. En aquesta tesis es presenten dos mecanismes addicionals de lubricació complementant la teoria general de les juntes rotacionals de llavi.

Tres bancs de proves s'han dissenyat i construït en el transcurs d'aquesta investigació. El primer dispositiu permet mesurar la força radial entre la junta i l'eix. El segon consta d'un tub transparent que permet mesurar l'àrea de contacte de la junta sota diferents pressions quan l'eix està en repòs. Aquest aparell també permet mesurar la mínima diferència de pressió necessària per garantir la estanqueïtat de la junta. Finalment, el tercer banc de proves replica el funcionament d'un segell de tub de popa un cop instal·lat en un vaixell; amb la mateixa diferència de pressió, velocitat de l'eix i temperatura.

El coneixement obtingut sobre els lubricants i les juntes de llavi permet accelerar el procés de desenvolupament dels segells de tub de botzina en combinació amb els EALs. A llarg termini, la recerca presentada conduirà a una nova generació de juntes amb una major vida útil i un menor vessament de lubricant en el medi aquàtic.

Acknowledgements

I would like to start with the people who tricked me into this adventure: Andreas Almqvist from the Luleå University of Technology for engaging me in the world of tribology back in 2012. Anders Lundgren, Andreas Bamueller, Per Eskilson, Ola Rolandson, Pontus Wettrell and Robin Wilson for encouraging me to take a PhD.

The professionals in Wijk bij Duurstede who counselled me during the last four years and permit me to publish this research: Roy van den Nieuwendijk, Vikram Ramesh, Robert van Herwaarden, Berend Schakel, Patricia Visser, Federico Quinci, Stefan Lampaert, Dennis Vriesema and Ruud Muis.

The international collaboration that actually worked. To those who replied to my spam: Nigel Marx and Marc Masen for making it possible for me to conduct tests at the Imperial College of London. For the great time in Paris, Poitiers and Angoulême: Aurelian Fatu, Pascal Jolly, Mohamed Jarray and Thibaud Plantegenet from the University of Poitiers. Ian Sherrington and Wilbert Sinzara from the University of Central Lancashire for the interesting discussions on stern tube seals. Christoph Burkhart from the University of Kaiserslautern. Wojciech Litwin from the Gdańsk University of Technology. Simon Feldmedth and Sumbat Bekgulyan from the University of Stuttgart. Wilma Dierkes and Jacques Noordermeer of the University of Twente for teaching elastomer chemistry to a non-chemist. Francesc Pérez-Ràfols from the Luleå University of Technology for reminding me that it could be worse (or at least colder). Manfred Jungk and Carol Koopman for giving me the chance to present my work at the ELGI Workshop. Richard Salant, Rob Dwyer-Joyce, Harry van Leeuwen, Kees Venner, Luis San Andres, Dirk Fabry, Bas van der Vorst, Maoui Abdelghani, Pieter Baart, M'hammed El Gadari, Guillermo Morales-Espejel and Piet Lugt for their advice.

I am also very thankful to the superheroes who hide at University of Twente: Erik de Vries, Dries van Swaaij, Robert Jan Meijer, Walter Lette, Leo Tiemersma and Henk-Jan Moed.

The colleagues who did not miss a single 12 o'clock lunch: Laura Cordova, Matthias Feinäugle, Elahe Hadavi, Michel Klaassen, Matthijs Oomen, Luigi Capuano, Tanmaya Mishra, Melkamu Mekicha, Pramod Shetty, Aydar Akchurin, Dennis Ernens, Nadia Vleugels, Naveed Ur Rahman, Can Wang, Febin Cyriac, Yuchen Luo,

Marina Morales, Dimitri Sergachev, Marek Mezera, Sietse van der Linden, Pedro Amoroso, Mohammad Bazrafshan, Leon Jacobs, Arka Bhakta, Shivam Alakhramsing, Hasib Mustafa, Ida Binti, Nurul Hilwa and Yuxin Zhou. Belinda Bruinink, Linda Mensink and Debbie Zimmerman for the cookies.

My friends whom I hope never have to deal with tribology: Sandro Meucci, Magda Polewska, Carles Belmonte, Caroline Gevaert, Laura Grana-Saurez, JuanRi Borrallo, Shayan Nikoohemat, Ieva Dobraja, Desire Grandke, Sebastian Gräve and Therese Noll. The Cube bouldergym. Victor Gil, Adrià Lombera and Pere Nogués. The Predators. The Bar14 crew. Laurent Pont, Lorena Villanueva, Ignacio Garcia and Elena Fernández. My family for their unconditional support and inspiration.

Ultimately, thanks to the pubs and restaurants that temporarily closed during spring 2020 so I could focus on writing this thesis.

Contents

Nomenclature

Roman symbols

A_m	Amplitude of the equivalent sinusoidal roughness profile	[m]
A_0, A	Initial and current specimen section	[m^2]
A_w, B_w	Constants of Walther's formula	[−]
a, n	Carreau-Yasuda constants	[−]
b	Contact width (in x direction, axial direction)	[m]
$\boldsymbol{b}^*$	Distortional part of left Cauchy-Green tensor	[−]
C_{i0}	Yeoh hyper-elastic model parameters	[Pa]
C_p	Specific heat capacity	[J/(kg · K)]
$\boldsymbol{C}_{r/z/\varphi}$	Compliance matrices	[m/N]
C_i, χ, Ψ	Constants	
D_s	Shaft liner diameter	[m]
D_{ri}	Inner diameter of the garter spring when assembled	[m]
$D_{G\,i}$	Inner diameter of the garter spring when mounted	[m]
d_s	Distance between jaws of the split-shaft setup	[m]
$d_{r/z/\varphi}$	Displacement in radial, axial and circumferential direction	[m]
E	Young modulus	[Pa]
E'	Storage modulus	[Pa]
E''	Loss modulus	[Pa]
E^*	Complex elasticity modulus	[Pa]
E_{eq}	Equivalent elastic modulus	[Pa]
F_f	Friction force	[N]
$F_{r_{tot}}$	Total radial force between the seal and the shaft	[N]
F_r	Radial inwards force per unit length $\mathrm{F_r} = \mathrm{F_{r_{tot}}}/(\pi \mathrm{D_s})$	[N/m]
F_c	Load in the circumferential direction	[N]
F_I	Spring pretension	[N]
F	Load applied on the specimen	[N]
F_m	Pulling force exerted by the stepper motor	[N]

f_{xz}, f_{yz}	Total shear load	[N]
G	Duty parameter $G = \eta u b / F_{r_{tot}}$	[−]
g	Cavitation index	[−]
g_0	Gravity constant	$[m/s^2]$
h	Fluid film thickness	[m]
h_{min}	Minimum fluid film thickness	[m]
h_{cen}	Central fluid film thickness	[m]
$h_{tank_{1/2}}$	Distance between the oil tank height and the sensors	[m]
$\boldsymbol{I}$	Unit tensor	[−]
I_1^*	Distortional part of the first invariant of the right Cauchy-Green tensor	[−]
J	Jacobian: determinant of the deformation gradient	[−]
k	Thermal conductivity	$[W/(m \cdot K)]$
k_ρ	Slope of the density equation	$[kg/(K \cdot m^3)]$
$K_{\Delta T}$	Proportionality factor for the contact temperature	$[m^2 \cdot K/W]$
K_q	Suction coefficient	[−]
K_s	Skewness of the surface roughness	[−]
$L_{x/y}$	Length of the computational domain in the x and y directions	[m]
L_0, L	Initial and current specimen length	[m]
$\dot{m}_{x/y}$	Mass flow rate in the x and y directions	[kg/s]
$N_{x/y}$	Number of asperities in the circumferential and axial directions	[−]
p	Pressure	[Pa]
p_c	Cavitation pressure	[Pa]
P_{spring}	Pressure on the spring side of the seal	[Pa]
P_{back}	Pressure on the back side of the seal	[Pa]
q	Flow rate across the seal	$[m^3/s]$
$\bar{q}$	Normalized flow rate $\bar{q} = q/u_{shaft}$	$[m^3/m]$
Q_d	Heat dissipated density $Q_d = \Gamma\omega/(\pi D_s b)$	$[W/m^2]$
Q_f	Friction heating, power dissipation $Q_f = \Gamma\omega$	[W]
$q_{x/y}$	Volume flow rate in the x and y directions	$[m^3/s]$
R_{tip}	Roundness of the tip of the seal	[m]
R^2	Coefficient of determination	[−]
$R_{x/y}$	Effective radius of curvature in the x and y directions	[m]

r, z, φ	Radial, axial and circumferential cylindrical coordinates	[m, m, rad]
s	Cauchy stress $s = F/A$	[Pa]
S	Spring stiffness	[N/m]
s_0, s_1	Circumferential variable	[m]
S_a	Average surface roughness	[m]
S_q	Root Mean Square (RMS) of the surface roughness	[m]
S_p	Height of the tallest surface roughness peak	[m]
S_v	Height of the deepest surface roughness valley	[m]
S_{z5}	Average maximum surface height difference	[m]
S_k	Average maximum surface height difference	[−]
t	Time	[s]
$t_{recovery}$	Time for the specimens to recover	[s]
$t_{relaxation}$	Time for the relaxation test	[s]
T	Temperature	[K]
T_0	Reference temperature	[K]
T_g	Glass transition temperature	[K]
T_{sump}	Temperature of the surrounding oil (oil bath)	[K]
T_c	Temperature at the seal-shaft contact	[K]
U_x	Dimensionless velocity parameter in x direction	[−]
u, v, w	Linear velocity in x, y and z directions	[m/s]
u_e	Elastic deformation from Boussinesq solution	[m]
$u_{a/b}$	Linear velocity in x direction of surfaces a and b	[m/s]
$v_{a/b}$	Linear velocity in y direction of surfaces a and b	[m/s]
$\bar{x}, \bar{y}, \bar{h}, \bar{p}$	Dimensionless variables	[−]
x, y, z	Coordinate system	[m]
x, y, x', y'	Coordinates of the surface in Boundary Elements model	[m]
$w_{a/b}$	Linear velocity in z direction of surfaces a and b	[m/s]
w	Normal load	[N]

W_x	Dimensionless load parameter in x direction	$[-]$

Greek symbols

α	Seal angle at the back side of the seal	$[°]$
α_T	Thermal expansion coefficient	$[1/K]$
β	Seal angle at the spring side of the seal	$[°]$
γ_L	Surface tension	$[N/m]$
$\dot{\gamma}$	Shear rate $\dot{\gamma} = u/h$	$[s^{-1}]$
$\dot{\gamma}_c$	Critical shear rate $\lambda_c = \dot{\gamma}_c^{-1}$	$[s^{-1}]$
Γ	Frictional torque $\Gamma = \Gamma_0 + \Gamma_\eta$	$[N \cdot m]$
Γ_0	Dry torque	$[N \cdot m]$
Γ_η	Viscous torque	$[N \cdot m]$
Γ_{cell}	Torque on the load cell	$[N \cdot m]$
δ	Phase lag between stress and strain	$[°]$
δ_{cell}	Cell initial position	$[m]$
$\Delta_{x/y}$	Root mean square slope in the x and y directions	$[-]$
Δp	Pressure difference $\Delta p = P_{spring} - P_{back}$	$[Pa]$
Δz	Hydrostatic height	$[m]$
ε	Radial misalignment	$[m]$
ϵ	Nominal (or engineering) strain $\epsilon = (L - L_0)/L_0$	$[-]$
$\dot{\epsilon}_{cycle/test}$	Strain rate for the Mullins cycling and the test respectively	$[s^{-1}]$
ϵ_{set}	Set strain	$[-]$
ϵ_0	Initial strain	$[-]$
$\eta_{\dot{\gamma},T}$	Dynamic viscosity at temperature T and shear rate $\dot{\gamma}$	$[Pa \cdot s]$
η_0	Dynamic viscosity at low shear rates	$[Pa \cdot s]$
η_∞	Dynamic viscosity at high shear rates	$[Pa \cdot s]$
Θ	Angular misalignment	$[°]$
κ	Bulk modulus	$[MPa]$
λ_p	Surface parameter (lambda ratio) $\lambda_p = h/\sigma_p$	$[-]$
λ_i	Principal stretches $\lambda_i = 1 + \epsilon_i$	$[-]$
$\lambda_{x/y}$	Root mean square wavelength in the x and y directions	$[m]$
λ_w	Shift factor of Walther's formula	$[-]$
μ	Overall coefficient of friction $\mu = F_f/F_{r_{tot}}$	$[-]$

μ_0	Dry friction coefficient resulting from asperity contact	$[-]$
ν	Poisson ratio	$[-]$
ν_T	Kinematic viscosity at temperature T	$[m^2/s]$
ρ_T	Density at temperature T	$[kg/m^3]$
ρ_c	Density of the lubricant at the cavitation region	$[kg/m^3]$
σ	Nominal (or engineering) stress $\sigma = F/A_0$	[Pa]
σ_0	Initial nominal stress	[Pa]
σ_p	Combined root mean square roughness $\sigma_p = \sqrt{S_{q_1}^2 + S_{q_2}^2}$	[m]
τ_{xz}, τ_{yz}	Viscous shear stress	[Pa]
ϕ	Dimensionless cavitation variable	$[-]$
ϕ_s	Characteristic sealing proportionality parameter	$[-]$
ψ	Elastic strain energy density	$[(N \cdot m)/m^3]$
ω	Angular velocity	[rad/s]

(This page is intentionally left blank)

Abbreviations

BC	Boundary Condition
BE	Boundary Elements
CGM	Conjugate Gradient Method
DMA	Dynamic mechanical testing
EAL	Environmentally Acceptable Lubricant
EHL	Elastohydrodynamic Lubrication
EP	Extreme pressure
EPA	United States Environmental Protection Agency
FE	Finite Elements
FTIR	Fourier-Transform Infrared Spectroscopy
GPC	Gel Permeation Chromatography
HEES	Hydraulic Environmental Synthetic Esters
HEPG	Hydraulic Environmental Polyglycols
HEPR	Hydraulic Environmental Poly-α-olefins
HETG	Hydraulic Environmental Triglycerides
HL	Hydrodynamic Lubrication
IEHL	Isoviscous elastohydrodynamic lubrication
IR	Infrared
LIF	Laser-induced fluorescence
NOAA	National Oceanic and Atmospheric Administration
OEM	Original Equipment Manufacturer
PAG	Polyalkylene Glycols
PAO	Poly-α-olefins
PLL	Partial Loss Lubricant
PPD	Pour point depressants
REACH	Registration, Evaluation, Authorisation and Restriction of Chemicals
TDMA	Tri-Diagonal Matrix Algorithm
TEHL	Thermo Elastohydrodynamic Lubrication
UV	Ultraviolet
VGP	Vessel General Permit
VI	Viscosity Index
VII	Viscosity Index Improvers
WLF	William-Landel-Ferry

(This page is intentionally left blank)

Part I

(This page is intentionally left blank)

1. Introduction

This chapter describes the main components in the sealing system of propeller-driven ships and introduces the new Environmentally Acceptable Lubricants (EALs) used in the stern tube. The scope of the research and the outline of the thesis are presented.

1.1. The stern tube seal system

Most ships are driven by the engine-shaft-propeller arrangement shown in Figure 1-1. The stern tube is a metal tube welded to the hull of the ship connecting the engine chamber and the outside of the ship. The shaft driving the propeller and later transmitting its thrust to the hull goes through the stern tube. A couple of journal bearings are placed within the stern tube, carrying the weight of the shaft and the propeller while allowing rotation of the shaft. To decrease the frictional torque on the bearings the stern tube is flooded with lubricant so the bearings operate while fully immersed in oil. Finally, to ensure the lubricant stays within the stern tube, two sets of rotary lip seals are installed at each end of the tube, namely stern tube seals. The stern tube seal is one of the largest rotary lip seals, along with the seal used in hydropower turbines and wind turbines.

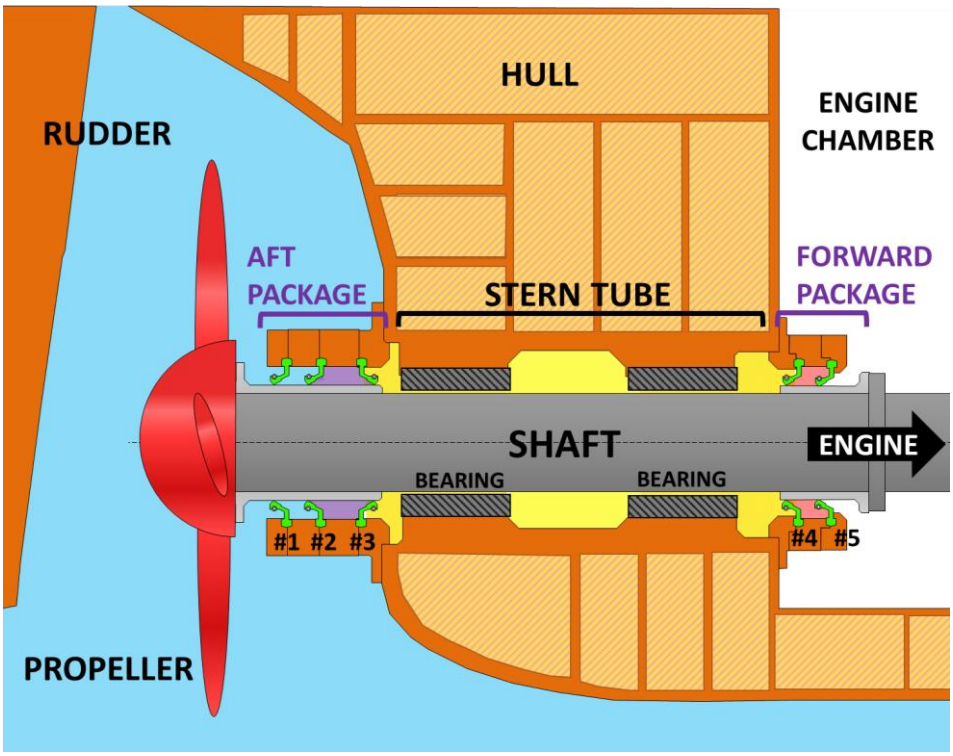

Figure 1-1. Disposition of the stern tube oil tanks in a ship.

The function of the stern tube seals is to prevent water entering the stern tube as well as to minimize the lubricant spillage to the marine environment and engine chamber. To increase the reliability of the system, a few sealing rings are mounted in line at both ends of the stern tube conforming the aft and forward stern tube seals packages shown in Figure 1-1 and Figure 1-2. This special type of sealing rings constitutes the only barrier between the stern tube lubricant and the environment.

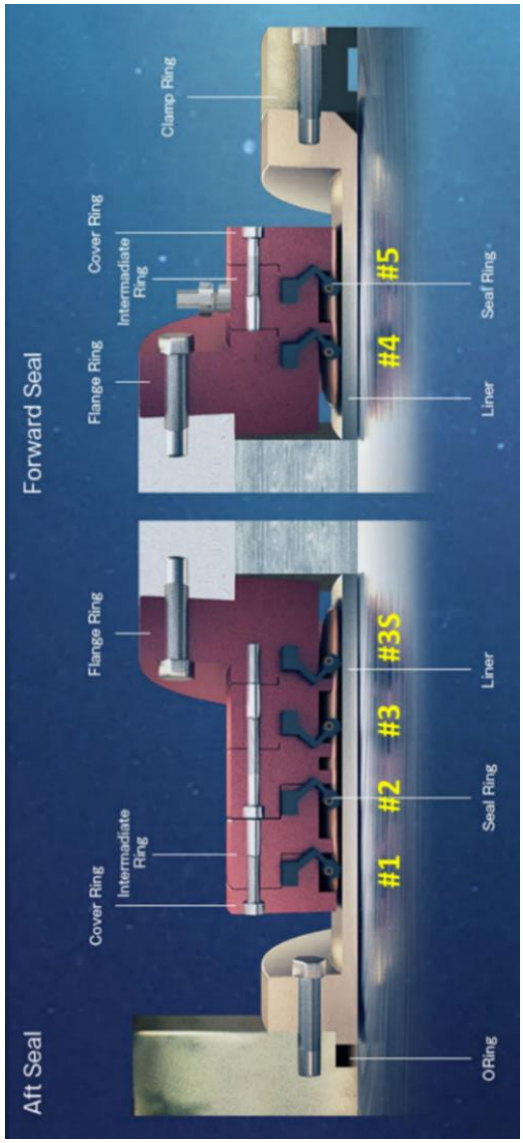

Figure 1-2. Aft and forward stern tube seal packages. Source: Kemel Eagle Industry.

The propeller of a ship is located below the sea water level, hydrostatically pressurizing the outermost sealing ring. Note that the draught of the ship varies between the loaded and unloaded situations impacting the operating conditions of the seal. Furthermore, the hydrostatic pressure at seal #1 oscillates with the sea waves [1]. To counteract the head of sea water on the outermost seal, the spaces between the stern tube seals are independently pressurized by a set of oil tanks, as shown in Figure 1-3. By filling each tank to a particular oil height the hydrostatic pressure at each space between seals can be set. The pressure difference over each seal differs from seal to seal according to its position (#1, #2, #3, #3S, #4 and #5 in Figure 1-2). The disposition of the oil tanks, together with the working pressures within the stern tube, is of relevance and is examined in detail later in this thesis.

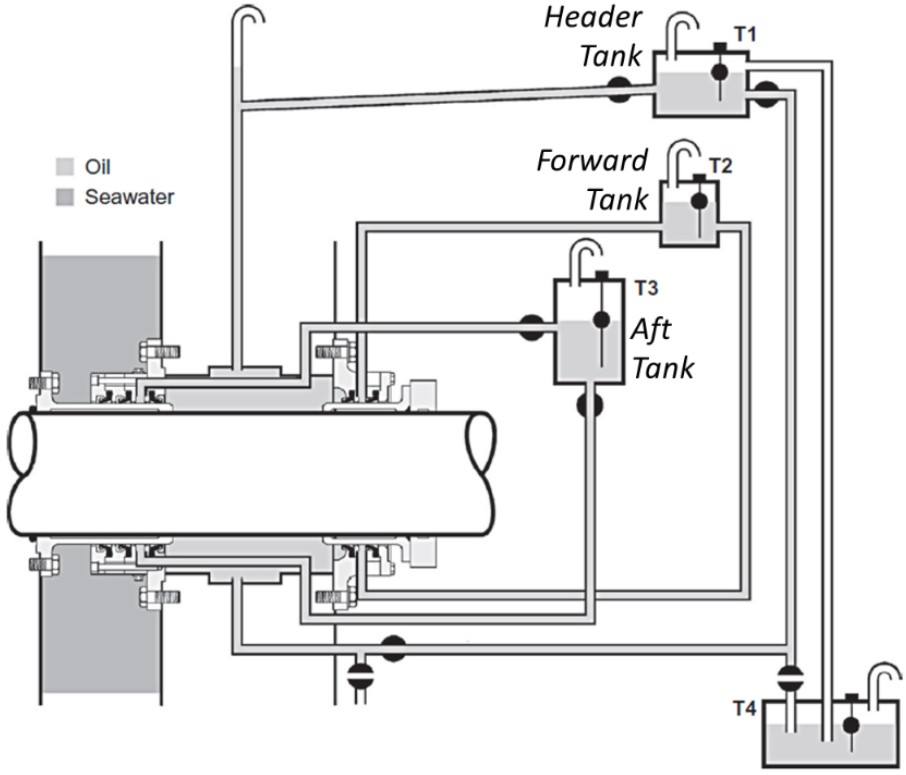

Figure 1-3. Disposition of the oil tanks feeding the chambers between the stern tube seals. Source: Wärtsilä.

Although various seal dispositions exist, the arrangement shown in Figure 1-2 is the most common one [2]. Seal #1 faces the water side and works as a dirt excluder. This outermost seal is rapidly worn out, hence seal #2 also faces the water. Seals #3, #3S and #4 face seal the oil in the header tank, i.e. the oil lubricating the stern tube bearings. Seal #3S, omitted in some designs (see Figure 1-1), acts as a back-up for seal #3. Seal #3S operates under no-pressure difference conditions, i.e. as a standby sealing ring, and can be brought into operation when the primary #3 seal fails. Ultimately, seal #5 prevents the leakage of the lubricant into the engine chamber.

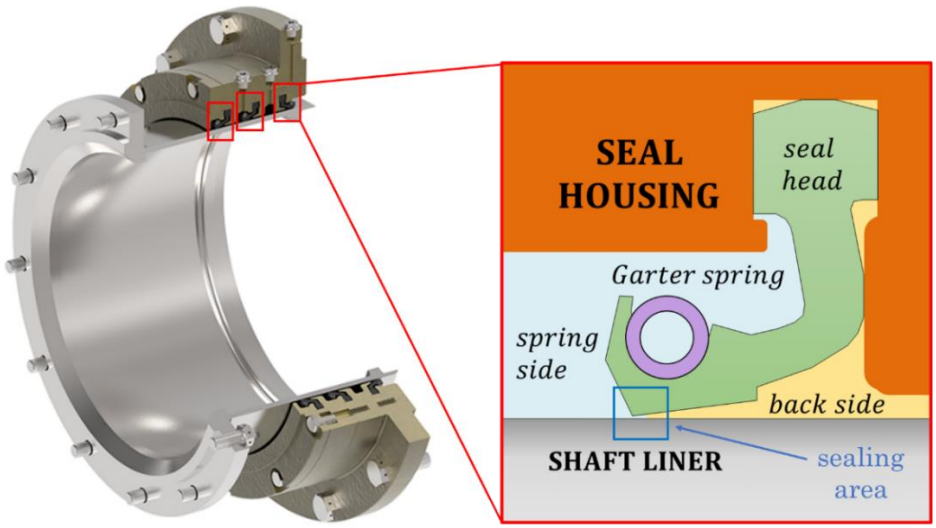

Figure 1-4. Stern tube seal aft package. Source: Wärtsilä.

Typically, all the seals of a stern tube are of the same type, irrespective of their position. The only difference is that the garter spring of the outermost is made of Hastelloy instead of stainless steel (see Figure 1-4). Additionally, some manufacturers use special compounds for the seals in contact with the sea water where lubrication is particularly difficult [2]. The stern tube seals are mounted on the shaft liners, as shown in Figure 1-2. Consequently, the shaft liner can be easily replaced when grooved or corroded, thus avoiding the disassembly of the shaft. Additionally, it is simpler to machine the shaft liners down to the required surface finish [3]. Sometimes spacer parts are mounted between the housing rings and the hull, offsetting the position of the

seal tip. This way, a fresh un-grooved surface is provided to the seal tip, allowing for an additional use of the shaft liner. To prevent disassembling the propeller when replacing the seals, stern tube seals are cut, mounted around the shaft and bonded. Using a specialized glue and a heating device the two cut surfaces are bonded together in such a way that the splitting line becomes almost unnoticeable. The life of stern tube seals usually spans two and five years depending on the operating conditions. However, to prevent costly unexpected failures while sailing the seals are replaced every time the ship is in dry dock.

Figure 1-5. Stern tube profile.

Stern tube seals are usually made of fluoroelastomer compounds, specifically FKM compounds (see Figure 1-5). This saturated elastomer, often referred to by its trademark Viton®, stands out for its temperature resistance and inertness. The high bonding energy between the carbon and the bulky fluorine atoms shields the polymer back bond from chemical attacks [4]. The inherent polarity resulting from bonding carbon and fluorine molecules makes fluoroelastomers extremely resistant to mineral oils and fats, i.e. non-polar media [5]. The forming monomers of FKM elastomer analysed in this thesis are vinylidene fluoride ($H_2C=CF_2$), tetrafluoroethylene ($F_2C=CF_2$) and hexafluoropropylene ($F_2C=CF\text{-}CF_3$). FKM can be readily cured with bisphenol; however, the highly fluorinated FKM types require cure-site monomers and they are cured with peroxides. Fluoroelastomers are often filled with non-reinforcing carbon black and wax is added as

a processing aid, easing the release of the parts from the mould [5]. Stern tube seals are generally manufactured via compression moulding although they can also be extruded. These production methods allow the manufacturing of complex geometries, decreasing the amount of tooling required. The purpose of the compression moulding is to add a specific amount of uncured elastomer into a mould. Subsequently, the mould is closed and held under pressure until the elastomer flows, filling all the cavities of the mould. The moulds are heated up until sufficient crosslinking is achieved and the elastomer is able to keep the shape of the mould by itself. Next, the seals are demoulded and placed in an air-circulating oven for post-curing. The seals are left in the oven long enough to reach the optimal elastomer properties. The poor thermal conductivity of fluoroelastomers complicates the curing stage, especially for the thicker sections of the seal. If the elastomer does not reach the necessary temperature for sufficient time, a partially-cured state is left on the finished part, leading to undesirable mechanical and chemical consequences for the seal. Ultimately, the seam line of the seal is removed by rubbing an abrasive cloth around the seal tip. The seals are then packed together with a suitable garter spring, as shown in Figure 1-6.

Figure 1-6. Package of 200 millimetres stern tube seal with its garter spring.

It is worth mentioning that rotary lip seals are not suitable for separating two liquids from each other [6]. Therefore, even when

several lip seals are installed in line, some of the lubricant is continuously spilled to the ocean. Furthermore, the loss of stern tube lubricant is considered an inevitable part of the normal operation of a ship [7]. Hence the lubricant tanks are periodically refilled to compensate for the amount of oil spilled to the ocean. The leakage of stern tube lubricant to the environment depends on elements such as seal design, vessel type, draught, shaft diameter and ship condition. As an example, the stern tubes of barge carriers, tankers and navy ships "consume" (i.e. spill) between 10 and 20 litres per day [7]. To the best of the author's knowledge, there is no standard method for predicting the flow rate resulting from a particular stern tube arrangement.

1.2. Environmentally Acceptable Lubricants (EALs)

It is estimated that about 50% of the lubricants end up in the environment while the other 50% are recycled or burned [8]. When the lubricant is spilled to the ocean the environmental consequences are amplified since a small quantity of oil can contaminate a large volume of water. In 2001, Pavlakis [9] revealed that the majority of vessel discharges of oil to the Mediterranean Sea occurred due to routine operational discharges. Sea-going vessels use lubricants in gear boxes, thrusters, controllable pitch propellers, stabilizers, stern tubes, rudder bearings, dredges and grabs, but the major source of leakage is the stern tube, i.e. through the stern tube seals [9]. The operational discharges from stern tube leakage into (sea)port waters alone are estimated to be between 37 million and 61 million litres per year, which is more than the total amount of engine oil present in all passenger vehicles in the Netherlands [7]. With marine pollution becoming a matter of increasing concern, more focus has been placed on solving the spillage of contaminants through the stern tube system. Instead of improving the sealing system, the United States Environmental Protection Agency (EPA) decided to act on the root problem, i.e. the lubricant.

For over 100 years traditional petroleum (mineral) based oils were used for the lubrication of the stern tube bearings. The EPA, in the Vessel General Permit of 2013, stated that *"All ships greater than 79 feet must use an Environmentally Acceptable Lubricant (EAL) in all oil-to-sea interfaces, unless technically infeasible"* [10]. This limitation

made it mandatory for the stern tube oil of the majority of ships sailing within U.S. waters to be replaced by a more environmentally friendly lubricant. This way, the environmental impact is limited even though the stern tube lubricant consumption is greater. For a lubricant to be labelled as an EAL it must meet specific requirements of non-toxicity, biodegradability and non-accumulativity [10]. Already existing labelling programmes, e.g. the German Blue Angel, the European Ecolabel or the Nordic Swan, are used to indicate the suitability of a lubricant to be used in applications where there is a risk of environmental damage [11]. The European Ecolabel [12], for example, includes such requirements as a minimum share of renewable raw materials and a biodegradability interval and it limits the use of some organic compounds and most metals [3]. Hence the lubricants possessing the European Ecolabel automatically qualify as EALs [10]. Within the EU, the substances allowed to be used in a lubricant must fulfil the requirements typified in the Registration, Evaluation, Authorisation and Restriction of Chemicals (REACH) regulation.

A lubricant is usually made of a base oil (or a blend of base oils) together with an additive package. The additives are specifically tailored to the applications and improve the base performance of the base oil. The composition of the additive package is wide and can contain, among other things, anti-oxidants, rust and corrosion inhibitors, detergents and dispersants, anti-foaming agents, anti-wear, extreme pressure inhibitors (EP), plasticizers, oiliness agents, pour point depressants (PPD), viscosity index improvers (VII), friction modifiers or emulsifiers. Both base oil and additive formulation must meet the VGP legislation so the final formulation can be labelled as an EAL; consequently, the type of additives allowed is also limited. The base oils which, if properly formulated, can lead to an EAL are listed in the VGP [10], leaving to the ship owner the decision of which one to use (Table 1-1).

Table 1-1. List of base oils suitable for the formulations of EALs.

Type of base oil	**Abbreviation**	**Source**
Polyalphaolefins (PAOs)	HEPR	Synthetic
Triglycerides (vegetable oil based)	HETG	Natural
Polyglycol (PGs) or Polyalkylene (PAGs)	HEPG	Synthetic
Saturated and Unsaturated Synthetic Esters	HEES	Synthetic

Therefore, as a result of the 2013 VGP a competition to find the best-performing EAL replacing the traditionally mineral oil-based lubricants began. The lubricant manufacturers generally opted for an ester-based solution; however, a few HEPG and HEPR for the stern tube lubrication are readily available in the market. As well as being more costly [10], some EALs showed incompatibilities with the material used for the stern tube seals. Both the base oil and the additives used in the final EAL formulations can compromise the fluoroelastomer seals. The poor hydrolytic stability of some EALs also challenges the reliability of the system. Larger seal wear rates were often reported when operating with EALs. bringing the attention back to the working mechanisms of rotary lip seals and the underlying tribology. Costly early visits to the dry dock result from operating with an unsuitable lubricant (see Figure 1-7).

Figure 1-7. Severe swelling and blistering may result when a non-compatible elastomer/EAL pair is selected. The dumbbell-shaped specimens were initially of the same size.

1.3. Research scope

The research conducted aims to develop a model of a stern tube seal to predict its functional behaviour under conditions similar to typical operating conditions in a vessel. Special attention is paid to the stern tube lubricant, as stern tube seals are shown to be unreliable when operating with some of the new Environmentally Acceptable Lubricants (EALs). This study focuses solely on a specific, but common, seal profile. Complementary to the actual results obtained, this investigation aims to establish a strategy for modelling rotary lip seals in an efficient and reliable way so it can be used in the design process of a stern tube seal. This may ultimately lead to a new generation of more effective and hence more environmentally friendly stern tube seals.

The objectives of this thesis can be summarized as follows:

- To gain and understanding of the working mechanism behind the operation of stern tube seals. To analyse the decisive variables governing the behaviour of the seals.
- To develop a validated model on the typical operating conditions of a stern tube seal.
- To compare the traditional mineral oil-based lubricants and the Environmentally Acceptable Lubricants (EALs) in a stern tube from a tribological standpoint.

1.4. Outline of the thesis

This thesis focuses on the working mechanism of large pressurized rotary lip seals when lubricated with Environmentally Acceptable Lubricants (EALs). The thesis is divided into two parts: Part I and Part II. Part I poses the problem, reviews the literature on rotary lip seals and describes the research conducted during the four years prior to the publication of this thesis. Part II comprehends the studies published by the author and his co-authors resulting from this research. The articles compiled are also available online. Figure 1-8 shows the correlation between the chapters of this thesis and the publications presented in Part II.

Part I is divided into six chapters. *Chapter 1* introduces the stern tube system, presents the problem when using the new EALs and describes

the scope of the research. *Chapter 2* reviews the published literature on rotary lip seals and defines the research gap. *Chapter 3* comprises the experimental methods and the characterization of the seal material, the lubricants, the surfaces and the garter spring. *Chapter 4* shows the three dedicated setups which were built during this thesis. The setups are designed to simulate specific aspects of the real stern tube seal application allowing for the validation of computational models. *Chapter 5* describes the various models of the stern tube seal developed. The validation of the models by the dedicated setups presented in *Chapter 4* is also included in this section. *Chapter 6* shows the experimental results obtained with the stern tube investigated under common operating conditions. The last chapter, *Chapter 7*, provides a discussion and reviews the conclusions obtained from this research.

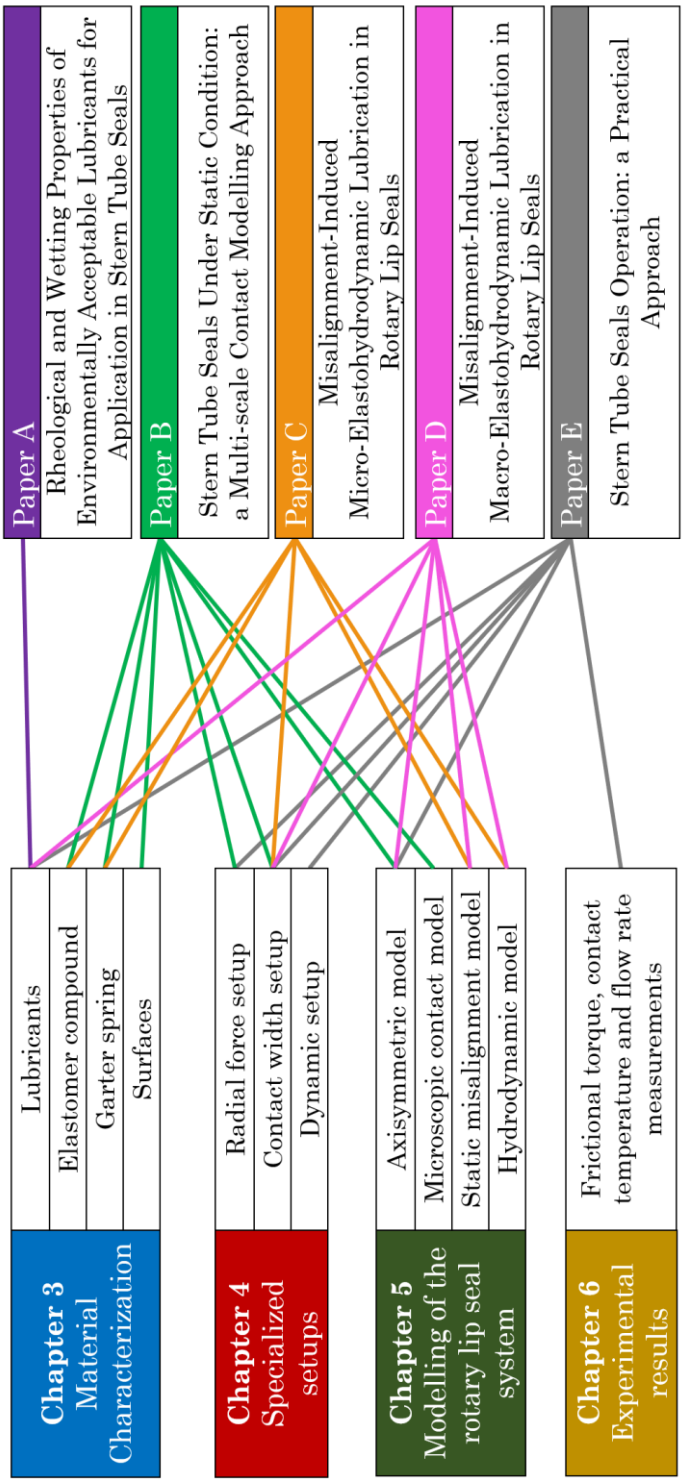

Figure 1-8. Correspondence of the chapters to the published studies resulting from this research.

(This page is intentionally left blank)

2. State of the art

This chapter reviews the relevant scientific literature on rotary lips seals. The research conducted on the aligned and misaligned operation of these seals is summarized, along with the strategies for modelling them. Subsequently, the research gap is outlined.

2.1. Literature review

2.1.1. Lubrication regime of rotary lip seals

The first rotary lip seals date from 1930s and soon became the most widely used component for sealing rotary shafts [2]. Initially it was thought that, as in the case of static seals, providing enough contact force between the seal and the shaft would guarantee the tightness of the rotating contact. Therefore, as in dry tribological pairs, the ability to dissipate the frictional heat generated determines the operating temperature and often the service time of the component. Consequently, the radial load minimizing the temperature in the contact while keeping the gap tight was sought.

It was not until the 1950s that engineers started questioning such an approach. In 1957, Jagger [13] engineered a smart testing setup which allowed the radial load of the seal to be tuned while rotating. As

described in the comprehensive review paper of Salant [14], Jagger modified the seal design so that the sealing force was directed in the axial instead of the radial direction while keeping a similar seal profile, as shown in Figure 2-1a. This new disposition allowed the contact to be easily loaded by adding dead weight to the seal carrier. Whether the setup in Figure 2-1a still resembles a radial seal or is closer to an axial seal is a matter for discussion. The sealing counter face platform was rotated using a motor and the frictional torque was measured by a spring balance attached to the seal carrier. Jagger started testing with an unloaded seal carrier and filled the inner part (spring side) of the seal with a lubricant. Such an arrangement led to copious leakage across the sealing tip. Next, keeping the angular speed of the platform constant, Jagger progressively added weight to the seal carrier until the lubricant stopped leaking out of the seal. The torque was measured at various operating points and the results are shown in Figure 2-1b.

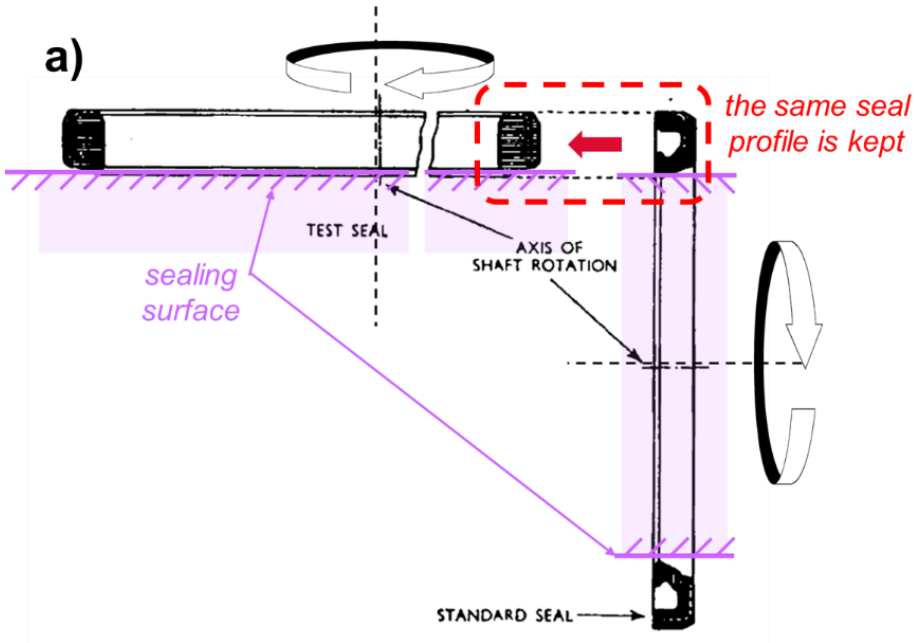

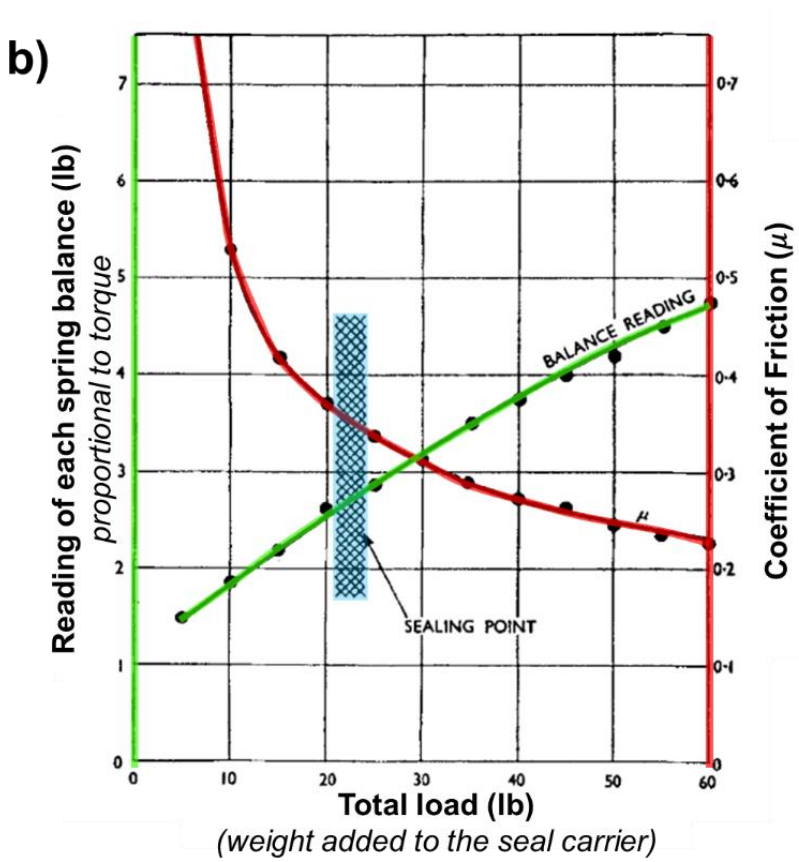

Figure 2-1. Cross section of the seal modified by Jagger (a). Measured values of friction over a range of applied loads (b). Figure based on [13].

The first peculiarity observed in Figure 2-1 is the non-zero ordinate intercept of the load-frictional torque curve. In other words, a significant friction force was present even when the normal load was almost null. This differs from the dry contact pairs, e.g. Coulomb-like contacts, where the frictional force is proportional to the load. Secondly, a change in slope was expected when the seal transited from a viscous (leakage) to a "dry" (no leakage) contact. Contrarily, a smooth torque transition between the non-leaking and leaking situations was observed. Jagger concluded that a continuous film of lubricant may be present between the seal and the shaft, preventing direct asperity contact [13]. Note that the coefficients of friction μ deduced from the torque measurements in rotary lip seals are significantly larger than the μ obtained in journal bearings (see Figure 2-1). The fluid film

thickness of rotary lip seals is at least one order of magnitude lower than in plane journal bearings [15]. Therefore, if operating with a Newtonian lubricant, radial lip seals present ten times larger shear rates and consequently one order of magnitude larger coefficient of friction than for traditional journal bearings.

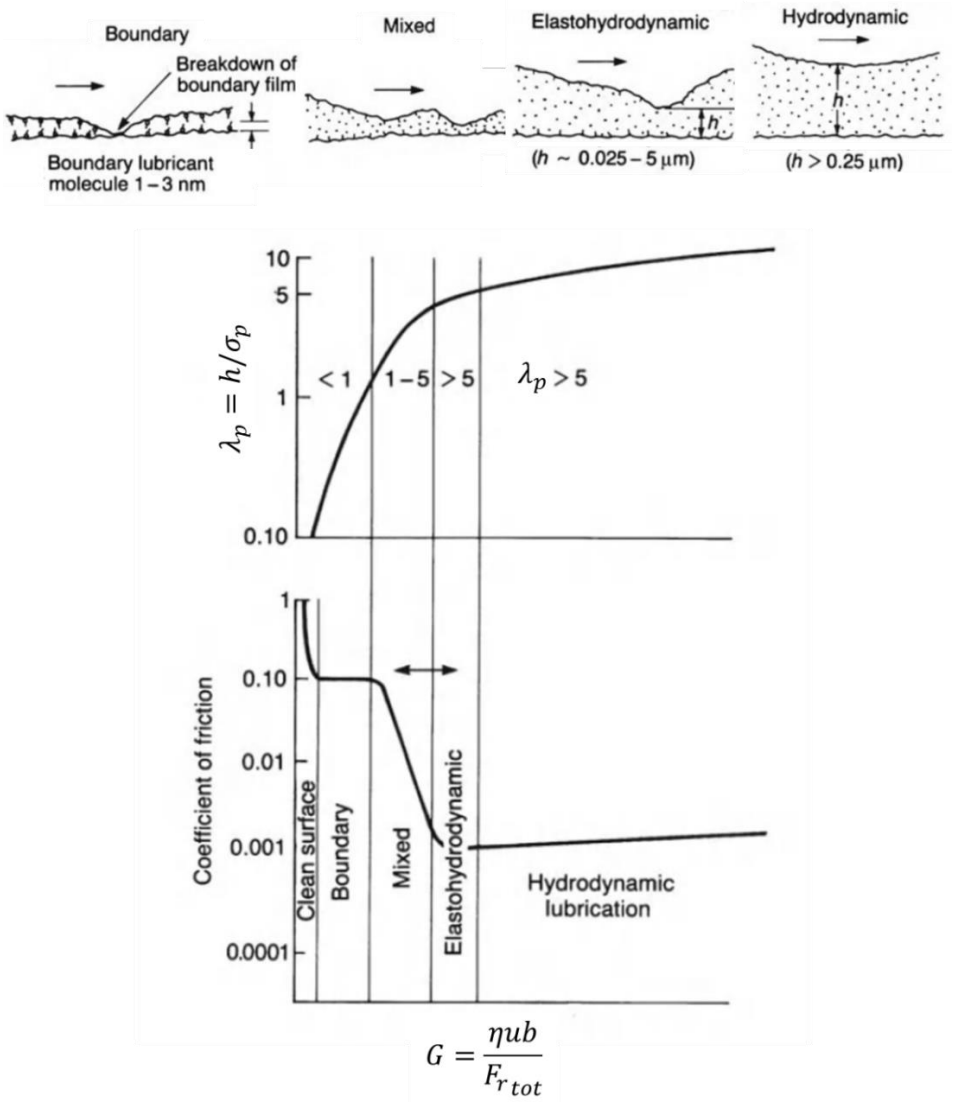

Figure 2-2. Stribeck curve showing the lubricant film parameter λ_p and coefficient of friction. Based on [16].

The Stribeck curve has been used in an attempt to classify the lubrication regime of rotary lip seals [17]. As shown in Figure 2-2, it is possible to determine the lubrication regime by observing the relationship between the coefficient of friction μ and the dimensionless duty parameter $G = \eta u b / F_{r_{tot}}$. The dynamic viscosity η, the velocity u and the contact width b on the numerator of the duty parameter promote the hydrodynamic action. Therefore the duty parameter is the ratio between the hydrodynamic pressure build-up and the normal loading of the contact. Note that neither the roughness of the surfaces nor the gap characteristics are accounted for by the duty parameter. When it comes to rotary lip seals, both dry and boundary lubrication regimes were spotted at very low shaft velocities [14]. Furthermore, a linear relationship between the duty parameter and the coefficient of friction was observed under common steady state operating conditions. A proportionality constant ϕ_s, also known as the characteristic seal number, can be found for each specific seal $\mu = \phi_s G^{1/3}$ [18]. This strengthens the hydrodynamic lubrication hypothesis [14].

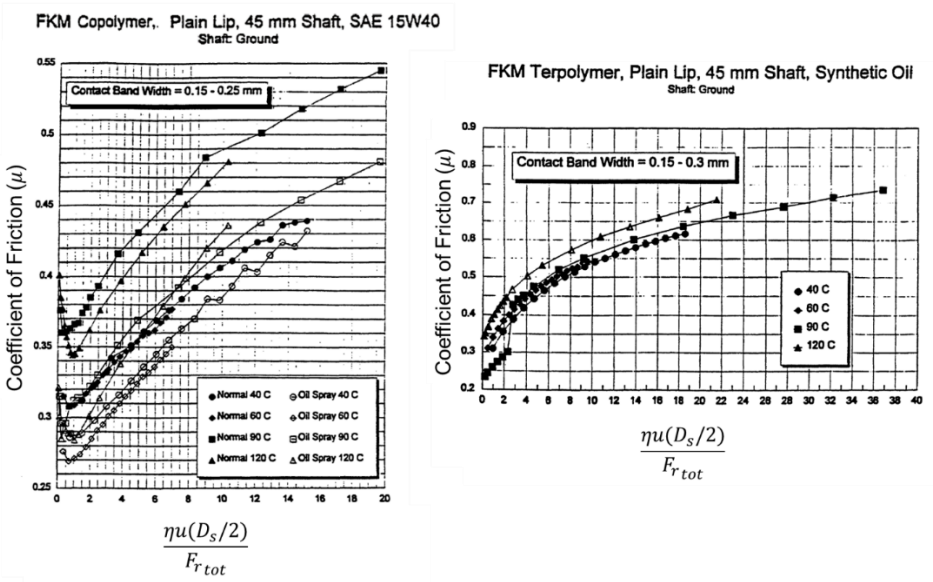

Figure 2-3. Stribeck curves measured by Johnston [19]. *Some of the seals did not show the minimum coefficient of friction from the boundary and mixed lubrication.*

An extensive study was presented by Johnston [19] showing the Stribeck curve obtained for several seal designs (see Figure 2-3). Surprisingly, 50% of the seals did not evidence the boundary and mixed lubrication regimes and immediately showed a monotonic increase of the friction coefficient with increasing shaft velocity. The results showed an important spread on the results and Johnston concluded that the duty parameter G was not sufficient to characterize the behaviour of a seal: additional variables needed to be taken into account. Johnston also noticed that the wear rate of lubricated rotary lip seals was not proportional to the sliding distance, as would be expected from dry contact. Contrarily, the contact width remained constant after an initial break-in period, further strengthening the thesis based on the wear-less hydrodynamic lubrication regime.

As shown in Figure 2-2, the lambda ratio $\lambda_p = h/\sigma_p$ determines the lubrication regime of a lubricated contact pair. It is based on comparing the mean film thickness height h to the composite standard deviation of undeformed surface heights of the two surfaces $\sigma_p = \sqrt{S_{q_1}^2 + S_{q_2}^2}$. When it comes to elastomeric seals, the soft nature of the material, e.g. NBR, HNBR, PTFE or FKM, will deform under the fairly low hydrodynamic loads. This lubrication regime is known as soft elastohydrodynamic lubrication (soft EHL) and, due to the compliance of the seal material, the surface parameter λ_p based on the undeformed roughness becomes less meaningful. Under soft EHL the value of λ_p varies between 1 and 5, making it difficult to clearly determine in which lubrication regime the rotary lip seals actually work. Hence, according to Figure 2-2, rotary lip seals may operate under the mixed lubrication regime which is the transition regime between the elastohydrodynamic and the boundary lubrication. In that region both asperity contact and hydrodynamics are of a similar magnitude so both must be considered. In other words, the friction force in rotary lip seals is influenced by two terms, one constant and another one velocity-dependent. The first and second terms explain why the frictional torque-velocity curve shown by Wennehorst [15] in Figure 2-4 and the μ-normal load curve of Jagger [13] shown in Figure 2-2 each present a non-zero ordinate intercept.

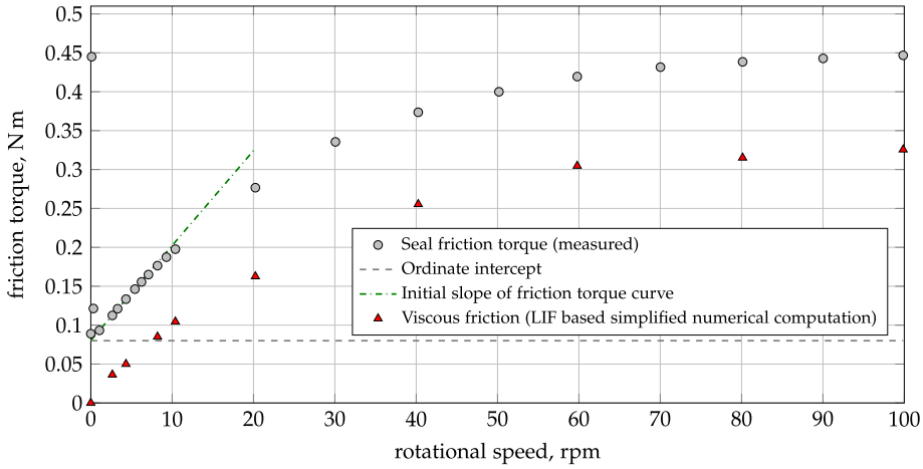

Figure 2-4. Friction-velocity curves presented by Wennehorst [15]. *The experimental measurements present a non-zero ordinate intercept.*

Wennehorst attributes the velocity-independent friction to a second order μ-EHL instead of to direct asperity contact [15]. Although direct asperity contact may occur, lubricated contacts do not often show adhesion due to the physisorbed or chemisorbed or chemically reacted films generated in the contact pair [16].

Stakenborg tested rotary lip seals on a transparent shaft [20] and observed lubricant cavitation on the contact when the shaft was rotated beyond a particular shaft angular velocity. The location of the cavitating region varied with the shaft velocity. The cavitation started on the back side of the seal pointing towards a hydrodynamic phenomenon, not a thermally-induced phenomenon.

A complementary argument against the initial belief in a tight leak-free seal is the reverse pumping mechanism shown in Figure 2-5. This is an inherent characteristic of rotary lip seals also referred as back, inwards or upstream pumping mechanism [2]. Rotary lip seal manufacturers realized that the rotation of the shaft induces the transport of lubricant from one side of the seal to the other [22]. Typically this mechanism drives the oil from the back side to the spring side of the seal. Kawahara [23] conducted an extensive study on the reverse pumping of the rotary lip seals. A specific testing

procedure was developed to measure the reverse pumping capacity of a seal [6]. The test consists in applying a precise amount of lubricant to the back side of the seal with a syringe and measuring how long it takes for the lubricant to travel to the other side of the seal (see Figure 2-5). Kawahara defined a suction coefficient for rotary lip seals and related it to the circumferential displacement of the tip of the seal. When the frictional torque is simultaneously monitored, a clear decrease in friction is experienced while the liquid is being pumped. If the seal were to be tightly pressed against the shaft, no flow could develop. Rotary lip seals are sometimes referred to as leakage-free seals [24], but this is a misnomer. Even when sealing air-to-liquid, air is pumped to the spring side [22], [23]. This becomes clear when sealing a liquid-to-liquid interface. Jagger [13] dyed the lubricants at each side of the seal using two different colours and he observed that a lubricant mixture was found at both sides of the seal. In fact, rotary lip seals cannot separate two liquids effectively [6], [25].

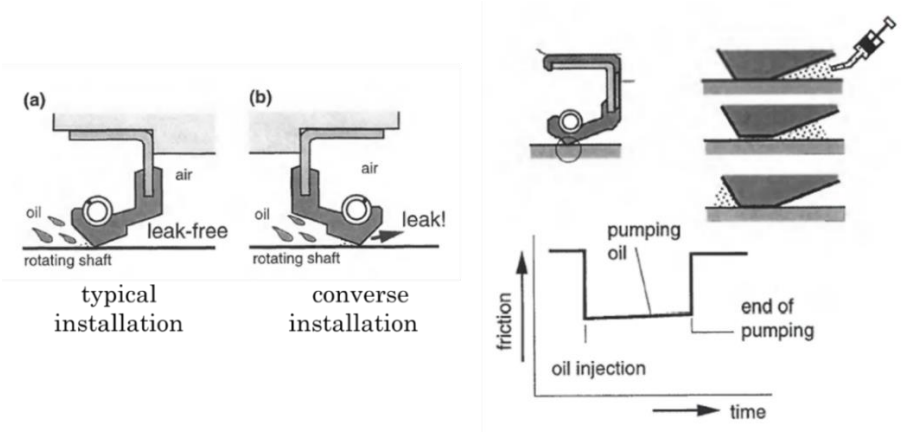

Figure 2-5. Inwards pumping ability of rotary lip seals (left) and syringe pumping test (right) [21].

Direct measurements of the film thickness were attempted by several authors using a wide range of techniques. Electrical resistance, capacitance, laser induced fluorescence technique [15] or magnetic fluids [26], among others, have been used to measure the separation between the seal and the shaft. Typically, the film thickness measurements found in literature range from 0.1 to 5 micrometres. Pol and Gabelli [26] tuned the rotary seal system to promote the hydrodynamic action. They showed that by increasing the fluid viscosity, lowering the load and widening the contact, they could

generate a fluid film thickness of 10 μm, i.e. unequivocally operating under the full film lubrication regime. Although the seal was modified, they successfully proved that microscale hydrodynamics could fully carry the lip seal radial force, leading to a continuous lubricant film. Recently, Wennehorst [15] showed film thicknesses way smaller than the combined roughness of the counterparts, i.e. $\lambda_p < 1$ (see Figure 2-6). Despite the low lambda ratio, the seal material conforms over the shaft, leading to a new surface topography that may prevent the direct asperity contact.

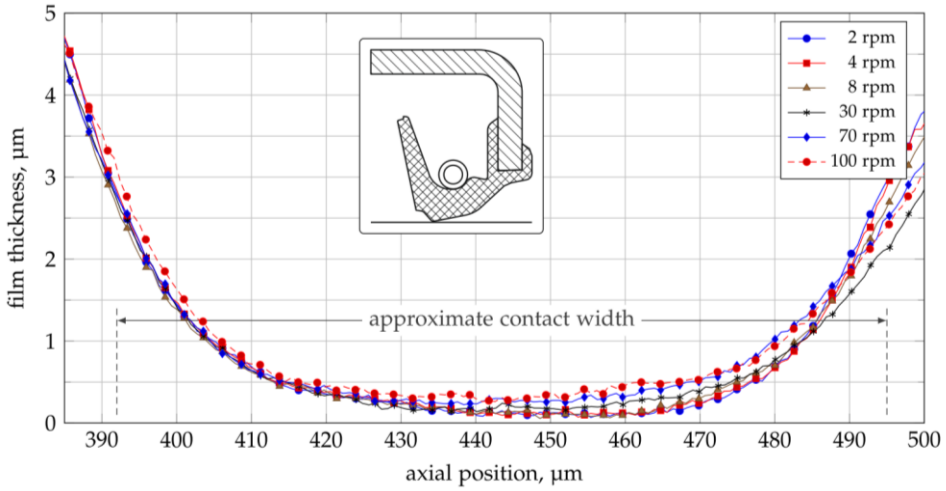

Figure 2-6. Average film thickness profiles at different rotational speeds presented by Wennehorst [27].

To conclude, hydrodynamics were repeatedly evidenced in the operation of rotary lip seals. Nevertheless, the two questions posed by Salant [14] still prevail nowadays: what is the source of the hydrodynamics? If a partial or complete separation develops in rotary lip seals, why do rotary lip seals show zero leakage?

2.1.2. Operating mechanism of rotary lip seals

The evidence of hydrodynamic action on the seal-shaft interface puzzled the researchers for decades. The hydrodynamic pressure developing within a thin film of liquid flowing between two plates is captured via the widely-known Reynolds partial differential equation (PDE). The one-dimensional generalized Reynolds equation is shown

in Eq. 2-1. The right hand side (RHS) terms of the formula describe the pressure-generation mechanisms contributing to the generation of a micrometres-thin liquid layer [28].

$$\frac{\partial}{\partial x}\left(\frac{\rho h^3}{12\eta}\frac{\partial p}{\partial x}\right) = \frac{h(u_a+u_b)}{2}\frac{\partial \rho}{\partial x} + \frac{\rho h}{2}\frac{\partial}{\partial x}(u_a+u_b) + \frac{\rho(u_a+u_b)}{2}\frac{\partial h}{\partial x} + \rho\left(w_a - w_b - u_a\frac{\partial h}{\partial x}\right) + h\frac{\partial \rho}{\partial t} \qquad \textit{Eq. 2-1}$$

The wedge term $\frac{\rho(u_a+u_b)}{2}\frac{\partial h}{\partial x}$ is the primary pressure build-up mechanism in hydrodynamic components such as journal bearings, thrust bearings and reciprocating seals. To achieve a reasonable amount of fluid load-carrying capacity a convergent gap profile such as a wedge in the direction of the velocity is usually required. Further insight into the Reynolds PDE terms is described in *Section 5.3* of this thesis. Rotary lip seals do not show a wedge profile in the circumferential direction and therefore alternative hydrodynamic pressure generation mechanisms must be considered.

In the late 1980s, the dominant role of the surface roughness of the seals to leakage was detected [29]. Horve noticed that the seals that exhibited a large amount of asperities on the contact surface, i.e. after the seal has run in, showed a more reliable operation and longer service times than the ones with few asperities (see Figure 2-7). The determining role of roughness directed researchers into the microscopic scale to explain the hydrodynamics observed in the seal-shaft interface. Even today, the operation of rotary lip seals is explained via micro-hydrodynamic lubrication. When the shaft rotates, the microscopic wedges left between the seal and shaft asperities suffice to generate hydrodynamic action. Such pressure build-up suffices to partially or totally carry the radial load of the seal [30].

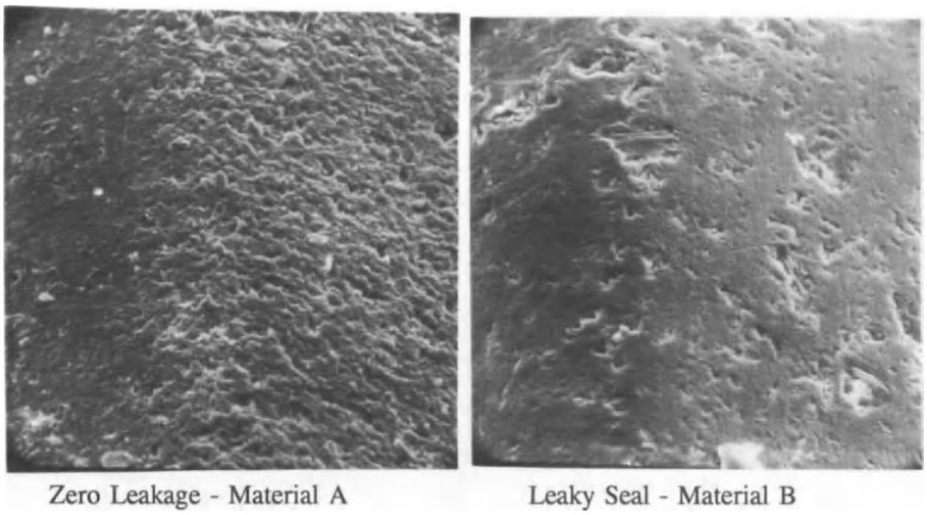

Figure 2-7. Roughness profile of a well-functioning seal and a leaky seal [29].

Horve [29] also noticed that the surface roughness is substantially different before and after testing a rotary lip seal. The elastomer formulation, the manufacturing method and the running-in process determine whether enough micro-asperities are generated on the seal surface, i.e. after peeling off the outer layer of the seal [19]. A too smooth shaft surface would not peel off the elastomer surface sufficiently while an excessively rough shaft surface profile would further wear the seal, both leading to premature failure. The adequate hardness and roughness parameters for the seal counter face are usually specified for the seal suppliers. The lead on the shaft surface was shown to also play a role in the leakage rate of a seal. To achieve a lead-free machining treatment, shafts are often plunge ground and roller burnished [3]. Note that the softer seal material deforms over the shaft surface, ultimately taking on the shaft roughness profile. Furthermore, Kunstfeld [3] showed that the deformation of the asperities is partially plastic as the reverse pumping ability of seals that have been run in one direction and then reversed is lower than that of seals that have been operated exclusively in one direction.

It was observed that both the direction and the magnitude of the reverse pumping were linked to the morphology of the contact pressure profile between the seal and the shaft [2]. Kawahara [23] showed that an asymmetric contact pressure profile between the seal and the shaft induces a flow rate in the direction of the maximum pressure on the

profile, see Figure 2-8. He showed that the suction (upstream pumping) of a rotary lip seal depends on the tangential distortion of the lip. On the other hand, a seal with symmetric contact pressure profile does not pump in any direction. As explained in 2.1.1, even when no oil is left to pump to the back side of the seal, air ingress to the spring side occurs [29]. The midline where the maximum pressure profile develops is often referred as the equator of the sealing contact.

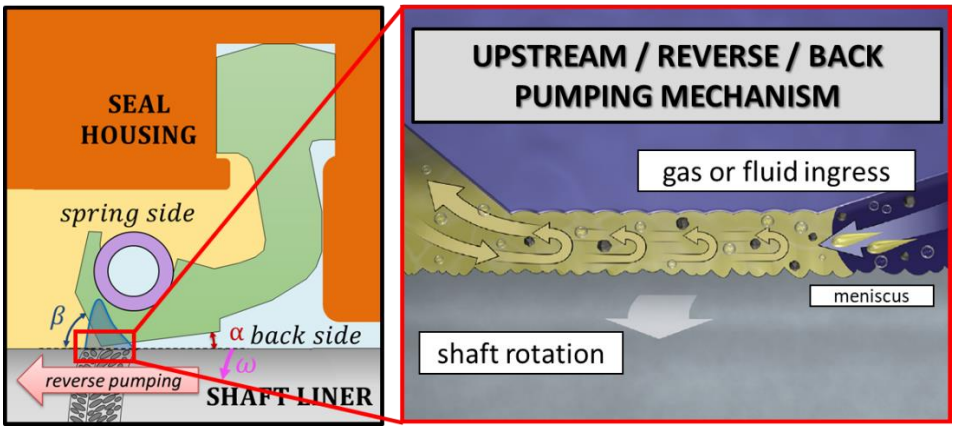

Figure 2-8. Reverse pumping mechanism. Based on [31].

Kamüller and Kawahara [23] measured the tangential displacement of the seal tip as a consequence of the contact pressure distribution. The non-symmetric pressure profile common in lip seals leads to a non-uniform circumferential displacement of the seal tip [32], [33]. Important manufacturing parameters like the tip angles, the position of the garter spring or the length of the beam lead to a pressure profile which determines the back pumping ability of the seal [2]. Note that this last statement connects the micro and macroscales of rotary lip seals.

The hydrodynamic and the apparently leak-free operation of rotary lip seals are both explained by the presence of hydrodynamics generated by the microscopic convergent gap profiles left between the seal and shaft asperities. The reverse pumping ability relies on the non-uniform distortion of the seal micro-asperities along the contact [6]. Due to the non-symmetric contact pressure profile, the seal asperities deform into vane-shaped ridges capable of pumping fluid in the axial direction [2]. Such an approach suggests that rotary lip seals work in a similar fashion to a set of viscous micro-pumps (or a herringbone bearing) [33].

The location of the equator of the pressure profile determines which is the overall direction of the axial flow. Whether or not these flattened ridges develop depends on the seal topography, the amount of drag (tangential load) and the elastomer properties. Such an approach can explain both the lift-off and the leak-less operation of rotary lip seals. Whether the hydrodynamic pressure build-up is sufficient to partially or completely lift the seal tip is specific to the application and the operating conditions. As the hydrodynamics develop within the asperities of the surfaces, and the seal surface is hydrodynamically distorted, rotary lip seals work under the μ-soft-EHL regime [15].

Seal researchers have hypothesized about alternative working mechanisms that could complement the generally accepted μ-soft-EHL theory. Among others, the presence of an air-liquid meniscus on the back side of the seal [20], the viscoelasticity of the seal material [34] the non-Newtonian lubricant behaviour and the seal-shaft misalignment [24], [29] are believed to contribute to the operation of rotary lip seals. Further information on the secondary working mechanisms can be found in [14], [24], [35].

2.1.3. Misalignment in rotary lip seals

In 2.1.1 the lack of a convergent gap profile in the circumferential direction in perfectly aligned seals was introduced, and it was discussed that, consequently, basically no hydrodynamic pressure can be generated. However, when the nominal parallelism is lost, a wedge profile may appear. The implications of operating under a misaligned condition were studied by a few researchers. Pinedo [36] and Tasora [37] investigated the seal-shaft misalignment of lip seals under static conditions. When it comes to its dynamic operation, the wobbling of the shaft may result in dynamic loading of the seal, leading to an oscillating frictional torque [26] (see Figure 2-9). Fazekas [38] studied the behaviour of O-rings when installed at a slant, showing lower running temperatures, higher flow rates and lower wear rates than concentric seals. Additionally, the measured frictional torque of canted O-rings is often lower and more stable [22].

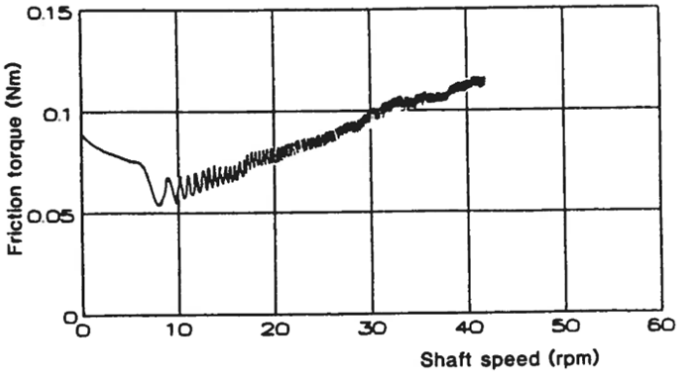

Figure 2-9. Friction torque under dynamic misalignment [26].

A few researchers noticed the implicit axial displacement of the seal tip when the seals are misaligned [6], [24], [29], [39]. Therefore, analogously to reciprocating seals, the dynamic misalignment may lead to hydrodynamics with its subsequent flow rates. Horve [29] engineered the device shown in Figure 2-10, isolating the reciprocating motion of the tip from the rotation of the shaft. He showed that no leakage developed when only the reciprocating motion of the lip occurred.

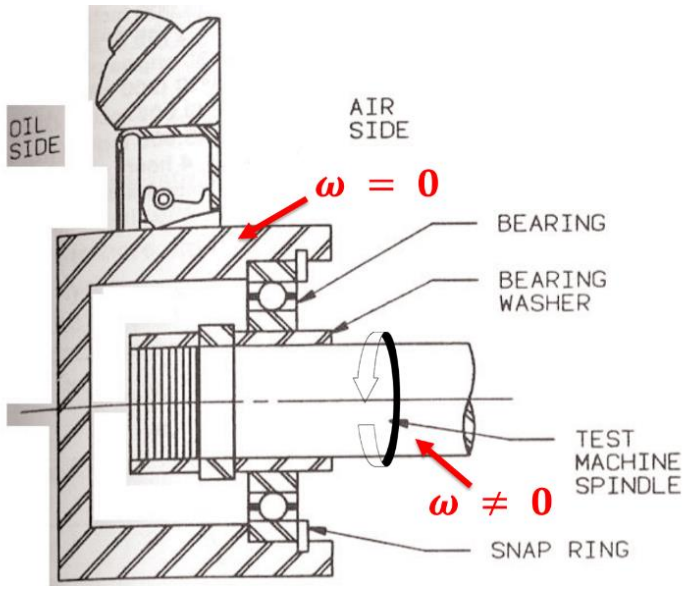

Figure 2-10. Setup for testing the pumping capacity of the reciprocating motion of the tip seal to dynamic misalignment. Based on [29].

Ishiwata [40] assumed that any rotating shaft has an indispensable eccentric motion and conducted a study on the followability of the seal. The loci of displacement of the tip of the seal were captured under various angular velocities, lip-shaft interferences and dynamic eccentricities. Softer seals showed better followability than stiffer ones and the garter spring was found to positively contribute to the seal followability. Ishiwata reported that eccentric seals leaked even when the lip accurately followed the shaft. Schuck [41] compared the frictional torque and leakage of shafts with a circular profile to shafts with triangular polygonal-profile cross section. The noncircumferential shaft profiles showed a lower frictional torque however they leaked at the lowest shaft velocities.

Sansalone [42] and Van der Vorst [43] investigated the followability of rotary seals when misaligned, considering the viscoelastic properties of the elastomeric seal. They showed that the seal followability depends to a large extent on the viscoelastic properties of the material and hence the operating temperature and its proximity to the glass transition temperature. It is concluded that the type and magnitude of the misalignment, the garter spring force and the angular velocity of the shaft determine whether there is a loss of contact between the seal and the shaft. Mokhtar [44] tested U-type rotary lip seals with oil on the spring side and air on the back side. He found that, beyond a certain combination of misalignment and shaft velocity, the seals leaked. The flow rates under radial misalignment showed a completely different trend from the flow rates under angular misalignment.

Stakenborg and Van Leeuwen [45] suggested that the delayed response of the elastomer is key to developing hydrodynamic pressure build-up (VEHD theory [34]). As the shaft velocity increases, it becomes more challenging for the elastomer to follow the contour of the shaft. At some point, the elastomer is not quick enough to close the gap between the seal and the shaft and a convergent wedge develops, leading to hydrodynamic action. Ultimately, Arai [46] studied the followability of seals under dynamic misalignment. He concluded that lubricated seals showed better response to misalignment than when operated dry. This suction effect easing the followability of the seal was explained by cavitation developing along the seal-shaft interface.

2.1.4. Modelling of rotary lip seals

The first step when modelling a rotary lip seal is analysing the seal under static conditions, i.e. when the shaft is at rest. Axisymmetric finite-element (FE) modelling is the usual approach adopted to obtain the contact pressure and area between the seal and the shaft. The complexity of these models resides in the contact algorithms, the implementation of the constitutive material model used for the elastomer and, if the energy equation is resolved, the determination of the heat convective coefficients between the components and the surroundings. The validation of these thermomechanical models is done by measuring the total radial force between the seal and the shaft [47], [48] and, occasionally, by measuring the contacting width when assembled on a transparent shaft [49], as shown in Figure 2-11 and Figure 2-12 respectively.

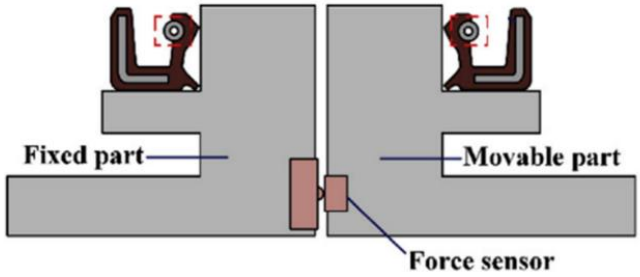

Figure 2-11. Split-shaft setup for measuring the radial force in lip seals [48].

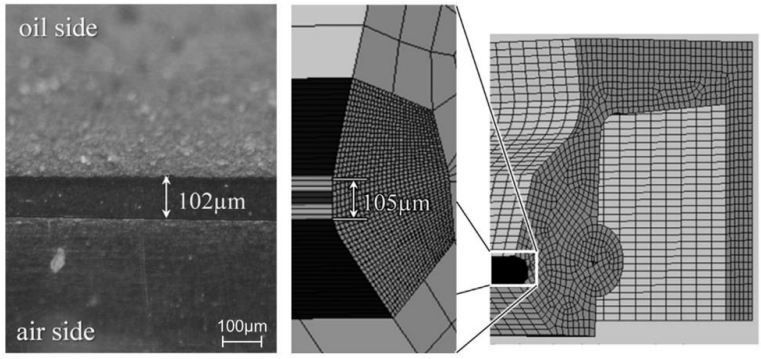

Figure 2-12. Measurement of the contact width of a rotary lip seal on a hollow glass shaft (left) and contact width on the respective FE model (right) [49].

Based on experimentation, analytical formulas were used to predict the operating conditions of rotary lip seals. The film thickness, for example, is often deduced using the equation describing the flow between two concentric cylinders – the Petroff equation [29]. Analytical formulae relating the operating condition to the frictional torque or tip temperature are usually calibrated against experimental data. Horve [50] presented an analytical model for predicting the seal pump rate due to misalignment. According to his model (see Figure 2-13), a perfectly concentric seal-shaft arrangement does not leak.

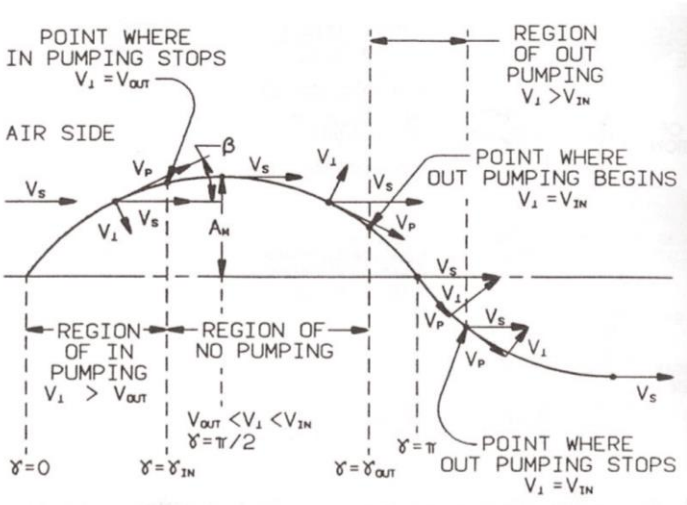

Figure 2-13. Model for misaligned seals of Horve [29]. *Sketch of the velocity components along a wavy contact profile.*

It was not until the 1990s that computational models for rotary lip seals were developed [2]. The models of rotary lip seals generally follow the same approach: the two-dimensional Reynolds PDE (or similar) is solved on a patch of the contact surface assuming fully-flooded conditions (see Figure 2-12). The results obtained on that patch are then extrapolated to the whole contact. Subsequently, the predictions of such models must be compared with the experimental results of a perfectly aligned rotary lip seal where both sides of the seal are flooded with lubricant.

The simplest hydrodynamic models (HL) solve the Reynolds PDE on a fixed gap profile. Next, the elastohydrodynamic (EHL) models include the deformation of the seal. Ultimately, thermo-elastohydrodynamic models (TEHL) models solve the energy equation and couple the

lubricant viscosity and the elastomer properties to the temperature. An extensive review of the soft-elastohydrodynamic models used in lip seals is found in [30].

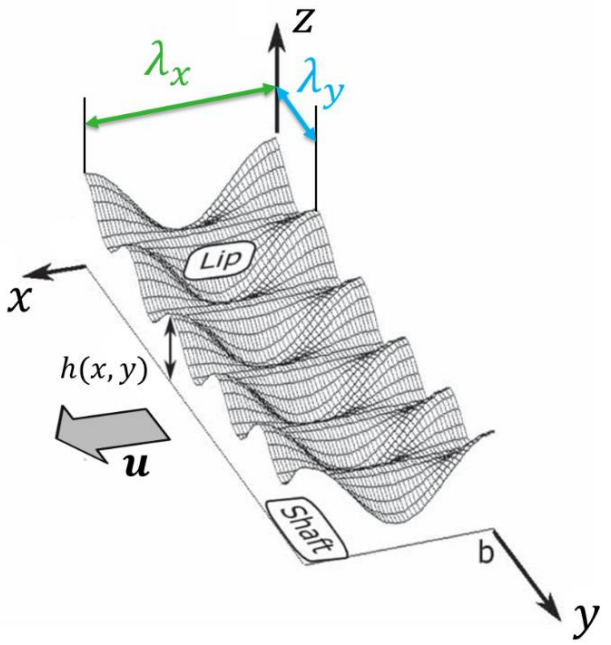

Figure 2-14. Schematic diagram of fluid film gap. Based on [51].

Gabelli [52] developed the first model of a rotary lip seal by solving the Reynolds PDE within two sliding parallel plates with a double-sinusoidal surface equivalent (see Figure 2-14). This early HL model disregarded the macroscopic deformation and focused on load-carrying capacity obtained from such a surface equivalent. Next, Salant [53] coupled the microscopic and the macroscopic scales via a radial and a circumferential stiffness matrices. This way, the radial and circumferential deformations resulting from the hydrodynamic viscous shearing could be computed. Some researchers used the Boussinesq half-space approximation to account for the seal distortion [54]. However, Elgadari [55] showed that this is inaccurate, leading to erroneous results. Therefore, the stiffness (or compliance) matrices are generally obtained with an off-line FE axisymmetric model [48], [56]–[58]. The whole idea behind reverse pumping is based on the distortion of the seal asperities due to the shearing loads, hence it is essential to account for it. Maoui [51] used a three-dimensional FE model to compute the stiffness matrices showing significantly different

pumping rates than when using the stiffness matrices obtained from axisymmetric models. Alternatively, [48], [59] account for the distortion of the lip by including flow factors in the Reynolds PDE. In other words, the flow factors depend on the circumferential distortion of the tip of the seal.

Several hydrodynamic models based on Salant [53] are found in literature testing various equivalent surfaces, e.g. one-sinusoidal surfaces [60], micro-undulations [53] and micro-asperities [61]. These models allowed the exploration of the effects of texturing the shaft [48], [56], [57], [62], [63] or the seal [64], [65] on the hydrodynamic pressure generation. The seal material have been modelled with elastic [66], hyperelastic [34], [45], [47], [56] and viscoelastic [42] constitutive material models. The effect of temperature [51] and the possible non-Newtonian nature of the lubricant [67] have also been investigated. The hydrodynamic load-carrying capacity deduced from these kinds of models shows that the assumption of full film lubrication is correct under the steady state conditions presented.

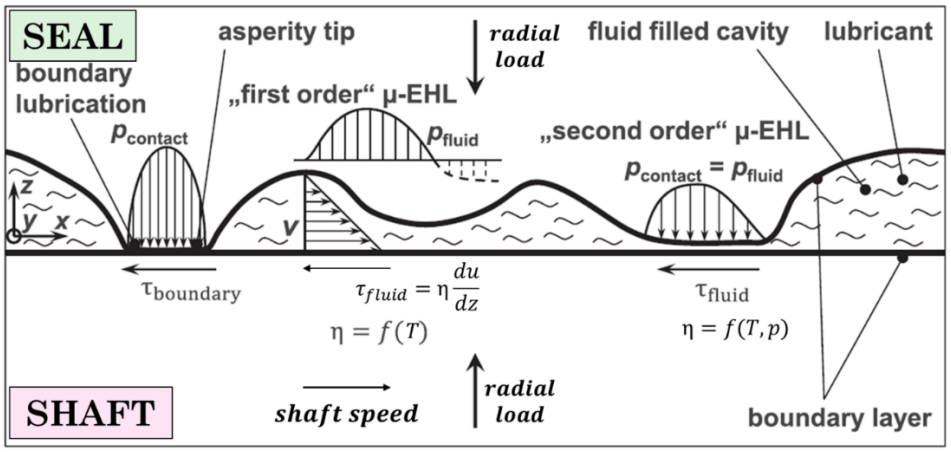

Figure 2-15. Lubrication regimes based on [27].

Mixed lubrication models have also been developed that include the contact between the shaft and seal asperities [48], [68]. Wennehorst [15] defined a second order elastohydrodynamic lubrication between the contacting parts, thereby preventing the direct asperity contact as shown in Figure 2-15. A few transient models are able to predict the film breakdown and reformation during the seal operation [68], [69]. Alternatively, a few researchers modelled the mixed lubrication regime by adding flow factors to the Reynolds PDE [70]. Most part of

the rotary lip seals operate with liquid on the spring side while air is present on the back side. The models reviewed until this point assume fully flooded conditions on both sides of the seal, hence they cannot replicate the oil-air interface typical in rotary lip seals. A few authors considered the meniscus formed on the air-oil transition [20], [71]. The validation of rotary lip seals models is complex and is generally made via frictional torque [15]. A few authors used the pumping rate predictions to validate their models [56].

Although literature on the functional behaviour of lip seals is available as mentioned above, literature on the recent Environmentally Acceptable Lubricants (EALs) is scarce. Although esters, poly-olefins and alkylene glycols have been around for years, the specific lubricant formulations (with their respective additive packages) for the stern tube application are new. Additionally, when combined with seawater, their properties may be different. Similarly, data specific to the fluoroelastomer compound used for the stern tube seal analysed is not available. The techniques used for the characterization of the lubricants and the elastomeric compound are detailed in *Chapter 3.1* and *Chapter 3.2* respectively.

2.2. Research gap

To the best of the author's knowledge, no research has been published specifically focusing on the operation of the stern tube seals, which is basically a set of large pressurized lip seals with a different fluid on each side of the seal. Up to the date of writing this thesis, there is insufficient knowledge of the actual operating conditions of stern tube seals to enable full research on these particular sealing components. As an example, the amount of water or the temperatures of the lubricant at the different sealing chambers of a stern tube are unknown. A water-in-oil emulsion may develop within the stern tube, changing the properties of the lubricating fluid and thereby conditioning the operation of the seals. Not even the static operation of a stern tube seal can be found in literature. The author believes that research on stern tube sealing technology has been kept by the original equipment manufacturers (OEMs). Hence, as part of their intellectual property, the details of the stern tube operation have not been disclosed. Although stern tube seals can be approached as large-sized rotary lip seals there is no evidence that stern tube seals work under the same principles as rotary lip seals. The poor shaft-seal alignment

and the fully-flooded operating conditions, among other peculiarities of stern tube seals, may lead to different lubrication mechanisms.

Moreover, the mechanisms governing rotary lip seals are not yet fully understood either. The complexity of measuring the actual operating conditions of rotary lip seals hampers the development of these sealing components. Such parameters as the film thickness, the contact temperature, the seal-shaft alignment, the distortion of the seal lip while running, the flow rate across the seal, the frictional torque and the actual wear rate are extremely challenging to measure. In the last 30 years significant progress has been made in understanding rotary lip seals. The hypotheses explaining the main phenomena evidenced in rotary lip seals have been consolidated (refer to 2.1.2). This approach justifies the presence of hydrodynamics, the extremely low seal wear rates and the reverse pumping mechanism. However, the secondary mechanisms described in literature suggesting alternative lubrication and sealing mechanisms have been researched to some extent [14], [35]. The validity of these secondary mechanisms [35], such as the role of the non-Newtonian nature of the lubricant, the consequences of operating under misaligned conditions and the presence of fluids vortexes, needs to be reviewed. These hypothetical secondary lubrication mechanisms are still present as the main micro-elastohydrodynamic theory cannot fully capture the behaviour observed in rotary lip seals. Additionally, the lubrication regime, i.e. whether actual seal-shaft contact occurs or not in a stern tube, is still uncertain. There is scarce research on the behaviour of lubricated rotary lip seals under misalignment [44], [72]. The few articles addressing misalignment on lubricated seals are basically experimental and their results are not conclusive. Even under static conditions, the literature on misaligned lip seals is missing [73].

When it comes to modelling, the uncertainties formulated in the former paragraph prevail. It is difficult to model what is not understood. Former researchers put all their efforts into replicating the micro-elastohydrodynamic lubrication mechanisms, hence models mirroring the secondary lubrication mechanisms are barely developed. The available models accounting for the distortion of the seal asperities are simplified by using an equivalent surface topography. Usually the hydrodynamics are estimated on a double-sinusoidal profile deduced from roughness parameters of the surface. The validity of such an equivalent surface can be questioned [15]. Models using the real surface topography are required [62], [74].

Furthermore, the validation of these kinds of models is usually done via the frictional torque. This allows for some calibration in terms of size of the characteristic cell length, fluid film thickness, surface equivalent, and, in cases of mixed-lubrication, a coefficient of friction to capture the contact between the asperities. Overall, more attention should be given to the models matching the pump rates measured across the seal. Also, the micro-elastohydrodynamic models found in literature hardly ever approach the seals running under pressurized conditions, such as stern tube seals. Additionally, the behaviour of a seal separating two liquids of different viscosities is not captured by the models found in literature. Ultimately, no attempt to model the misaligned operation of a rotary lip seal has been published in recent decades. The following research gaps were approached during this study:

- Rheological properties of the new Environmentally Acceptable Lubricants (EALs) and a comparison to traditional mineral oil-based stern tube lubricants.
- Thermo-mechanical characterization of the fluoroelastomer compound used for the stern tube seal analysed.
- Identification of the main operation mechanisms governing large-sized stern rotary lip seals, e.g. stern tube seals.
- Modelling of a stern tube seal and its validation under dynamic conditions.

This thesis analyses the operation of stern tube seals from a tribological standpoint. The focus of the research is placed on the understanding of the stern tube working principle allowing for the development of a reliable computational rotary seal model.

3. Material characterization

This chapter describes the experimental methods used to characterize the various components involved in the rotary lip seal system. The lubricant rheology (*Section 3.1*), the elastomer characteristics (*Section 3.2*), the garter spring (*Section 3.3*) and the roughness of the contacts (*Section 3.4*) are analysed in this chapter. Mathematical expressions are fitted to the results so they can be implemented in the rotary lip seal models presented in *Chapter 5*. *Paper A* relates to the rheological characterization of the stern tube lubricants. The characterization of the elastomer, the garter spring and the surface roughness analysis are shown in *Paper B* as input data for the seal axisymmetric model shown in *Section 5.2*.

3.1. Rheological properties of EALs

The rheological characteristics of the lubricant determines to a large extent the lubrication regime of the system. Therefore, a lot of attention must be paid when replacing the traditionally used mineral oil-based lubricants with the Environmentally Acceptable Lubricants (EALs). Adequate wetting characteristics between the fluid and the

solid surfaces is necessary to keep the lubricant within the contact zone. Five EALs from two different types – synthetic ester and PAO-based – have been characterized. A commonly used mineral oil-based stern tube lubricant was also included as a reference. The viscosity, the density and the surface tension of the lubricants listed in Table 3-1 were analysed and the results are shown in *Subsections 3.1.1, 3.1.2* and *3.1.3* respectively. Further information can be found in *Paper A*.

Table 3-1. Set of lubricants tested.

	Lubricant	**EAL?**	**Base Oil**	**Viscosity @ 40 °C (mm^2/s)**	**Viscosity @ 100 °C (mm^2/s)**
Lubricant 1	Supplier A	NO	Mineral	133	14
Lubricant 2	Supplier A	YES	Synthetic Ester	68	13.3
Lubricant 3	Supplier A	YES	Synthetic Ester	100	16.9
Lubricant 4	Supplier B	YES	PAO	68	13.5
Lubricant 5	Supplier B	YES	PAO	100	20
Lubricant 6	Supplier C	YES	Synthetic Ester	68	13.8

The properties were measured within the range of operating conditions expected in the stern tube seal applications. Public data on the real oil temperature within the various sealing chambers in a stern tube was not available at the time of writing this thesis. The range of temperature, pressure and shear rate considered are shown in Table 3-2.

Table 3-2. Operating conditions of stern tube seals.

	Minimum	**Maximum**
Temperature	20 °C	100 °C
Shear Rate	0 s^{-1}	10^7 s^{-1}
Pressure	cavitation pressure	10 MPa

3.1.1. Viscosity

The viscosity of lubricants is known to be dependent on temperature, pressure and shear rate. The maximum pressure expected in the stern tube seals is in the order of a few MPa, hence the viscosity dependence on the pressure was neglected as the pressure is not expected to have a large effect. For each operating condition, the temperature and shear rate were calculated on the basis of the average of five measurements. The temperature dependence of the lubricants at low shear rates was measured using the viscometer Brookfield Pro+II (Brookfield, USA) shown in Figure 3-1.

Figure 3-1. Viscometer used for measuring the viscosity at various temperatures at low shear rates.

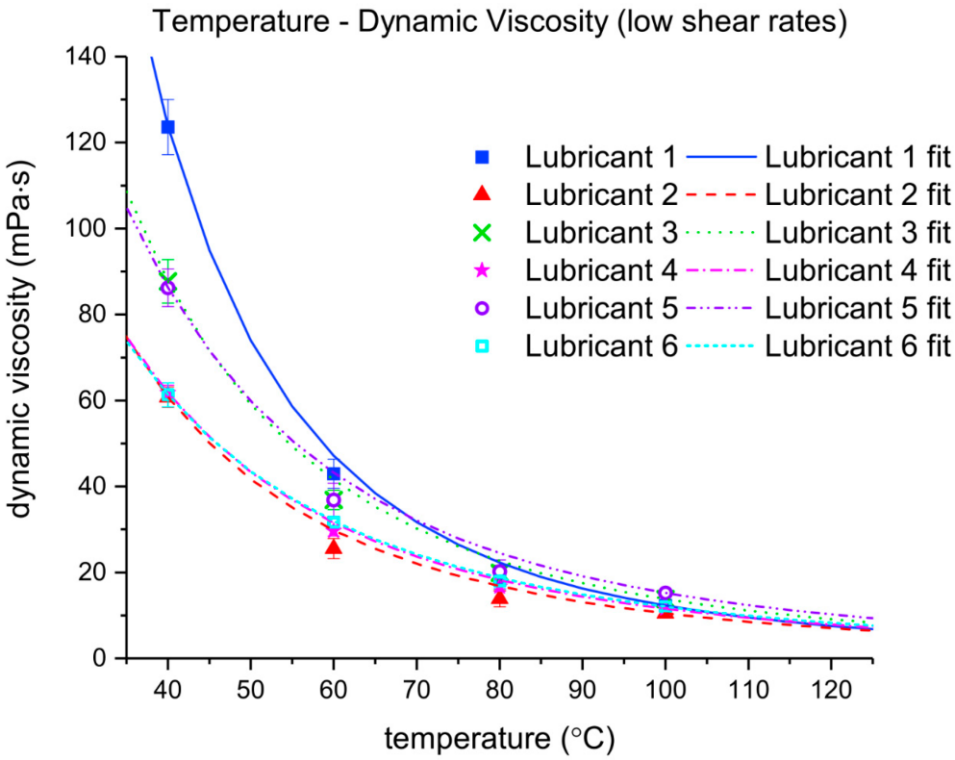

Figure 3-2. Comparison of the low shear rates viscosity at different temperatures for lubricants based on mineral oil (Lubricant 1), synthetic esters (Lubricants 2, 3, and 6) and poly-α-olefins (Lubricants 4 and 5) listed in Table 3-1. Results obtained with the Brookfield and Stabinger viscometer.

The results obtained are shown in Figure 3-2. For Newtonian fluids the Walther formula with a shift constant $\lambda_w = 0.7$ is frequently used to relate the kinematic viscosity and temperature for liquid petroleum products, see Eq. 3-1 [75].

$$log(log(\nu_T + \lambda_w)) = A_w - B_w\, log(T) \qquad \textit{Eq. 3-1}$$

The parameters obtained from fitting Eq. 3-1 to the measurements of each lubricant are listed in Table 3-3:

Table 3-3. Parameters obtained by fitting Walther's formula (Eq. 3-1) to the viscosity measurements.

	A_w	B_w	R^2
Lubricant 1	8.898	3.433	0.98
Lubricant 2	7.447	2.879	0.98
Lubricant 3	7.270	2.794	0.97
Lubricant 4	6.858	2.639	0.99
Lubricant 5	6.608	2.526	0.96
Lubricant 6	6.745	2.597	0.99

The Walther formula disregards the impact of the shear rate on the lubricant viscosity. Most rheometers do not reach the shear rate values occurring between the stern tube seal and the shaft liner, i.e. around 10^6 s^{-1} (see *Section 5.1*). The specialized Ultra Shear Viscometer (PCS Instruments, United Kingdom) shown in Figure 3-3 was used, allowing shear rates between 10^6 and 10^7 s^{-1} to be reached.

Figure 3-3. Ultra Shear Viscometer.

The measurement results obtained with the Ultra Shear Viscometer are shown in Figure 3-4. Three of the six lubricants showed a decrease in viscosity when tested at the highest shear rates, i.e. three lubricants showed shear thinning.

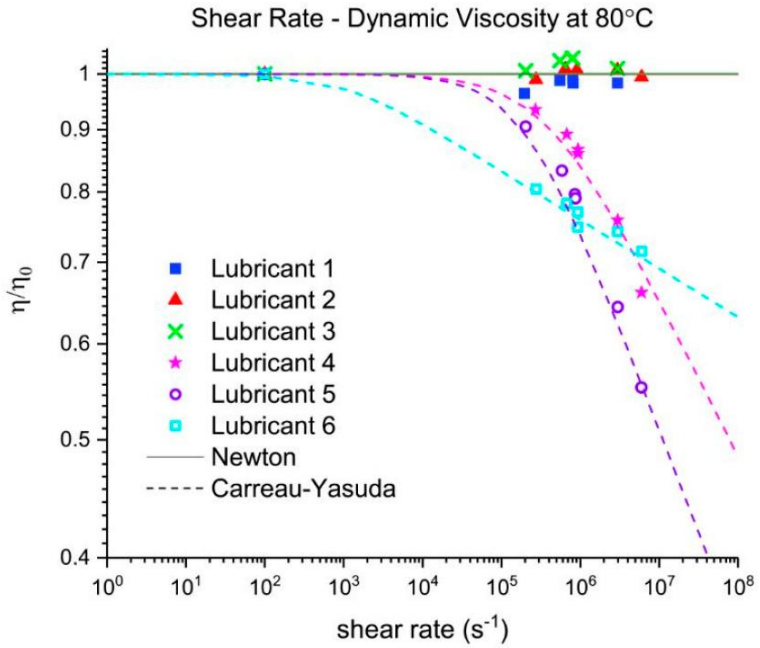

Figure 3-4. Normalized viscosity measurements at 80 °C and fitting of the Generalized Carreau-Yasuda model.

The Generalized Carreau-Yasuda model (Eq. 3-2) was chosen to model the lubricant shear thinning characteristics [76]. This relationship captures the transition between the low and high shear rates viscosities, η_0 and η_∞ respectively.

$$\eta_{\dot{\gamma}} = \eta_\infty + (\eta_0 - \eta_\infty)[1 + (\dot{\gamma}\lambda_c)^a]^{\frac{n-1}{a}} \qquad \textit{Eq. 3-2}$$

Eq. 3-2 was fitted to the three lubricants showing shear thinning, namely the lubricants 4, 5 and 6, and the parameters obtained are listed in Table 3-4.

Table 3-4. Fitting parameters of the Generalized Carreau-Yasuda model at 80 °C for the lubricants showing shear-thinning. The results are depicted in Figure 3-4.

	η_0	η_∞	a	n	$\dot{\gamma}_c = \lambda_c^{-1}$	R^2
Lubricant 4	18.06	0	0.90	0.87	3.84×10^5	0.97
Lubricant 5	24.205	0	1.06	0.83	1.92×10^5	0.98
Lubricant 6	18.54	0	1.00	0.96	0.10×10^4	0.99

To account together for the shear rate and the temperature dependencies on the viscosity an Arrhenius-shaped temperature-dependent term [77] was included in the Generalized Carreau-Yasuda model (Eq. 3-3).

$$\eta_{T,\dot{\gamma}} = \eta_{T,\infty} + \left(\eta_{T,0} - \eta_{T,\infty}\right)\left[1 + \left(\dot{\gamma}\lambda_c e^{\frac{T_0}{T}}\right)^a\right]^{\frac{n-1}{a}} \qquad \textit{Eq. 3-3}$$

In the same fashion as before, the parameters obtained from fitting lubricants 4, 5 and 6 to Eq. 3-3 are shown in Table 3-5.

Table 3-5. Fitting parameters of the temperature-dependent Generalized Carreau-Yasuda equation for the lubricants showing shear thinning.

	η_0	η_∞	a	n	$\dot{\gamma}_c = \lambda_c^{-1}$	T_0	R^2
Lubricant 4	η_T	0	0.9	0.7	2.9×10^{11}	4200	0.96
Lubricant 5	η_T	0	0.8	0.75	2.6×10^{11}	4500	0.98
Lubricant 6	η_T	0	1.0	0.95	5.0×10^9	4700	0.92

Figure 3-5 shows the lubricant viscosity predictions of Lubricant 5 obtained by using Eq. 3-3 with the parameters shown in Table 3-5. For the temperatures measured, it can be seen that the model can describe the measurement results well. The model also makes it possible to extrapolate viscosity data to temperatures where no measurements have taken place, as can be seen in Fig. 5.

At the end of each testing sequence, each lubricant sample was tested one last time at the initial shear rate, 10^6 s^{-1}. The viscosity of a sample that has undergone a wide range of shear rates is measured. In this way, the nature of the viscosity decrease, temporary or permanent, can be investigated. Table 3-6 shows that the lubricants recovered their initial viscosity after being tested at the highest shear rates, hence showing the reversible nature of the shear thinning.

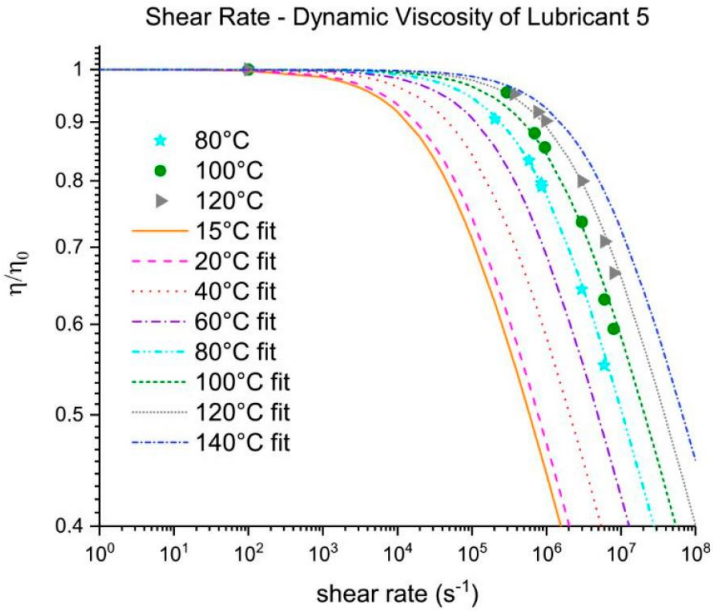

Figure 3-5. Normalized viscosity of Lubricant 5 as a function of the shear rate using the temperature-dependent Generalized Carreau-Yasuda expression (Eq. 3-3).

Table 3-6. Relative permanent viscosity loss after being tested.

	Viscosity Loss
Lubricant 1	-0.75%
Lubricant 2	0.09%
Lubricant 3	-0.17%
Lubricant 4	-1.02%
Lubricant 5	-0.54%
Lubricant 6	-3.60%

3.1.2. Density

The density of each lubricant listed in Table 3-1 was measured using a Stabinger viscometer SVM 3000 (Anton Paar, Austria). As well as the density, the device also provides the dynamic viscosity of the sample at 10^2 s^{-1}. The results are shown in Figure 3-6.

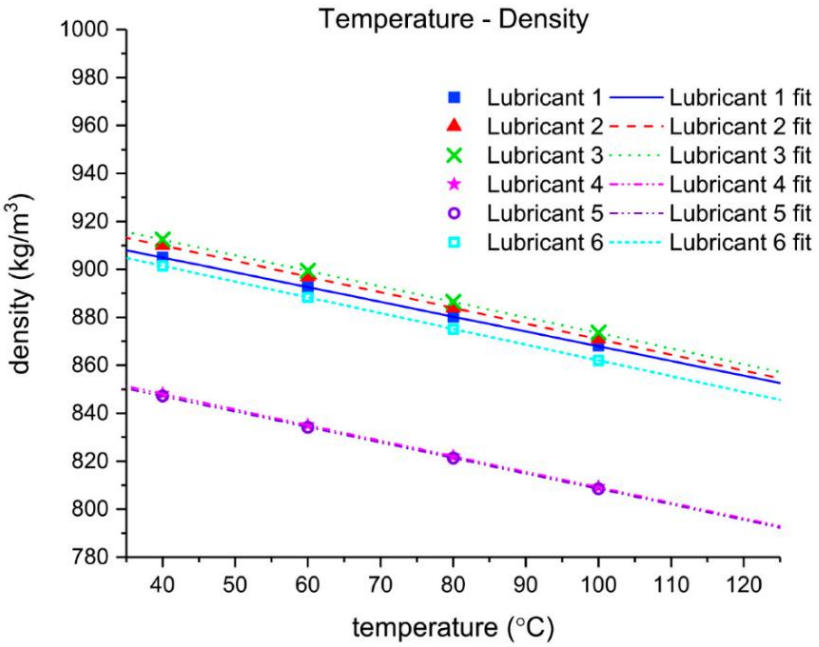

Figure 3-6. Density measurements of the lubricant listed in Table 3-1.

As depicted in Figure 3-6, the density shows a linear relationship with the temperature, which is to be expected. Hence a linear function fitted the density measurements according to Eq. 3-4.

$$\rho_T = \rho_{T_0} + k_\rho (T - T_0) \qquad \textit{Eq. 3-4}$$

The parameters obtained from fitting Eq. 3-4 to the measurements are listed in Table 3-7 showing a great accuracy for the linear regression.

Table 3-7. Parameters obtained from fitting the density measurements.

	k_ρ	$\rho_{T_0=0°C}$	R^2
Lubricant 1	-0.616	929.56	0.99
Lubricant 2	-0.652	936.09	0.99
Lubricant 3	-0.649	938.37	0.99
Lubricant 4	-0.649	874.02	0.99
Lubricant 5	-0.645	872.95	0.99
Lubricant 6	-0.657	927.74	0.99

3.1.3. Surface tension

The Wilhelmy plate method was used to measure the surface tension γ_L of the lubricants listed in Table 3-1. A DCAT11 tensiometer (DataPhysics, Germany) was used and the results are shown in Figure 3-7. Additionally, to explore the interaction of the lubricants with the seal material, a droplet of each lubricant was placed on a sheet of the seal material and the resultant contact angles were measured. No significant difference in contact angle was observed between the Environmentally Acceptable Lubricants (EALs) and the traditional mineral oil-based lubricant. Therefore, all the lubricants listed in Table 3-1 showed a similar wetting capability on the fluoroelastomer compound used for the stern tube seal.

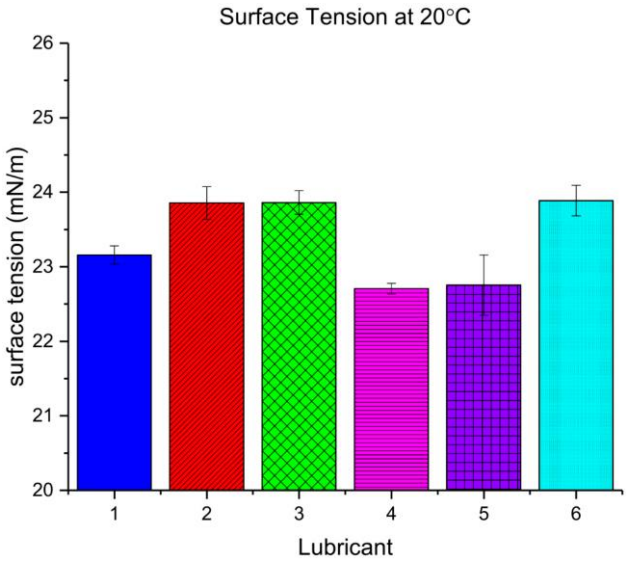

Figure 3-7. Surface tension measurements at room temperature.

3.1.4. Conclusions

Five EALs and one mineral oil-based stern tube lubricants were characterized in terms of viscosity, density and surface tension. Temperature-wise, the viscosity of the five EALs was shown to behave similarly to the mineral oil-based lubricant between 20 °C and 100 °C. As expected from their higher Viscosity Index (VI), the temperature-dependence of EALs is less than for the mineral oil tested. Under shear rates larger than 10^6 s^{-1}, some of the lubricants showed a temporary

viscosity decrease of up to 40%. The shear thinning could not be attributed to a specific type of EAL: both PAO-based and ester-based lubricants showed this characteristic. This may result from the specific type of Viscosity Index Improvers (VII) used for the formulation of each lubricant. The density of the PAO-based lubricants was shown to be lower than both the mineral oil-based and the ester-based lubricants. The surface tension of all the lubricants was found to be between 22 and 24 mN/m. For the interested reader, further information on the lubricant characterization can be found in *Paper A*.

3.2. Seal material

No material data was available for the particular fluoroelastomer used in the stern tube seal. Therefore, the fluoroelastomer compound was characterized extensively. The ultimate goal is to calibrate a constitutive model capturing the behaviour of the elastomer compound to be used in the finite element (FE) model of a seal. Hence, the number of tests required depends directly on the characteristics of the constitutive material model selected [78]. The simplest linear elastic homogeneous model is usually not sufficient to capture the response of elastomeric materials. The stress in elastomers is linearly proportional to strain only for very low strain values. Elastomers, especially when reinforced, show a different stress-strain path when loading them than when unloading them. The source of the hysteresis is the internal friction constraining both the extension and the contraction of the elastomer [79]. Furthermore, elastomers show a particular response depending on the loading mode, i.e. the stress-strain curve under uniaxial tension is different from the stress-strain curve under uniaxial compression [80]. Filled elastomers also show the so-called Mullins effect, consisting of a softening of the elastomers during its first stretches until their stress-strain response becomes stable [79]. The number of cycles to overcome the Mullins effect needs to be determined experimentally. Consequently, the stress-strain characteristic depends on the maximum strain previously encountered. The inherent viscoelasticity of the seal will relax the seal material when mounted on the shaft, leading to a lower sealing force in time [2]. The material will also creep when loaded. Ultimately, elastomers show strain rate dependency which means that the material stiffens when rapidly strained, so subjected to a high strain rate [78]. The relative contribution of the viscous component of the elastomer is directly related to the operating temperature or, more

accurately, to the temperature difference between the operating temperature and the elastomer glass transition temperature T_g [80]. Besides the inherent theoretical complexity of elastomers, practical issues arise when testing: the homogeneity of the mixture, the degree of curing, the anisotropy of the material, the dimensional accuracy of the samples and the testing apparatus can impact the results. It is imperative to establish a systematic meticulous method for the characterization of the elastomers to ensure the reliability and consistency of the results.
The first option considered was extracting the material samples from finished seals. That approach is convenient as the material tested is unequivocally the same one used in the real application. Unfortunately, the various samples cut out from the seals were shown to be significantly different; this was attributed to the cutting method. Additionally, the non-uniform curing of the final parts may also have influenced the results. The thick seal body becomes a challenge during the curing stage [81]. The poor thermal conductivity of elastomers leads to an uneven temperature distribution on the part being cured. This results in a poorer curing state on the core than on the outer regions of the seal. Therefore, if two suppliers use different curing times and temperatures, the final properties of an elastomer component can easily differ. Consequently, the material samples used for the tests were produced and stamped from independently cured material sheets. The curing of such specimens is easily guaranteed and consistency in the results was achieved.

3.2.1. Fluoroelastomer compound testing

Three different loading modes, namely simple tension, simple compression and planar extension, were implemented to characterize the fluoroelastomer compound used for the stern tube seal.

Simple tension test

The viscoelastic nature of the fluoroelastomer compound was investigated using a tensile tester BZ1.0/TH1S (Zwick/Roell, Germany). The characterization method shown in Figure 3-8 [82] was implemented, so the Mullins effect, the hysteresis and the viscoelasticity of the elastomer were analysed. Dumbbell B-type specimens were stamped from cured FKM compound sheets. The tests started by acclimatizing the sample at the testing temperature T_{test} for ten minutes. The tester load was zeroed and the sample clamped on

the tensile tester. Next, the contacting extensometers were positioned and a pretension of 0.1 MPa was imposed.

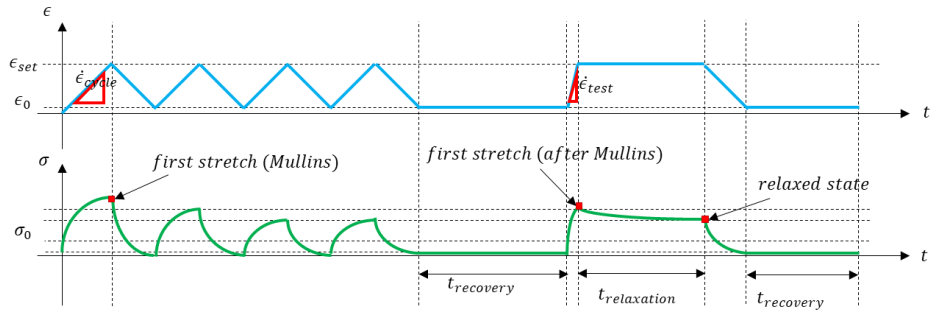

Figure 3-8. Testing sequence for a specific strain ϵ_{set}, strain rate $\dot{\epsilon}_{test}$ and testing temperature T_{test}.

The samples were initially loaded and unloaded up to a strain ϵ_{set} at a particular strain rate $\dot{\epsilon}_{cycle}$. This cycle was repeated until repeatable curves were obtained. After cycling, the specimens was left to recover at zero stress for a specific amount of time $t_{recovery}$. Previous characterization experiments showed that four cyclic loads suffice to the overcome the Mullins effect, reaching consistent stress-strain curves. Once the sample recovered, the specimen was once more deformed to the same strain ϵ_{set} at a specific strain rate $\dot{\epsilon}_{test}$. The strain ϵ_{set} was kept for a specific time $t_{relaxation}$ to study the relaxation of the material under a specific strain. After the relaxation, the material was left to recover at zero stress a second time. Once the cycle for a specific ϵ_{set} was completed the whole sequence was repeated for a larger strain. This way the Mullins effect, the strain rate dependency and the relaxation characteristics of the elastomer were independently captured. A sketch with the stress-strain curves obtained with the methods explained above are shown in Figure 3-9. The sequence was repeated for various temperatures T_{test} and strain rates $\dot{\epsilon}_{test}$.

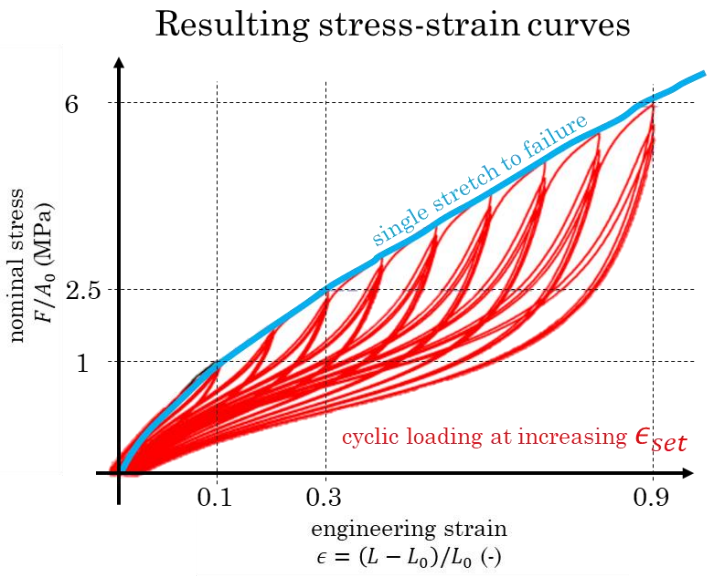

Figure 3-9. Sketch of stress-strain curves resultant from a testing sequence.

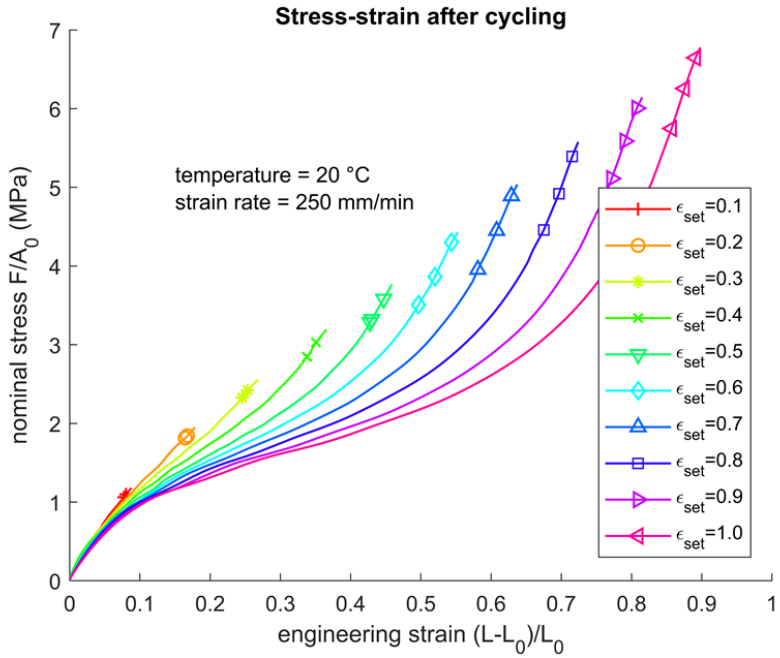

Figure 3-10. Stress-strain curves after Mullins and recovery at 20 °C (loading strain rate of 250 mm/min).

Figure 3-10 shows the results from the first stretch after recovering from the cyclic loading shown in Figure 3-8. It is observed that the stress-strain curve is to a considerable degree dependent on the largest strain situation the specimens have reached. In other words, the highest strain value that the seal has ever undergone.

The stress relaxation of the specimen after cycling at various strains is shown in Figure 3-11. This corresponds to the $t_{relaxation}$ period in Figure 3-8. The stress decay is normalized showing the non-linear viscoelastic nature of the material, i.e. the amount of relaxation depends on the amount of strain imposed up to +0.6 strain. Above +0.6 strain, the stress decay is approximately the same.

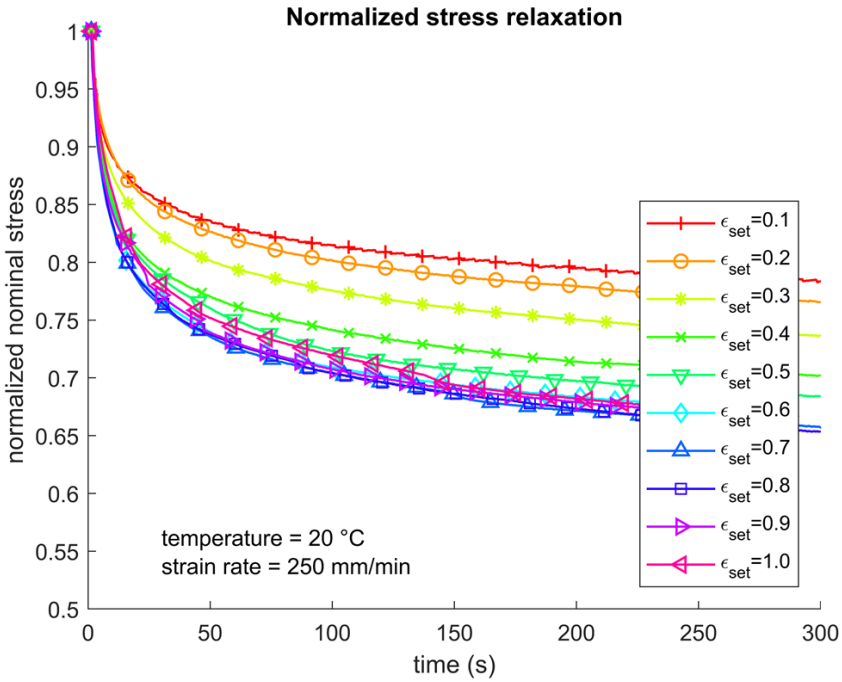

Figure 3-11. Normalized stress relaxation at various strains at 20 °C (loading strain rate of 250mm/min).

The effect of temperature on the elastomer response was also investigated. Following the same testing sequence, the temperature of the testing chamber was varied between 20 °C and 100 °C. Figure 3-12 shows the relative stress decay during the relaxation stage shown in Figure 3-8. A decrease of the viscous component with temperature is observed.

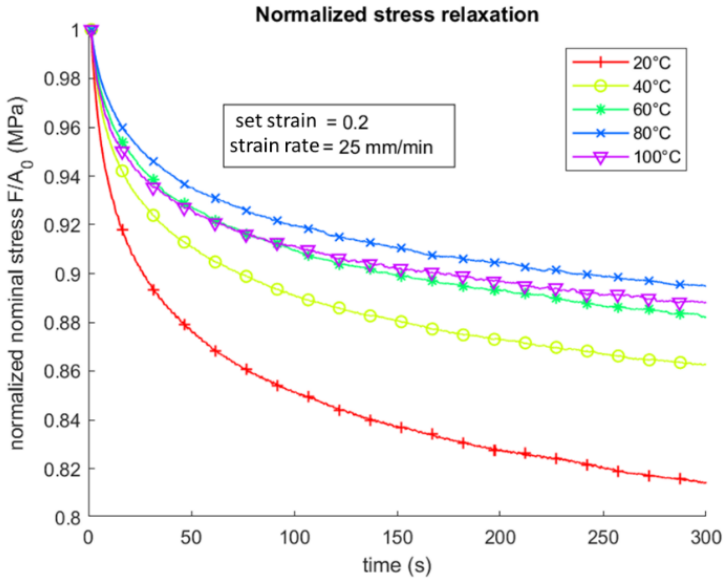

Figure 3-12. Normalized stress relaxation at various temperatures.

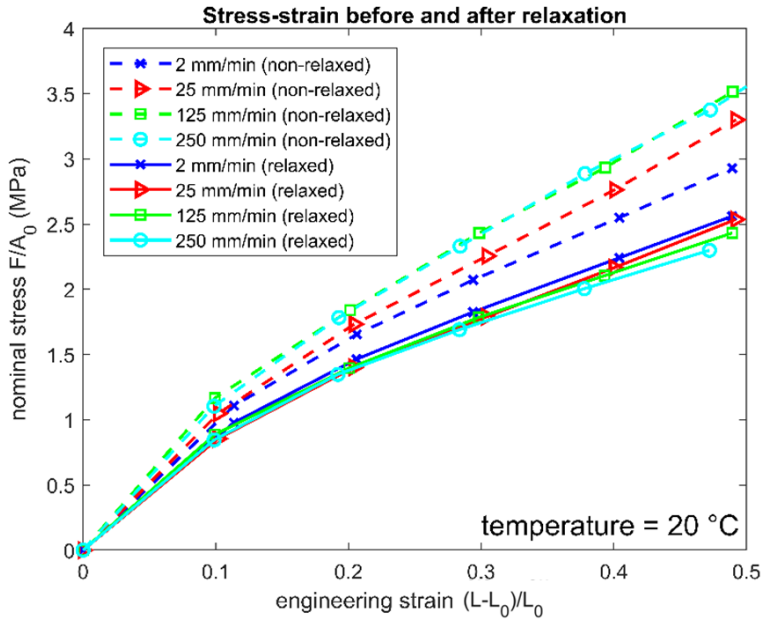

Figure 3-13. Stress-strain curves obtained by taking the maximum and the minimum stress value to build the non-relaxed and relaxed curves respectively.

Ultimately, the "non-relaxed" and "relaxed" stress-strain curves can be built as described in [82]. Using the stress-strain pairs of values at the beginning and end of the relaxation test for each strain shown in Figure 3-11, the "non-relaxed" and "relaxed" curves shown in Figure 3-13 were obtained. Notice that the relaxed stress situation after five minutes is independent of the strain rate used to bring the specimens to the set strain ϵ_{set}.

Compression test

Uniaxial compression tests were conducted to determine the response of the FKM filled compound to compressive loads (see Figure 3-14). The platens were lubricated to reduce the friction in the metal-elastomer interface.

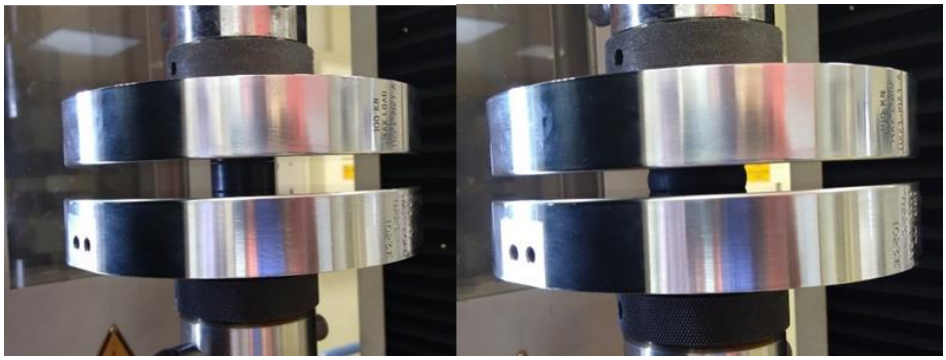

Figure 3-14. Uniaxial compression tests.

The specimen buttons were cycled up to -0.3 strain, showing a higher stiffness under compression than under tension.

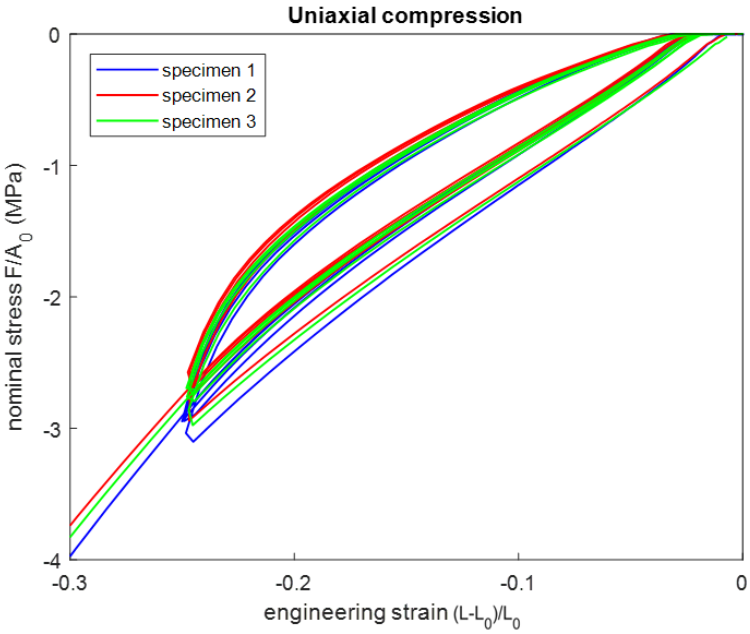

Figure 3-15. Cyclic loading of the fluoroelastomer compound under compression up to -0.3 strain at 20 °C.

Dynamic Mechanical Analysis (DMA)

Further, a DMA Gabo Eplexor 2000N (Netzsch, Germany) was used to get further insight into the temperature and frequency dependence of the fluoroelastomer compound. The results of a temperature sweep from -80 °C to 120 °C at a frequency of 2 Hz and 1% strain is shown in Figure 3-16. The proximity of the glass transition temperature T_g to the normal operating temperature makes the elastomer undergo a certain amount of temperature softening up to a temperature of 50 °C where the rubbery plateau is reached.

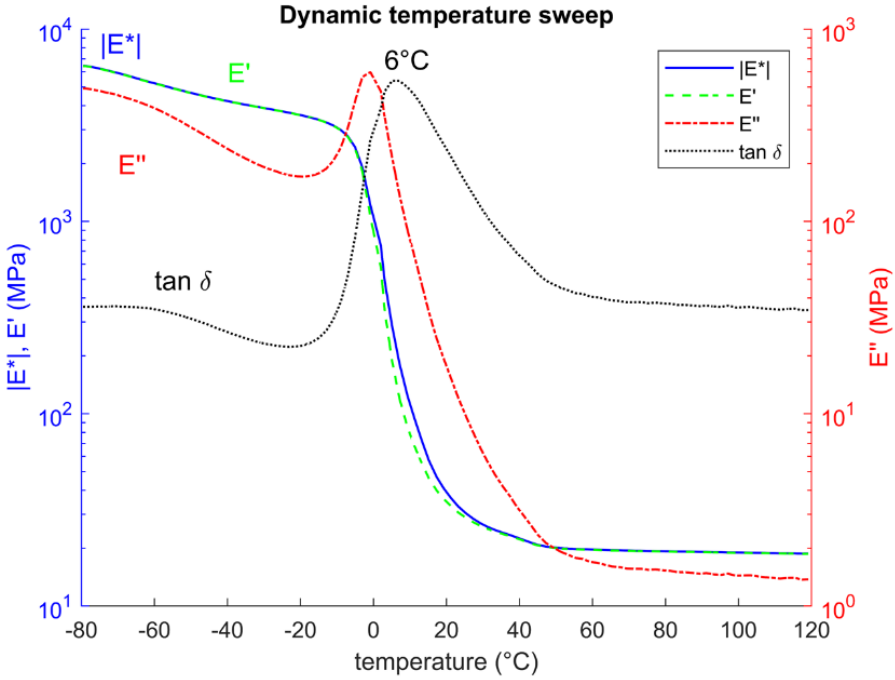

Figure 3-16. Dynamic mechanical analysis (DMA) temperature sweep.

3.2.2. Constitutive material model

A wide variety of constitutive material models are available in literature. The more sophisticated the model, the larger the number of specialized tests required for its calibration [78]. The best solution is to choose the simplest model that gives sufficiently accurate results for the application. As stern tube seals are expected to work for a few years, it was considered more relevant to focus on the relaxed state of the material instead of the initial state. Furthermore, by assuming that the seal sits on the shaft and no significant variable loads are applied to it, the viscous component was disregarded, making it feasible to use time-independent hyperelastic models. In fact, hyperelastic models are the most common material models used for modelling elastomeric seals [37], [49], [74], [83]. Therefore, a hyperelastic model was fitted to the "relaxed stress-strain curve" built from the characterization experiments shown in *Subsection 3.2.1*. The experimental results showed that the material stiffness is highly dependent on the maximum strain the samples had reached, i.e. the all-time maximum strain value up to which the Mullins softening

occurred. Note that stern tube seals are stretched beyond their mounting disposition when installed and that this maximum strain will impact the radial force exerted by the seal.

The hyperelastic Yeoh model was chosen for its simplicity as it depends only on the distortional part of the first invariant of the right Cauchy-Green tensor I_1^*. The strain energy density function of the Yeoh model is shown in Eq. 3-5 [78].

$$\psi(I_1^*) = \sum_{i=1}^{3} C_{i0}(I_1^* - 3)^i + \frac{\kappa}{2}(\mathrm{J} - 1)^2 \qquad \textit{Eq. 3-5}$$

$$I_1^* = \mathrm{J}^{\frac{3}{2}}(\lambda_1^2 + \lambda_2^2 + \lambda_3^2) \qquad \textit{Eq. 3-6}$$

$$s = \frac{2}{\mathrm{J}}[C_{10} + 2C_{20}(I_1^* - 3) + 3C_{30}(I_1^* - 3)^2]\mathrm{dev}[\mathbf{b}^*] + \kappa(\mathrm{J} - 1)\mathbf{I} \qquad \textit{Eq. 3-7}$$

The Yeoh hyperelastic constitutive material model is fitted to the relaxed stress-strain curves, yielding the Yeoh parameters C_{10}, C_{20} and C_{30}. The temperature of the oil in a stern tube is assumed to be constant and equal to 20 °C. Due to the poor thermal conductivity of the seal material, this implies that the temperature of most parts of the seal is also approximately 20 °C (see in *Section 5.1*). The seal material was therefore left temperature independent. The tension and compression curves obtained at 20 °C were used for the calibration of the model. The fitting of the curves was conducted using Abaqus/CAE® software and the parameters obtained are listed in Table 3-8. The final calibration of the constitutive model was done against the radial force results obtained with the split-shaft setup, to be explained in *Section 4.1* [27]. The models' predictions were towards the lower end of the radial force measurements and representative only of the seals exhibiting a lower radial force. There are several issues that can cause the spread on the seal-shaft radial force measurements: the dimensional accuracy of the seal (e.g. shrinkage), seal-shaft misalignment, friction while testing or the curing state of the seals.

Table 3-8. Parameters used for the Yeoh hyperelastic model.

Hyperelastic Yeoh parameters		
Parameter	C_{10}	2.50 MPa
Parameter	C_{20}	-0.61 MPa
Parameter	C_{30}	0.54 MPa
Bulk modulus	κ	10^4 MPa

3.2.3. Conclusions

The fluoroelastomer compound used for the stern tube seals was mechanically characterized under various loading modes. The stress-strain curve was shown to be fairly linear for strains between -0.1 and 0.1. The DMA revealed that at 20 °C the rubbery plateau is still not reached and the characteristics of the elastomer are quite temperature-dependent. Nevertheless, the temperature of the seals is determined to a large extent by the temperature of the stern tube lubricant, which is fairly constant. Due to the poor thermal conductivity of the elastomer, the temperature increase due to friction is localized at the contact. The relative stress relaxation of the material was shown to be dependent on the amount of strain. The results obtained after the majority of the relaxation has occurred allowed for the calibration of the Yeoh hyperelastic model implemented in the seal models presented in *Section 3.2*. The characterization of the elastomer was included in *Paper B*.

3.3. Garter spring characterization

A garter spring is a traditional coiled linear spring whose ends are connected together using a locking mechanism, often a threaded pin. This results in a circle-shaped spring as shown in Figure 3-17. Generally rotary lip seals incorporate a garter spring mounted on the elastomeric lip. The role of the garter spring is to provide an extra radial load to the sealing force. While the elastomeric material of the seal will relax in time, the garter spring load will not. The fluid film thickness variation while running does not change more than a few micrometres, and neither does the elongation of the garter spring. This means that the garter spring contributes an almost constant load in the radial direction. For this reason garter springs are sometimes referred as “constant load springs”.

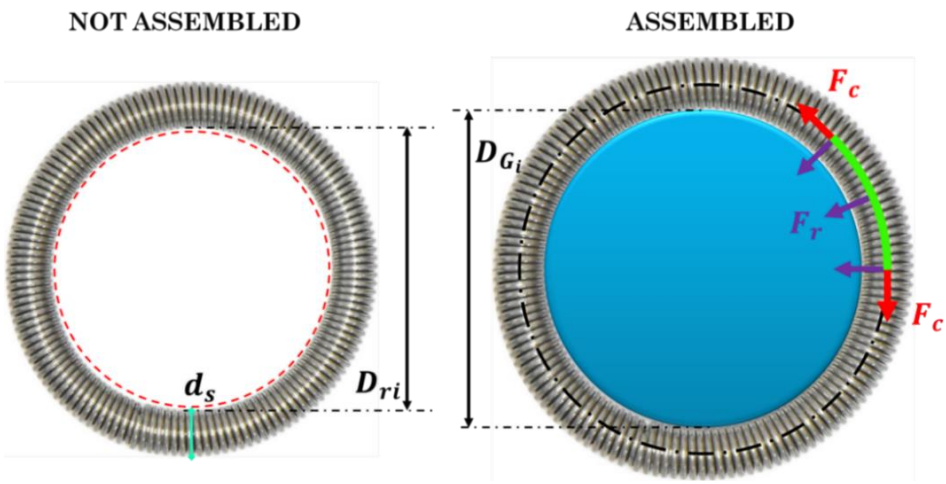

Figure 3-17. Garter spring load decomposition.

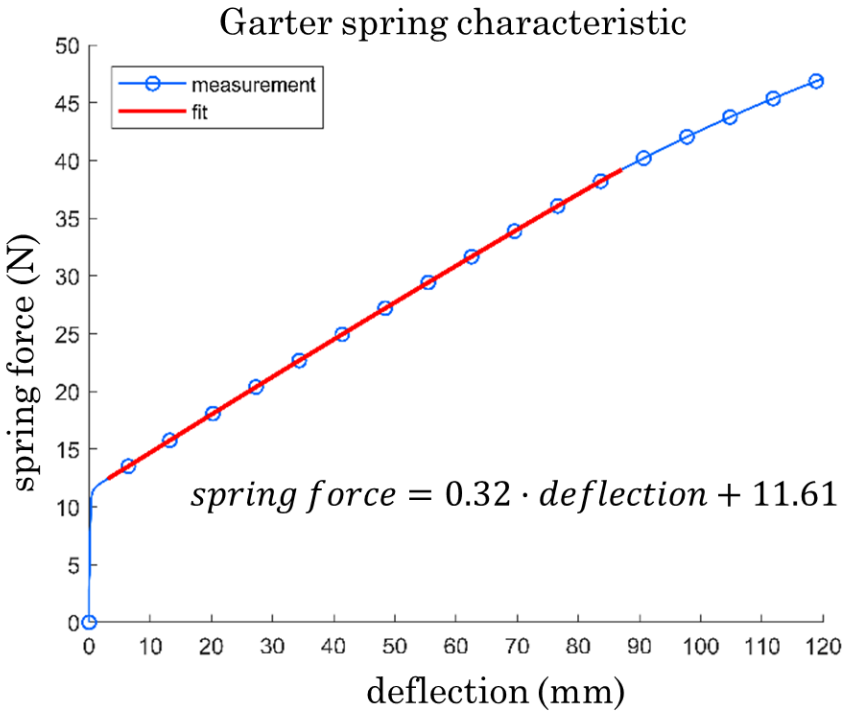

Figure 3-18. Garter spring measurement and linear fit.

The garter spring used in the seal under study was measured using a tensile tester BZ1.0/TH1S (Zwick/Roell, Germany). The spring was cut open on the opposite side of the locking mechanism [29], thereby allowing the locking mechanism to be included in the measurement [29]. The initial tension and the spring rate were then obtained by fitting a linear polynomial to the initial region of the spring, as shown in Figure 3-18.

The spring characteristic curve shown in Figure 3-18 corresponds to that in the circumferential direction when the two ends are connected, i.e. in garter spring configuration. Knowing the final elongation of the spring and the curvature of the shaft, and disregarding frictional forces, the radial load component can be deduced by decomposing the spring force into the radial direction (see Figure 3-19).

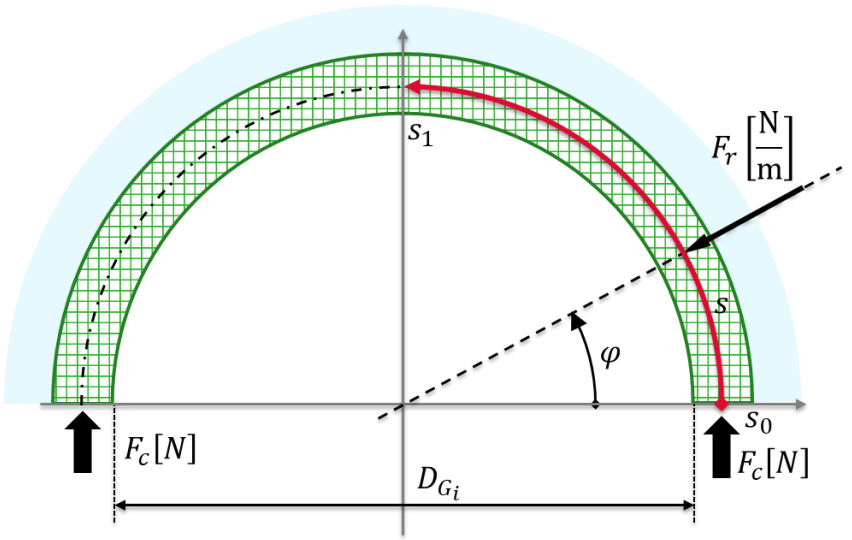

Figure 3-19. Garter spring force decomposition.

$$F_c = \int_{s_1}^{s_0} F_r \sin\varphi \, ds \qquad \textit{Eq. 3-8}$$

$$F_c = \int_0^{\frac{\pi}{2}} F_r \sin\varphi \frac{D_{G_i}}{2} d\varphi \qquad \textit{Eq. 3-9}$$

$$F_c = F_r \frac{D_{G_i}}{2} [-\cos\varphi]_0^{\frac{\pi}{2}} = F_r \frac{D_{G_i}}{2} \qquad \textit{Eq. 3-10}$$

$$F_{r_{tot}} = F_r \pi D_{G\,i} \qquad \textit{Eq. 3-11}$$

Ultimately, the radial force exerted by the garter spring when mounted is given by Eq. 3-12.

$$F_r = \frac{2F_c}{D_{G_i}} = 2\left[\frac{F_I}{D_{G_i}} + \pi S\left(1 - \frac{D_{ri}}{D_{G_i}}\right)\right] \qquad \textit{Eq. 3-12}$$

Further details of the calculation of the internal stress, the spring rate or the number of active coils can be found in [84]. It is worth mentioning that, by using a split-shaft setup such as that shown in *Section 4.1*, the garter spring contribution can be directly measured. By using a split-shaft setup, the inner diameter of the spring when mounted D_{G_i} does not need to be approximated.

3.4. Surface analysis

The surface roughness of a new seal is compared with the surface of a seal operated for 2,000 hours. The running-in stage was completed after 2,000 hours, when stable operating conditions were reached. Using a confocal microscope (Sensofar, Spain), large patches were measured with a lateral sampling of 0.217 μm. The x and y directions were set in the circumferential and axial direction respectively. A replica compound (Microset, United Kingdom) was used to bring the samples to the lab for its analysis on the confocal microscope.

3.4.1. Seal surface roughness

Figure 3-20 shows the measurement of the tip of a seal after running for 2,000 hours. The contact and non-contact regions are clearly visible. The seals are produced by compression moulding so the texture of the metal moulds are imprinted on the surface of the seals.

Both the seal and the shaft surface are smoothened as a result of the running-in process. A sample of the seal surface before and after testing is shown in Figure 3-21. Their roughness parameters are listed in Table 3-9.

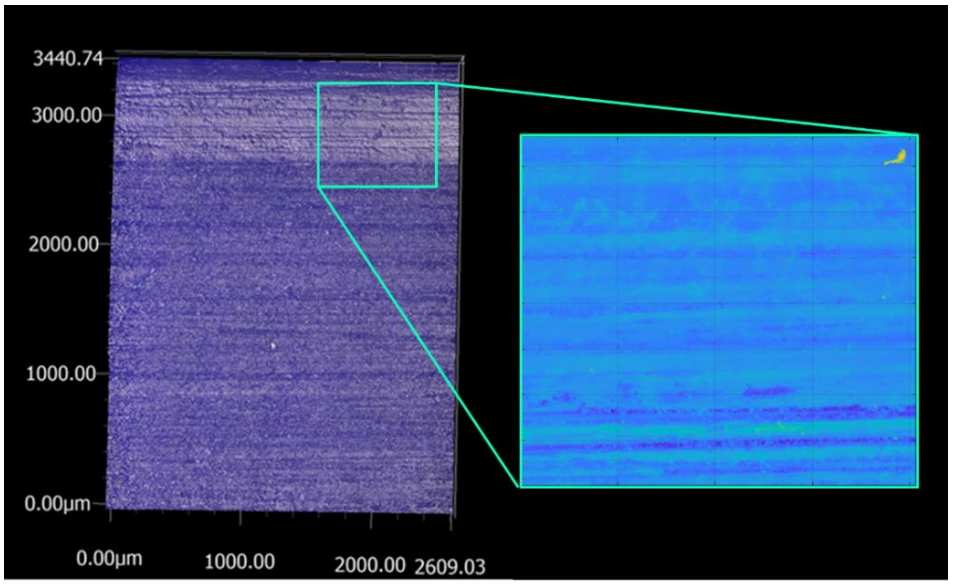

Figure 3-20. Caption of the seal tip after operating for 2,000 hours. The contact area is shown clearer on the top of the image. The turning marks are visible on both contact and non-contact areas.

Table 3-9. Seal surface roughness parameters before and after running-in.

		New seal	**Run-in seal**
S_a	$[\mu m]$	3.52	0.99
S_q	$[\mu m]$	4.61	1.24*
S_p	$[\mu m]$	30.46	11.15
S_v	$[\mu m]$	13.14	7.17
S_{z_5}	$[\mu m]$	43.44	18.25
S_k	$[-]$	0.87	0.05
K_s	$[-]$	4.39	3.67

** 0.85 **µm** and 1.23 **µm** in **x** and **y** direction respectively.*

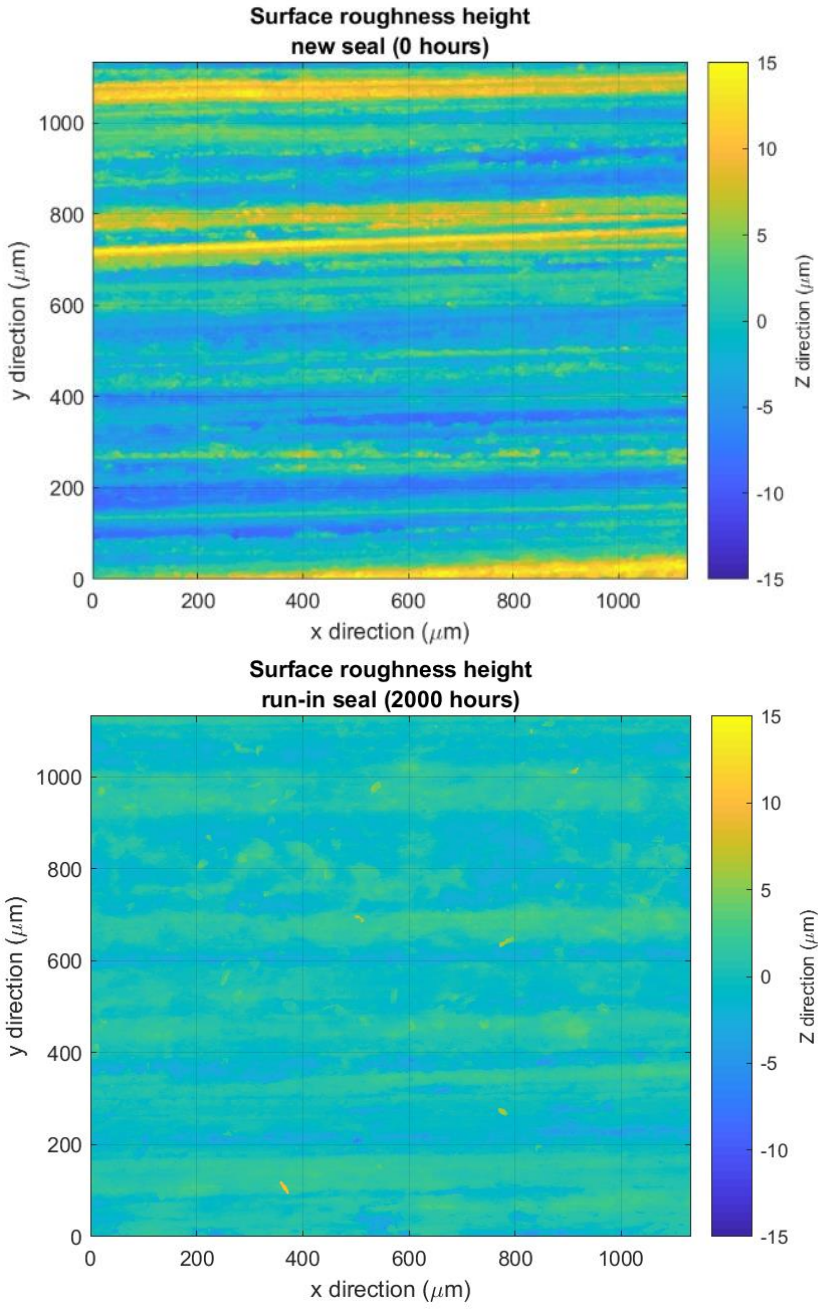

Figure 3-21. Comparison of the new surface topography before and after running for 2,000 hours.

3.4.2. Shaft liner surface roughness

The shaft liner surface roughness was measured before and after running for 2,000 hours. A replica compound made it possible to bring the shaft liner topography to the lab for analysis with the confocal microscope.

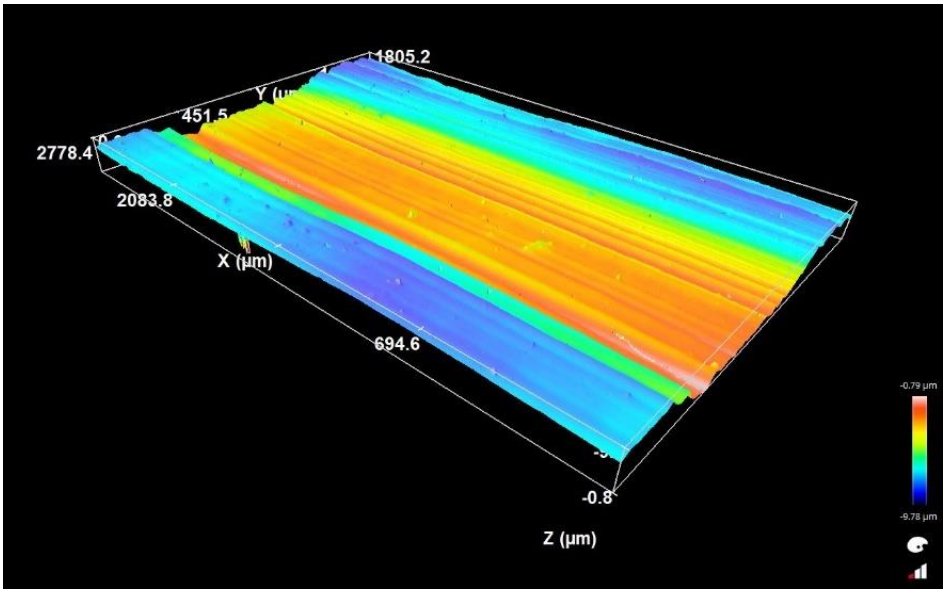

Figure 3-22. Confocal measurement of the surface roughness of the groove left on the shaft liner.

The surface roughness parameters of the shaft liner before and after running, i.e. within the groove, are shown in Table 3-10.

Table 3-10. Shaft surface roughness parameters before and after running-in.

		New shaft	**Run-in shaft**
S_a	$[\mu m]$	0.46	0.15
S_q	$[\mu m]$	0.59	0.19*
S_p	$[\mu m]$	1.33	0.94
S_v	$[\mu m]$	4.3	2.46
S_{z_5}	$[\mu m]$	5.61	3.40
S_k	$[-]$	-0.32	0.43
K_s	$[-]$	3.44	5.48

** 0.14 **µm** and 0.4 **µm** in **x** and **y** direction respectively.*

3.4.3. Seal tip profile

The seals are produced by compression moulding. As a result, a parting line is left at the tip of the seal which could impact the operation of the seal. To prevent that, the excess material on the parting line is in practice removed using an abrasive sponge. The resultant profile is therefore not the one indicated on the drawings, hence it needs to be measured (see Figure 3-23).

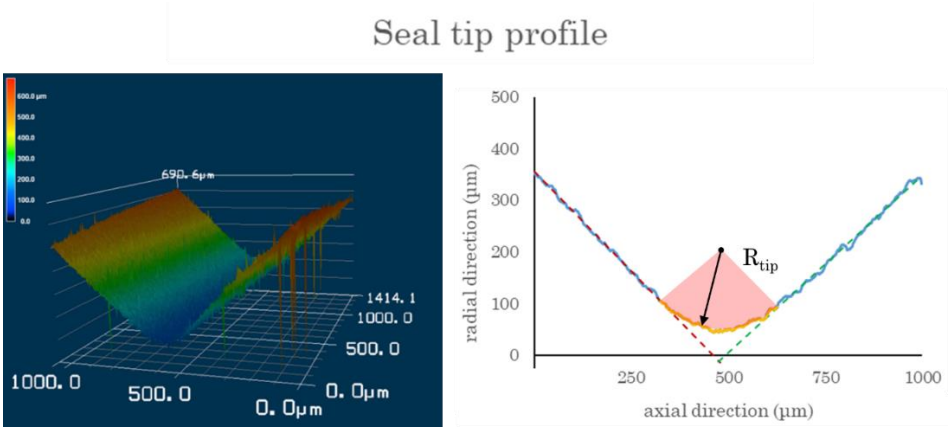

Figure 3-23. Measurement of the tip roundness profile R_{tip} left after polishing the seal tip.

Three different seals were scanned using the confocal microscope. The circumferential shape of the seal surface was removed and a rounded profile was fitted to the worn seal tip, as shown in Figure 3-23. A roundness of a few tenths of millimetres R_{tip} was implemented in the initial geometry of the FE stern tube seal model described in *Section 5.2*. The tip roundness was also used in the hydrodynamic model of a misaligned seal presented in *Section 5.4*.

3.4.4. Conclusion

It can be concluded that the shaft surface is ten times smoother than the seal surface roughness. The contact can therefore be interpreted as a soft rough seal surface contacting a rigid and smooth shaft surface. This assumption is commonly adopted in rotary lip seals literature and will be used in the models presented in *Chapter 5*.

4. Specialized setups

Three specialized setups were designed, assembled and calibrated during the present research. The setups were developed in collaboration with the sponsoring companies of this research. The setups allow specific characteristics of a rotary lip seal to be measured which otherwise could not easily be determined. The three setups developed are essential for the validation of the stern tube seal models, to be presented in *Chapter 5*. Furthermore, when working with extensive models such as rotary lip seals it is important to independently validate each of their parts. In some cases, as in rotary lip seals, the validation becomes more challenging than the modelling. The first device described in *Section 4.1* measures the static radial force exerted by the lip seal on the shaft. The overall sealing force is thereby obtained. The second setup shown in *Section 4.2* is based on a glass shaft allowing for the direct inspection of the shaft-seal contact also under static conditions. The contact width and leakage rates can be measured under various pressure differences and alignment conditions. Ultimately, a third setup – a rotary lip seal setup – is presented in *Section 4.3* to study the behaviour of stern tube seals

under real dynamic operating conditions. Temperature, frictional torque and flow rates are the outputs of this test rig.

4.1. Radial force test rig

It is not straightforward to measure the radial force between the seal and the shaft. An ingenious trick is frequently found in lip seals literature allowing for the measurement of the radial force [29], [49], [72]. The arrangement shown in Figure 4-1 consists of two shaft halves or jaws. When the two parts are set a few millimetres apart from each other they form a full cylinder (missing a slice of material in the middle). While one of the jaws is fixed, the other one sits on leaf springs and is therefore free to move. When the seal is mounted onto the jaws the radial force tends to bring the two jaws together. The load required to keep the jaws apart at a distance d_s can be related to the uniform radial load that the seal exerts on the shaft. When the shaft is static the radial load is the sealing force.

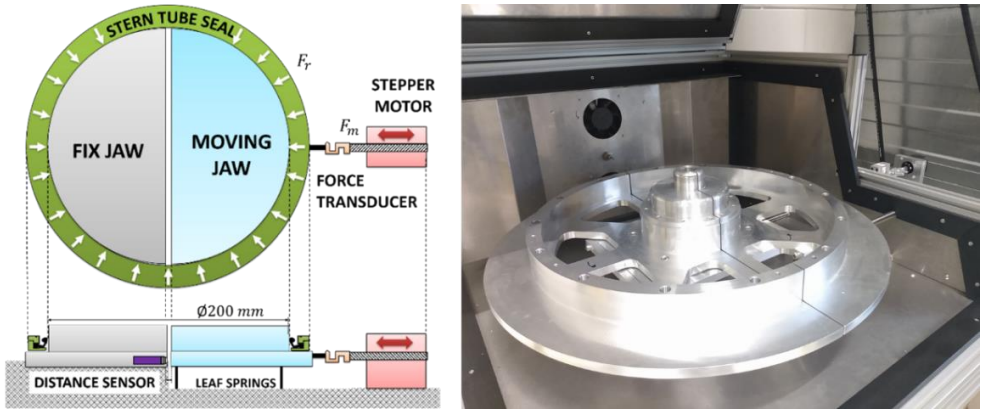

Figure 4-1. Large scale split-shaft setup using for measuring the radial force exerted by a seal.

Following this principle, the large split-shaft setup shown in Figure 4-1 was built to accommodate seals up to 600 millimetres in diameter. As observed in Figure 4-1, smaller diameters can also be fitted. The separation of the jaws is monitored by a capacity-distance sensor (Micro-Epsilon, Germany) and a high accuracy stepper motor (Haydon Kerk Motion Solutions, USA) is used to set the position of the moving jaw. By means of a control loop, the distance between the jaws is enforced while the S2M load cell (HBM, Germany) installed between the stepper motor and the moving jaw measures the pulling force F_m

required. The setup was designed such that the temperature on the testing chamber can be controlled. The stepper motor and the load cell are placed outside of the heating chamber to avoid accuracy issues.

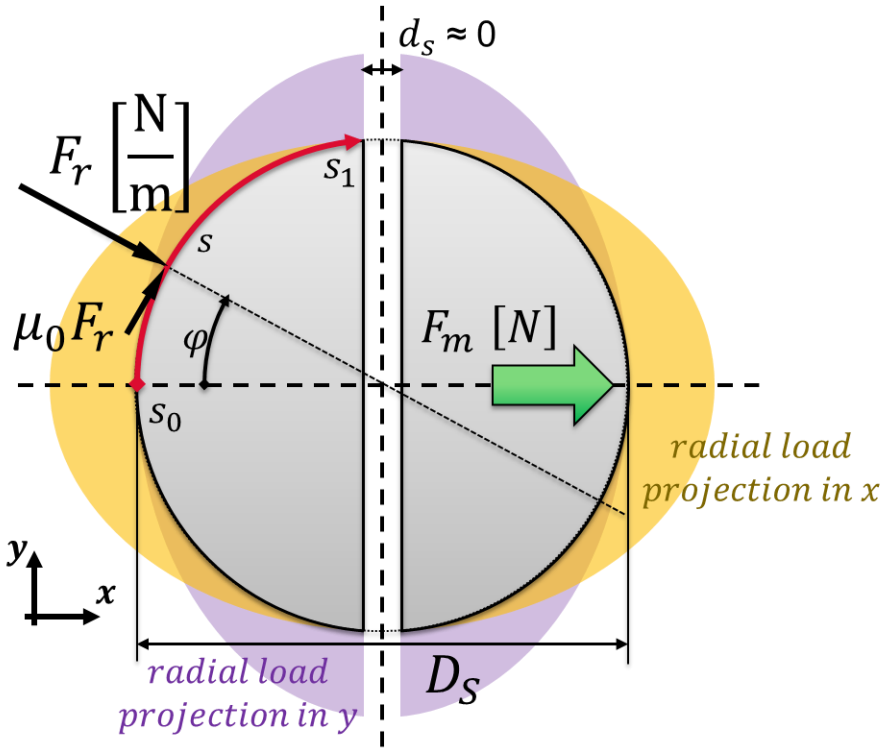

Figure 4-2. Radial force decomposition on a split-shaft setup arrangement.

This approach assumes that the gap between the jaws d_s is sufficiently narrow to be disregarded and that the radial force is uniformly distributed around the shaft. The pulling force exerted by the stepper motor F_m relates to the radial force F_r from the force balance, assuming a coefficient of friction μ_0 in the contact (Eq. 4-3).

$$F_r = \frac{F_{r_{tot}}}{\pi D_s} \qquad \text{Eq. 4-1}$$

$$F_m = 2\int_{s_0}^{s_1} (F_r \cos\varphi + \mu_0 F_r \sin\varphi)\, ds = D_s F_r \int_0^{\frac{\pi}{2}} (\cos\varphi + \mu_0 \sin\varphi) d\varphi \qquad \text{Eq. 4-2}$$

$$F_m = D_s F_r [\sin\varphi - \mu_0 \cos\varphi]_0^{\frac{\pi}{2}} = D_s F_r (1 + \mu_0) = \frac{F_{r_{tot}}}{\pi}(1 + \mu_0) \qquad \textit{Eq. 4-3}$$

The validation of the setup was carried out using elastomeric O-rings (FKM 190x6mm), as shown in Figure 4-3. The O-rings were characterized on a BZ1.0/TH1S tensile tester (Zwick/Roell, Germany) and then mounted on the 200-millimetre jaws of the split-shaft setup. The radial and circumferential force on the O-ring were related analogously to the garter spring calculation shown in *Section 3.3*. The measurements were carried out under both dry and lubricated conditions for comparison. No significant difference could be observed between these results. Good agreement was found between the predictions obtained with the garter spring formulae shown in *Section 3.3* and the measurements on the split-shaft setup.

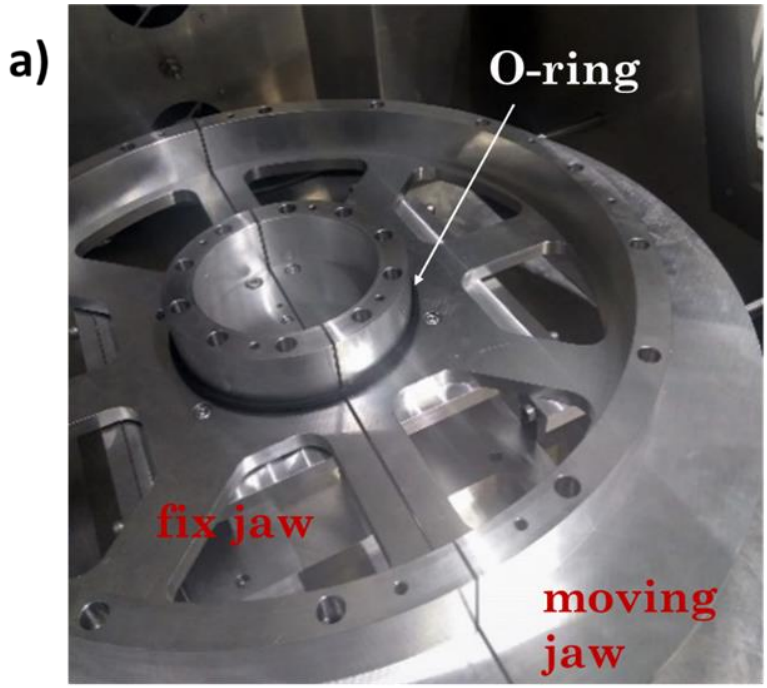

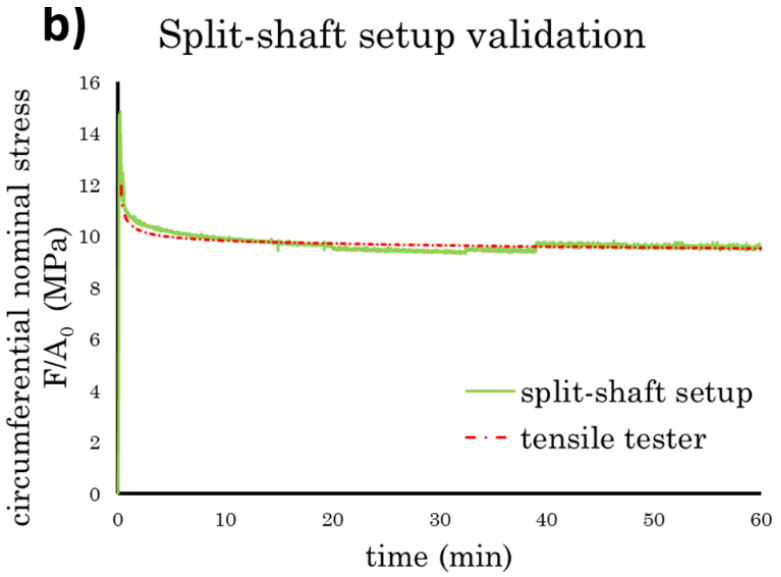

Figure 4-3. Validation of the split-shaft setup using 190x6 O-rings, a) setup b) results.

4.2. Contact width and leakage test rig

A setup with a hollow glass shaft was developed, making it possible to directly inspect the seal contact area. The setup replicates the static conditions of a stern tube seal, i.e. there are no rotating parts in this setup. Two pressure regulators allow for the independent pressurization of the top and bottom chambers of the seal (see Figure 4-4). A close-up of the contact area is obtained using a calibrated USB camera (Dino-Lite, China) allowing for the measurement of the contact width via image processing.

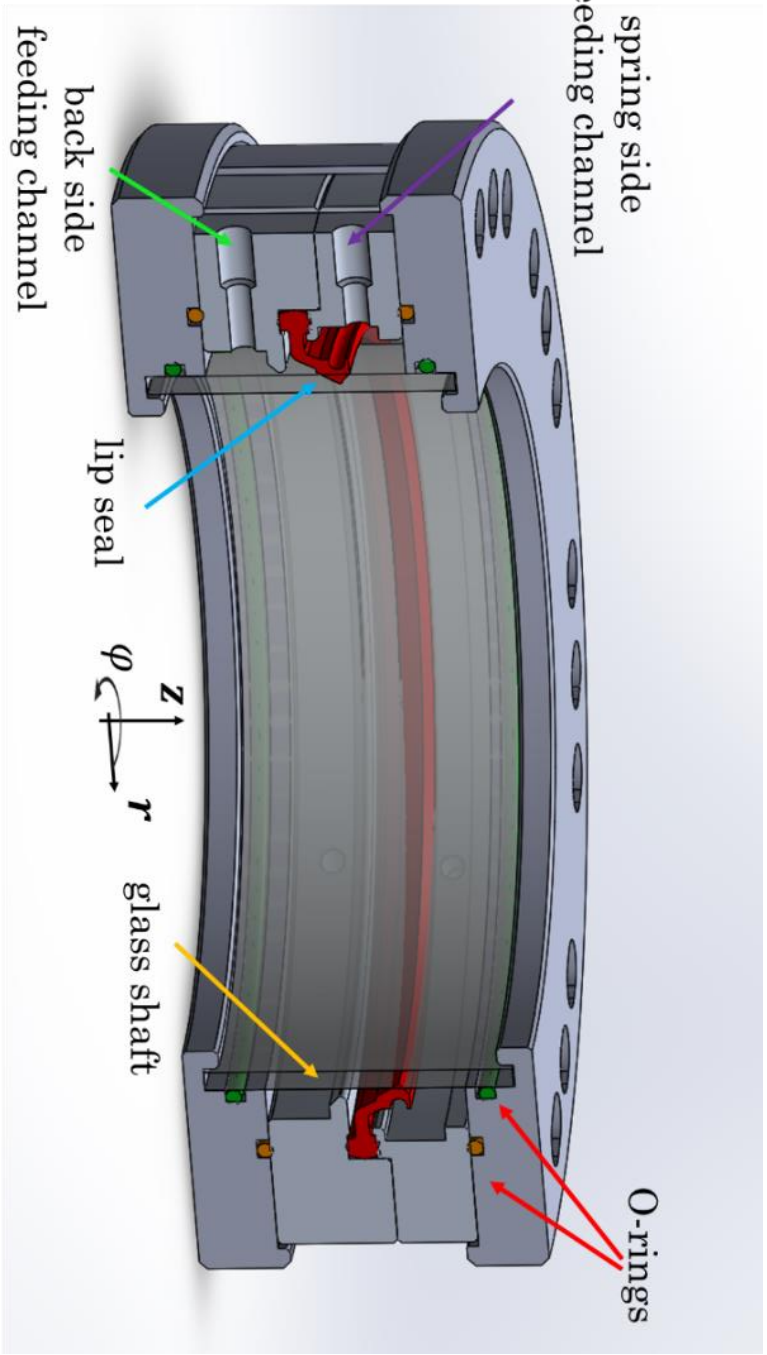

Figure 4-4. Glass shaft setup.

By setting a 90-degree mirror on a rotating table it was possible to analyse the whole contact area along the circumferential direction. The Frustrated Total Internal Reflection technique [85], [86] was used to inspect the contact area. A green laser beam is shot through the edge of the shaft so the light is (totally) internally reflected within the glass. When an object is brought into contact with the glass, the conditions at the boundary change allowing for the transmission of the light through the glass interface. If this object scatters light, the regions of contact (green) and non-contact (black) can clearly be discriminated as shown in Figure 4-5b. It is worth mentioning that under total reflection conditions, some light escapes the glass interface. This is known as the evanescent wave. The amplitude of this wave exponentially decays in the radial direction of the shaft typically dissipating within a few hundreds of micrometre. Consequently, when an object is brought close enough but not touching the glass, the evanescent wave is scattered leading to lower intensity green regions.

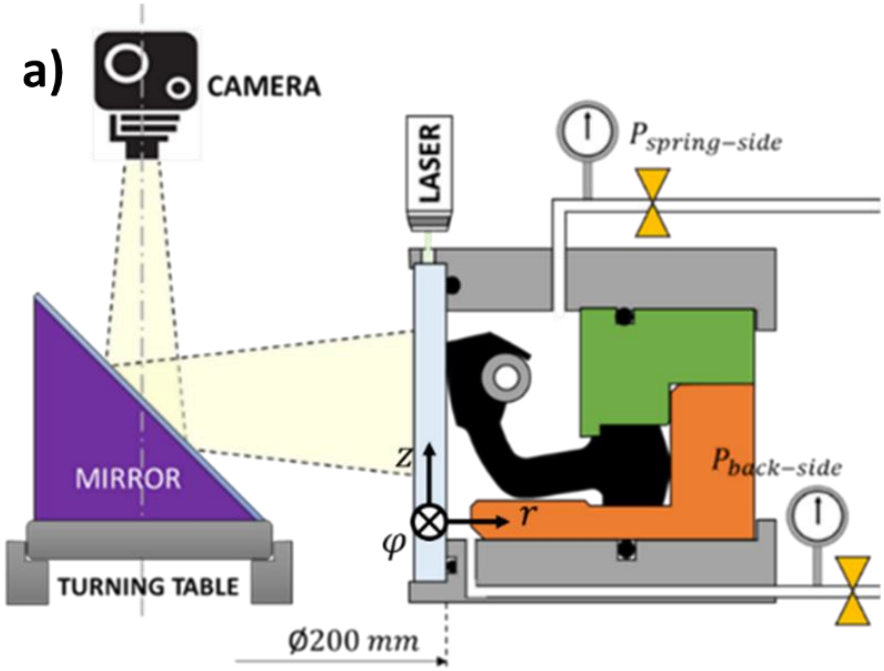

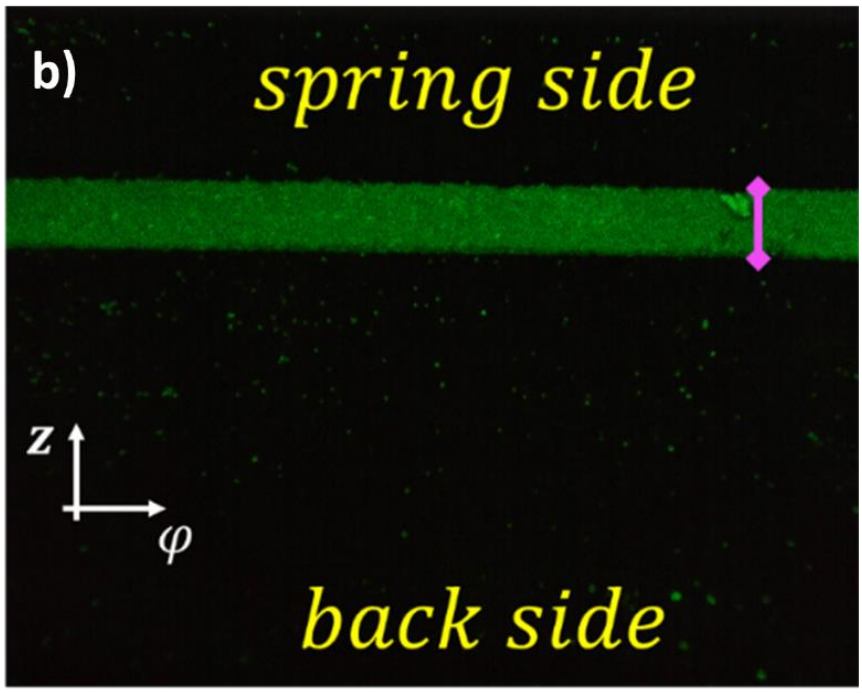

Figure 4-5. Specialized seal setup to observe the seal contact under various pressurization conditions, a) scheme b) snapshot of the contact zone.

The setup was designed to allow the seal to be offset with respect to the shaft. The two middle layers of the setup, i.e. the housing parts, can slide to a set position with respect to the shaft, as shown in Figure 4-6. Note that the characteristic undulations of the seal surface (see *Section 3.4*) can still be identified when the seal tip is compressed against the glass shaft. Figure 4-5 shows that, in addition to the back side, the peaks of the undulations are in contact with the shaft while the valleys are not. When the pressure difference Δp is increased, a shift of the contact area together with its widening occurs. Both phenomena were validated by the axisymmetric FE seal model presented in *Section 5.2*.

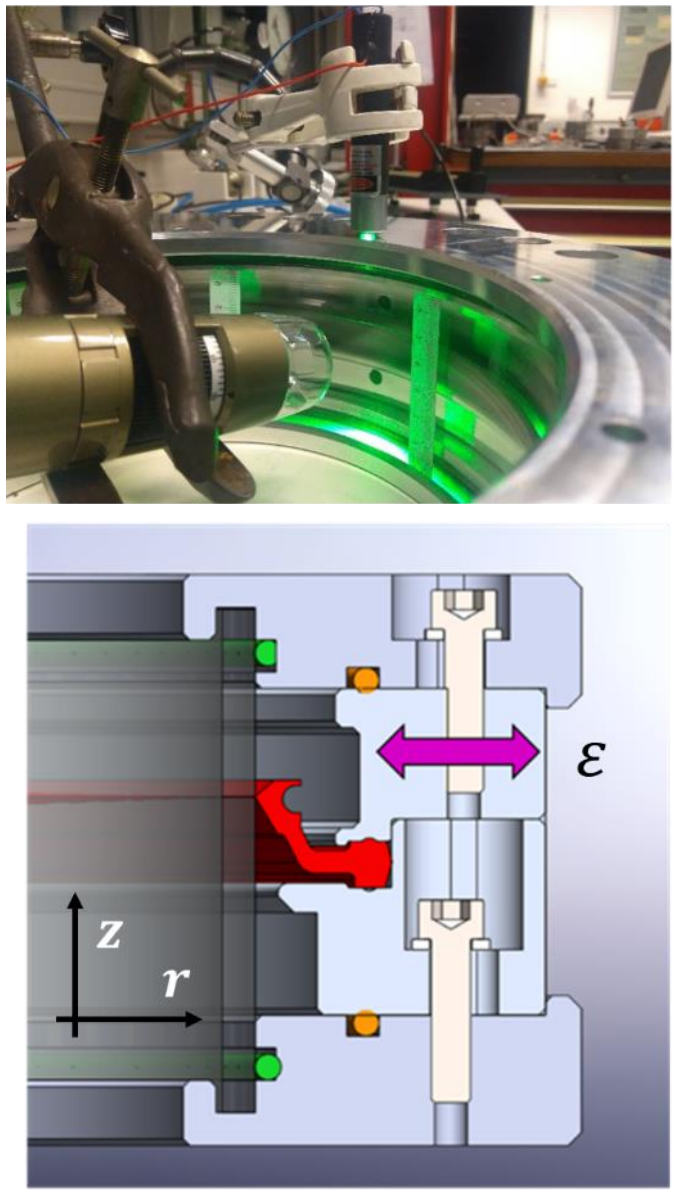

Figure 4-6. The glass shaft setup allows to set an offset between the seal and the shaft replicating the radial misalignment situation.

Additionally, this setup allowed the percolation threshold of the seal to be determined, i.e. the minimum contact pressure leading to a gastight contact. A flowmeter (EM-Technik, Germany) was installed at the outlet of the spring side chamber and the pressure on the back

side was slowly increased until leakage was observed. At a pressure difference Δp around -0.3 bar leakage was measured (see *Subsection 5.2.2*). Notice that the pressure on the back side P_{back} must be larger than the pressure on the spring side P_{spring} for leakage to occur, hence the negative value of the Δp (see Nomenclature).

4.3. Dynamic operation test rig

Ultimately, the behaviour of the stern tube seal was tested under dynamic conditions. The setup shown in Figure 4-7 was designed to fit a wide range of types and seal sizes. Note that this research focuses only on a specific type of stern tube seal with a nominal diameter of 200 millimetres and therefore all the results presented belong to that specific seal (see *Section 5.2*).

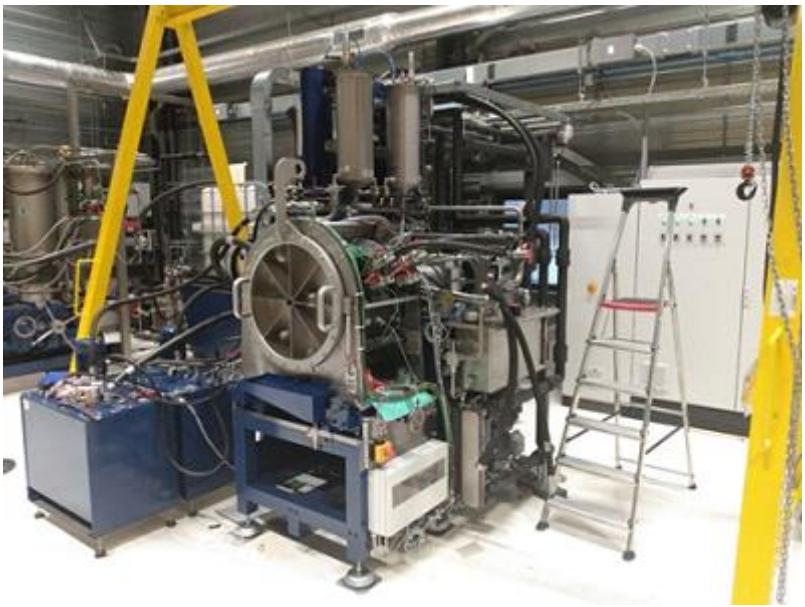

Figure 4-7. Single seal stern tube setup.

The setup allows the angular shaft velocity to be set while independently pressurizing the back and spring sides of the seal. Figure 4-8 shows the schematic of the rotary lip seals setup. The setup is driven by a 30 kW three-phase motor (Elsto Drives & Control, The Netherlands) coupled to the testing shaft by a toothed transmission belt. The shaft liner is mounted onto the testing shaft. The velocity of

the shaft is measured by a tachometer. NI LabView® is used for the control and monitoring of the test rig. Resembling the stern tube application, the testing seal (the main seal) is fully immersed in lubricant, hence an auxiliary rotary seal is required to prevent oil leakage towards the shaft drive. Approximately 80 litres of lubricant are necessary to fill the setup. The testing chamber, i.e. the drum, is supported by a set of flexors carrying the weight of the chamber while leaving its rotation almost unconstrained. The rotation of the drum is limited by a single lever incorporating a load cell (Futek, USA). The friction torque is therefore deduced from the reading of the load cell.

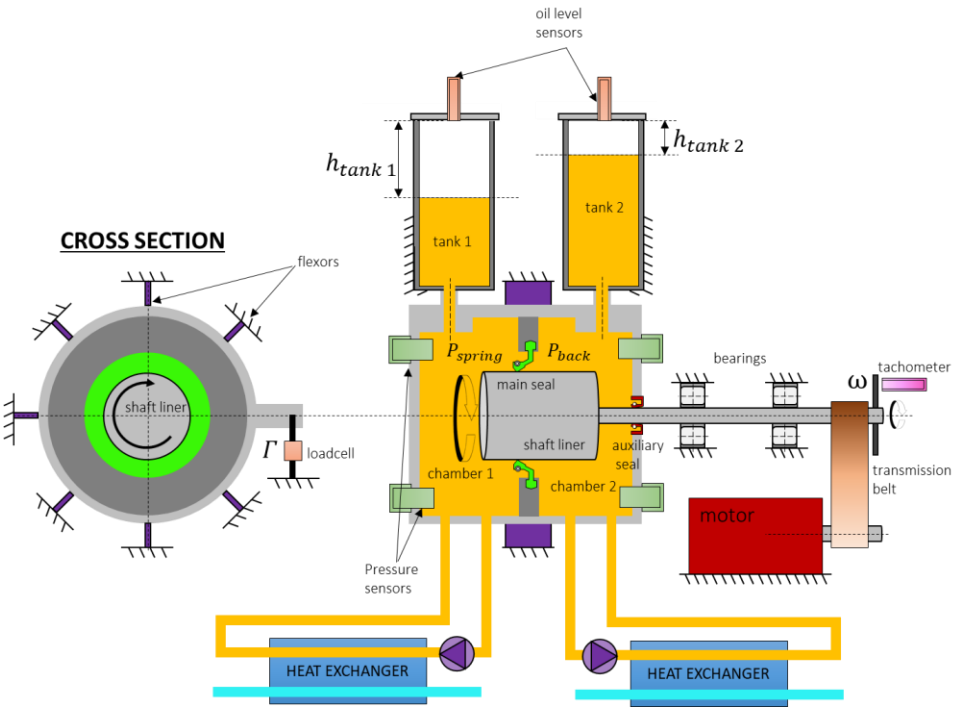

Figure 4-8. Schematic of the dynamic setup.

The pressure on the back and the spring sides, P_{back} and P_{spring} respectively, is set by pressurizing the air space left on the top of each tank. Two pairs of pressure gauges (Sensor Partners, The Netherlands) are located at each side of the seal at the top and bottom parts of the drum. The average pressure in each chamber is used to control the air pressure on the top of each tank. The temperature of the oil is controlled by pumping the oil at each side of the seal through two independent closed circuits equipped with heat exchangers (see

Figure 4-8). The temperature next to the seal tip, housing parts, flexors and the lubricant at each side of the seal are monitored by thermocouples. The position of the thermocouples is shown in Figure 4-9. The temperature in the contact is estimated from the temperature reading at the garter spring together with the finite-element axisymmetric seal model shown in *Section 5.2*.

This study focuses on the stationary operation of stern tube seals, so all the results presented belong to seals which have been run until all the temperatures and torque readings remained constant for at least one hour.

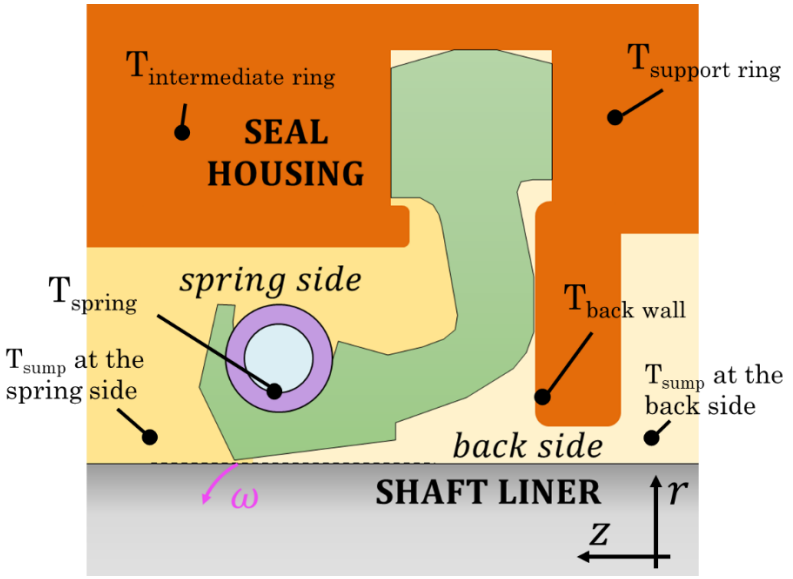

Figure 4-9. Position of the thermocouples on the dynamic setup.

The lubricant height variation on each tank is measured by two distance sensors located at the top of each tank. Although monitoring one tank should be enough to determine the flow rate across the seal, the oil height on both tanks are measured, thereby giving extra reliability to the results [46]. Since a pressure control loop is set at each tank, the variation of the oil columns does not impact the hydrostatic pressure applied to the seal, ensuring a constant operating pressure on both sides. The thermal expansion of the lubricant significantly impacts the volume of lubricant on each side of the stern tube seal [87]. The volume variation of the lubricant due to temperature is compensated using the density-temperature relation

obtained from the characterization of the lubricants shown in *Section 3.1*.

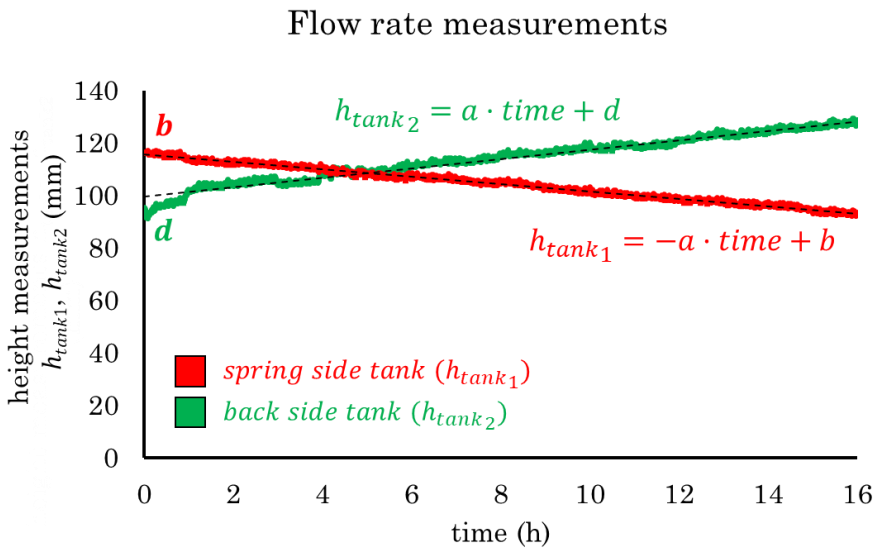

Figure 4-10. Flow rate measurement at 3 m/s and Δp = 1 bar. See experimental setup in Figure 4-8.

Most mineral oils contain between 8 and 12% in volume of dissolved air [88]. When the pressure of a liquid lubricant decreases beyond ambient, the dissolved gases are liberated, i.e. gaseous cavitation. Therefore it is important to allow the entrained gas to escape, otherwise air pockets are formed, distorting the leakage measurements. Note that the piping scheme of the stern tube system shown in *Section 1.1* has a set of breathers installed. The pumps used for the temperature-control circuits shown in Figure 4-8 may also contribute to the entrainment of air into the system. It then becomes essential to monitoring the oil height in both tanks. A test was accepted only when opposite flow rate values in tank 1 and tank 2 were derived, otherwise the results were discarded and the system purged.

When it comes to the torque measurements the drum connection to the oil tanks, the tubing used for the temperature control system, and the flexors restricted the rotation of the shaft. Consequently, the system stiffness had to be accounted for when deriving the overall frictional torque from the load cell readings. Slight variations on the temperature of the flexors supporting the drum were shown to impact the torque measurements. The operating conditions determine the

temperature distribution on the whole setup and subsequently also at the flexure hinges. Additionally, the pressure difference Δp between the spring side and back side was shown to deform the drum, also influencing the load cell readings. Therefore – and also to guarantee the accuracy of the measurements – the load cell was calibrated at every single operating point once stationary conditions were reached. In other words, when measuring the torque under a specific operating condition, a calibration procedure was conducted first.

The calibration is done by adding dead weights while running. This ensured that the temperature of the system was kept constant. Afterwards, a few motor start-and-stops were conducted, allowing the decrease in frictional torque to be measured when the shaft velocity became null. The contribution of the auxiliary seal and the lubricant to the overall torque was obtained by repeating the tests without the main seal installed.

4.4. Conclusions

The large radial force setup presented in *Section 4.1* and the glass shaft setup shown in *Section 4.2* made it possible to measure the loading and the width of the contact respectively. Additionally, the glass shaft setup was used to measure the maximum pressure difference that a seal can handle before leakage develops, i.e. the sealing limit. The results were used to validate the static axisymmetric model presented in *Section 5.2* under a wide range of pressures (Paper B). The glass shaft setup was also used to validate the three-dimensional misalignment model described in *Subsection 5.2.3* (*Paper C* and *Paper D*).

5. Modelling of rotary lip seals

Chapter 5 describes the modelling of the stern tube seal. This chapter is divided in four parts. First, *Section 5.1* reviews the main aspects concerning the operation of the stern tube seal and defines the boundary conditions of the model. The analytical formulae describing the operation of rotary lip seals are also presented in this section. The modelling of dynamic seals begins by approaching its static operation. The second part of this chapter comprises the models on which the seal is static, i.e. the shaft velocity is null and hence hydrodynamics are not involved. Both the static aligned (*Paper B*) and static misaligned (*Paper C*) situations are presented in *Section 5.2*. Next, the dynamic modelling of the rotary lip seal is approached. A distinction is made between the dynamic modelling under perfect alignment (*Section 5.3*) and the dynamic modelling under misaligned conditions (*Section 5.4*). *Section 5.3* details the typical strategy for modelling rotary lip seals when aligned, i.e. when the shaft is turning and the seal and the shaft are concentric. The final section, *Section 5.4,* focuses on the lubrication mechanisms induced by the seal-shaft misalignment. The two mechanisms considered in *Section 5.4* are presented in *Paper C* and

Paper D. Figure 5-1 summarizes the modelling work carried out during this research and relates the sections to the published papers.

Up to now, the many variables playing a significant role in the performance of rotary lip seals has hampered the understanding of the behaviour of these mechanical components. The post-analysis of the tested rotary lip seals shows a wide range of results, making it difficult to draw firm conclusions. For the last decades, with the use of computational models, a higher level of understanding has been reached. The main aspects that are relevant when modelling rotary lip seals are:

- A material model for the lip seal material.
- Realistic boundary conditions at the housing and the garter spring.
- Incorporation of seal and shaft surface topographies, i.e. roughness.
- Modelling the hydrodynamic pressure between the seal and the shaft.
- The rheological characteristics of the lubricant.
- Including the large deformations of the seal because of the loading of the seal-shaft interface.
- Thermal phenomena including the heating of the contact.
- Taking into account direct asperity contact, i.e. the mixed lubrication regime.
- Time-dependent phenomena, e.g. viscoelasticity.
- Chemical interactions between the seal, the shaft and the lubricant.

Some of the bullet points listed above are research fields in their own right and hence several simplifications must be made when modelling rotary lip seals. For example, time-dependent phenomena and the chemical interaction between the seal, the shaft and the lubricant are beyond the scope of this research.

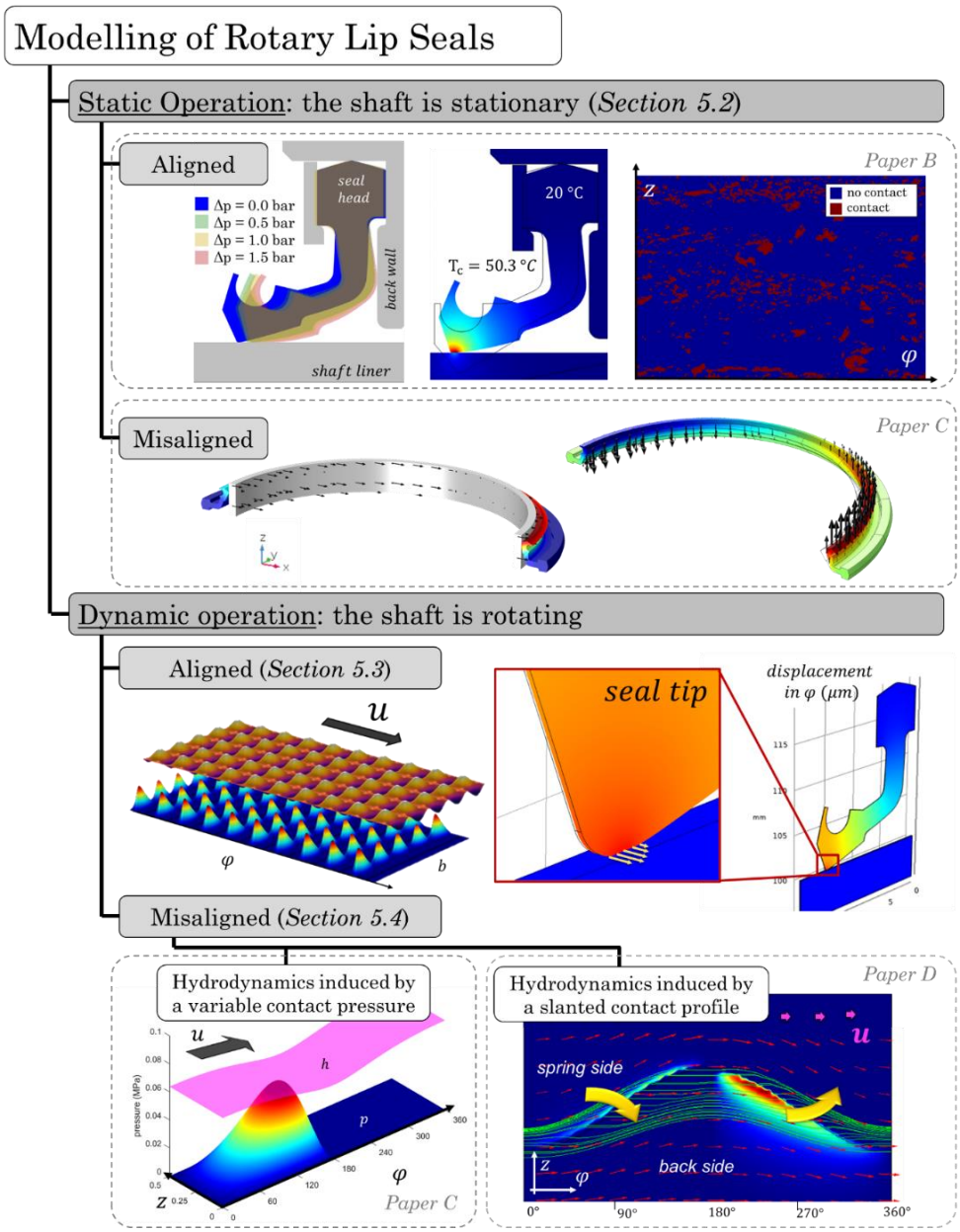

Figure 5-1. Schematic of the modelling part presented in Chapter 5.

5.1. Analytical analysis

The operating conditions of the sealing rings used at the stern tube of a vessel are reviewed in this section. Figure 5-2 shows the typical disposition of the lubricant tanks for the stern tube of a ship. The shaft angular velocity and the hydrostatic pressure of the tanks define the operating conditions of the seals.

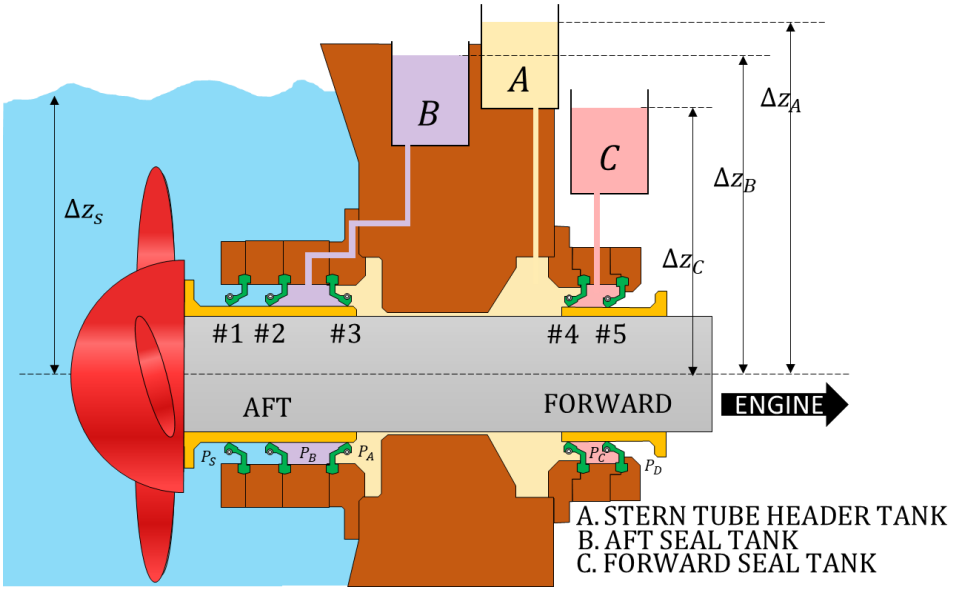

Figure 5-2. Disposition of the stern tube oil tanks in a ship.

5.1.1. Hydrostatic pressure in the stern tube

Stern tube seals are hydrostatically pressurized hence the load applied to the seal depends exclusively on the height and the density of the column of liquid sitting on top of them (Eq. 5-1) [1].

$$\Delta p = \rho \, g_0 \, \Delta z \qquad \textit{Eq. 5-1}$$

As shown in Figure 5-2, three independent tanks supply the lubricant to the chambers between the seals [1]. This way, a specific pressure difference can be set on the seals and adjusted to the loading situation of the ship. Table 5-1 shows typical oil height levels of the lubricant tanks when the ship is loaded and unloaded.

Table 5-1. Liquid height of the lubricant tanks with respect to the axis of the propulsion shaft.

Seawater		
Δz_s (m)	Unloaded	4.58
	Loaded	9.40
Aft tank (B)		
Δz_B (m)	Unloaded	1.82
	Loaded	2.59
Header tank (A)		
Δz_A (m)	Unloaded	13.76
	Loaded	14.92
Forward tank (C)		
Δz_C (m)	Unloaded	0.91
	Loaded	0.94

The hydrostatic pressure is calculated via Eq. 5-1 from the average liquid heights Δz (Table 5-1), assuming seawater and lubricant densities of 1029 kg/m^3 and 850 kg/m^3, respectively. Note that pressurized lip seals generally have the higher pressure on the spring side and the lower on the back side. Seal #1 in Figure 5-2 usually becomes worn after a short time and works as a dirt excluder, preventing the entrainment of larger particles to the system [2]. Consequently, in Table 5-2 seal #1 is assumed to hold no pressure difference.

Table 5-2. Average pressure difference across each seal shown in Figure 5-2 under loaded and unloaded conditions.

Pressure difference across each seal Δp_h (bar)		
	Unloaded	Loaded
seal #1	0.00	0.00
seal #2	0.31	0.73
seal #3	1.00	1.03
seal #4	1.07	1.17
seal #5	0.08	0.08

The oil height of the aft tank is designed to supply a hydrostatic pressure lower than that of the water side at all times. This way, if seal #2 fails, the natural leakage would always be directed towards the stern tube, preventing any oil spillage. In a similar fashion, the large

hydrostatic pressure supplied by the header tank frustrates the entrainment of water to the stern tube bearings. However, under normal ship operation lubricant spillage to the environment and water ingress to the stern tube are common [7]. It is worth mentioning that. because of the vertical disposition of the sealing rings, a hydrostatic pressure gradient is also found from the top to the bottom of the seal. The magnitude of the pressure gradient depends on the diameter and will be addressed in *Section 5.4*.

5.1.2. Shaft angular velocity and lubricant shear rate

The linear velocity of the shaft depends on the rotational speed and the diameter of the shaft liner, as shown in Eq. 5-2. For most ships the tangential velocity u ranges from 0 to 6 m/s [2]. The maximum lubricant shear rate can be approximated by assuming a 1-micrometre-thick lubricant film at the seal-shaft contact (see Eq. 5-3).

$$u = \omega D_s/2 \qquad \textit{Eq. 5-2}$$

$$\dot{\gamma} = \frac{\partial u}{\partial z} = \frac{u}{h} = \frac{6}{10^{-6}} = 6 \times 10^6 \left[\frac{1}{s}\right] \qquad \textit{Eq. 5-3}$$

5.1.3. Operating temperature

As shown in Figure 5-3, the sea surface temperature varies according to the location of the ship. A significant amount of heat is released by the operation of the stern tube seals [2], hence mild temperatures are expected within the stern tube when in operation. For simplicity, the oil lubricating the stern tube seal was assumed to be at the average sea surface temperature, i.e. 20 °C.

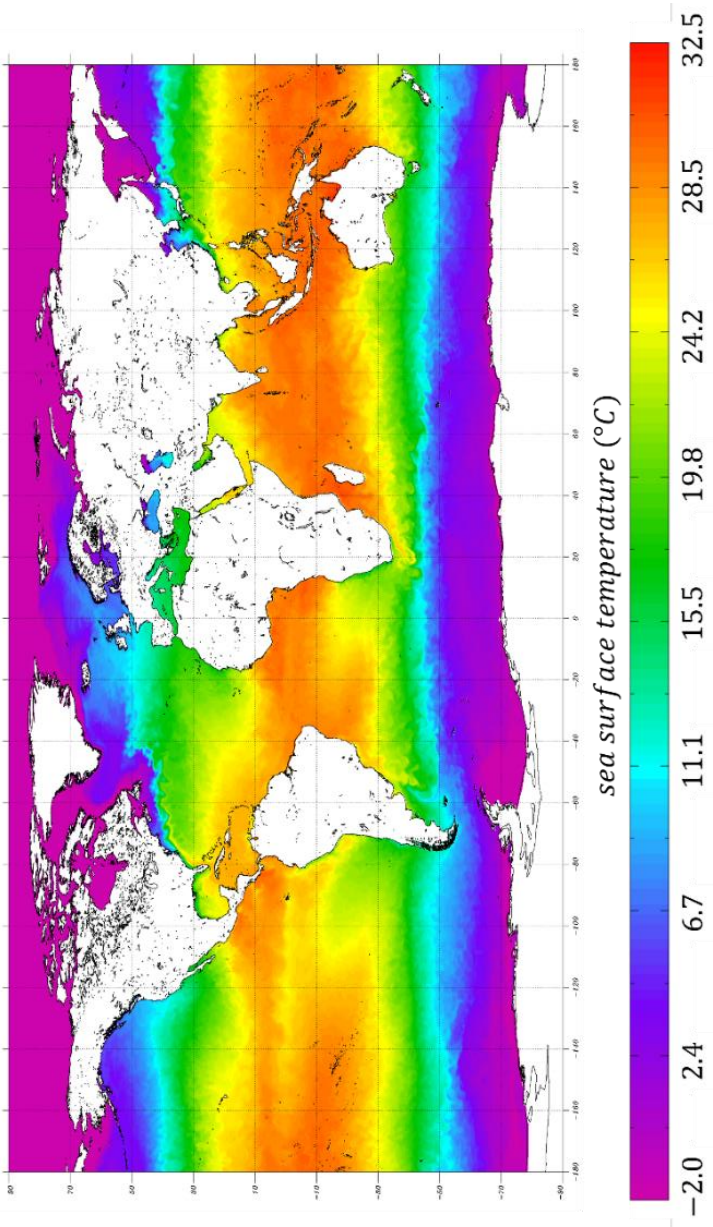

Figure 5-3. Sea surface temperature (14th February 2020. NOAA)

5.1.4. Frictional torque and fluid film thickness

In the literature, no measurements are available on the thickness of the lubricant layer between a stern tube seal and the shaft liner while running. The lubricant film thickness for smaller non-pressurized rotary lip seals is in the order of 1 micrometre [14] and advanced techniques are required for its measurement. The film thickness is typically deduced from the frictional torque measurements using a model. Therefore a suitable friction model must be selected.

The straightforward approach consists in applying Petroff's equation for two rotating concentric cylinders [29], [32]. The frictional force Γ exclusively derives from the viscous shear stress between the laminar layers of lubricant as shown in Eq. 5-4 to Eq. 5-7.

$$\Gamma = F_f D_s/2 \qquad \textit{Eq. 5-4}$$

$$F_f = \tau_{xz}(\pi D_s b) \qquad \textit{Eq. 5-5}$$

$$\tau_{xz} = \eta\,\dot{\gamma} \qquad \textit{Eq. 5-6}$$

$$h = \frac{\pi b\,\eta\omega D_s^3}{4\Gamma} \qquad \textit{Eq. 5-7}$$

This way, from the measurement of the frictional torque an initial approximation of the film thickness can be obtained if hydrodynamic lubrication is considered. It is important to account for the variation of the viscosity variation with temperature. The Petroff's model can be extended to the mixed lubrication regime by adding a dry term to the seal frictional torque equation, as shown in Eq. 5-8. The dry frictional torque term Γ_0 captures the non-negligible torque measured at the lowest shaft angular velocities. The radial force between the shaft and the seal $F_{r_{tot}}$ is obtained beforehand, as shown in *Section 4.1* and the coefficient of friction μ_0 is set to match the frictional torque-velocity ordinate intercept [15]. Engelke [87] showed that fairly good predictions can be obtained by assuming the gap to be the sum of the mean peak roughness of both surfaces ($h \simeq S_{p_a} + S_{p_b}$) and $\mu_0 = 0.3$ [87].

$$\Gamma = \Gamma_0 + \Gamma_\eta = \mu_0 F_{r_{tot}} \frac{D_s}{2} + \eta \frac{b}{h} \omega \frac{\pi D_s^3}{4} \qquad \textit{Eq. 5-8}$$

Significantly more sophisticated computational models are presented in literature, but the idea behind them is the same: the fluid film thickness is calculated from the measured torque so the friction predicted by the model from shearing the fluid film matches the torque measurements. These more advanced computational models generally work with an equivalent surface topography instead of the real surface roughness; their accuracy, in terms of film thickness, can therefore be called into question.

5.1.5. Contact temperature and friction heating

The contact temperature is a key parameter when it comes to the material properties and thermal expansion. Furthermore, the wear rate and degradation of the seal and lubricant are closely related to it [2]. The high friction heating Q_f ($Q_f = \Gamma\omega$), the small seal-shaft contact area and the poor heat conductivity of the seal material lead to an elevated contact temperature. Avoiding more complex computational models, Eq. 5-9 can be used to predict the contact temperature T_c under different operation conditions [87]. Once more, the parameter $K_{\Delta T}$ must be obtained from experiments.

$$T_c = T_{sump} + K_{\Delta T}\frac{\Gamma\omega}{\pi D_S b} \qquad \textit{Eq. 5-9}$$

Notice that an estimate of the contact temperature, the lubricant viscosity and the frictional torque can be obtained iterating between Eq. 5-8 and Eq. 5-9 [87].

5.1.6. Coefficient of friction

The overall coefficient of friction μ is calculated from the frictional torque measurements and the static radial load between the seal and the shaft (Eq. 5-10):

$$\mu = \frac{2\Gamma}{\pi {D_s}^2 F_r} \qquad \textit{Eq. 5-10}$$

Hirano realized that the friction coefficient of rotary lip seals is proportional to the duty parameter $G = \eta u b / F_{r_{tot}}$ as shown in Eq. 5-11 [23]. Once more, the seal characteristic constant ϕ_s must be

determined from experiments. Note that ϕ_s varies when sealing and when pumping lubricant, i.e. when plenty of lubricant is available at the intake side (see Figure 2-5).

$$\mu = \phi_s G^{1/3} = \phi_s \left(\frac{\eta u b}{F_{r_{tot}}}\right)^{1/3} \qquad \textit{Eq. 5-11}$$

5.1.7. Lubricant migration across the seal

According to shipowners, there is a rule of thumb when it comes to stern tube spillage: the maximum acceptable leakage rate in L/day is the diameter of the shaft in millimetres divided by 100. According to that, a 200 millimetres shaft allows a maximum leakage rate of 2 L/day. Neither the angular velocity, nor the seal design, nor the lubricant are considered, so such a rule must be taken only as a reference.

Although a partial or full separation of the seal and the shaft surfaces occurs, the applicability of the Poiseuille flow formula (Eq. 5-12) for rotary lip seals is controversial. The lubricant in rotary lip seals is shown to flow from the back side to the spring side even under ambient conditions on both sides of the seal.

$$q = \frac{dp}{dx}\frac{h^3}{12\eta}\pi D_s \qquad \textit{Eq. 5-12}$$

Stern tube seals operate fully flooded on both sides of the seal, hence their flow rates must be compared to those of traditional rotary lip seals when installed converse, i.e. when plenty of lubricant is available at the intake. Kawahara [23] defined a dimensionless suction coefficient K_q characterizing the flow rate in rotary lip seals for its converse operation. Kawahara found Eq. 5-13 to reliably predict the flow rate in the seals he tested based on experimental data [89].

$$q = K_q u D_s^2 G^{1/2} = K_q u D_s^2 \left(\frac{\eta u b}{F_{r_{tot}}}\right)^{1/2} \qquad \textit{Eq. 5-13}$$

5.2. Static modelling

Finite Elements (FE) models of pressurized rotary lip seals present several nonlinearities and therefore converging to a solution often becomes a challenge. The seal undergoes large deformations, resulting in geometric nonlinearities. Further, elastomeric materials do not show a linear constitutive relation between the stress and strain, causing material nonlinearities. Also, volumetric locking is likely to occur due to the almost incompressible nature of elastomeric materials. In the modelling shown in this thesis, the mixed formulation of the virtual energy equation, also referred as the u-P formulation, was used to prevent volume locking. Both the shaft and the housing components are assumed rigid as their stiffnesses are a few orders of magnitude larger than that of the seal. The garter spring load is set constant as the elongation of the spring barely changes during its operation [48]. A contact model is required at the sealing surface, hence this boundary condition depends on the displacement of the body (kinematic nonlinearity). Ultimately, nodal loads resulting from the pressure boundary conditions must be updated as the seal deforms (kinetic nonlinearity). The model is stationary, hence the solutions obtained are history-independent. In this thesis, the commercial software COMSOL Multiphysics® is used.

5.2.1. Axisymmetric seal FE model (aligned)

The geometry of the seal has been provided by a stern tube seal OEM and therefore the exact dimensions of the seal will not be disclosed in this thesis. The parametrized geometry is shown in Figure 5-4.

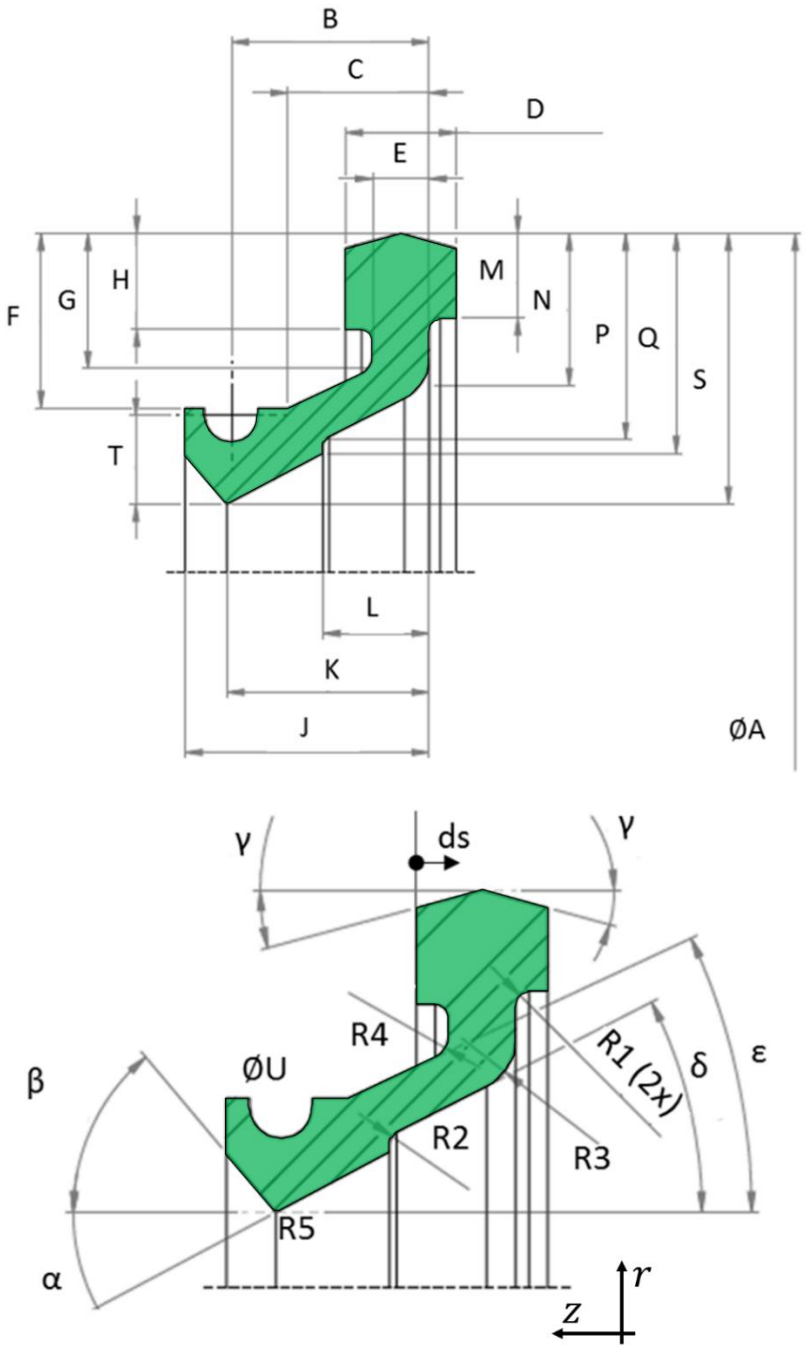

Figure 5-4. Geometry of the 200 millimetres stern tube seal with parameters as defined in the model.

The seal head is clamped between two housing parts, namely the intermediate ring and the support ring. A circular groove is present on both the intermediate and housing rings preventing the slippage between the seal head and the housing parts. These grooves are not shown in Figure 5-5.

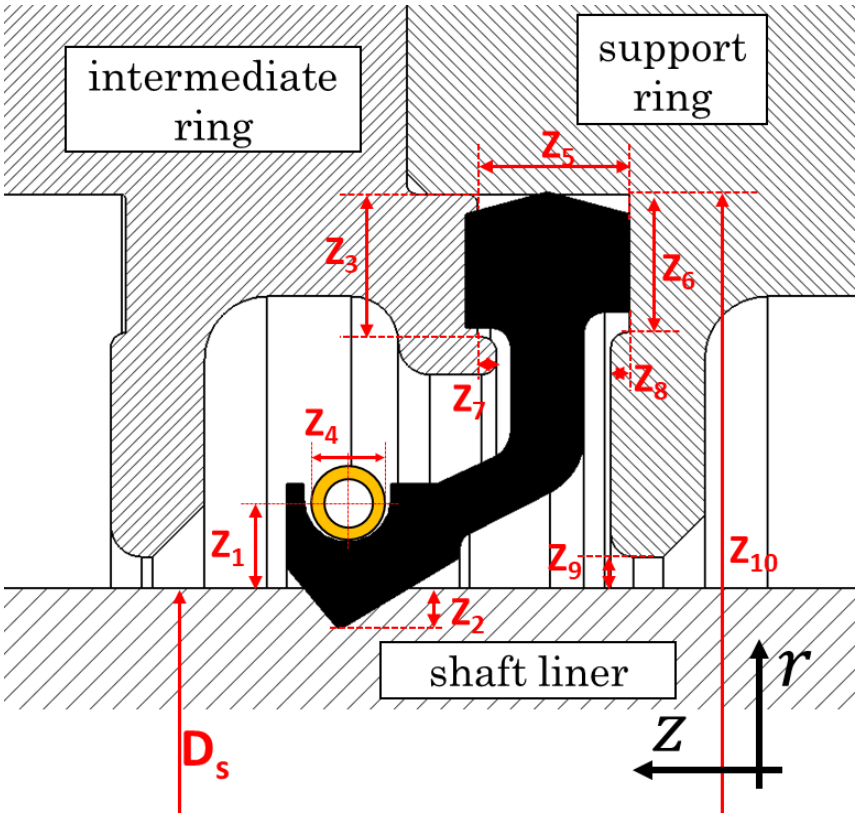

Figure 5-5. Geometry of the surrounding hardware: shaft liner, garter spring and housing parts.

The geometry of the shaft, seal and housing parts is meshed with second order quad elements, as shown in Figure 5-6. The penalty term contact algorithm was used on the shaft-housing interfaces, not a single nodal displacement of the seal was prescribed. The contact between the seal and the shaft liner was modelled using the Augmented Lagrangian method for a more accurate prediction of the contact area and contact pressure profile.

Boundary designation	Location
1	A-B
2	B-C
3	C-D
4	D-E
5	E-F
6	F-G
7	G-H
8	H-I
9	I-A

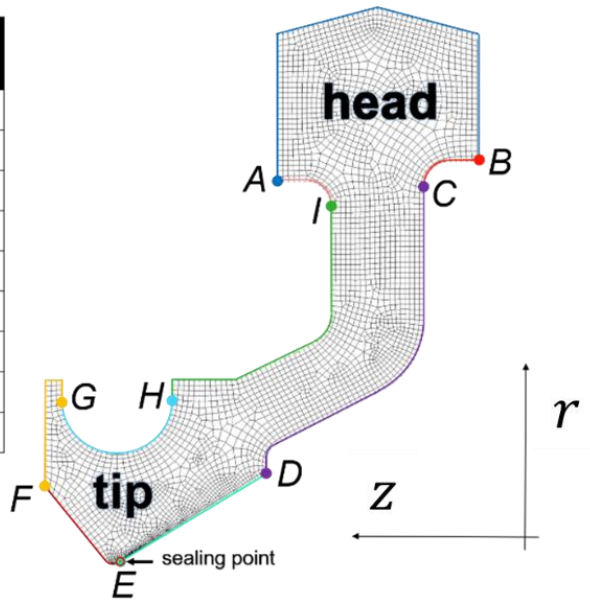

Figure 5-6. Mesh of the selected stern tube seal model with the numbering of the boundaries.

Regardless of whether the material properties are temperature-dependent or not, the thermal expansion of the parts must be included. The frictional heat partition between the seal and the shaft is made according to Charron's relation [90]. The virtual work and energy equations are solved iteratively until convergence is reached [91].

As detailed in *Chapter 3*, the Yeoh hyperelastic model was shown to accurately capture the behaviour of the seal material. The parameters C_{10}, C_{20} and C_{30} for the relaxed situation listed in Table 3-8 are used. The additional material properties are listed in Table 5-3. Note that the axisymmetric model used the Yeoh hyperelastic model and therefore the Young modulus and Poisson ratio shown in Table 5-3 are used for other models, e.g. the Boundary Elements (BE) contact model discussed in *Subsection 5.2.2* (*Paper B*).

Table 5-3. Material properties used for the stern tube seal hardware (and for BE model).

		Stern tube seal	Shaft liner	Seal housing
E	$[MPa]$	14.0	200×10^3	106.5×10^3
ν	$[-]$	0.49	0.27	0.35
ρ	$[kg/m^3]$	1900	7700	8800
C_p	$[J/(kg \cdot K)]$	1670	1909.7	376
k	$[W/(m \cdot K)]$	0.25	25	60
α_T	$[1/K]$	275×10^{-6}	10×10^{-6}	18.5×10^{-6}

The boundary conditions listed in Table 5-4 and Table 5-5 were implemented for solving the virtual work and the heat energy equations, respectively.

Table 5-4. Boundary conditions for solving the virtual work equation.

Position	Boundary number	BC
Seal head and back-up wall	1, 2, 3, 9	Contact model (Penalty Term)
Seal tip	4, 5	Contact model (Augmented Lagrangian) Coulomb friction
Spring groove	7	Spring radial load
Spring side of the seal	5, 6, 7, 8, 9	Pressure load
Back side of the seal	2, 3, 4	Pressure load

Table 5-5. Boundary conditions for solving the energy balance equation.

Position	Boundary number	BC
Seal head and back-up wall	1, 2, 3, 9	Temperature
Seal tip	4, 5	Thermal contact: continuity
Spring side of the seal	5, 6, 7, 8, 9	Convection
Back side of the seal	2, 3, 4	Convection

It was shown useful to solve the model in multiple steps easing its convergence. The solution for each step is used as an initial estimate for the following one. Better convergence was obtained when the seal was initially mounted on the shaft and later the garter spring and pressure boundary conditions were applied. As shown in Figure 5-2, each sealing ring of a ship works under its particular operating conditions according to their location in the stern tube. Figure 5-7 shows the deformation of the seal under various pressure levels obtained with the axisymmetric model.

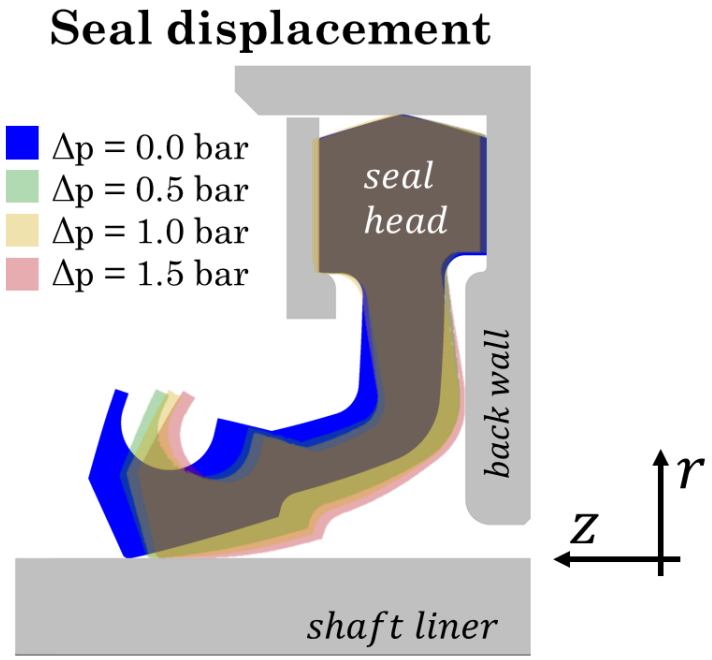

Figure 5-7. Contour of the stern tube seal under various pressure differences ($\mu_0 = 0.0$).

The results revealed that the tip of the seal slides along that shaft as the pressure increases. The role of the back wall becomes evident when the pressure difference exceeds 1 bar. The contact pressure and seal tip profiles are shown in Figure 5-8 and Figure 5-9 respectively.

It is shown that the contact area rapidly increases once the back wall prevents further sliding of the tip. Notice that for the reverse pumping to occur, a skewed contact pressure profile is required among others. Consequently, no reverse pumping is expected at pressure differences below 0.5 bar.

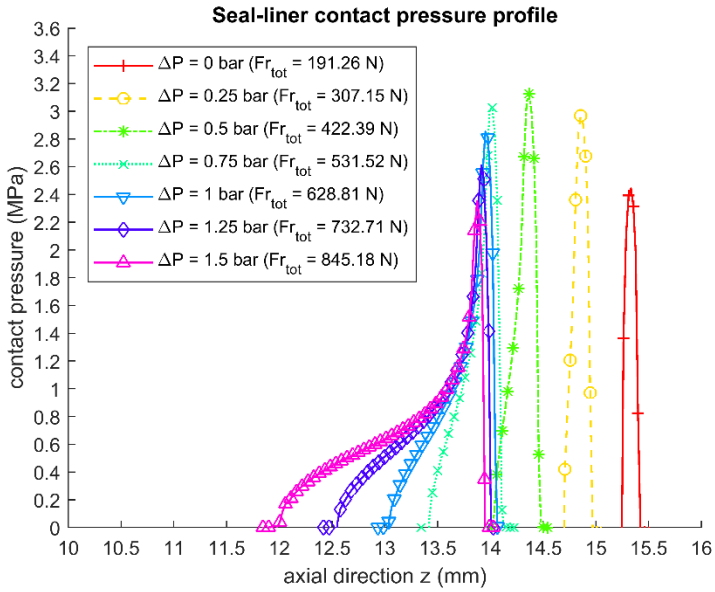

Figure 5-8. Contact pressure profiles under a range of pressure differences (μ_0=0.0).

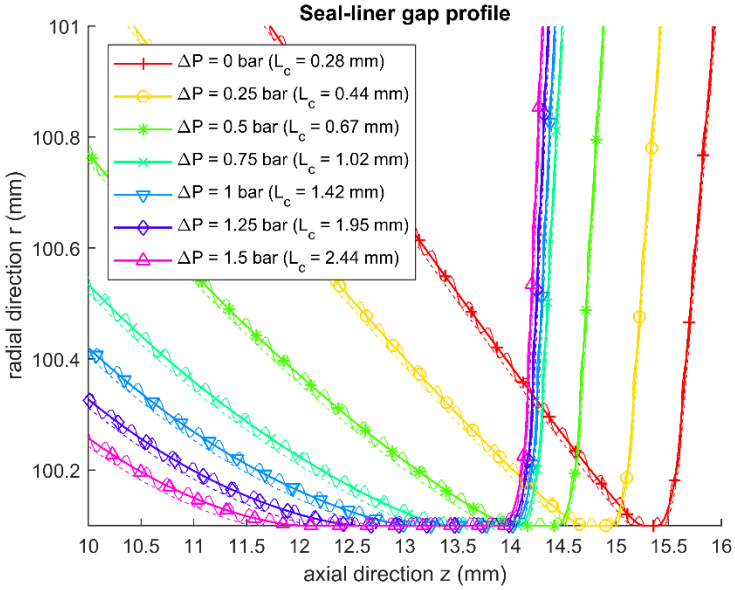

Figure 5-9. Gap profile under a range of pressure differences (μ_0=0.0). A wavy profile with an amplitude of $S_{z_5}/2$ is overlapped on the seal tip profile showing the magnitude of the elastomer roughness.

Great importance is given to the validation of the model. The radial force measurements were carried out using the split-shaft setup described in *Section 4.1*. Four different configurations were tested allowing validation of the implementation of the material model, the boundary conditions and the garter spring as shown in Table 5-6.

Table 5-6. The four configurations tested using the split-shaft test rig.

Configuration	Seal	Garter spring	Housing
A	YES	NO	NO
B	YES	YES	NO
C	YES	NO	YES
D	YES	YES	YES

Figure 5-10 shows the good agreement found between the model and the radial force measurements. Differences in the initial geometry, different curing degrees, or differences in the maximum strain the seal had undergone can explain the variability of the results.

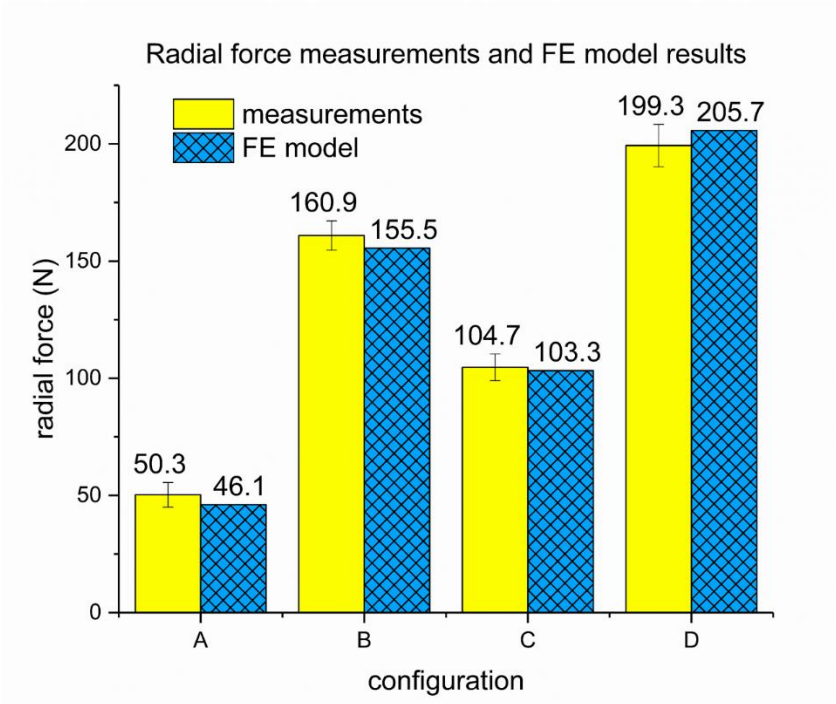

Figure 5-10. Radial force measured under the four configurations described in Table 5-6. The results obtained by the FE model are also shown.

The model was further validated by comparing the contact width predictions with the contact area measured using the glass shaft setup described in *Section 4.2*. The undulations of the seal roughness profile are clearly evidenced on the shaft captions, as shown in Figure 5-11. The FE model assumes a perfectly smooth seal surface and hence a difference between the measured and predicted contact width is expected (see Figure 5-12). In order to account for the seal roughness, a sinusoidal profile with the same period of the surface roughness undulation and an amplitude of $S_{z_5}/2$ was overlapped to the seal contact profile obtained by the FE model as shown in Figure 5-9.

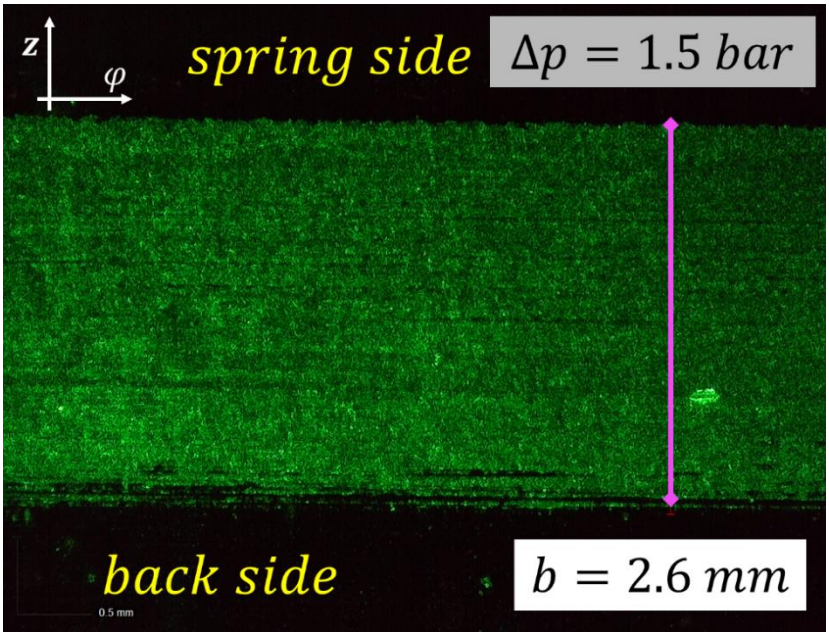

Figure 5-11. Contact width measurement at 1.5 bar pressure difference using the glass shaft setup presented in Section 4.2.

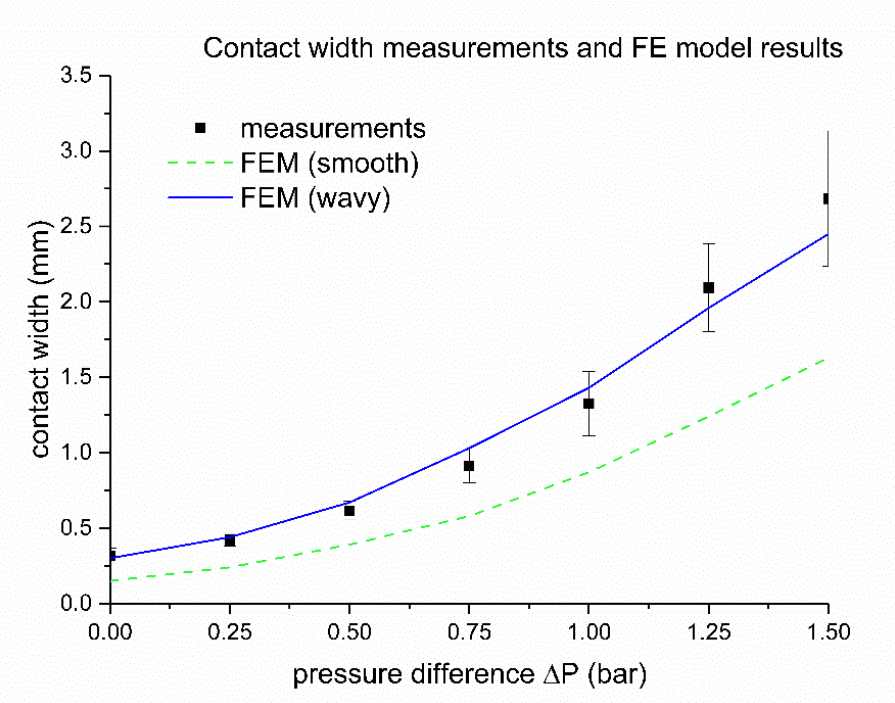

Figure 5-12. Contact width measurement under various pressure differences using the hollow glass shaft setup. The prediction of the FE model (smooth) and when adding $S_{z_5}/2$ (wavy) as in Figure 5-9 are also shown.

5.2.2. Microscopic surface contact model

The loading of the surface roughness of the seal was modelled using a Boundary Element-based (BE) contact model assuming a semi-infinite half-space and homogeneous mechanical properties [92]. For that purpose, the surface patch is assumed to repeat itself in the circumferential direction of the contact, i.e. cell periodicity. The contact model uses the Conjugate Gradient Method (CGM) to estimate the local deformation and the pressure distribution resulting from loading the patch as shown in *Paper B*. The seal asperities were assumed to be linearly elastic for such low strains using the properties listed in Table 5-3. Adhesion was assumed negligible due to the presence of contaminant layers on the contact. Therefore the Boussinesq solution for elastic deformation was used (see Eq. 5-14). A smooth countersurface was considered so the initial gap was exclusively defined by the surface topography of the seal.

$$u_e(x,y) = \frac{1-\nu^2}{\pi E}\int_{-\infty}^{+\infty}\int_{-\infty}^{+\infty}\frac{p(x',y')}{\sqrt{(x-x')^2+(y-y')^2}}dx'dy' \qquad \textit{Eq. 5-14}$$

The loading of the contact patch was obtained from the axisymmetric model shown in *Subsection 5.2.1*. The roughness measurements obtained with the confocal microscope (see *Section 3.4*) were used as input into the BE model and the pressure distribution and surface distortion were computed for various loading conditions. Figure 5-13 shows the limiting situation where the applied normal load is just enough to seal the contact. The areas in pink are the first sealing islands spanning from side-to-side in the circumferential direction, i.e. where a gas tight situation is considered. In this limiting case where the contact pressure is 0.80 MPa two sealing lines developed simultaneously.

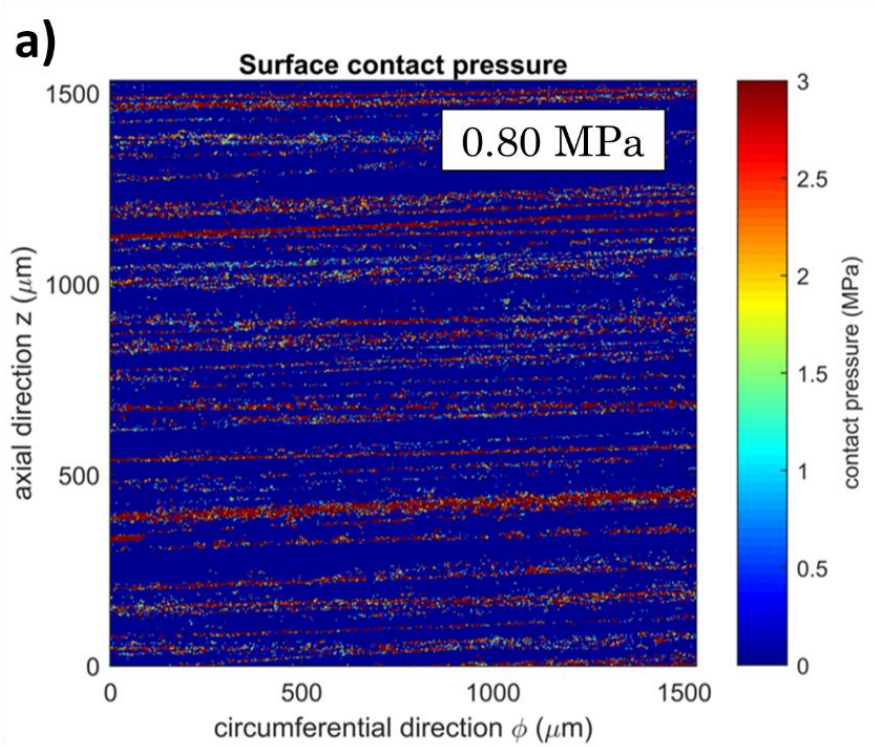

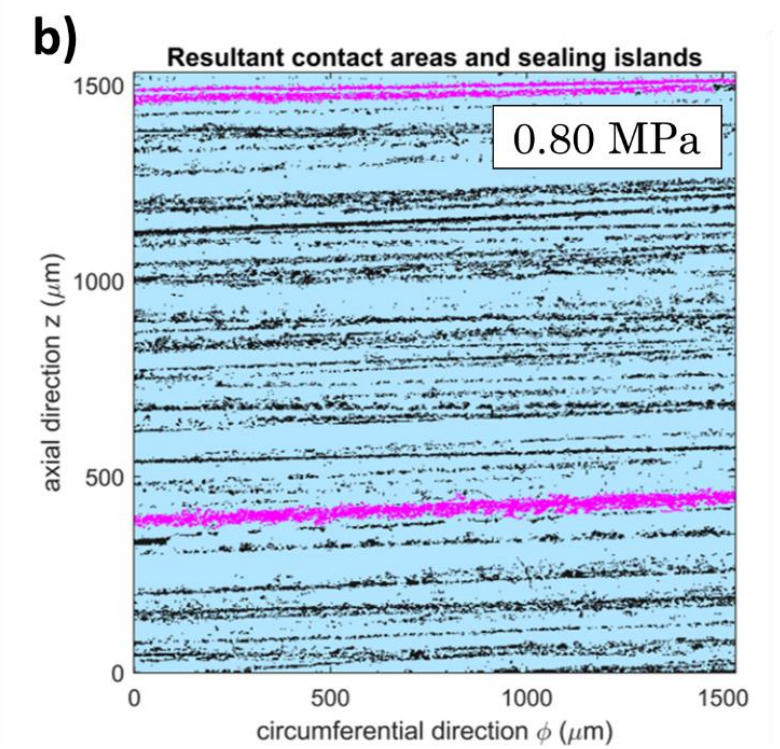

Figure 5-13. Pressure distribution (a) and resultant contact areas depicted in black and pink (b). The areas in pink are the first sealing islands spanning from side-to-side in the circumferential direction, i.e. where a gas tight situation is considered.

To further validate the models presented, the percolation threshold of the seal was determined experimentally using the glass shaft setup shown in *Section 4.2*. A flowmeter was installed at the spring side and the pressure on the back side was slowly increased. Once leakage was detected, the pressure was further increased so a trend line could be fitted, overcoming the limitations of the flowmeter. To replicate the same situation with the BE model, the boundary conditions of the axisymmetric model were matched with those of the glass shaft setup. Figure 5-14 shows the maximum contact pressure predicted by the FE model when the pressure difference decreases. In the same Figure 5-14, the flow rate measurements are plotted showing good agreement with the percolation threshold predicted by the model.

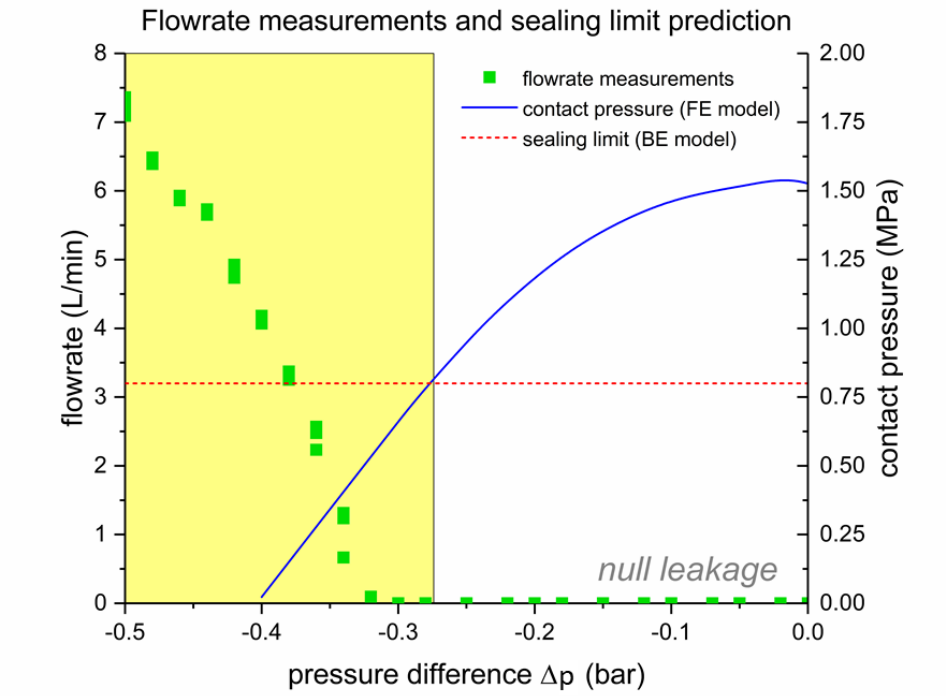

Figure 5-14. Flow rates measured on the glass shaft setup under various pressure differences (dots). The maximum contact pressure predicted by the FE model when the seal is inversely pressurized (solid line). The dashed line shows the minimum contact pressure required for a tight surface, i.e. sealing limit, predicted by the BE model (Subsection 5.2.2). The shaded part corresponds to the pressure differences where leakage is expected.

5.2.3. Three-dimensional FE model for misalignment conditions

Three potential sources of misalignment in the stern tube seal application were analysed: bore-to-shaft misalignment, the hydrostatic pressure gradient, and the non-uniform temperature distribution.

The four general cases of bore-to-shaft misalignments are shown in Figure 5-15. In the real application a combination of the radial and angular misalignments is expected. As the seal is assumed to operate under stationary conditions, the dynamic misalignments were disregarded.

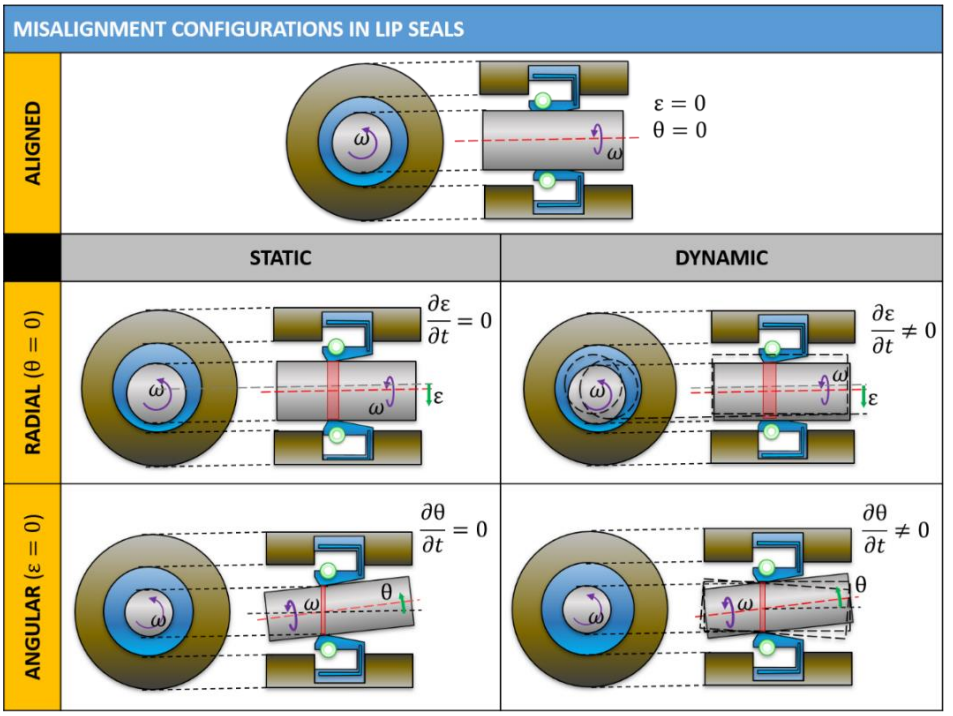

Figure 5-15. Classification bore-to-shaft misalignment in lip seals.

It is not possible to model misalignment with an axisymmetric model. The symmetric nature of the misalignments studied allowed half the geometry to be modelled, as shown in Figure 5-16. Both the radial and angular misalignments were modelled by prescribing the displacement of the shaft.

To decrease the complexity of the model, the two-dimensional axisymmetric model presented in *Subsection 5.2.1* was used to model the clamping of the seal head beforehand. The resultant geometry was extruded in the circumferential direction and was used for modelling the shaft misalignment. The displacement of the seal head was then prevented, allowing the model to be solved with a single contact, i.e. the one between the seal and the shaft. The shaft was assumed rigid and the penalty term formulation was used to ease the overall convergence of the model. The resolution of the mesh in the circumferential direction was refined until the contact pressure predicted agreed with that obtained by the axisymmetric model shown in Figure 5-8.

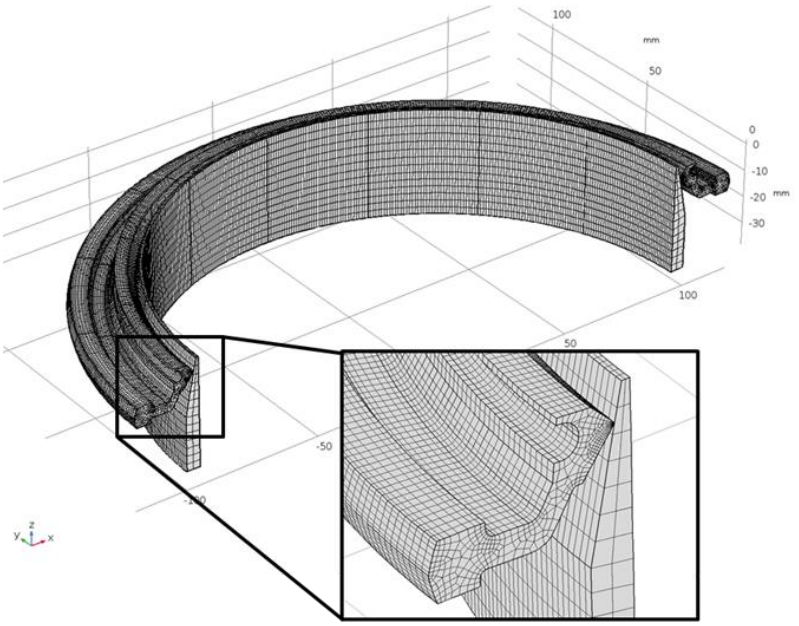

Figure 5-16. Three-dimensional model of the seal. Note the taper shaft part required for its concentric assembly.

The displacements of the seal deduced from the radial and angular misalignments are shown in Figure 5-17. On the top plots, the black arrows indicate the displacement of the shaft. The seal is coloured according to the magnitude of the seal displacement. On the bottom plots, the axial displacement of the seal with respect to the assembled concentric situation is shown. The magnitude of the displacements is shown in Figure 5-18 and Figure 5-19.

The position of the contact profiles obtained under various radial and angular misalignments are shown in Figure 5-18 and Figure 5-19 respectively. The three-dimensional FE model shows good agreement with the measurements performed on the glass shaft setup when misaligned (see *Section 4.2*). While the minimum and maximum displacements of the slanted contact profile are accurately predicted, the transition between zero and 180 degrees differ slightly from the measurements. A linear elastic model was used for the FE model and can explain the inaccuracy. Additionally, the initial seal geometry and the measuring procedure also contribute to the discrepancies observed.

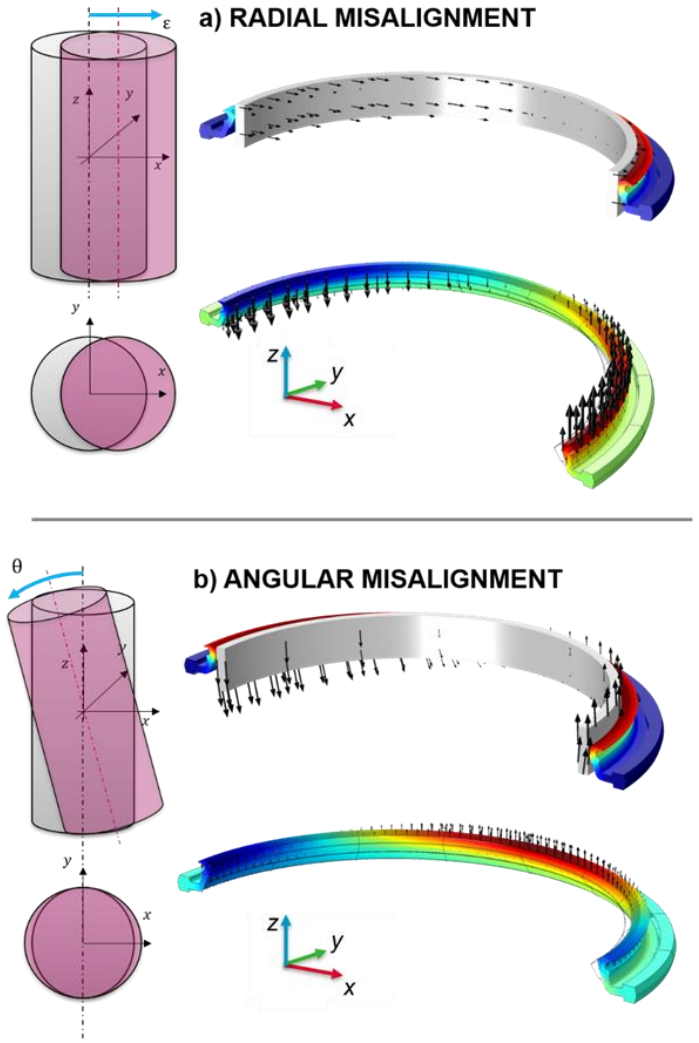

Figure 5-17. Seal displacement due to radial (a) and angular (b) misalignments.

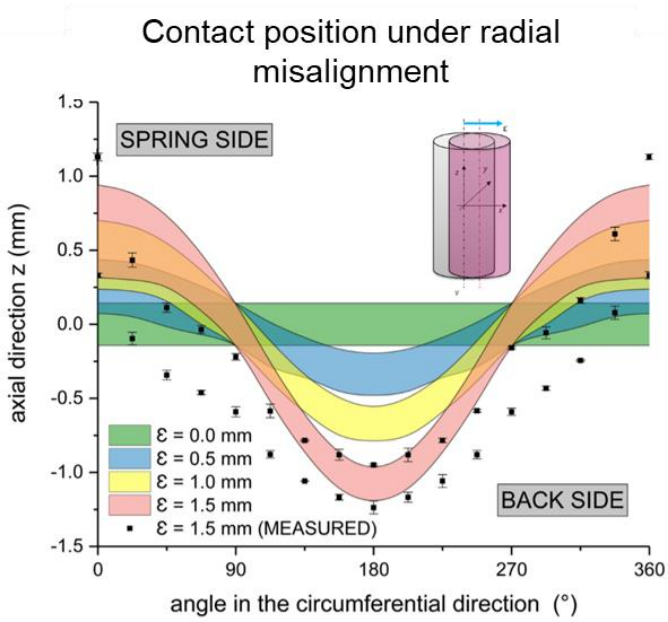

Figure 5-18. Contact position around the shaft for various radial misalignments (Δp = 0 bar).

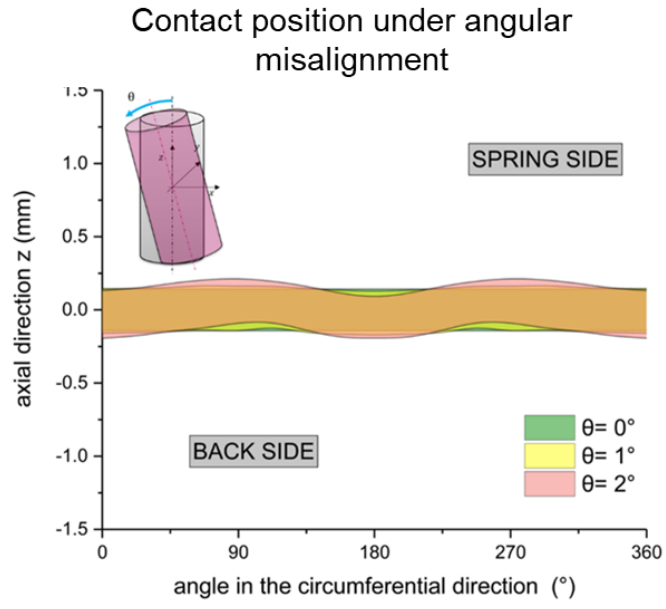

Figure 5-19. Contact position around the shaft for various angular misalignments (Δp = 0 bar).

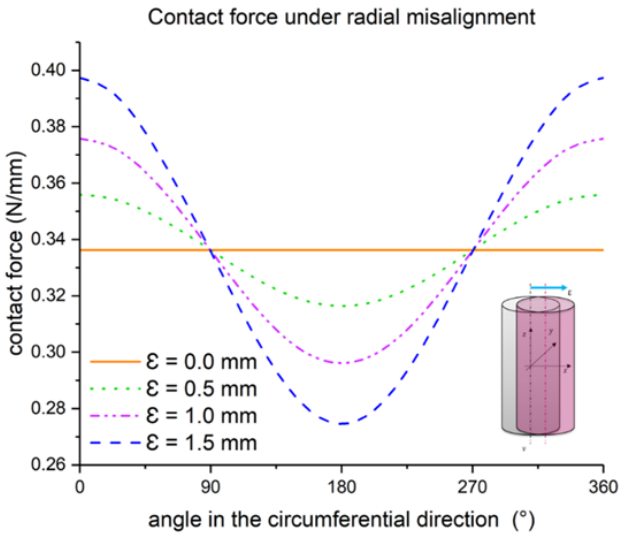

Figure 5-20. Contact force around the shaft for various radial misalignments (Δp = 0 bar).

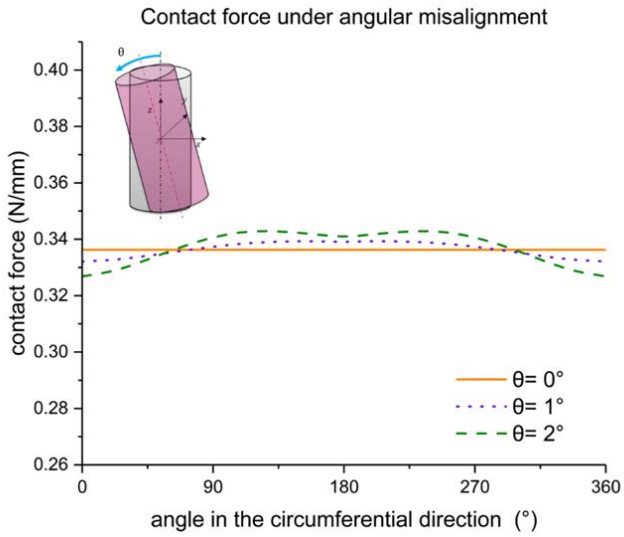

Figure 5-21. Contact force around the shaft for various angular misalignments (Δp = 0 bar).

Besides the two bore-to-shaft static misalignments, the impact of the hydrostatic pressure gradient along the seal and presence of hot spots along the seal were also investigated. No significant displacement was found when a gradient of hydrostatic pressure was set as a boundary condition. The pressure head gradient depends directly on the diameter of the seal, hence it may play a more significant role in larger seals. Ultimately, the non-uniform thermal expansion occurring due to the presence of hot spots on the contact was analysed [72]. A temperature gradient along the seal contact was prescribed on the three-dimensional seal, as shown in Figure 5-22.

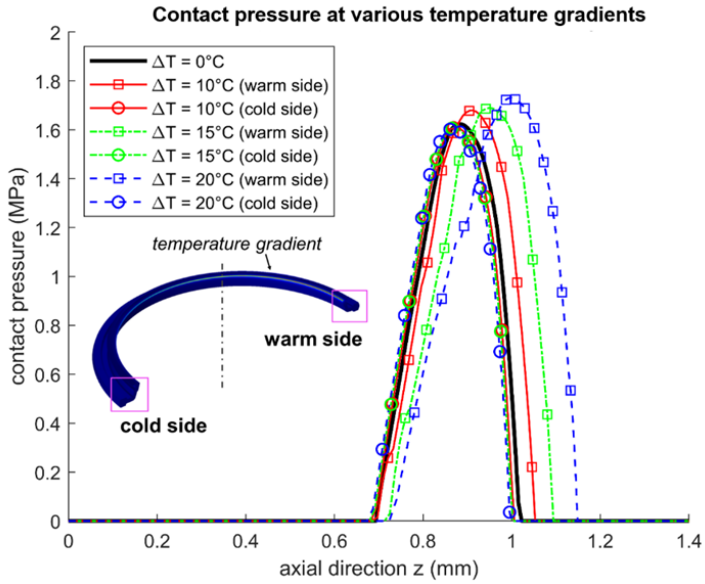

Figure 5-22. Contact force around the shaft for various temperature gradients (Δp = 0 bar).

Counterintuitively, a temperature increase on the tip results in a larger contact force [46]. The contact area increases slightly at the warmer part of the seal because of the material properties.

5.3. Dynamic modelling when aligned

In this section the shaft velocity is included: the shaft is not at rest anymore and hydrodynamics come into play. Hydrodynamic pressures are calculated by solving the Reynolds partial differential equation (PDE) at the seal-shaft interface. The soft seal surface deforms easily as a result of this hydrodynamic pressure and this can be considered by coupling the Reynolds PDE to a mechanical model as the one shown in *Section 5.2*. The study focuses on the stationary operation of rotary lip seals, so time-dependent phenomena such as the viscoelasticity of the seal material are not tackled.

5.3.1. The Reynolds PDE

The Reynolds PDE describes the pressure distribution in fluid film by assuming a viscous laminar flow. The Reynolds PDE is a simplification of the Navier-Stokes equation and its derivation can be found in [28]. The main characteristics of the Reynolds PDE is that the equation neglects inertia effects and body forces. Further, a Newtonian lubricant with constant viscosity and density is assumed. Other assumptions are no slip at the boundaries as well as a fluid film thin enough for a pressure gradient across the film to be disregarded. A generalized expression of the 2D Reynolds equation is shown in Eq. 5-15 [28].

$$\frac{\partial}{\partial x}\left(\frac{\rho h^3}{12\eta}\frac{\partial p}{\partial x}\right)+\frac{\partial}{\partial y}\left(\frac{\rho h^3}{12\eta}\frac{\partial p}{\partial y}\right) = \frac{\partial}{\partial x}\left(\frac{\rho h(u_a+u_b)}{2}\right)+\frac{\partial}{\partial y}\left(\frac{\rho h(v_a+v_b)}{2}\right) + \rho\left(w_a-w_b-u_a\frac{\partial h}{\partial x}-v_a\frac{\partial h}{\partial y}\right)+h\frac{\partial \rho}{\partial t} \qquad \textit{Eq. 5-15}$$

The specific physical significance of each of the terms of the Reynolds equations is summarized in Table 5-7. A more detailed explanation can be found in [93].

Table 5-7. Physical meaning of the terms in the Reynolds equation.

Poiseuille term		
$\frac{\partial}{\partial x}\left(\frac{\rho h^3}{12\eta}\frac{\partial p}{\partial x}\right)+\frac{\partial}{\partial y}\left(\frac{\rho h^3}{12\eta}\frac{\partial p}{\partial y}\right)$	*Eq. 5-16*	Flow rate due to a pressure gradient, i.e. pressure-driven or Poiseuille terms.
Couette term		
$\frac{\partial}{\partial x}\left(\frac{\rho h(u_a+u_b)}{2}\right)+\frac{\partial}{\partial y}\left(\frac{\rho h(v_a+v_b)}{2}\right)$	*Eq. 5-17*	Flow rate due to the motion of the surfaces, i.e. surface velocity-driven or Couette terms.
Density wedge term (thermal wedge)		
$\frac{\partial \rho}{\partial x}\left(\frac{h(u_a+u_b)}{2}\right)+\frac{\partial \rho}{\partial y}\left(\frac{h(v_a+v_b)}{2}\right)$	*Eq. 5-18*	The pressure comes from the rate at which the lubricant density changes along the sliding direction. If the temperature of the film increases while being dragged, uneven densities develop which need to be compensated by a pressure gradient on the film.
Stretch term		
$\frac{\partial (u_a+u_b)}{\partial x}\left(\frac{\rho h}{2}\right)+\frac{\partial (v_a+v_b)}{\partial y}\left(\frac{\rho h}{2}\right)$	*Eq. 5-19*	There is a gradient of velocity along the surface. This term may become important when one of the surfaces, e.g. an elastomeric surface, deforms significantly in the sliding direction, but it is usually ignored.

<table>
<tr><td></td><td>Physical wedge term</td><td></td></tr>
<tr><td></td><td>$$\frac{\partial h}{\partial x}\left(\frac{\rho(u_a+u_b)}{2}\right)+\frac{\partial h}{\partial y}\left(\frac{\rho(v_a+v_b)}{2}\right)$$ Eq. 5-20</td><td>The fluid is dragged from a thicker to a narrower gap. This is the best known arrangement providing pressure generation.</td></tr>
<tr><td colspan="3">Squeeze term</td></tr>
<tr><td colspan="2">$$\rho\left(w_a-w_b-u_a\frac{\partial h}{\partial x}-v_a\frac{\partial h}{\partial y}\right)$$ Eq. 5-21</td><td rowspan="5">The normal squeeze accounts for the pressure generation as a result of varying the film thickness. It is the main mechanism in animal joints acting as a cushioning effect. The translational squeeze term accounts for the pressure generated by the sliding of the surfaces.</td></tr>
<tr><td></td><td>Normal squeeze term</td></tr>
<tr><td></td><td>$$\rho(w_a-w_b)$$ Eq. 5-22</td></tr>
<tr><td></td><td>Translational (geometric) squeeze term</td></tr>
<tr><td></td><td>$$\rho\left(-u_a\frac{\partial h}{\partial x}-v_a\frac{\partial h}{\partial y}\right)$$ Eq. 5-23</td></tr>
<tr><td colspan="3">Local expansion term</td></tr>
<tr><td colspan="2">$$h\frac{\partial \rho}{\partial t}$$ Eq. 5-24</td><td>This term accounts for the time rate of density change. If the temperature of the lubricant increases, for example, the excess volume of lubricant generates a pressure increase.</td></tr>
</table>

When modelling rotary lip seals, it is common to disregard the squeeze term and the local expansion term leaving only the physical wedge as a pressure generation term (see Eq. 5-25). Only the velocity of the shaft u_a is considered.

$$\frac{\partial}{\partial x}\left(\frac{h^3}{12\eta}\frac{\partial p}{\partial x}\right)+\frac{\partial}{\partial y}\left(\frac{h^3}{12\eta}\frac{\partial p}{\partial y}\right)=\left(\frac{u_a}{2}\right)\frac{\partial h}{\partial x} \qquad \textit{Eq. 5-25}$$

The fact that rotary lip seals do not present an apparent convergent gap, i.e. a wedge, in the direction of the velocity casts some doubts on the source of the hydrodynamic action.

5.3.2. Solution of the Reynolds PDE

Finite differences are used to solve the Reynolds PDE in the seal-shaft interface, as shown in Figure 5-23. A uniformly spaced grid is defined in the x and y directions with N and M nodes respectively.

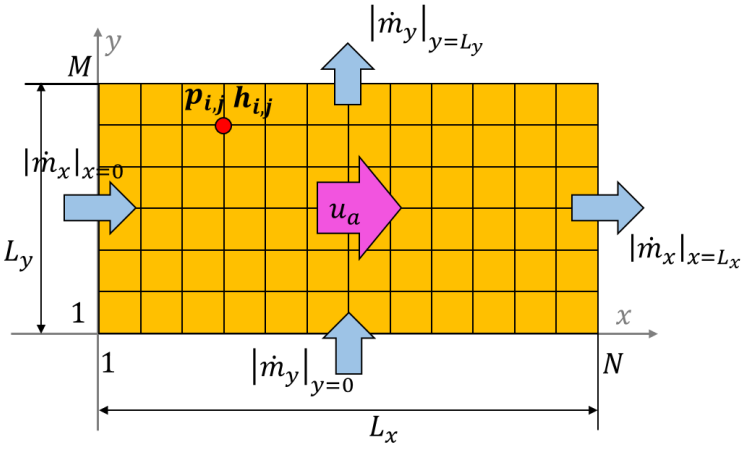

Figure 5-23. Computational domain.

The simplified Reynolds PDE shown in Eq. 5-25 assumes constant viscosity, density and surface velocity. Only the velocity in x of one of the surfaces, i.e. u_a, is included. A dimensionless form of it is obtained as follows.

$$\bar{x}=\frac{x}{L_x};\quad \bar{y}=\frac{y}{L_y};\quad \bar{h}=\frac{h}{\sigma};\quad \bar{p}=\frac{p\sigma^2}{6\eta u_a L_x};\quad \sigma=\sqrt{\sigma_{q_1}^2+\sigma_{q_2}^2} \qquad \textit{Eq. 5-26}$$

$$\frac{\partial}{\partial \bar{x}}\left(\bar{h}^3\frac{\partial \bar{p}}{\partial \bar{x}}\right)+\left(\frac{L_x}{L_y}\right)^2\frac{\partial}{\partial \bar{y}}\left(\bar{h}^3\frac{\partial \bar{p}}{\partial \bar{y}}\right)=\frac{\partial \bar{h}}{\partial \bar{x}} \qquad \textit{Eq. 5-27}$$

The differential terms are described by finite differences using Eq. 5-28 to Eq. 5-33 via the central difference approximation.

$$\frac{\partial \bar{p}}{\partial \bar{x}} \cong \frac{\bar{p}_{i+1,\,j} - \bar{p}_{i-1,\,j}}{2\Delta\bar{x}} \qquad \textit{Eq. 5-28}$$

$$\frac{\partial \bar{p}}{\partial \bar{y}} \cong \frac{\bar{p}_{i,\,j+1} - \bar{p}_{i,\,j-1}}{2\Delta\bar{y}} \qquad \textit{Eq. 5-29}$$

$$\frac{\partial^2 \bar{p}}{\partial \bar{x}^2} \cong \frac{\bar{p}_{i+1,\,j} - 2\bar{p}_{i,j} + \bar{p}_{i-1,\,j}}{\Delta\bar{x}^2} \qquad \textit{Eq. 5-30}$$

$$\frac{\partial^2 \bar{p}}{\partial \bar{y}^2} \cong \frac{\bar{p}_{i,\,j+1} - 2\bar{p}_{i,j} + \bar{p}_{i,\,j-1}}{\Delta\bar{y}^2} \qquad \textit{Eq. 5-31}$$

$$\frac{\partial \bar{h}}{\partial \bar{x}} \cong \frac{\bar{h}_{i+1,\,j} - \bar{h}_{i-1,\,j}}{2\Delta\bar{x}} \qquad \textit{Eq. 5-32}$$

$$\frac{\partial \bar{h}}{\partial \bar{y}} \cong \frac{\bar{h}_{i,\,j+1} - \bar{h}_{i,\,j-1}}{2\Delta\bar{y}} \qquad \textit{Eq. 5-33}$$

Next, by combining Eq. 5-27 with the expressions above, Eq. 5-36 is reached.

$$\frac{\partial^2 \bar{p}}{\partial \bar{x}^2} + \left(\frac{L_x}{L_y}\right)^2 \frac{\partial^2 \bar{p}}{\partial \bar{y}^2} + \frac{\partial \bar{h}}{\partial \bar{x}} \frac{3}{\bar{h}} \frac{\partial \bar{p}}{\partial \bar{x}} + \left(\frac{L_x}{L_y}\right)^2 \frac{\partial \bar{h}}{\partial \bar{y}} \frac{3}{\bar{h}} \frac{\partial \bar{p}}{\partial \bar{y}} = \frac{1}{\bar{h}^3} \frac{\partial \bar{h}}{\partial \bar{x}} \qquad \textit{Eq. 5-34}$$

$$\frac{\bar{p}_{i+1,\,j} - 2\bar{p}_{i,j} + \bar{p}_{i-1,\,j}}{\Delta\bar{x}^2} + \left(\frac{L_x}{L_y}\right)^2 \frac{\bar{p}_{i,\,j+1} - 2\bar{p}_{i,j} + \bar{p}_{i,\,j-1}}{\Delta\bar{y}^2} + \frac{\partial \bar{h}}{\partial \bar{x}} \frac{3}{\bar{h}} \frac{\bar{p}_{i+1,\,j} - \bar{p}_{i-1,\,j}}{2\Delta\bar{x}} + \left(\frac{L_x}{L_y}\right)^2 \frac{\partial \bar{h}}{\partial \bar{y}} \frac{3}{\bar{h}} \frac{\bar{p}_{i,\,j+1} - \bar{p}_{i,\,j-1}}{2\Delta\bar{y}} = \frac{1}{\bar{h}^3} \frac{\partial \bar{h}}{\partial \bar{x}} \qquad \textit{Eq. 5-35}$$

$$\bar{p}_{i,j}\left(-\frac{2}{\Delta\bar{x}^2} - \left(\frac{L_x}{L_y}\right)^2 \frac{2}{\Delta\bar{y}^2}\right) + \bar{p}_{i+1,\,j}\left(\frac{1}{\Delta\bar{x}^2} + \frac{\partial \bar{h}}{\partial \bar{x}} \frac{3}{\bar{h}} \frac{1}{2\Delta\bar{x}}\right) + \bar{p}_{i-1,\,j}\left(\frac{1}{\Delta\bar{x}^2} - \frac{\partial \bar{h}}{\partial \bar{x}} \frac{3}{\bar{h}} \frac{1}{2\Delta\bar{x}}\right) + \bar{p}_{i,\,j+1}\left(\left(\frac{L_x}{L_y}\right)^2 \left(\frac{1}{\Delta\bar{y}^2} + \frac{\partial \bar{h}}{\partial \bar{y}} \frac{3}{\bar{h}} \frac{1}{2\Delta\bar{y}}\right)\right) + \bar{p}_{i,\,j-1}\left(\left(\frac{L_x}{L_y}\right)^2 \left(\frac{1}{\Delta\bar{y}^2} - \frac{\partial \bar{h}}{\partial \bar{y}} \frac{3}{\bar{h}} \frac{1}{2\Delta\bar{y}}\right)\right) = \frac{1}{\bar{h}^3} \frac{\partial \bar{h}}{\partial \bar{x}} \qquad \textit{Eq. 5-36}$$

Finally, the unknown $\bar{p}_{i,j}$ can be isolated so each node depends on the four nodes surrounding it, rendering Eq. 5-37.

$$\bar{p}_{i,j} = A_{i,j}\,\bar{p}_{i-1,j} + B_{i,j}\bar{p}_{i,j-1} + C_{i,j}\,\bar{p}_{i+1,j} + D_{i,j}\bar{p}_{i,j+1} + E_{i,j} \qquad \textit{Eq. 5-37}$$

The constants $A_{i,j}$, $B_{i,j}$, $C_{i,j}$, $D_{i,j}$ and $E_{i,j}$ are specific for each grid point:

$$\chi = \left(\frac{2}{\Delta\bar{x}^2} + \left(\frac{L_x}{L_y}\right)^2 \frac{2}{\Delta\bar{y}^2}\right) \qquad \textit{Eq. 5-38}$$

$$A_{i,j} = \frac{1}{\chi}\left(\frac{1}{\Delta\bar{x}^2} - \frac{\partial\bar{h}}{\partial\bar{x}}\frac{3}{\bar{h}}\frac{1}{2\Delta\bar{x}}\right) \qquad \textit{Eq. 5-39}$$

$$B_{i,j} = \frac{1}{\chi}\left(\frac{L_x}{L_y}\right)^2\left(\frac{1}{\Delta\bar{y}^2} - \frac{\partial\bar{h}}{\partial\bar{y}}\frac{3}{\bar{h}}\frac{1}{2\Delta\bar{y}}\right) \qquad \textit{Eq. 5-40}$$

$$C_{i,j} = \frac{1}{\chi}\left(\frac{1}{\Delta\bar{x}^2} + \frac{\partial\bar{h}}{\partial\bar{x}}\frac{3}{\bar{h}}\frac{1}{2\Delta\bar{x}}\right) \qquad \textit{Eq. 5-41}$$

$$D_{i,j} = \frac{1}{\chi}\left(\frac{L_x}{L_y}\right)^2\left(\frac{1}{\Delta\bar{y}^2} + \frac{\partial\bar{h}}{\partial\bar{y}}\frac{3}{\bar{h}}\frac{1}{2\Delta\bar{y}}\right) \qquad \textit{Eq. 5-42}$$

$$E_{i,j} = -\frac{1}{\chi}\frac{1}{\bar{h}^3}\frac{\partial\bar{h}}{\partial\bar{x}} \qquad \textit{Eq. 5-43}$$

The pressure at each node of the computational domain can be calculated, given a specific gap profile h, surface velocity and fluid viscosity as input data. The pressure at the nodes located at the edges of the computational domain are specified according to the boundary conditions, hence they are not included in the iteration scheme. The pressure at each node is calculated line by line following the Tri-Diagonal Matrix Algorithm (TDMA) until the resulting pressure field convergences to a solution. Eq. 5-44 is defined as the convergence criterion.

$$\frac{\left(\sum_{i=1}^{N}\sum_{j=1}^{M}\bar{p}_{i,j}\right)_k - \left(\sum_{i=1}^{N}\sum_{j=1}^{M}\bar{p}_{i,j}\right)_{k-1}}{\left(\sum_{i=1}^{N}\sum_{j=1}^{M}\bar{p}_{i,j}\right)_k} \leq 10^{-8} \qquad \textit{Eq. 5-44}$$

Once the pressure distribution in the domain is solved, the load-carrying capacity, shear stresses and flow rates can be calculated. The load-carrying capacity w is estimated by adding together all the nodal pressures:

$$w = \int_0^{L_y}\int_0^{L_x} p\, dxdy \qquad \textit{Eq. 5-45}$$

The total shear stress components are calculated in the same fashion:

$$f_{xz} = \int_0^{L_y}\int_0^{L_x}\tau_{xz}dxdy = \int_0^{L_y}\int_0^{L_x}\left(\frac{h}{2}\frac{\partial p}{\partial x} - \frac{\eta u_a}{h}\right)dxdy \qquad \textit{Eq. 5-46}$$

$$f_{yz} = \int_0^{L_y}\int_0^{L_x} \tau_{yz} dxdy = \int_0^{L_y}\int_0^{L_x} \left(\frac{h}{2}\frac{\partial p}{\partial x}\right) dxdy \qquad \textit{Eq. 5-47}$$

The flow rate in each direction is obtained via Eq. 5-48 and Eq. 5-49.

$$\dot{m}_x = \rho q_x = \rho \int_0^{L_y} \left(-\frac{h^3}{12\eta}\frac{\partial p}{\partial x} + \frac{u_a h}{2}\right) dy \qquad \textit{Eq. 5-48}$$

$$\dot{m}_y = \rho q_y = \rho \int_0^{L_x} \left(-\frac{h^3}{12\eta}\frac{\partial p}{\partial y}\right) dx \qquad \textit{Eq. 5-49}$$

A higher order finite difference term is used to approximate the pressure gradients $\partial p/\partial x$ and $\partial p/\partial y$ at the boundaries of the domain, leading to more accurate estimates of the flow rate at the boundaries (Eq. 5-50 and Eq. 5-51).

$$\left|\frac{\partial p}{\partial x}\right|_{x=0} = \frac{-25p_{i,j} + 48p_{i+1,j} - 36p_{i+2,j} + 16p_{i+3,j} - 3p_{i+4,j}}{12\Delta x} \qquad \textit{Eq. 5-50}$$

$$\left|\frac{\partial p}{\partial y}\right|_{y=L_y} = \frac{-25p_{i,j} + 48p_{i,j-1} - 36p_{i,j-2} + 16p_{i,j-3} - 3p_{i,j-4}}{12\Delta y} \qquad \textit{Eq. 5-51}$$

5.3.3. Universal cavitation algorithm

When the lubricant is dragged through a divergent gap profile, i.e. a negative wedge, the Reynolds equation predicts a pressure decrease. If the lubricant pressure decreases beyond a lubricant-specific value, cavitation develops. The limiting pressure is called the cavitation pressure p_c. The Reynolds equation is unable to predict cavitation, hence more advanced algorithms must be used to account for it. As the lubricant flow rate across the seal-shaft interface is what is of interest here, a mass-conserving algorithm is required. Among other methods [94], the Elrod cavitation model [95] was selected as it has already proved useful for the rotary lip seals application [57], [60], [69]. Instead of the hydrodynamic pressure, the Elrod algorithm solves for a universal dependent variable ϕ. The density and the lubricant pressure are related through the bulk modulus κ [94], as shown in Eq. 5-52 and Eq. 5-53.

$$\phi = \frac{\rho}{\rho_c} \qquad \textit{Eq. 5-52}$$

$$p = p_c + g\kappa \ln(\phi) \qquad \textit{Eq. 5-53}$$

This new partial differential equation applies to both the full film region and the cavitation domains. Within the cavitation domain, the gap is not fully filled by liquid and the variable ϕ represents the relative amount of liquid present, i.e. the fractional film content. Subsequently, $(1-\phi)$ is the gas fraction. Along the full film domain, the variable ϕ can be understood as the density ratio and is always greater than 1. A switch function g determines whether the fluid is within the full film or cavitation zones, as shown in Eq. 5-58.

$$\frac{\partial p}{\partial x} = \frac{\partial p}{\partial \phi}\frac{\partial \phi}{\partial x} = \frac{g\kappa}{\phi}\frac{\partial \phi}{\partial x} \qquad \textit{Eq. 5-54}$$

$$\frac{\partial}{\partial x}\left(\frac{\rho h^3}{12\eta}\frac{\partial p}{\partial x}\right) + \frac{\partial}{\partial y}\left(\frac{\rho h^3}{12\eta}\frac{\partial p}{\partial y}\right) = \frac{1}{2}(u_a)\frac{\partial(\rho h)}{\partial x} \qquad \textit{Eq. 5-55}$$

$$\frac{\partial}{\partial x}\left(\frac{p_c \phi h^3}{12\eta}\frac{\partial p}{\partial \phi}\frac{\partial \phi}{\partial x}\right) + \frac{\partial}{\partial y}\left(\frac{p_c \phi h^3}{12\eta}\frac{\partial p}{\partial \phi}\frac{\partial \phi}{\partial y}\right) = \frac{1}{2}(u_a)\frac{\partial(p_c \phi h)}{\partial x} \qquad \textit{Eq. 5-56}$$

$$\frac{\partial}{\partial x}\left(\frac{g\kappa h^3}{12\eta}\frac{\partial \phi}{\partial x}\right) + \frac{\partial}{\partial y}\left(\frac{g\kappa h^3}{12\eta}\frac{\partial \phi}{\partial y}\right) = \frac{1}{2}(u_a)\frac{\partial(\phi h)}{\partial x} \qquad \textit{Eq. 5-57}$$

$$full\ film\ zone \begin{cases} \phi > 1 \\ g = 1 \end{cases} \qquad cavitation\ zone \begin{cases} 0 < \phi < 1 \\ g = 0 \end{cases} \qquad \textit{Eq. 5-58}$$

The partial differential equation is turned non-dimensional as follows,

$$\bar{x} = \frac{x}{L_x};\quad \bar{y} = \frac{y}{L_y};\quad \bar{h} = \frac{h}{\sigma};\quad \Psi = \frac{6\eta(u_a)L_x}{\kappa\sigma^2} \qquad \textit{Eq. 5-59}$$

$$\frac{\partial}{\partial \bar{x}}\left(g\,\bar{h}^3\frac{\partial \phi}{\partial \bar{x}}\right) + \left(\frac{L_x}{L_y}\right)^2\frac{\partial}{\partial \bar{y}}\left(g\,\bar{h}^3\frac{\partial \phi}{\partial \bar{y}}\right) = \Psi\frac{\partial(\bar{h}\phi)}{\partial \bar{x}} \qquad \textit{Eq. 5-60}$$

In a similar fashion to that shown by the general Reynolds case, the following terms can be expressed using the finite differences method, leading to:

$$\phi_{i,j} = A_{i,j}\,\phi_{i-1,j} + B_{i,j}\phi_{i,j-1} + C_{i,j}\,\phi_{i+1,j} + D_{i,j}\phi_{i,j+1} + E_{i,j} \qquad \textit{Eq. 5-61}$$

Analogously to the procedure followed when solving the Reynolds PDE in *Subsection 5.3.2*, the constants $A_{i,j}$, $B_{i,j}$, $C_{i,j}$, $D_{i,j}$ and $E_{i,j}$ are obtained with Eq. 5-62 to Eq. 5-67.

$$\chi = \frac{1}{\Delta\bar{x}^2} g_{i,j} \left(\bar{h}^3_{i+\frac{1}{2},j} + \bar{h}^3_{i-\frac{1}{2},j} \right) + \frac{1}{\Delta\bar{y}^2} g_{i,j} \left(\bar{h}^3_{i,j+\frac{1}{2}} + \bar{h}^3_{i,j-\frac{1}{2}} \right) + \frac{\Psi}{\Delta\bar{x}} h_{i,j}(1 - g_{i,j}) \quad \textit{Eq. 5-62}$$

$$A_{i,j} = \frac{1}{\chi} \left\{ \frac{1}{\Delta\bar{x}^2} \left[\bar{h}^3_{i-\frac{1}{2},j} g_{i-1,j} \right] + \frac{\Psi}{\Delta\bar{y}^2} \left[\bar{h}_{i-1,j} \left(1 - g_{i-1,j} \right) \right] \right\} \quad \textit{Eq. 5-63}$$

$$B_{i,j} = \frac{1}{\chi} \frac{1}{\Delta\bar{y}^2} \left[\bar{h}^3_{i,j-\frac{1}{2}} g_{i,j-1} \right] \quad \textit{Eq. 5-64}$$

$$C_{i,j} = \frac{1}{\chi} \frac{1}{\Delta\bar{x}^2} \left[\bar{h}^3_{i+\frac{1}{2},j} g_{i+1,j} \right] \quad \textit{Eq. 5-65}$$

$$D_{i,j} = \frac{1}{\chi} \frac{1}{\Delta\bar{y}^2} \left[\bar{h}^3_{i,j-\frac{1}{2}} g_{i,j-1} \right] \quad \textit{Eq. 5-66}$$

$$E_{i,j} = -\frac{1}{\chi} \left\{ -\frac{\Psi}{\Delta\bar{x}} \left[\frac{g_{i-1,j}\, h_{i-1,j}}{2} (2 - g_{i,j}) - \frac{g_{i,j} h_{i,j}}{2} (g_{i-1,j} - 2 + g_{i+1,j}) + \frac{g_{i+1,j} g_{i,j} h}{2} \right. \right.$$
$$\left. + \frac{1}{\Delta\bar{x}^2} \left[\bar{h}^3_{i+\frac{1}{2},j} g_{i+1,j} - \left(\bar{h}^3_{i+\frac{1}{2},j} + \bar{h}^3_{i-\frac{1}{2},j} \right) g_{i,j} + \bar{h}^3_{i-\frac{1}{2},j} g_{i-1,j} \right] + \quad \textit{Eq. 5-67}$$
$$\left. \left. + \frac{1}{\Delta\bar{y}^2} \left[\bar{h}^3_{i,j+\frac{1}{2}} g_{i,j+1} - \left(\bar{h}^3_{i,j+\frac{1}{2}} + \bar{h}^3_{i,j-\frac{1}{2}} \right) g_{i,j} + \bar{h}^3_{i,j-\frac{1}{2}} g_{i,j-1} \right] \right\}$$

Once more, the nodal $\phi_{i,j}$ values are updated until the results converges to a specific tolerance. A high value of the bulk modulus κ brings difficulties in the numerical model due to the high sensitivity of the pressure to the density ratio ϕ. Further discussion on the role of κ to the convergence of the algorithm can be found in [96].

If vapour cavitation develops when the universal cavitation algorithm has been solved, it is important to account for both the full film and the cavitation zones when estimating the lubricant shear stress and the flow rates. The viscous shearing can be obtained as in Eq. 5-68 and Eq. 5-69.

$$\tau_{xz} = \frac{h}{2} \frac{\partial p}{\partial x} - \phi \frac{\eta}{h} u_a \quad \textit{Eq. 5-68}$$

$$\tau_{yz} = \frac{h}{2} \frac{\partial p}{\partial y} \quad \textit{Eq. 5-69}$$

Hence, making use of the relation shown in Eq. 5-54, the expressions for the flow rates render [95],

$$\dot{m}_x = \int_0^{L_y} \left(-\frac{\rho_c h^3 g\kappa}{12\eta} \frac{\partial \phi}{\partial x} + \phi \frac{\rho_c u_a}{2} h \right) dy = \int_0^{L_y} \left(-\frac{\rho_c h^3 \phi}{12\eta} \frac{\partial p}{\partial x} + \phi \frac{\rho_c u_a}{2} h \right) dy \quad \textit{Eq. 5-70}$$

$$\dot{m}_y = \int_0^{L_x} \left(-\frac{\rho_c g\kappa h^3}{12\eta} \frac{\partial \phi}{\partial y} \right) dx = \int_0^{L_x} \left(-\frac{\rho_c h^3 \phi}{12\eta} \frac{\partial p}{\partial y} \right) dx \quad \textit{Eq. 5-71}$$

5.3.4. Distortion of the gap profile

The space left between the seal and the shaft – the gap – is affected by the deformation of the seal and the shaft. Typically in rotary lip seals the distortion of the gap is accounted for by the influence coefficient method [30], [97]. This strategy is analogous to the one used to predict the local displacements and contact pressure of a rough surface by the Boussinesq model (*Subsection 5.2.2*). In that case, the compliance matrices C_r, C_z and C_φ were directly obtained from the surface material properties assuming an infinite isotropic half-space [98] . When it comes to predicting the deformation of a seal, the compliance matrices must be tailored to each specific seal [55]. The displacement in radial, axial and circumferential direction is then related to the loading of the surface via Eq. 5-72, Eq. 5-73 and Eq. 5-74 [97] respectively.

$$(d_r)_i = \sum_{k=1}^{N} (\boldsymbol{C}_r)_{ik} \, (p \Delta z \Delta \varphi)_k \quad \textit{Eq. 5-72}$$

$$(d_z)_i = \sum_{k=1}^{N} (\boldsymbol{C}_z)_{ik} \, (\tau_{zr} \Delta z \Delta \varphi)_k \quad \textit{Eq. 5-73}$$

$$(d_\varphi)_i = \sum_{k=1}^{N} (\boldsymbol{C}_\varphi)_{ik} \, (\tau_{\varphi r} \Delta z \Delta \varphi)_k \quad \textit{Eq. 5-74}$$

The compliance matrices are obtained beforehand using the FE model of the seal shown in *Section 5.2*. The linear perturbation method is typically used [61]. It is essential to account for the distortion of the seal in the circumferential direction [32] as it plays a key role in the reverse pumping mechanism of rotary lip seals. Axisymmetric models cannot capture the displacements in the circumferential direction, hence more advanced models are required.

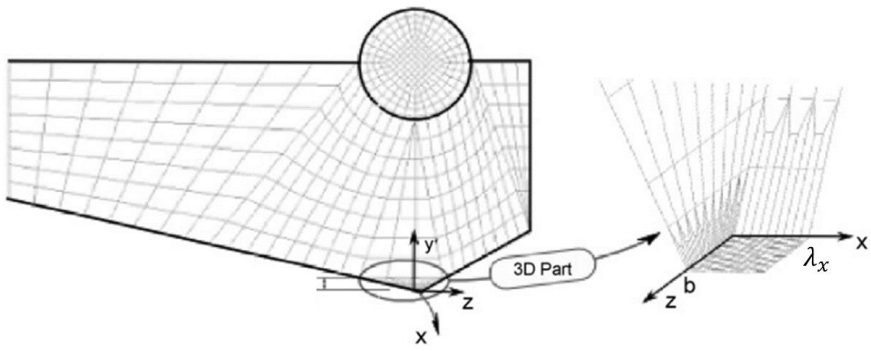

Figure 5-24. Lip seal finite element mesh [99].

Typically, the two-dimensional axisymmetric model of the seal is coupled to a three-dimensional model, i.e. non-axisymmetric, as shown in Figure 5-24. The three-dimensional model represents the tip of the seal where the circumferential loads and displacements can occur [99]. Maoui [97] showed that more accurate results were obtained by using a fully three-dimensional model for the seal, particularly for the flow rate. The influence coefficient matrix for the radial displacement (Eq. 5-72) was used in the misalignment-induced model presented in *Paper D* (*Subsection 5.4.2*).

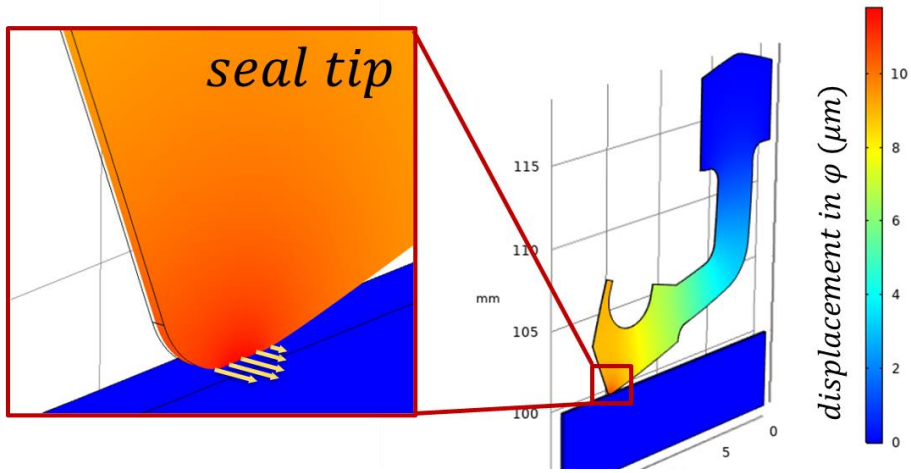

Figure 5-25. Three-dimensional model of the seal to account for axial, radial and circumferential direction displacements.

A three-dimensional model shown in Figure 5-25 was used to estimate the out-of-plane deformations. The geometry presented in the 2D

axisymmetric model (*Section 5.2*) was revolved in the circumferential direction so the radial, axial and circumferential deformations of the seal can be computed. By setting continuity conditions for the seal faces, the arch of the revolution can be set small decreasing the number of elements of the model. The FE software used allowed to directly couple the displacement of the model shown in Figure 5-25 to the surface patch were the hydrodynamic pressure is solved. This way, both the seal and the surface patch models are solved iteratively until convergence is reached, i.e. in-line.

5.3.5. Elastohydrodynamic model (aligned)

This is the generalized approach for modelling rotary lip seals [55], [58], [61], [99]. The focus of this research is not on modelling the primary lubrication mechanism of rotary lip seals. Comprehensive micro-elastohydrodynamic models are already available in literature, hence this type of model is deal with only briefly.

Micro-elastohydrodynamic models calculate the hydrodynamic pressure occurring on a patch of the seal-shaft interface on a microscopic level. A surface equivalent profile representing the separation between the asperities of the seal and the shaft is used. The morphology of the equivalent gap profile is determined from the surface roughness characteristics of both counterparts, using Eq. 5-75 and Eq. 5-76 and according to [27] (see Figure 5-26). Generally, the results obtained with this kind of hydrodynamic model lead to a hydrodynamic load-carrying capacity greater than the seal radial force, validating the full film lubrication regime assumption [56].

$$\lambda_{x/y} = 2\pi \frac{\sigma_p}{\Delta_{x/y}} \qquad \textit{Eq. 5-75}$$

$$\mathrm{A_m} = \sqrt{2}\sigma_p \qquad \textit{Eq. 5-76}$$

$$R_{x/y} = \frac{1}{\sqrt{2}\,\sigma_p}\left(\frac{\lambda_{x/y}}{2\pi}\right)^2 \qquad \textit{Eq. 5-77}$$

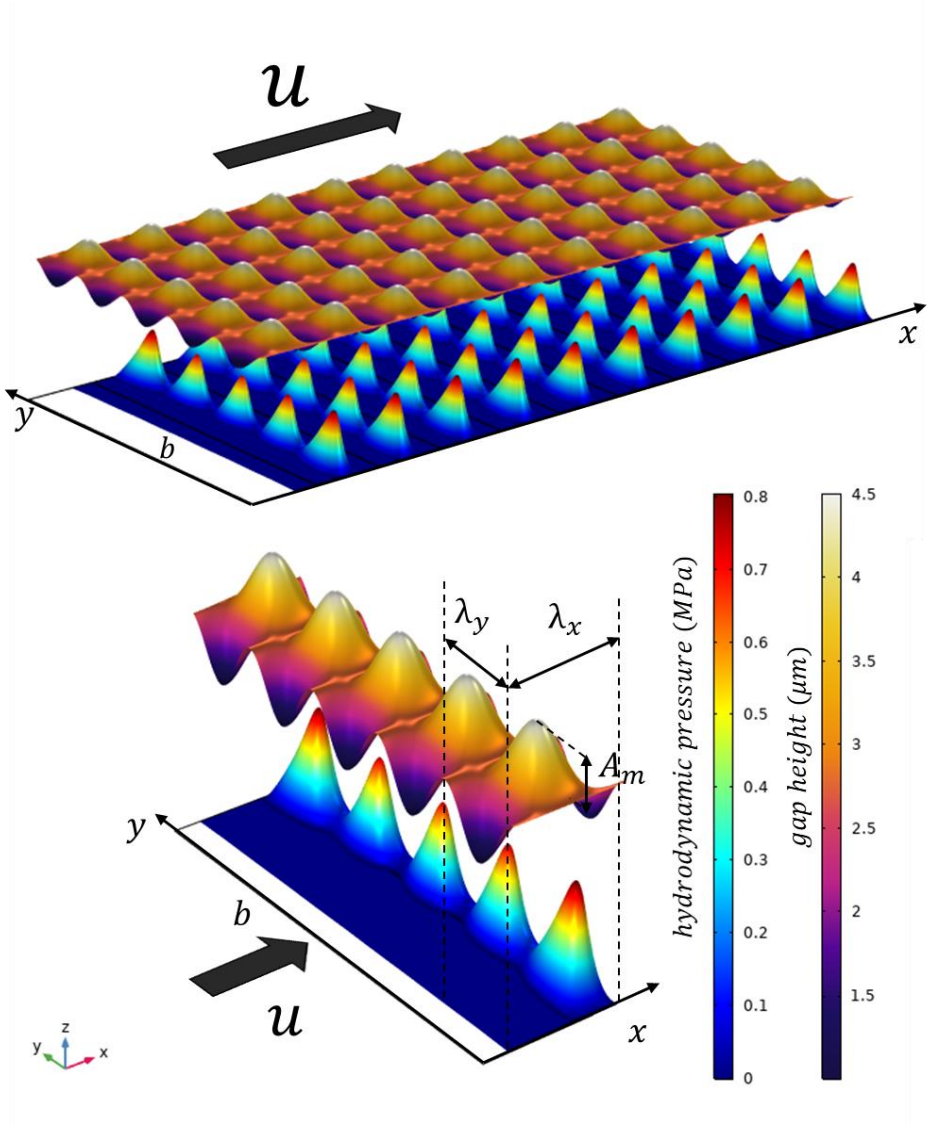

Figure 5-26. Example of the hydrodynamic pressure obtained with a bi-sinusoidal equivalent gap profile.

A surface equivalent for the stern tube was obtained using the surface measurements shown in *Section 3.4*. The distortion of the seal was included by coupling the hydrodynamic patch model and the three-dimensional seal model [51]. In this case, the initial geometry of the model is the assembled configuration [61]. Note that the radial load balance is not imposed and therefore the minimum film thickness is

left as an input. The thermal effects are disregarded. Favourable conditions for the generation of hydrodynamics are set, i.e. shaft velocity of 5 m/s and lubricant viscosity of 50 mPa·s. A bi-sinusoidal gap profile is defined with a λ_x, λ_y and A of 35.9 µm, 28.3 µm and 1.7 µm respectively. A minimum gap height of 1 µm is set. Figure 5-27 shows the pressure distribution and resultant gap profile obtained for the case $\Delta p = 0$ bar.

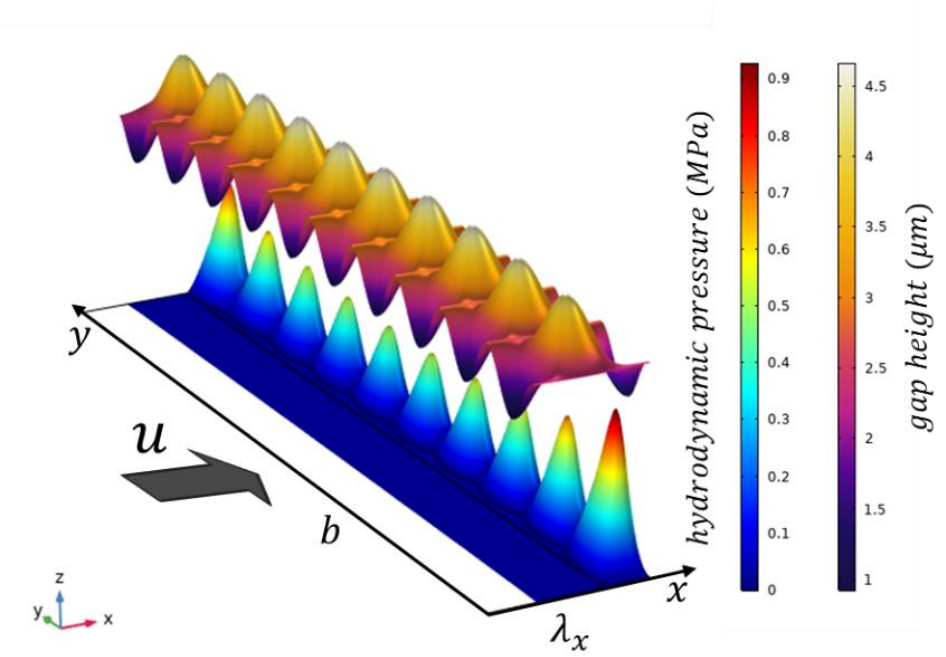

Figure 5-27. Resultant hydrodynamic pressure build-up and gap profile on the surface patch.

The results obtained exhibit a load-carrying capacity of only 12.7% of the radial load shown in Figure 5-10. As expected, this percentage increases when reducing the separation between the seal and the shaft. A larger contact width or a larger number of asperities also leads to a greater load-carrying capacity. In fact, the equivalent surface profile determines to a large degree the results obtained with this kind of model [15], [54]. The results suggest that, under the common stern tube seal operating conditions, part of the load is carried by direct asperity contact [68]. Developing a mixed-lubrication model [15], [48] for the stern tube analysed is beyond the scope of this thesis and is left as future work.

5.4. Dynamic modelling under a misaligned configuration

The alignment between the seal and the shaft liner is difficult to guarantee, in the same way as perfect roundness is impossible to achieve. The consequences of running under a misaligned configuration are analysed in this section. As shown in *Subsection 5.2.3*, two phenomena promote hydrodynamics when the alignment is lost. First, the contact pressure between the seal and the shaft shows a gradient in the circumferential direction. Second, the slant of the contact profile leads to a normal-to-contact velocity component. Both phenomena lead to hydrodynamics on the macroscopic scale.

5.4.1. Contact pressure gradient

One of the main consequences of operating under misaligned conditions is the loss of the uniform contact pressure and contact width in the circumferential direction. The resultant seal configurations caused by misalignment were shown in *Subsection 5.2.3* and published in *Paper C*. The gradient of pressure in the circumferential direction varies as a result of operating under misalignment. By applying the isoviscous elastohydrodynamic lubrication theory (I-EHL) as in [15], the film thickness in the circumferential direction can be predicted. Following the approach shown in *Subsection 5.3.5* to obtain a surface equivalent from the roughness characteristics of the seal, the non-uniform radial load is distributed according to the number of bumps in the axial direction (see Figure 5-28).

Taking the pressure distribution from the largest axial misalignment case studied ($\varepsilon = 1.5\ mm$) the central film thickness is predicted using the EHL approach of Chittenden [100] (Eq. 5-78 to Eq. 5-81). The radius of the elliptical asperities $R_{x/y}$ was calculated using Eq. 5-77 as in [15].

$$\frac{h_{cen}}{R_x} = 8.28\left(1 - e^{-0{,}86\left(\frac{R_y}{R_x}\right)^{2/3}}\right) U_x^{0{,}65} W_x^{-0{,}21} \qquad \textit{Eq. 5-78}$$

$$U_x = \eta u/(E_{eq} R_x) \qquad \textit{Eq. 5-79}$$

$$W_x = w/(E_{eq}R_x^2) \qquad \textit{Eq. 5-80}$$

$$E_{eq} = \frac{2}{\frac{(1-\nu_1^2)}{E_1} + \frac{(1-\nu_2^2)}{E_2}} \qquad \textit{Eq. 5-81}$$

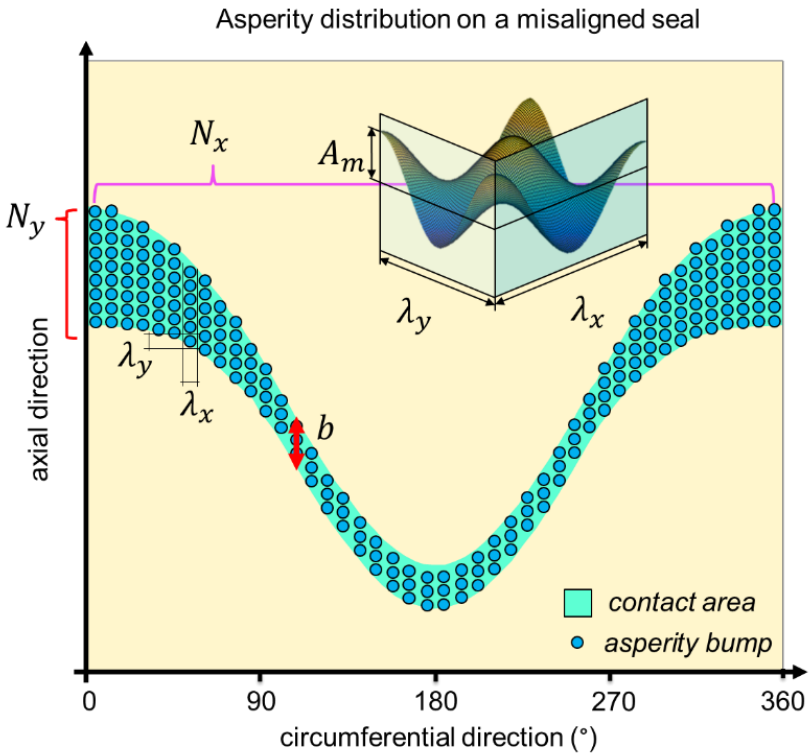

Figure 5-28. Distribution of asperities on the contact area profile of a slanted seal (see Nomenclature).

The hydrodynamic pressure which arises from the gap profile shown in Figure 5-29 is predicted by solving the universal cavitation algorithm shown in *Subsection 5.3.3*.

The minimum separation between the shaft and the seal significantly impacts the resultant built-up pressure [28]. Consequently, the sensitivity of the hydrodynamic pressure to the minimum film thickness value is analysed.

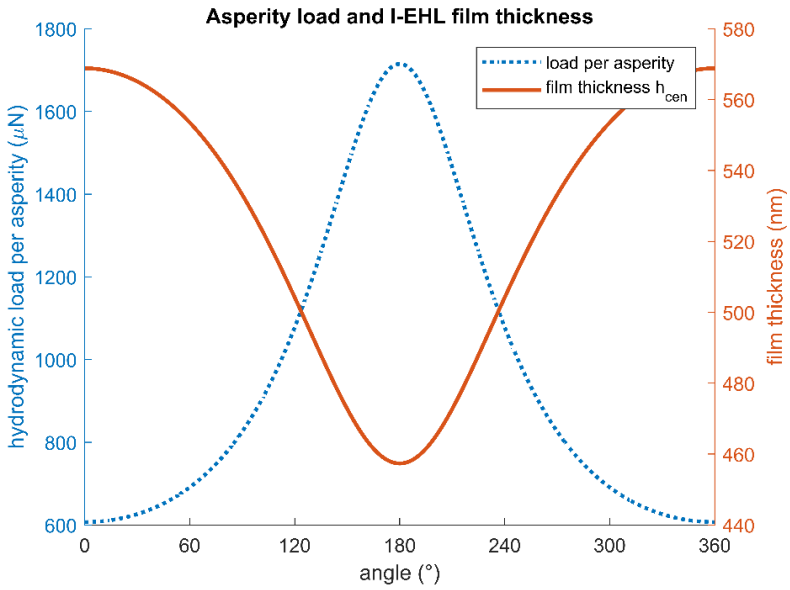

Figure 5-29. Asperity loading and fluid film thickness for the seal with a 1.5 mm radial misalignment offset. ($\varepsilon = 1.5\ mm$, $\eta = 100\ mPa \cdot s$, $\kappa = 10^7\ Pa$, $u_a = 1\ m/s$, $b = 0.5\ mm$).

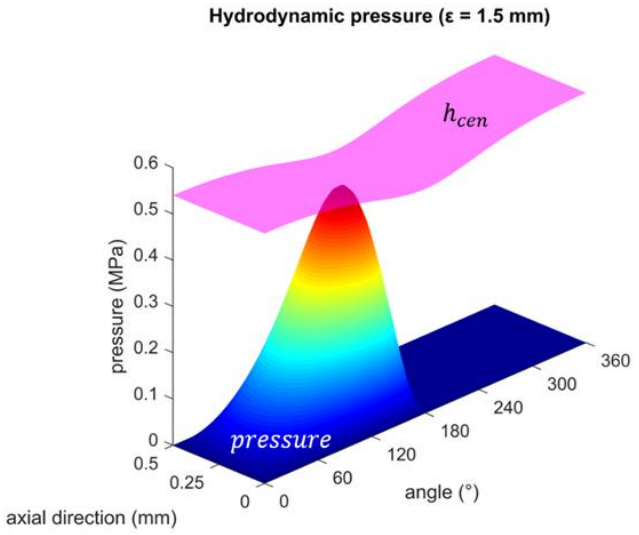

Figure 5-30. Hydrodynamic pressure build-up under radial misalignment offset ($\varepsilon = 1.5\ mm$, $\eta = 100\ mPa \cdot s$, $\kappa = 10^7\ Pa$, $u_a = 1\ m/s$, $b = 0.5\ mm$). The I-EHL film thickness from Figure 5-28 is magnified and shown in pink.

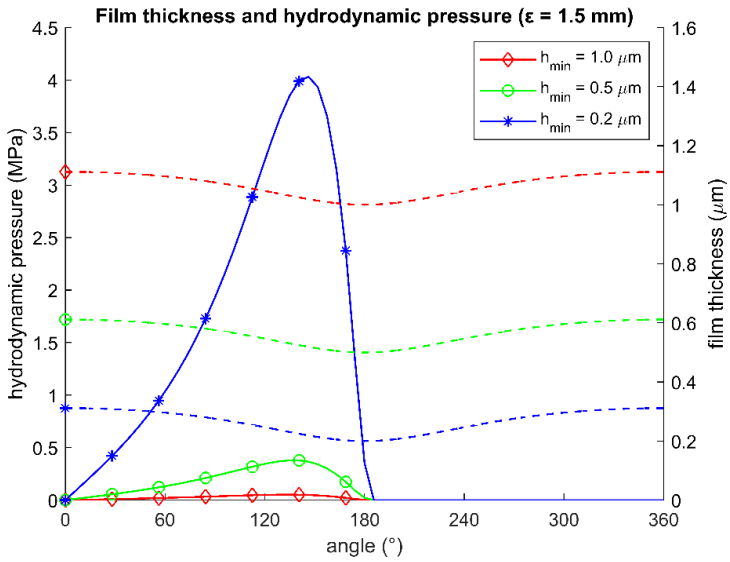

Figure 5-31. Sensitivity of the hydrodynamic pressure to the variation of the minimum film thickness ($\varepsilon = 1.5\ mm$, $\eta = 100\ mPa \cdot s$, $\kappa = 10^7\ Pa$, $u_a = 5\ m/s$, $b = 0.5\ mm$).

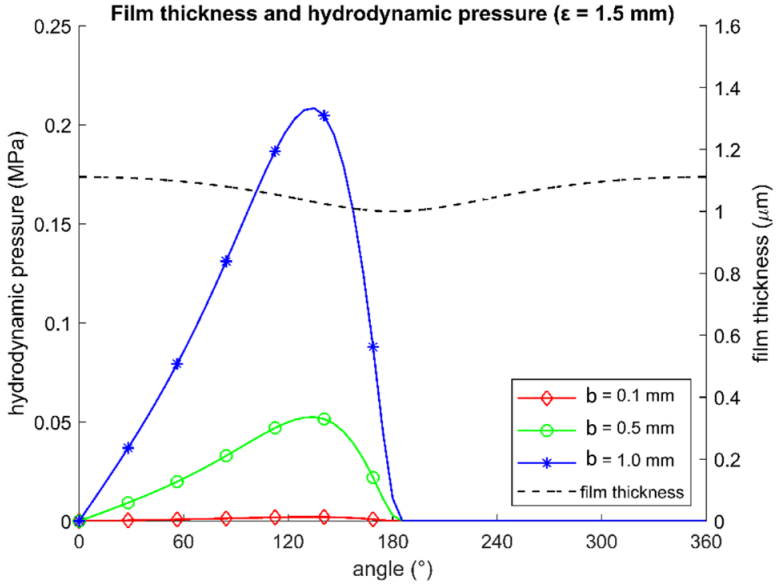

Figure 5-32. Sensitivity of the hydrodynamic pressure to the variation of the contact width ($\varepsilon = 1.5\ mm$, $\eta = 100\ mPa \cdot s$, $\kappa = 10^7\ Pa$, $u_a = 5\ m/s$, $h_{min} = 1\ \mu m$).

The pressure build-up resulting from a microscopic wedge (see dashed lines in Figure 5-31) is in the same order of magnitude as the contact pressure of the seal. It is worth mentioning that seal surface will deform before those pressures are reached. Ultimately, the impact of the contact width was also analysed and is shown in Figure 5-32. The minimum separation h_{min} is in this case set to 1 micrometre.

It is shown that an increase in the contact width, e.g. through wear, can lead to a significant pressure build-up, hence it has the potential to distort the seal contact. Note that by modelling the seal contact as a slender bearing the contact width is set constant. In reality the contact profile varies in the circumferential direction, leading to a non-zero normal-to-contact velocity [50].

5.4.2. Normal-to-contact velocity

Horve developed an analytical model accounting for the misalignment of rotary lip seals [29], [50]. Horve's model assumes that the seal-shaft misalignment is responsible for all the oil migration, i.e. a null flow rate results from a perfectly aligned seal (see Figure 5-33). The model developed in this thesis builds on the pioneering work of Horve by including the hydrodynamic pressure generation and the consequent deformation of the seal.

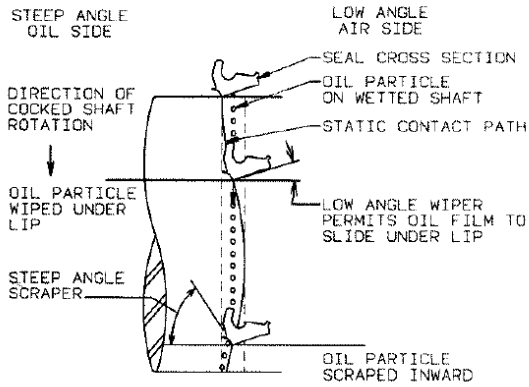

Figure 5-33. Seal design with wavy contact on the shaft [50].

Under radial misalignment, the contact area between the seal and the shaft is not straight anymore. Instead a sinus-shaped profile develops.

When the contact profile deviates from the circumference, two convergent and two divergent gap profiles are formed with the potential to generate hydrodynamic action. The hydrodynamic pressure distribution of operating under a static radial misalignment is sketched in Figure 5-34 (see *Subsection 5.2.3*).

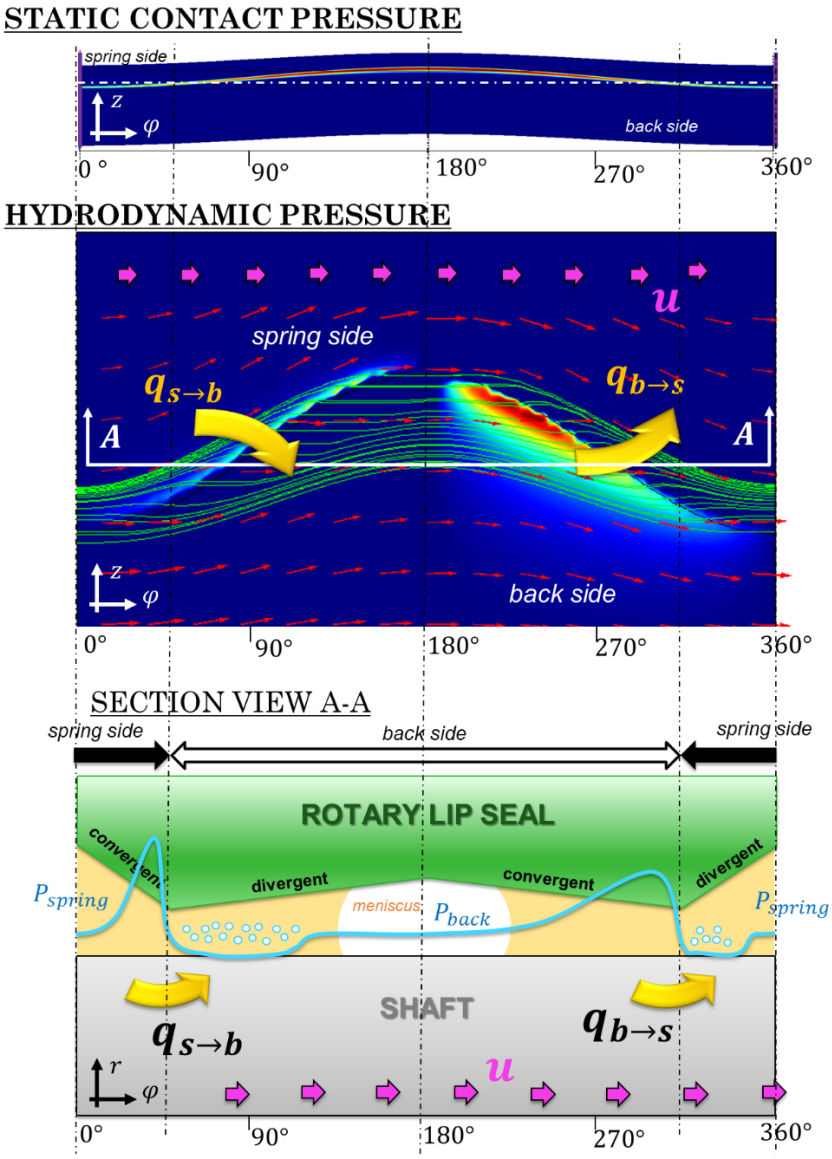

Figure 5-34. Sketch of the hydrodynamic pressure build-up from operating with a slanted contact profile.

As explained in *Paper D*, the strategy followed consists in decomposing the shaft velocity component in the normal-to-the-contact and tangential-to-the-contact directions. By setting a curvilinear coordinate along the shaft the computational domain is substantially simplified as shown in Figure 5-35.

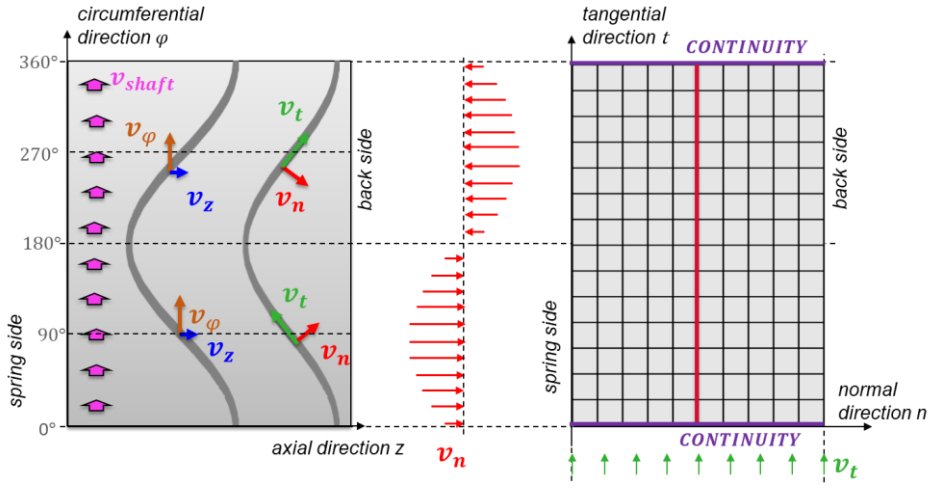

Figure 5-35. Decomposition of the shaft velocity in normal and tangential components.

When studying the seal response to a static misalignment under ambient conditions (*Section 5.2.3*), it was observed that the tip of the seal rotates mainly around a hinge point instead of deforming. Consequently, the gap profile under radial static misalignment can be simplified to the geometry shown in Figure 5-36. For further information the reader is referred to *Paper D*. An elevation colourmap with fringes is used in Figure 5-36b to easily identify the points of the same height.

Next, the finite difference code solving the universal cavitation algorithm presented in *Section 5.3* was used to predict the hydrodynamic pressure build-up resulting from the shaft velocity component normally oriented to the contact. The deformation of the seal was included using the compliance matrix method described in *Subsection 5.3.4* and is shown in Figure 5-37. The axisymmetry of the seal allowed only the nodes along one section of the seal to be loaded when building the compliance matrix.

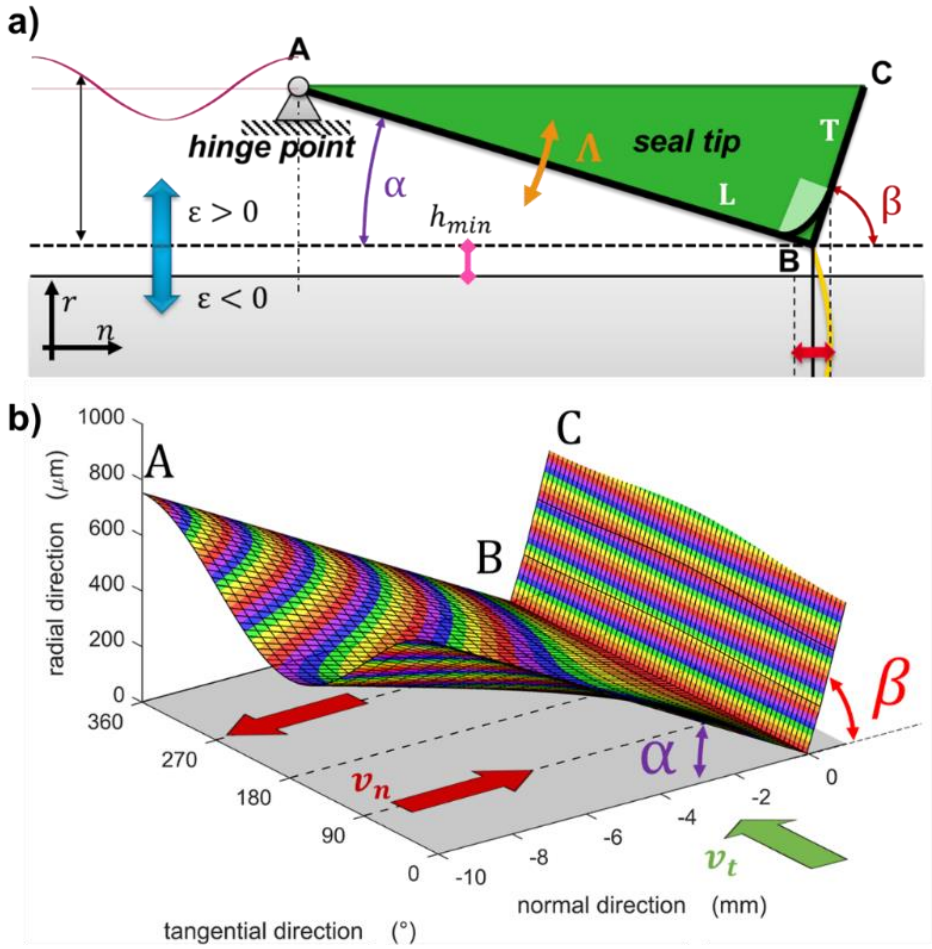

Figure 5-36. Radially misaligned shaft-seal gap based on a hinge point.

The Elrod algorithm and the compliance matrix are computed iteratively until the results converge to a solution. The flow rates across the sealing line in each direction are obtained from the pressure distribution according to Eq. 5-70. As an example, a sinusoidal gap profile is used as input to the model, and the results are shown in Figure 5-38.

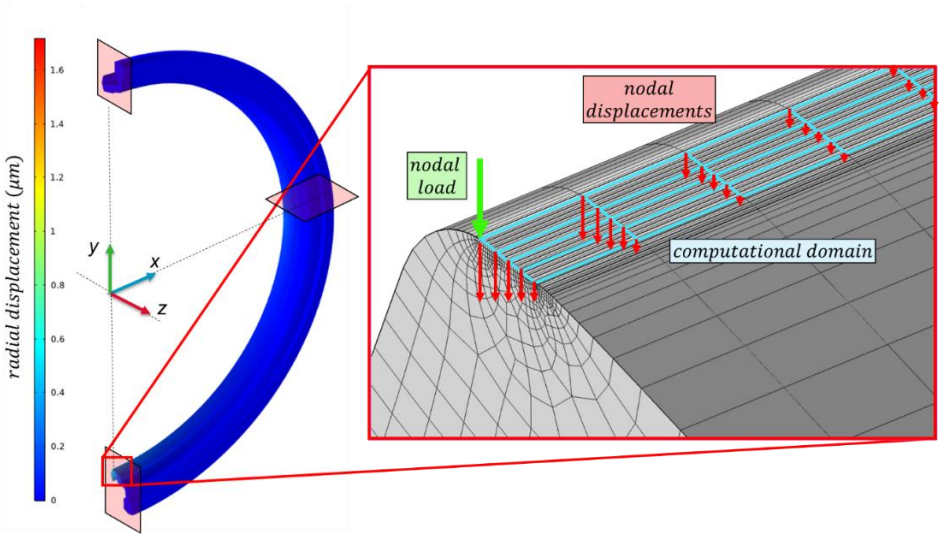

Figure 5-37. Assembly of the compliance matrix by the linear perturbation method. Note that the resolution of the grid is reduced in this figure.

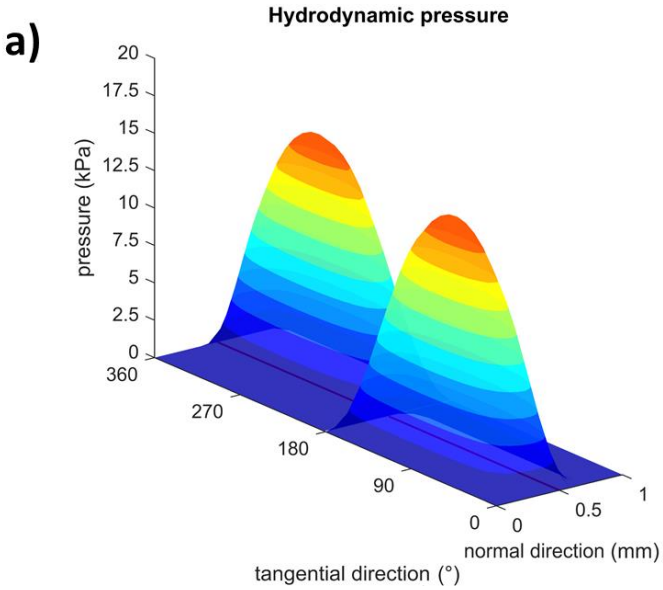

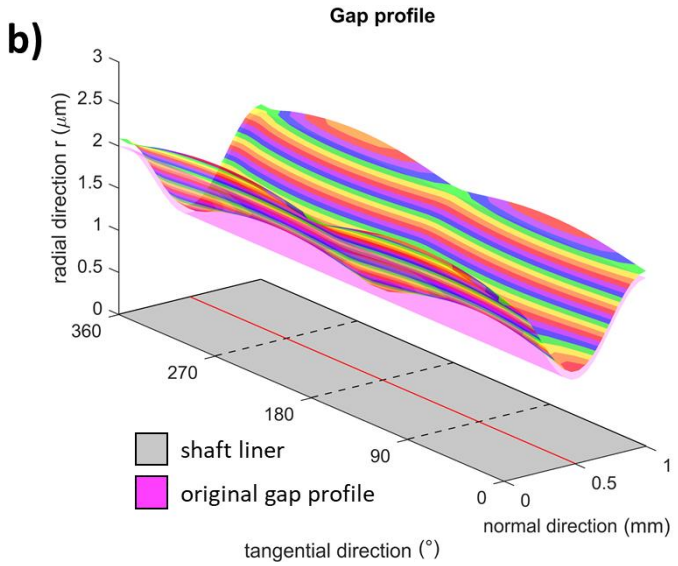

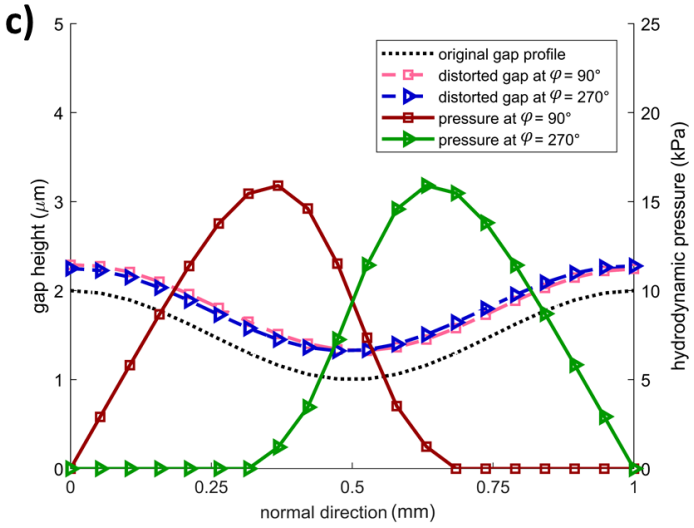

Flow rates	
$q_{b\to s}$	$0.44\ \mathrm{mm}^3/\mathrm{s}$
$q_{s\to b}$	$0.44\ \mathrm{mm}^3/\mathrm{s}$
$q_{b\to s} - q_{s\to b}$	$0.0\ \mathrm{mm}^3/\mathrm{s}$

Figure 5-38. Results with a sinusoidal gap profile ($\varepsilon = 1\ mm$, $h_{min} = 1\ \mu m$, $u = 3\ m/s$, $\eta = 50\ mPa \cdot s$, $\kappa = 10^7\ P$).

Figure 5-38 shows that the resultant pressure build-up becomes almost symmetric when a symmetric gap profile is defined with fluids of equal viscosity on both sides. Slight differences are observed because the nodes on the surface present particular stiffnesses according to their position on the lip. The distortion of the lip in each direction is not identical. Note that the flow rates in each direction are almost the same, hence a zero net flow rate is predicted. As expected, the oil migration occurs in both directions.

The impact of the shaft radial offset ε, the seal angles α and β, the shaft liner velocity u and the lubricant dynamic viscosity η can be analysed individually using the model developed. Figure 5-39 shows the influence of the gap profile on the pressure generation and thereby the expected flow rates.

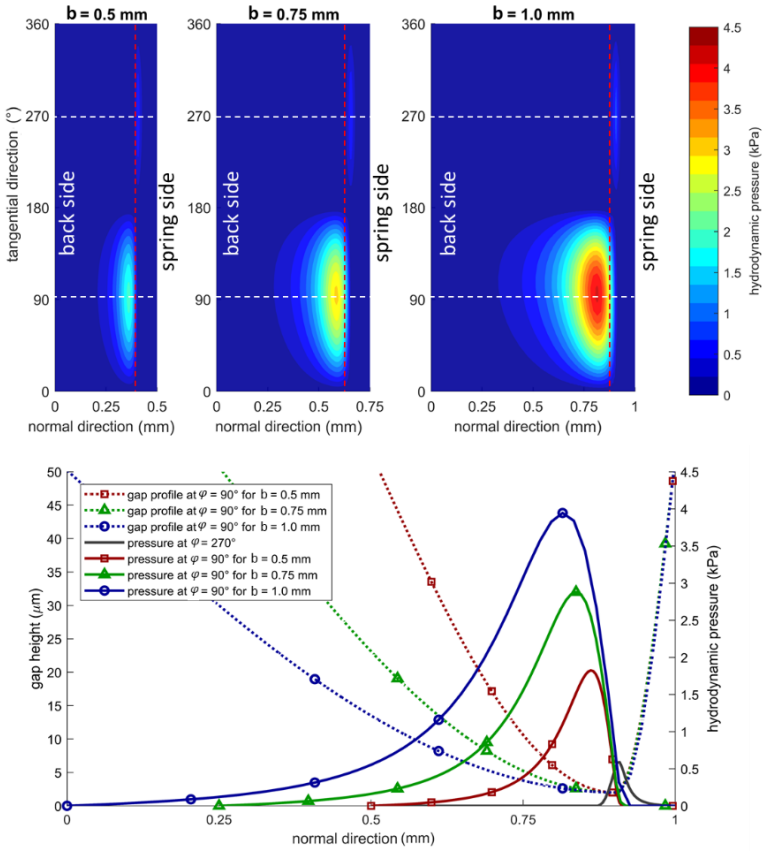

Figure 5-39. Results with various rigid gap profiles ($\varepsilon = 1\ mm$, $h_{min} = 2\ \mu m$, $u = 3\ m/s, \eta = 50\ mPa \cdot s, \kappa = 10^7\ Pa$).

Finally, the gap profile estimated in *Paper B* [101] under non-pressurized conditions is replicated using the hinge model. Figure 5-40b shows the asymmetric pressure distribution obtained from the seal analysed, leading to a non-zero net flow rate.

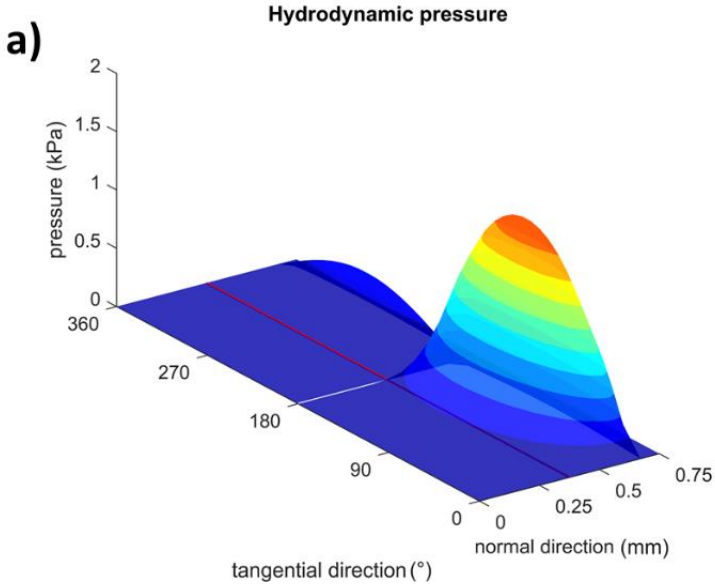

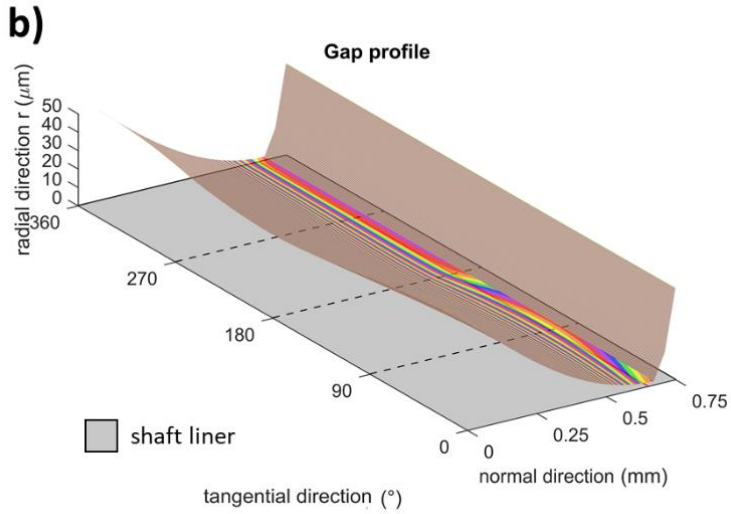

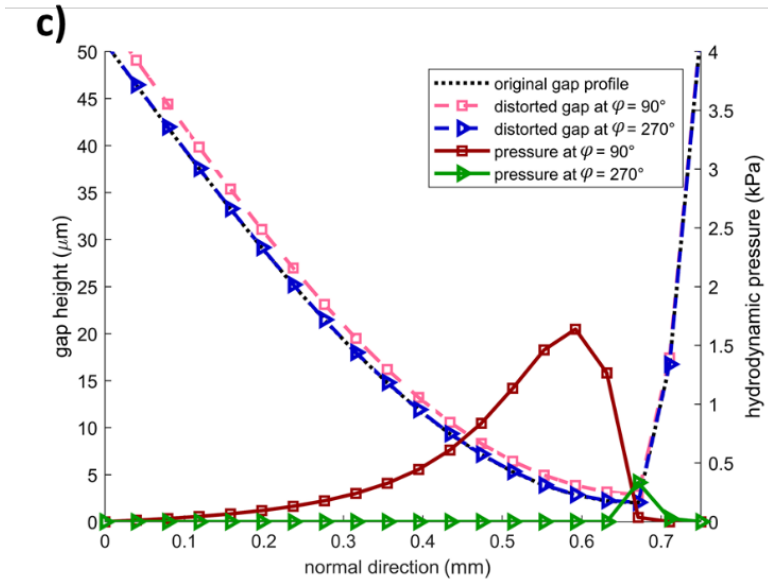

Flow rates	
$q_{b\to s}$	1.15 mm^3/s
$q_{s\to b}$	0.65 mm^3/s
$q_{b\to s} - q_{s\to b}$	0.5 mm^3/s

Figure 5-40. Hydrodynamic pressure build-up the spring side gap profile between the seal and the shaft ($\varepsilon = 0.5\ mm$, $h_{min} = 2\ \mu m$,$u = 3\ m/s$, $\eta = 50\ mPa \cdot s$, $\kappa = 10^7\ Pa$).

The hydrodynamic pressures predicted from a radial misalignment is smaller than the uniformly distributed radial load measured with the split-shaft setup (*Paper B).*First, because the pressures reached are smaller than the radial loading and second because they are not uniformly distributed in the circumferential direction. Therefore, the model assumes that the hydrodynamics occurring between the seal and the shaft liner provides a constant separation between the seal and the shaft in the circumferential direction. Furthermore, it is assumed that the lubricant is fully available at both sides of the seal, hence starvation does not occur.

5.5. Conclusions

The use of mathematical models for analysing rotary lip seals is crucial. However, being able to validate a model is as important as developing it. Typically, computational models are an ensemble of a few small models. In the present case, the rheological model (*Section 3.1*), the constitutive seal material model (*Section 3.2*), and the static axisymmetric model (*Subsection 5.2.1*), are the building blocks of the dynamic models presented in *Chapter* 5. It is paramount to validate each of the models independently as the inaccuracies of each of them accumulate in the overall model. Great effort went into validating the axisymmetric static model presented in *Section 5.2*, showing a step-by-step strategy for its validation. Hydrodynamic models to study the dynamic operation of rotary lip seals were also presented. The two misalignment-induced mechanisms modelled in *Section 5.4* showed that when the alignment is lost the primary lubrication mechanism can be easily distorted. Consequently, the seal-shaft concentricity must be analysed and the models validated with experiments.

(This page is intentionally left blank)

6. Dynamic experimental results

Chapter 6 shows the empirical results obtained with the dynamic seal setup presented in *Section 4.3*. The applicability of the analytical expressions shown in *Section 5.1* are reviewed for the stern tube seal application. The film thickness under various operating conditions is indirectly calculated and the lubrication regime of stern tube seals is determined.

6.1. Results

The stern tube seal analysed was tested under the twelve operating conditions listed in Table 6-1. The shaft and the seal operate under aligned conditions, meaning that the seal and the shaft are assembled concentrically. The mineral oil-based lubricant characterized in *Section 3.1*, i.e. Lubricant 1, was used for all the tests. There are no stern tube seal measurements available in the literature so the results can be compared only with measurements of significantly smaller non-

pressurized lip seals. The validity of the already existing lip seal theory presented in *Section 5.1* is therefore reviewed for the stern tube application.

Table 6-1. Operating conditions of the tests with the dynamic setup.

	Pressure difference	**Shaft velocity**	**Oil sump temperature**
	Δp **[bar]**	u **[m/s]**	T_{sump} **[°C]**
1	0.0	1	20
2	0.0	3	20
3	0.0	5	20
4	0.5	1	20
5	0.5	3	20
6	0.5	5	20
7	0.75	1	20
8	0.75	3	20
9	0.75	5	20
10	1.0	1	20
11	1.0	3	20
12	1.0	5	20

This research focuses on the steady state operation of stern tube seals, i.e. once the transient stage is over. The transient stage was considered to be over once the temperature and the friction torque readings stabilize, showing a variation of less than 5% for at least 1 hour. Each operational point was tested at least three times and its average as well as the minimum and maximum is presented in the results depicted in the figures below. The parasitic torque of the auxiliary seal and the lubricant is subtracted from the torque readings, leading to the values shown in Figure 6-1.

The heat dissipation is deduced directly from the product of the frictional torque and the shaft angular velocity, as shown in Figure 6-2.

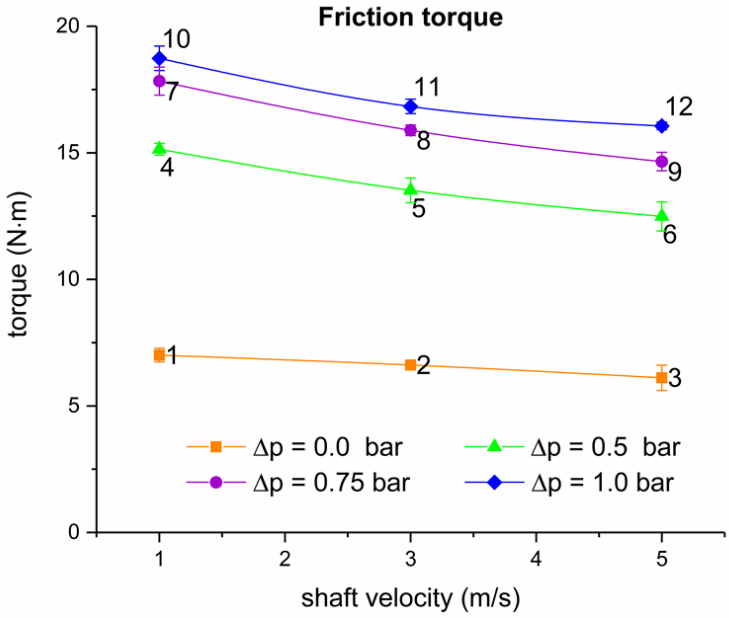

Figure 6-1. Main seal frictional torque measurements for various pressure differences and shaft velocities.

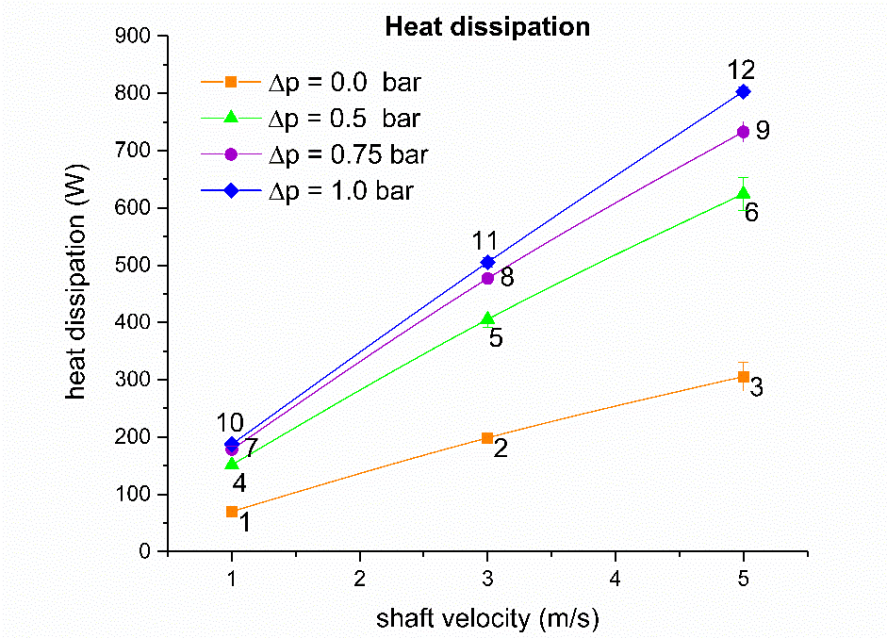

Figure 6-2. Heat dissipated at the seal-shaft contact.

The temperature at the contact is extrapolated from the readings of the thermocouple placed at the garter spring groove using a FEM model, as performed in [102]. Here, the axisymmetric model of the seal presented in *Subsection 5.2.10* is used to correlate the contact temperature to the measurements, as shown in Figure 6-3. The heat released in the contact boundary was deduced from the torque measurements. This approach may lead to some inaccuracy as the heat convection coefficients of the system were deduced from the twelve operating points.

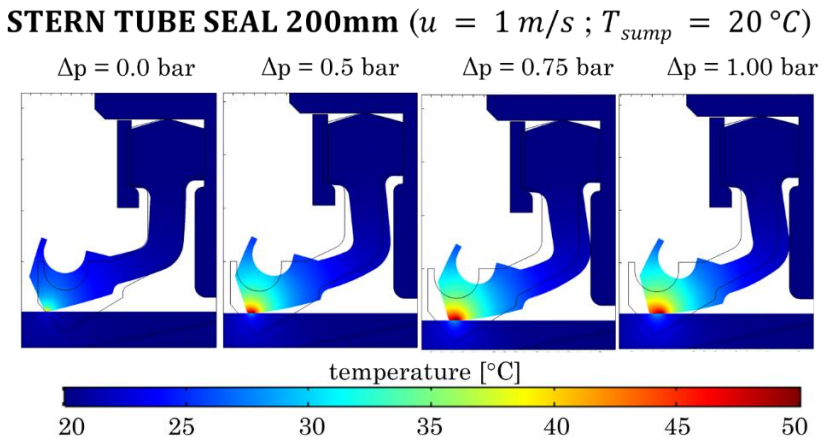

Figure 6-3. The temperature at the contact is obtained from the FE model presented in Paper B. Thermocouple measurements were placed close to the contact for its validation.

The temperature at the contact between the seal and the shaft for the twelve operating conditions was shown to be really consistent, with low variability of the steady-state temperature (see Figure 6-4).

The measurement of the oil migration across the seal requires long testing times. The volume of lubricant was shown to be strongly coupled to the operating temperature due to thermal expansion and therefore susceptible to the slight room temperature variations. The flow rate values deduced from the variation of the oil tanks level is shown in Figure 6-5.

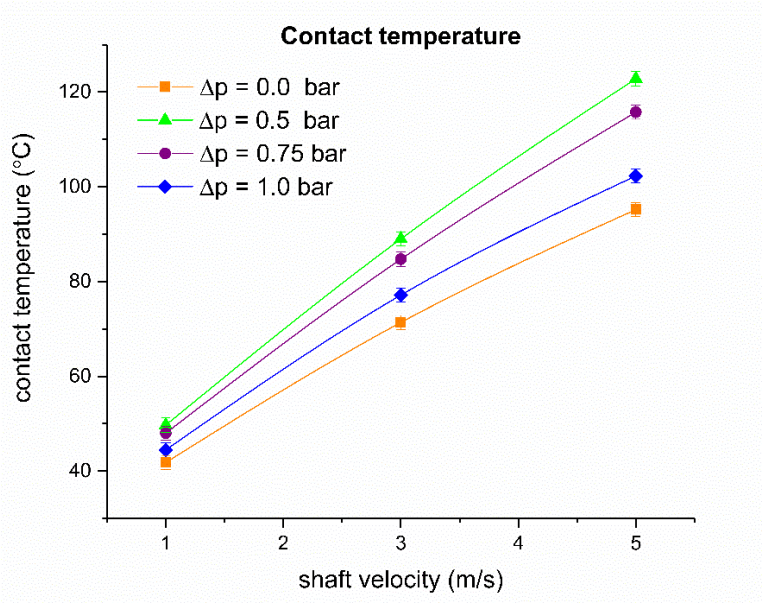

Figure 6-4. Contact temperature predicted from the garter spring temperature measurements via the FE model presented in Paper B.

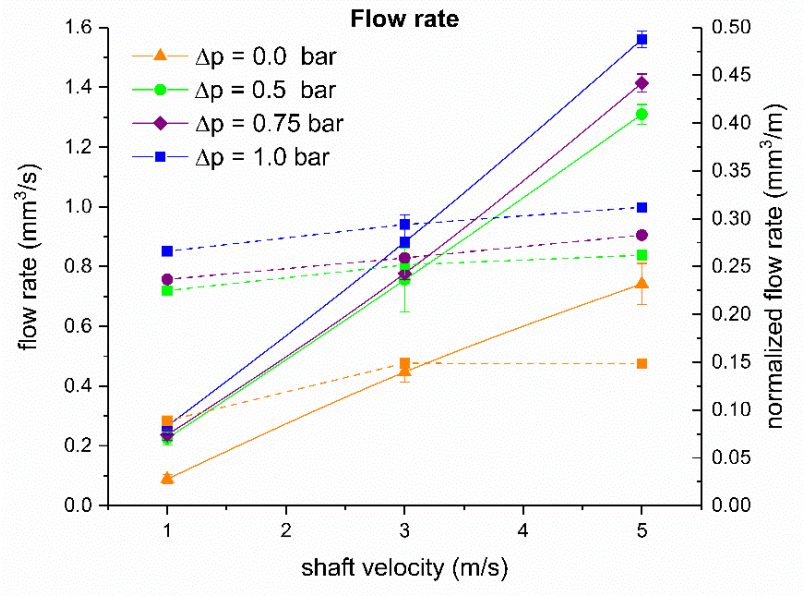

Figure 6-5. Flow rate measurements from spring side to back side of the seal. The flow rate q and the normalized flow rate $\bar{q} = q/u$ are plotted in continuous and dashed lines, respectively.

The coefficient of friction for each operation point is calculated from the measured torque and the radial load measured using the split-shaft setup shown in *Chapter 4* (Eq. 5-10). The duty parameter $G = \eta u b / F_{r_{tot}}$ is used in Figure 5-30 to obtain the plot the Stribeck curve of the stern tube seal tested. The dynamic viscosity of the lubricant is obtained from the contact temperature and using the Walther viscosity-temperature relationship as shown in *Section 3.1*.

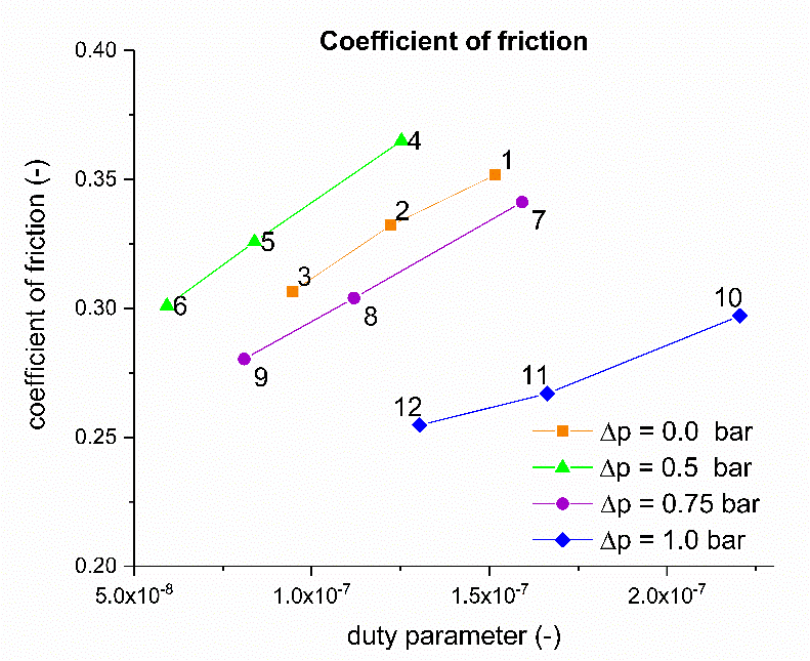

Figure 6-6. Stribeck curve.

The results show that the operating conditions belong to the right side of the characteristic minimum of the Stribeck curve. Hirano [18] showed that the coefficient of friction of rotary lip seals is proportional to the cubic root of the duty parameter G as in Eq. 5-11, see also Figure 5-29. This relation also holds for the measurements done in the context of this analysis. Using the data and Eq. 5-11, a characteristic sealing proportionality factor ϕ_s can be attributed to each seal, basically being the slope of the curve in Figure 6-7.

The contact temperature was shown to correlate well with the heat dissipated density as shown in Figure 6-8. Therefore, the temperature difference between the sump temperature and the contact can be predicted using Eq. 5-9.

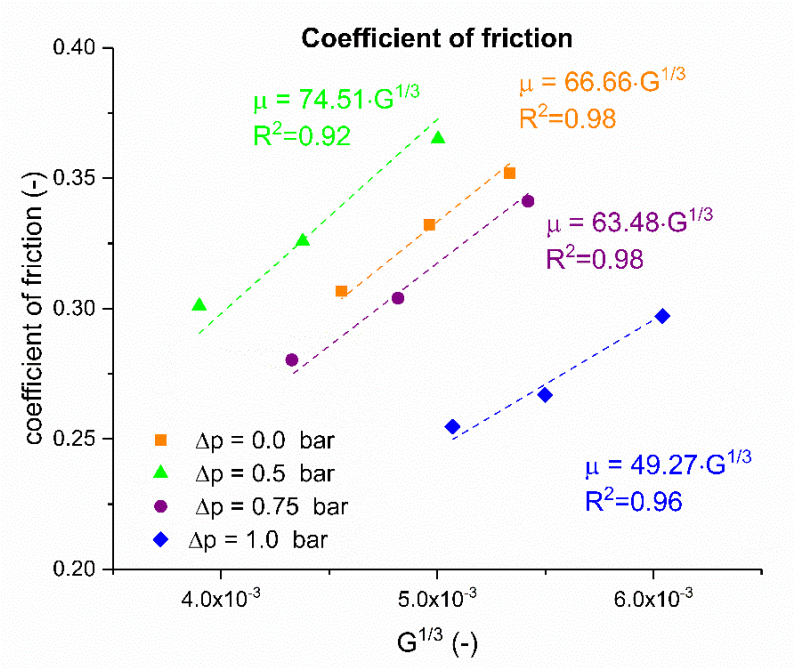

Figure 6-7. Sealing number as shown in [18].

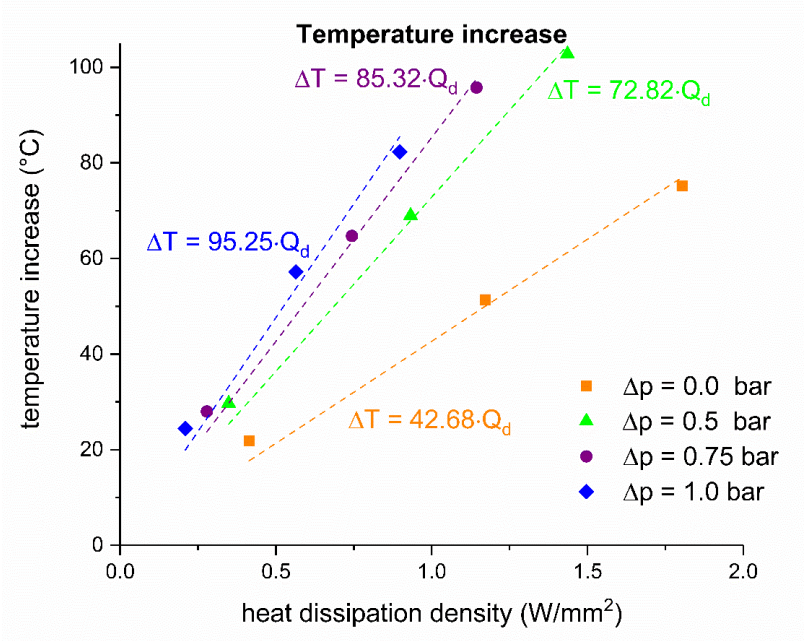

Figure 6-8. Temperature increase at the contact.

Kawahara [23] showed that the dimensionless flow rate across a seal correlates well with the square root of the duty parameter G as shown in Figure 6-9. Eq. 5-13 showed to be valid to predict the flow rate of the stern tube seal tested. Note that rotary lip seals typically show an oil migration from the back side to the spring side of the seal, i.e. upstream. However, the flow rate measured on the stern tube is in the opposite direction.

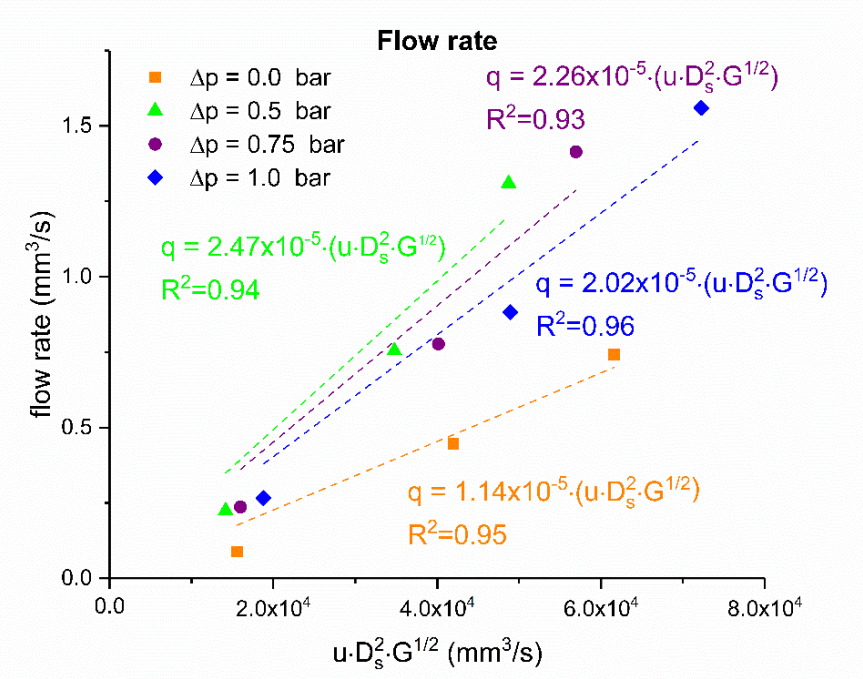

Figure 6-9. Flow expression for the flow rate as shown in [23] .

No direct measurement of the film thickness was conducted. However, using both the torque and the flow rate measurements the separation between the seal and the shaft can be indirectly determined. Eq. 5-8 was used to estimate the film thickness assuming a μ_0 of 0.0 and 0.1. Alternatively, using the Poiseuille flow equation (Eq. 5-12), the required separation leading to the flow rate values shown in Figure 6-5 is calculated. The flow rate at $\Delta p = 0$ bar is subtracted from all the flow rate measurements. The results obtained using both methods are shown in Figure 6-10.

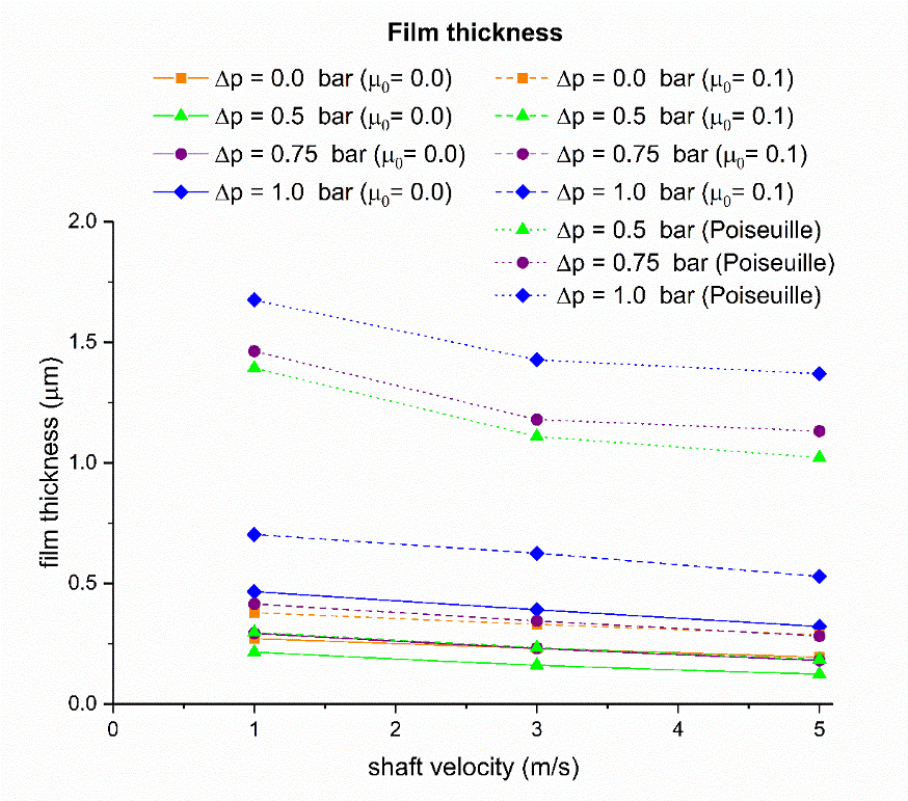

Figure 6-10. Film thickness prediction.

6.2. Discussion

The measuring techniques applied for characterizing the dynamic operation of a stern tube seal were shown to be reliable. Consistent readings of the frictional torque, temperature and flow rate are presented for a wide range of pressure differences and shaft velocities. The temperature was shown to play a major role impacting the torque and flow rate readings and hence it is important to compensate for it. Figure 6-6 shows that the coefficient of friction μ increases when the Duty parameter G increases implying that the stern tube seal analysed operates beyond the minimum of the traditional Stribeck curve, i.e. hydrodynamic lubrication. This is shown by the shaded area in Figure 6-11.

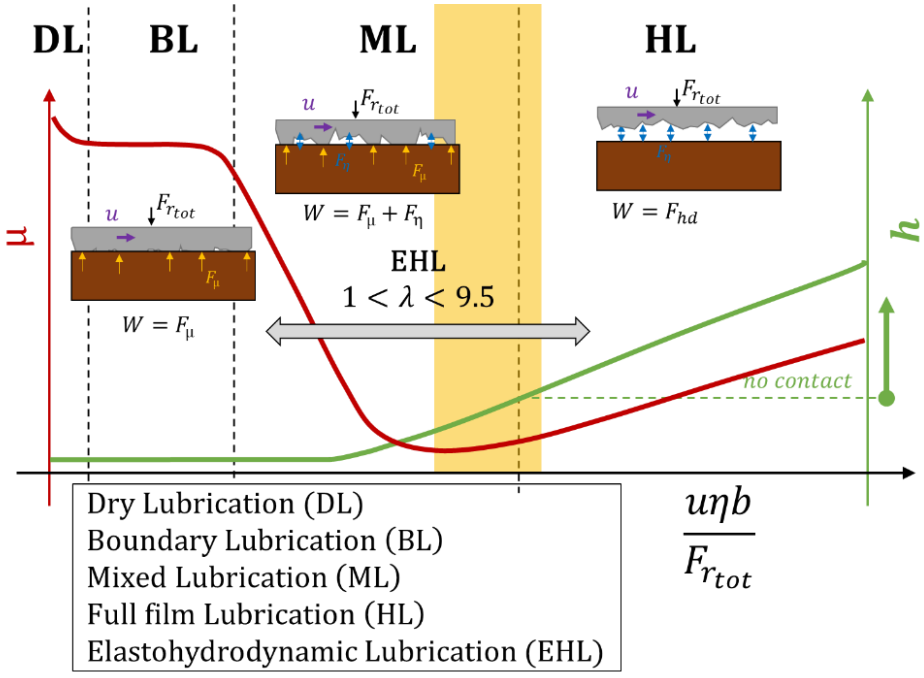

Figure 6-11. The measurements suggest that the stern tube seal analysed operates within the shaded region on the Stribeck curve.

Twelve operating conditions were tested and, although the amount of tests is limited, few correlations are suggested. The formulae presented in *Section 5.1* corresponds to seals operating under ambient pressure conditions [18], [23], [89] and their applicability to pressurized seals was reviewed. The coefficient of friction showed a linear correlation with the cubic root of the Duty parameter (Figure 6-7) as observed in smaller rotary lip seals [23]. The use of ϕ_s for determining if a seal would leak or not is not useful for stern tube seals as these operate immersed in liquid on both sides (except seal #5 in Figure 5-2). The contact temperature was shown to be proportional to the heat dissipation density (Figure 6-8). Note that the temperature at the contact did not increase monotonically with the pressure difference (Figure 6-4). The increase of the contact area at the larger pressure differences leads to a lower heat dissipation density and hence a lower contact temperature. The dimensionless flow rate was shown to be proportional to the square root of the Duty parameter as in [23] (Figure 6-9). The lubricant flows from the spring side to the back side for all the tests conducted. That is contradictory with the flow rates reported for the converse operation of traditional rotary lip seals [29]. Instead,

the lubricant migrates in the natural flow direction showing a larger flow rate as the pressure difference increases. Insufficient reverse pumping can explain it. The reverse pumping requires a skewed pressure profile to occur [2]. Figure 5-8 shows that when $\Delta p = 0$ bar the profile is almost symmetric. The same figure shows that at larger pressure differences the maximum of the pressure profile shifts towards the spring side. Note that this is not a guarantee of an efficient reverse pumping mechanism as the surface roughness and the stiffness of the seal are also of importance. The fact that some flow rate occurs even when the pressure difference is null suggests that the shaft has a lead and therefore some oil migration is induced by the rotation of the shaft. Varying the direction of rotation of the shaft may shed some light on the issue.

Figure 6-10 shows the film thicknesses predicted from both the torque and the flow rate measurements. The flow rate measured when $\Delta p = 0$ bar is subtracted to all the measurements before estimating the fluid film thickness via the Poiseuille flow (Eq. 5-12). Both methods lead to film thicknesses of the same magnitude. Notice that the various oil migration mechanisms are not independent from each other. It is likely that the flow rate induced by the screw thread on the shaft is strongly coupled to the film thickness and hence it cannot be considered pressure-independent. An extended discussion on the results obtained can be found in *Paper E*.

6.3. Conclusions

The experimental setup presented in *Section 4.3* is proven to successfully measure the friction torque, the contact temperature and the oil migration of a the stern tube analysed. From the results obtained is deduced that the stern tube operates in the hydrodynamic lubrication regime near the transition between the mixed lubrication regime and the hydrodynamic lubrication regime as shown in Figure 6-11. Noteworthy is that the frictional torque decreased when increasing the shaft velocity leading to narrower film heights. As expected, the temperature at the contact was shown to be proportional to the heat dissipation density. The flow rate measured at a null pressure difference suggests the presence of a lead on the shaft [3]. Further experiments are required to draw solid conclusions. The migration of lubricant was observed to flow from the spring side to the

back side. That is in the opposite direction as in traditional oil seals when installed converse. Furthermore, in real ships, the lubricant leaks out of the stern tube opposing the natural flow direction [7]. The results obtained need to be compared to in-situ measurements of the flow rates of the stern tube seals on a ship.

7. Discussion, Conclusions and Recommendations

7.1. Discussion

The analysis of a dynamic seal begins by studying its static condition. For stern tube seals, this corresponds to when the propulsion shaft is stationary: not rotating. Two specialized setups were built to study the static characteristics of the seal (*Paper B*). The large split-shaft setup shown in *Section 4.1* was used to measure the radial loading of the seal-shaft interface. The operating temperature impacts the radial force via thermal expansion and material properties. The latter is especially important when operating outside of the rubber plateau, i.e. when the operating temperature approaches the glass transition temperature of the elastomer. The elastomer starts relaxing as soon as the seal is mounted on the shaft and hence following a procedure for measuring the radial load of the seal is necessary. The radial load measurements showed a spread of ± 5 % for seals of the same size and type. The variation in the initial dimensions, the material properties, the testing procedure and the maximum stretch the seals have experienced can cause the spread in the results. The contact width

between the seal and the shaft was measured using the glass shaft setup presented in *Section 4.2*. The setup allowed to measure the characteristics of the seal when pressurized which is not feasible with the traditional split-shaft setup. The measured contact width showed good agreement with the FE model predictions. The images taken through the glass shaft revealed that there is a smooth transition between the contact and non-contact regions due to the presence of surface roughness. The undulated topography of the seal is clearly visible at the back side of the seal. The glass shaft setup made possible to find the percolation threshold, i.e. the minimum pressure difference leading to a gas tight contact (*Section 5.2*). The setup was also used to investigate the distortion of the contact area when the seal is radially misaligned (*Section 5.4).* The static measurements are paramount for the validation of all the lip seal models presented.

The study of the dynamic operation of stern tube seals require a specialized setup replicating the stern tube seal system, including the operating conditions. The frictional torque, the temperature near the contact and the oil migration across the seal were measured using the test rig presented in *Section 4.3*. The parasitic friction from the auxiliary seal and the lubricant viscous shear had to be mapped beforehand so this can be subtracted from the experiments conducted with the stern tube seal (see *Chapter 6*). Both the torque and the flow rate measurements were shown to be susceptible to temperature variations and hence it was proven essential to account for them.

The complex deformation and lubrication mechanisms behind rotary lip seals are not fully understood and consequently rotary lip seals cannot be modelled with a high level of detail. Although sophisticated rotary lip seals models are present in literature, these are based on the micro-elastohydrodynamic lubrication and hence disregard any alternative lubrication mechanism [14]. As shown in *Section 5.3*, these hydrodynamic models assume a continuous separation between the seal and the shaft, i.e. full film lubrication regime. The separation between the seal and the shaft is simplified by using a surface equivalent, typically a bi-sinusoidal surface profile [24], [56]. The surface equivalent is deduced from the surface roughness characteristics and hence these models typically require from experimental results for its calibration. Further discussion on the topic can be found in [54] and [15]. Additionally, experiments showed that the shaft velocity-friction torque curve shows a positive ordinate intercept in rotary lip seals. Consequently, a “dry term” conflicting

with the full film lubrication assumption is often included in the torque equation [49], [87], [102].

The research carried out in this thesis focuses on the implications of operating under a misaligned situation, i.e. when the alignment between the seal and the shaft is lost. Two different lubrication mechanisms were presented complementing the primary mechanisms based on the micro-hydrodynamic lubrication. The first mechanism arises from the non-uniform loading of the seal when the shaft is offset (*Paper C*). The second one is based on the fact of operating with a slanted contact profile (*Paper D*). Both mechanisms can distort the primary lubrication mechanism influencing the overall operation of the seal.

It is concluded that complementary validation techniques are necessary for a more detailed modelling of the seal shaft-interface. In fact, the limitation when modelling rotary lip seals nowadays resides in the validation of the models. Accurate measurements of the flow rate or the film thickness [27] under various operating conditions will help to establish more reliable models. Furthermore, the fact that each researcher tests and models a particular seal, makes it the results vaguely comparable. A "Contact-Mechanics challenge" [103] for the modelling of rotary lip seals is necessary.

The results obtained with the dynamic setup presented in *Section 4.3* shed some light to the operation of stern tube seals. Although the film thickness was not measured, the frictional torque readings suggest that the stern tube seal analysed operates at the right-side of the minimum friction coefficient value of the Stribeck curve (*Paper E*). As in [19], the boundary lubrication regime was not observed under the operating points tested. Especially interesting is the direction of the oil migration. *Section 6.1* shows that lubricant flows from the higher pressure to the lower pressure side. It is known that lubricant escapes the stern tube and it is spilled to the environment as a result of normal sailing [7]. According to the results obtained, the oil migration occurs in the opposite direction, i.e. toward the stern tube. Consequently, the actual operating conditions of a stern tube seal of a ship are put at stake. The presence of water (or emulsions), the seal-shaft misalignment in a ship, the interaction between the various seals of a ship and the presence of a lead on the shaft surface must be further analysed.

Great importance was given to the characterization of the Environmentally Acceptable Lubricants (EALs) for the stern tube lubrication (*Paper A*). The results showed that, in terms of rheology, EALs behave fairly similarly compared to the traditional mineral oil-based lubricants. Few EALs exhibited shear thinning which decreases the load carrying capacity of the hydrodynamic film. This leads to more asperity contact and hence larger wear rates are expected. However, the shear thinning is not attributed to the fact of being an EAL as not all the EALs analysed showed this phenomenon. It is thought that the shear thinning is a consequence of the type of viscosity improvers (VIIs) used in their particular formulation. In short, shear thinning also occur in mineral oil-based lubricants.

Although this research did not focus on the chemical aspects of EALs, it was inevitable to deal with them during the experimental phase of this thesis. The author wants to emphasize the importance of treating the seal material and the lubricant as a whole and not separately. This statement applies to any tribological system however in this case it is from special importance due to the inherent incompatibility between fluoroelastomers and the main types of EALs. Severe swelling and blistering results when the lubricant-elastomer pair is not carefully selected. Furthermore, the most part of EALs are synthetic ester-based making them prone to hydrolysis when in contact with water. It is crucial to ensure the compatibility of the elastomer, the EAL and water before approaching the operation of stern tube seals from a mechanical standpoint.

7.2. Conclusions

The rotary lip seals tribo-system was studied for the particular case of a stern tube seal. The system was approached from both a modelling and an experimental standpoint. Some of the topics reviewed are research fields on its own and hence one of the challenges when conducting this research was allocating the right amount of effort to each field. Among them, the rheological characterization of EALs, the characterization of the seal material, the lubrication mechanisms and the experimental validation of the models have been given a greater importance.

The main findings of this research can be summarized as follows:

- The rheological and wetting characteristics of EALs were shown to be similar to the traditional mineral oil-based lubricants used for the stern tube lubrication. Shear thinning was measured in some EALs at shear rates around 10^6 s^{-1} which is a common value for the stern tube application. Shear thinning was not observed in all the EALs and hence it is not attributed to the base oil used for its formulation.

- The step-by-step strategy combining modelling and validation of a two-scale static lip seal model is shown to be successful. The model presented is able to predict the radial force, contact width and the percolation threshold of the stern tube seal analysed. The role of each of the seal components is revealed hence facilitating the development of new lip seal designs.

- The thorough validation of the static FE model was proven essential in the study of lip seals. Variations on the dimensions and the material properties of the seals can lead to important misestimates when the radial load is solely deduced from FE models. Additionally, by validating the pressurized situation in terms of contact width, the overall accuracy of the model is ensured.

- The implications of operating a rotary lip seal under misaligned conditions was studied using hydrodynamic models. Two misalignment-induced lubrication mechanisms where presented. Both the non-uniform radial force and also the slanted contact profile result in a hydrodynamic pressure built-up on the macroscopic level. These two mechanisms can distort the primary lubrication mechanism leading to a bidirectional migration of lubricant across the seal, i.e. from the spring to the back side and vice versa. Consequently, sealing two liquids using a rotary lip seal becomes unfeasible.

- The knowledge on the operating conditions of a stern tube seal is nowadays insufficient. Due to the difficult accessibility to the sealing chambers little is known on the actual operating conditions within a stern tube. Therefore, an experimental setup resembling the stern tube seal application was developed

and built to investigate the seal under typical operating conditions.

- The torque, temperature and flow rate measurements revealed that the stern tube analysed operates at the right-side of the minimum friction coefficient value of the Stribeck curve, i.e. at the right hand side of the transition between the elastohydrodynamic and the full hydrodynamic regime.
- The experimental measurements show a strong coupling between the primary variables involved, especially to the temperature of the system. The results obtained were consistent and previous trends observed for smaller rotary lip seals were shown suitable to the application of stern tube seals.
- The elastomer-lubricant compatibility must be resolved before discussing the tribological system. The traditional fluoroelastomeric compounds used for the stern tube seals are often incompatible with the Environmentally Acceptable Lubricants. The hydrolytic stability of ester-based EALs must also be considered.

The theory and models presented in this study can be used to predict the overall behaviour of a stern tube seal when operated together with an Environmentally Acceptable Lubricant (EAL). On the longer term, the knowledge gained will give the seals and lubricants manufacturers the opportunity to redesign their products on an efficient and reliable way. The approach presented in this thesis for analysing a stern tube seal is applicable to any other type of rotary lip seal.

7.3. Recommendations

The research conducted focused on gathering knowledge on the stern tube system and identifying the primary variables leading to a successful sealing. A set of computational and experimental tools were developed to support for the further development of these stern tube seals.

In order to validate the models in a real seal, in-situ measurements of the stern tube under operating conditions are required. It is

paramount to ensure that the setup developed is representative of a stern tube seal of a ship.

This thesis reached its end at the beginning of the testing stage. The machinery and the procedures for measuring the main variables involved in the operation of stern tube seals result from this research. The twelve operating points analysed are not sufficient for a complete characterization of the system. A comprehensive design of experiments must be conducted for that purpose. The flow rate results suggest that there is a lead on the shaft surface. Further flow rate measurements on various surface roughness profiles are required to confirm it. Switching the direction of rotation can evidence the presence of a screw thread on the shaft. The temperature at the contact is extrapolated from a thermocouple near the contact, hence a deviation from the actual temperature may be present. It is recommended to further investigate the characteristics of the thermal contact conductance of the seal-shaft interface. The dynamic setup presented was designed in such a way that a radial or an angular misalignment can be simulated. The two misalignment-induced lubrication mechanisms presented in this thesis can then be validated. In short, further experimental work is required.

From the modelling side, the next logical step is developing a mixed-lubrication model for the stern tube seal when aligned. This model must be able to predict the torque, flow rate and temperature measured on the dynamic setup. The seal viscoelasticity, the presence of a meniscus, the lubrication of with a water-in-oil emulsion or transient phenomena may be included to the model.

When it comes to “improving” the seal, the direction to follow is not clear. Is a greater lubricant spillage preferred to a higher wear rate? Is it allowed to spill lubricant as long as it is an EAL? Is the lubricant spillage to the environment better than the water entrainment into the stern tube? The answers to these questions are of an economic rather than a tribological nature. They must therefore be answered by the manufacturers and the end users of stern tube seals. Furthermore, upcoming legislative measures point towards a more environmentally friendly sealing of the shaft, eventually leading to a fully water lubricated stern tube. At some point in time, a prototype for an improved seal will need to be placed on a real ship. In that sense, there is a need for accelerated tests of rotary lip seals.

(This page is intentionally left blank)

8. References

[1] S. Yamajo and I. Matsuoka, “Advanced Technology of Propeller Shaft Stern Tube,” in *Advanced Naval Propulsion Symposium*, 2008, pp. 1–14.

[2] R. Flitney, “Rotary Seals,” in *Seals and Sealing Handbook*, 6th ed., Waltham: Butterworth-Heinemann, 2014, pp. 105–288.

[3] T. Kunstfeld and W. Haas, “Shaft surface manufacturing methods for rotary shaft lip seals,” *Seal. Technol.*, no. 7, pp. 5–9, 2005.

[4] K. Uneyama, *Organofluorine Chemistry*. Blackwell Publishing Ltd, 2006.

[5] J.G. Drobny, “Fluoroelastomers Handbook: The Definitive User’s Guide,” 2nd Ed., Elsevier, 2016, pp. 17–40.

[6] H.K. Müller and B.S. Nau, “Rotary Lip Seals,” in *Fluid Sealing Technology: Principles and Applications*, New York: Marcel Dekker Inc., 1998, pp. 73–110.

[7] D.S. Etkin, “Worldwide analysis of in-port vessel operational lubricant discharges and leakages.” Cortlandt Manor, pp. 2–9, 2008.

[8] I. Madanhire and C. Mbohwa, "Lubricant Additive Impacts on Human Health and the Environment," in *Mitigating Environmental Impact of Petroleum Lubricants*, Cham: Springer International Publishing, 2016, pp. 17–34.

[9] P. Pavlakis, D. Tarchi, A.J. Seiber, G. Ferraro, and G. Vincent, "On the monitoring of illicit vessel discharges. A reconnaissance study in the Mediterranean Sea." pp. 3–6, 2001.

[10] United States Environmental Protection Agency: Office of Wastewater Management, "Environmentally Acceptable Lubricants." Washington, pp. 1–20, 2011.

[11] A. Eder and L. Dammer, "Knowledge Based Bio-based Products ' Pre-Standarization (Work package 5)," Hürth, 2015.

[12] V.G. Candela, K. Renata, W. Oliver, J.R.C. Dir, R.M. Rosa, H. Carme, F. Natalia, and E. Leitat, "Revision of the European Ecolabel Criteria for Lubricants Criteria proposal for revision of EU Ecolabel criteria," Seville, 2018.

[13] E.T. Jagger, "Rotary Shaft Seals: The Sealing Mechanism of Synthetic Rubber Seals Running at Atmospheric Pressure," *Proc. Inst. Mech. Eng. Part J J. Eng. Tribol.*, vol. 171, no. 1, pp. 597–616, 1957.

[14] R.F. Salant, "Theory of lubrication of elastomeric rotary shaft seals," *Proc. Inst. Mech. Eng. Part J J. Eng. Tribol.*, vol. 213, no. 3, pp. 189–201, 1999.

[15] B. Wennehorst, "On Lubrication and Friction in Soft Rough Conformal Sliding Contacts," Ph.D. dissertation, Leibniz Universität Hannover, 2016.

[16] J.A. Norris, K.J. Stabile, and R.H. Jinnah, *An introduction to tribology.*, vol. 17, no. 1. 2008.

[17] M. Ogata, T. Fujii, and Y. Shimotsuma, "Study on fundamental characteristics of rotating lip-type oil seals.," *Tribol. Ser.*, vol. 11, no. XVIII(ii), pp. 553–560, 1987.

[18] F. Hirano and H. Ishiwata, "The Lubricating Condition of a Lip Seal," *Proc. Inst. Mech. Eng.*, vol. 180, no. 3B, pp. 187–196, 1965.

[19] D.E. Johnston and R. Vogt, "Rotary shaft seal friction, the

influence of design, material, oil and shaft surface," *SAE Tech. Pap.*, no. 41 2, 1995.

[20] M.J.L. Stakenborg, "On the sealing mechanism of radial lip seals," Ph.D. dissertation, Eindhoven University of Technology, 1988.

[21] B.S. Nau, *Fluid Sealing*, vol. 8. Dordrecht: Springer Netherlands, 1992.

[22] L.A. Horve, "Understanding The Sealing Mechanism Of The Radial Lip Seal For Rotating Shafts," in *Fluid Mechanics and its Applications*, Dordrecht: Springer Netherlands, 1992, pp. 5–19.

[23] Y. Kawahara, M. Abe, and H. Hirabayashi, "An Analysis of Sealing Characteristics of Oil Seals," *ASLE Trans.*, vol. 23, no. 1, pp. 93–102, 1980.

[24] P.G.M. van Bavel, "The Leakage-Free Operation of Radial Lip Seals," Ph.D. dissertation, Eindhoven University of Technology, 1997.

[25] D.E. Johnston, "Rotary shaft seals," *Tribol. Int.*, vol. 19, no. 4, pp. 170–174, 1986.

[26] G. Poll and A. Gabelli, "Formation of Lubricant Film in Rotary Sealing Contacts: Part II—Lubricant Film Modeling."

[27] B. Wennehorst and G.W.G. Poll, "Soft micro-elastohydrodynamic lubrication and friction at rough conformal contacts," *Proc. Inst. Mech. Eng. Part J*, vol. 231, no. 3, pp. 302–315, 2017.

[28] B.J. Hamrock, S.R. Schmid, and B.O. Jacobson, *Fundamentals of Fluid Film Lubrication*, 2nd ed. New York: CRC Press, 2004.

[29] L.A. Horve, *Shaft seals for dynamic applications*. New York: Marcel Dekker Inc., 1996.

[30] R.F. Salant, "Soft elastohydrodynamic analysis of rotary lip seals," *Proc. Inst. Mech. Eng. Part C*, vol. 224, no. 12, pp. 2637–2647, 2010.

[31] Freudenberg Simrit GmbH & Co. KG, "Simmerrings and Rotary Seals," in *Simrit Catalog 2007*, 2007, pp. 15–166.

[32] H. van Leeuwen and M. Wolfert, "The sealing and lubrication principles of plain radial lip seals: an experimental study of local tangential deformations and film thickness," in *Elastohydrodynamics*, 1996, pp. 219–232.

[33] H.K. Müller, "Concepts of sealing mechanism of rubber lip type rotary shaft seals," in *11th International Conference on Fluid Sealing*, 1987, p. K1 698-709.

[34] M.J.L. Stakenborg, "Visco-Elastohydrodynamic (VEHD) Lubrication in Radial Lip Seals: Part 1 - Steady-State Dynamic Viscoelatic Seal Behavior," *Trans. ASME*, vol. 112, p. 578, 1990.

[35] P. Baart, "Grease lubrication in radial lip seals," Luleå University of Technology, 2009.

[36] B. Pinedo, J. Aguirrebeitia, M. Conte, and A. Igartua, "Tri-dimensional eccentricity model of a rod lip seal," *Tribol. Int.*, vol. 78, pp. 68–74, 2014.

[37] A. Tasora, E. Prati, and T. Marin, "A method for the characterization of static elastomeric lip seal deformation," *Tribol. Int.*, vol. 60, pp. 119–126, 2013.

[38] M.S. Kalsi and G.A. Fazekas, "Feasibility Study of a Slanted O-Ring as a High Pressure Rotary Seal," *ASME*, p. 302, 1973.

[39] M.J. Gawlinski, "Lip Motion and Its Consequences in Oil Lip Seal Operation," in *Ninth International Conference on Fluid Sealing*, 1981, p. D2 111-124.

[40] H. Ishiwata, "Effect of shaft eccentricity in oil seals," in *Second International Conference on Fluid Sealing*, 1964, pp. H2-17 to H2-32.

[41] O. Schuck and H.K. Müller, "Rotary shaft seals at large dynamic eccentricities," in *9th International Conference on Fluid Sealing*, 1981, p. D1 103-110.

[42] M. Sansalone, S. Blachere, and M. Gohlke, "Onto fast, Automated and Advanced Viscoelastic Modelling of Rubber Materials for Sealing Applications," in *18th International Sealing Conference*, 2014, pp. 685–699.

[43] B. van der Vorst and M. Organisciak, "Fast Analytical Model for

Followability Prediction of Rotary Shaft Seals," in *19th International Sealing Conference*, 2016.

[44] M.O.A. Mokhtar, M.A.A. Mohamed, M.E. El-Giddawy, and S.A.Y. Yassen, "On the effect of misalignment on the performance of U-type lip seal," *Wear*, vol. 223, no. 1–2, pp. 139–142, 1998.

[45] H. van Leeuwen and M.J.L. Stakenborg, "Visco-Elastohydrodynamic (VEHD) Lubrication in Radial Lip Seals: Part 2 - Fluid film formation," *Trans. ASME*, vol. 112, pp. 584–591, 1990.

[46] Y. Arai, "Sealing theory in oil seals - 1," in *JSLE-ASLE International Lubrication Conference*, 1976, pp. 830–839.

[47] G. Di Benedetto, M. Organisciak, G. Popovici, and A. Stijepić, "Film thickness prediction of radial lip seal," *FME Trans.*, vol. 37, no. 2, pp. 87–90, 2009.

[48] D. Liu, S. Wang, C. Zhang, and M.M. Tomovic, "Numerical study of the effects of textured shaft on the wear of rotary lip seals," *Tribol. Int.*, vol. 138, pp. 215–238, 2019.

[49] D. Frölich, B. Magyar, and B. Sauer, "A comprehensive model of wear, friction and contact temperature in radial shaft seals," *Wear*, vol. 311, no. 1–2, pp. 71–80, 2014.

[50] L. Horve, "A Macroscopic View of the Sealing Phenomenon for Radial Lip Oil Seals," in *10th Int. Conf. on Fluid Sealing*, 1984, p. K2 710-731.

[51] A. Maoui, M. Hajjam, and D. Bonneau, "Analysis of three-dimensional non-axisymmetric elastic effects of the lip on the thermoelastohydrodynamic radia lip seal behaviour," *Proc. Inst. Mech. Eng. Part J*, 2007.

[52] A. Gabelli, "Micro-elastohydrodynamic lubricant film formation in rotary lip seal contacts," *Tribol. Ser.*, vol. 14, pp. 57–68, 1989.

[53] R.F. Salant and A.L. Flaherty, "Elastohydrodynamic analysis of reverse pumping in rotary lip seals with microundulations," *J. Tribol.*, vol. 116, no. 1, pp. 56–62, 1994.

[54] H. Mizuta and J. Sugimura, "Numerical Study of the Effect of

Lip Surface Roughness on Lubrication of Radial Shaft Seals with a Simple Sinusoidal Model," in *International Tribology Conference*, 2013, vol. 1, pp. 104–110.

[55] M. Elgadari, A. Fatu, M. Hajjam, M. Belhaq, and K. Zerbane, "About numerical modelling of rotary lip seals," in *STLE Annual Meeting & Exhibition*, 2012, pp. 1–3.

[56] M. El Gadari, A. Fatu, and M. Hajjam, "Effect of grooved shaft on the rotary lip seal performance in transient condition: Elasto-hydrodynamic simulations," *Tribol. Int.*, vol. 93, pp. 411–418, 2016.

[57] M. El Gadari, A. Fatu, and M. Hajjam, "Shaft roughness effect on elasto-hydrodynamic lubrication of rotary lip seals: Experimentation and numerical simulation," *Tribol. Int.*, vol. 88, pp. 218–227, 2015.

[58] M. Hajjam and D. Bonneau, "Elastohydrodynamic analysis of lip seals with microundulations," *Proc. Inst. Mech. Eng. Part J*, vol. 218, no. 1, pp. 13–22, 2004.

[59] D. Liu, S. Wang, J. Shi, C. Zhang, and M. Tomovic, "Numerical analysis of rotary lip seal performance deterioration," *Proc. 2016 IEEE 11th Conf. Ind. Electron. Appl. ICIEA 2016*, pp. 1078–1083, 2016.

[60] P.G.M. Van Bavel, T.A.M. Ruijl, H.J. Van Leeuwen, and E.A. Muijderman, "Upstream Pumping of Radial Lip Seals by Tangentially Deforming, Rough Seal Surfaces," *J. Tribol.*, vol. 118, no. 2, pp. 266–275, 1996.

[61] R.F. Salant and A.L. Flaherty, "Elastohydrodynamic analysis of reverse pumping in rotary lip seals with microasperities," *J. Tribol.*, vol. 117, no. 1, pp. 53–59, 1995.

[62] X. Jia, S. Jung, W. Haas, and R.F. Salant, "Numerical simulation and experimental study of shaft pumping by plunge ground shafts with rotary lip seals," *Tribol. Int.*, vol. 48, pp. 155–161, 2012.

[63] X. Jia, S. Jung, W. Haas, and R.F. Salant, "Numerical simulation and experimental study of shaft pumping by laser structured shafts with rotary lip seals," *Tribol. Int.*, vol. 44, pp. 651–659, 2011.

[64] G. Marek, “On friction reduction in rubber lip seals for rotating shafts,” *Seal. Technol.*, vol. 40, pp. 8–11, 1997.

[65] A.S. Yang, C.Y. Wen, and C.S. Tseng, “Analysis of flow field around a ribbed helix lip seal,” *Tribol. Int.*, vol. 42, no. 5, pp. 649–656, 2009.

[66] F. Shi and R.F. Salant, “Numerical study of a rotary lip seal with a quasi-random sealing surface,” *J. Tribol.*, vol. 123, no. 3, pp. 517–524, 2001.

[67] M. Hajjam and B. Dominique, “Non-Newtonian effects on elastohydrodynamic behaviour of rotary lip seals,” *Proc. Inst. Mech. Eng. Part J*, vol. 220, no. 2, pp. 79–85, 2006.

[68] D. Shen and R.F. Salant, “A transient mixed lubrication model of a rotary lip seal with a rough shaft,” *Tribol. Trans.*, vol. 49, no. 4, pp. 621–634, 2006.

[69] M. Hajjam and D. Bonneau, “A transient finite element cavitation algorithm with application to radial lip seals,” *Tribol. Int.*, vol. 40, no. 8, pp. 1258–1269, 2007.

[70] M. Yildiz, “Modeling and Simulation of Oil Leakage in Radial Lip Seals,” M.S. thesis, Middle East Technical University, 2010.

[71] R.F. Salant, “Elastohydrodynamics of the rotary lip seal,” *Lubr. Sci.*, vol. 9, no. 2, pp. 111–125, 1997.

[72] W. Sinzara, I. Sherrington, E.H. Smith, H. Brooks, and A. Onsy, “Effects of Eccentric Loading on Lip Seal Performance,” in *6th European Conference on Lubrication Management and Technology*, 2018.

[73] B. Pinedo, “Effect of Mounting Misalgnments on The Tribological Behavior of Elastomeric Seals: Analytical Predictive Models and Experiental Validation,” University of Bilbao, 2016.

[74] J.F. Wenk, L.S. Stephens, S.B. Lattime, and D. Weatherly, “A multi-scale finite element contact model using measured surface roughness for a radial lip seal,” *Tribol. Int.*, vol. 97, pp. 288–301, 2016.

[75] C.J. Seeton, “Viscosity-temperature correlation for liquids,”

Tribol. Lett., vol. 22, no. 1, pp. 67–78, 2006.

[76] N. Marx, L. Fernández, F. Barceló, and H. Spikes, "Shear Thinning and Hydrodynamic Friction of Viscosity Modifier-Containing Oils. Part I: Shear Thinning Behaviour," *Tribol. Lett.*, vol. 66, no. 3, pp. 1–14, 2018.

[77] E.R.G. Eckert and J.N. Shadid, "Viscous heating of a cylinder with finite length by a high viscosity fluid in steady longitudinal flow -II. Non-Newtonian Carreau model fluids," *Int. J. Heat Mass Transf.*, vol. 35, no. 10, pp. 2739–2749, 1992.

[78] J. Bergström, "Elasticity/Hyperelasticity," in *Mechanics of Solid Polymers*, 1st Ed., vol. 76, no. 3, Elsevier, 2015, pp. 209–307.

[79] MSC.Software, "White Paper - Nonlinear finite element analysis of elastomers." pp. 1–70, 2010.

[80] A.N. Gent, *Engineering with Rubber: How to Design Rubber Components*, 3rd ed. Munich: Hanser Publishers, 2012.

[81] A.L. Moore, *Fluoroelastomers Handbook : the Definitive User's Guide and Databook*, 2nd ed. Norwich: William Andrew Publishing, 2006.

[82] T. Dalrymple, J. Choi, and K. Miller, "Elastomer rate-dependence : A testing and material modeling methodology," in *172nd Technical Meeting of the Rubber Division of the American Chemical Society, Inc.*, 2007.

[83] Chung Kyun Kim and Woo Jeon Shim, "Analysis of contact force and thermal behaviour of lip seals," *Tribol. Int.*, vol. 30, no. 2, pp. 113–119, Feb. 1997.

[84] "Chapter 8: Garter Springs," in *Design handbook: engineering guide to spring design*, Barnes Group Inc, 1981, pp. 56–59.

[85] C.H. Hidrovo and D.P. Hart, "Development of a dual purpose visualization technique for the study of rotating shaft seals," in *3rd ASME/JSME Joint Fluids Engineering Conference*, 1999, pp. 1–6.

[86] A. Gabelli and G. Poll, "Formation of Lubricant Film in Rotary Sealing Contacts: Part I—Lubricant Film Modeling," *J. Tribol.*, vol. 114, no. 2, pp. 280–287, 1992.

[87] T. Engelke, “Einfluss der Elastomer-Schmierstoff-Kombination auf das Betriebsverhalten von Radialwellendichtringen (in German),” Ph.D. dissertation, Leibniz Universität Hannover, 2011.

[88] O. Pinkus, *Thermal Aspects of Fluid Film Technology*. New York: ASME Press, 1990.

[89] H. Hirabayashi, “A study of sealing phenomena on oil seals,” *ASLE Trans.*, vol. 22, no. 1, pp. 46–55, 1979.

[90] A. Yevtushenko and P. Grzes, “Finite element analysis of heat partition in a pad/disc brake system,” *Numer. Heat Transf. Part A Appl.*, vol. 59, no. 7, pp. 521–542, 2011.

[91] Robert D. Cook, D.S. Malkus, M.E. Plesha, and R.J. Witt, *Concepts and Applications of FEA*, 4th ed. Wiley, 2001.

[92] M. Bazrafshan, M.B. de Rooij, M. Valefi, and D.J. Schipper, “Numerical method for the adhesive normal contact analysis based on a Dugdale approximation,” *Tribol. Int.*, vol. 112, no. April, pp. 117–128, 2017.

[93] Y. Hori, *Hydrodynamic Lubrication*. Tokyo: Springer-Verlag, 2006.

[94] A. Almqvist and P. Wall, “Modelling Cavitation in (Elasto)Hydrodynamic Lubrication,” in *Advances in Tribology*, InTech, 2016, pp. 197–213.

[95] A.Z. Szeri, *Fluid Film Lubrication*, 2nd ed. New York: Cambridge University Press, 2011.

[96] L.S. Andrés, “Liquid cavitation in fluid film bearings,” *Modern Hydrodynamic Lubrication Theory (Lecure Notes)*. Texas A&M University Libraries, pp. 13–15, 2009.

[97] A. Maoui, M. Hajjam, and D. Bonneau, “Analysis of three-dimensional non-axisymmetric elastic effects of the lip on the thermoelastohydrodynamic radia lip seal behaviour,” *Proc. Inst. Mech. Eng. Part J*, vol. 221, no. 8, pp. 859–868, 2007.

[98] K.L. Johnson, *Contact mechanics*. Cambridge: Cambridge University Press, 1985.

[99] A. Maoui, M. Hajjam, and D. Bonneau, “Effect of 3D lip

deformations on elastohydrodynamic lip seals behaviour," *Tribol. Int.*, vol. 41, pp. 901–907, 2008.

[100] R.J. Chittenden, D. Dowson, and C.M. Taylor, "Paper VIII(ii) The lubrication of elliptical conjunctions in the isoviscouselastic regime with entrainment directed along either principal axis," *Tribol. Ser.*, vol. 11, no. ii, pp. 247–260, 1987.

[101] F.X. Borras, M. Bazrafshan, M. B De Rooij, and D. J Schipper, "Stern tube seals under static condition: A multi-scale contact modeling approach," *Proc. Inst. Mech. Eng. Part J*, May 2020.

[102] M. Organisciak, P. Baart, and A. Paykin, "Theoretical and experimental study of the frictional losses of radial shaft seals for industrial gearbox," *Power Transmission Engineering*, pp. 58–63, 2015.

[103] M.H. Müser, W.B. Dapp, R. Bugnicourt, P. Sainsot, N. Lesaffre, T.A. Lubrecht, B.N.J. Persson, K. Harris, A. Bennett, K. Schulze, S. Rohde, P. Ifju, W.G. Sawyer, T. Angelini, H. Ashtari Esfahani, M. Kadkhodaei, S. Akbarzadeh, J.J. Wu, G. Vorlaufer, A. Vernes, S. Solhjoo, A.I. Vakis, R.L. Jackson, Y. Xu, J. Streator, A. Rostami, D. Dini, S. Medina, G. Carbone, F. Bottiglione, L. Afferrante, J. Monti, L. Pastewka, M.O. Robbins, and J.A. Greenwood, "Meeting the Contact-Mechanics Challenge," *Tribol. Lett.*, vol. 65, no. 4, 2017.

Part II

(This page is intentionally left blank)

ROTARY LIP SEAL OPERATION WITH ENVIRONMENTALLY ACCEPTABLE LUBRICANTS

COMPILATION OF PUBLICATIONS

F. Xavier Borras Subirana

(This page is intentionally left blank)

Paper A

Rheological and Wetting Properties of Environmentally Acceptable Lubricants (EALs) for Application in Stern Tube Seals

F.X. Borras, M.B. de Rooij and D.J. Schipper

Lubricants 2018 https://doi.org/10.3390/lubricants6040100

Paper B

Stern Tube Seals Under Static Condition: a Multi-scale Contact Modelling Approach

F.X. Borras, M. Bazrafshan, M.B. de Rooij, and D.J. Schipper

Proceedings of the Institution of Mechanical Engineers, Part J 2020. https://doi.org/10.1177/1350650120925583

Paper C

Misalignment-Induced Micro-Elastohydrodynamic Lubrication in Rotary Lip Seals

F.X. Borras, M.B. de Rooij, and D.J. Schipper

Lubricants 2020 https://doi.org/10.3390/lubricants8020019

Paper D

Misalignment-Induced Macro-Elastohydrodynamic Lubrication in Rotary Lip Seals

F.X. Borras, M.B. de Rooij, and D.J. Schipper

Tribology International 2020 https://doi.org/10.1016/j.triboint.2020.106479

Paper E

Stern Tube Seals Operation: a Practical Approach

F.X. Borras, R. van den Nieuwendijk, V. Ramesh, M.B. de Rooij, and D.J. Schipper

(submitted to Advances in Mechanical Engineering)

(This page is intentionally left blank)

Paper A

(This page is intentionally left blank)

Rheological and Wetting Properties of Environmentally Acceptable Lubricants (EALs) for Application in Stern Tube Seals

F.X. Borras[1], M.B. de Rooij[1] and D.J. Schipper[1]

[1]University of Twente, Surface Technology and Tribology, Enschede, The Netherlands

(This page is intentionally left blank)

Abstract: The use of Environmentally Acceptable Lubricants (EALs) for stern tube lubrication is increasing. Although the machine components of a sailing vessel are designed to operate together with mineral oil-based lubricants, the latter are being replaced by the less environmentally harmful EALs. Little is known about the rheological performance of EALs, particularly at the high shear rates that occur in stern tube seals. In this study, the viscosity and wetting properties of a set of different EALs are analysed and compared with traditional mineral oil-based lubricants using a set of experimental techniques. Some of the EALs present Newtonian behaviour whereas other show shear thinning. No significant difference in surface tension was observed between the different lubricants.

Keywords: Lubricant, Marine, Rheology, EAL, Stern tube, Environmental, Shear thinning.

1. Introduction

Applications in which oil-water interfaces are inevitable, such as hydroelectric power plants, logging and mining industries, or sailing vessels, represent a potential hazard for the environment. Apart from the potential risk of an environmental catastrophe in the case of an accident, these applications cause regular spillage of lubricant under normal operation. Though a large amount of lubricants are recycled or burned, it is estimated that about 50% of the lubricants end up in the environment [1]. The environmental consequences escalate when the lubricant is mixed with water since a small quantity of oil can contaminate a large amount of water.

In marine applications, lubricants are required in gear boxes, thrusters, controllable pitch propellers, stabilizers, stern tube bearings and seals, rudder bearings, dredges, and grabs. These mechanical components all have an oil-to-sea interface, representing a potential source of oil spillage to the aquatic environment. Even during normal sailing, there is a continuous lubricant spillage into the sea through the stern tube seals (Figure 1) [2]. This type of rotary lip seals operates under pressurized conditions and is designed to minimize both the lubricant leakage as well as the water ingress to the stern tube.

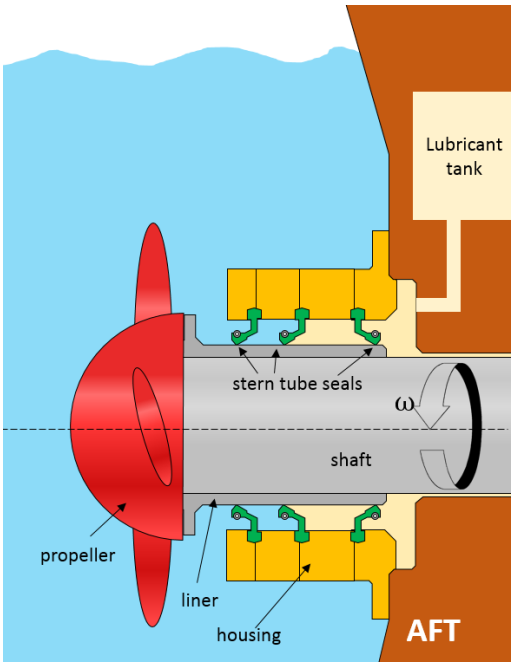

Figure 1. *Traditional stern tube arrangement in a marine vessel.*

Governmental regulations limit the use of certain lubricants in applications where there is a risk of environmental damage. The German Blue Angel, the European Eco-label, and the American Vessel General Permit (VGP) labelling programs are the most well-known. In December 2013, the use of Environmentally Acceptable Lubricants (EALs) became mandatory in large ships sailing within the coastal waters of the United States [3,4]. To minimize seawater pollution, all oil-to-sea interfaces of sailing vessels must use these more environmentally friendly lubricants. Any lubricant can be labelled as an EAL as long as it meets certain criteria: biodegradability, minimum toxicity, and bioaccumulation potential. Consequently, a wide range of lubricants tailored to fit this new legislation have been introduced to the marine lubricants segment.

The American VGP 2013 only allows the following four kinds of base oils for the formulation of EALs: hydraulic oil environmental triglyceride (HETG), hydraulic oil environmental ester synthetic (HEES), hydraulic oil environmental polyglycol (HEPG or PAG), and poly-α-olefins including related hydrocarbon products (HEPR or PAO)

[4]. The first group are lubricants obtained from plants and animal fats. Although more economic than synthetic esters, their quick aging when exposed to water and heat makes them unsuitable for hydraulic systems [4]. The stricter European Eco-Label program restricts the content of a high fraction of natural esters or synthetic esters made from renewable resources in the formulation of a marine lubricant [5].

The second kind of base oils for EALs results from reacting carboxylic acids and alcohols to obtain synthetic esters (i.e., esterification reaction). These have been the obvious choice for most ship owners. These base oils can be specially tailored to the application by selecting the proper acids and alcohols to form specific esters. Synthetic esters are susceptible to hydrolysis and have compatibility problems with the elastomeric stern tube seals [4].

Petroleum-based PAG's are obtained from ethylene or propylene oxide via polymerisation. The proportion of these dictates their solubility in water (i.e., polarity). Their maximum operation temperature is limited and they are also often incompatible with the elastomer compounds from which the stern tube seals are made [6].

Poly-α-olefin (PAO) is a synthetic compound obtained from polymerizing α-olefin. PAO is non-polar in nature, so HEES and PAG, both polar, have a higher affinity to metal surfaces. Consequently, PAOs are often mixed with esters, acting as carrier of the polar additives [7] to increase the additive solubility. There is an ongoing discussion as to whether or not PAOs are actually EALs, since they do not meet any renewable source standards and only the low viscosity types are biodegradable. In addition, they are not listed with the other three EALs in the VGP 2013 [3]. Both the base oil and additive formulation must meet the VGP legislation so the final formulation can be labelled as an EAL; consequently, the type of additives allowed is also limited [8].

Several EALs are readily available in the market, making the selection of a suitable lubricant rather complex. The current trend, as shown in the VGP 2018 draft, is that such environmental regulations become stricter with time. Nevertheless, EALs have caused controversy since they became mandatory. In addition to being more costly than mineral oil-based lubricants, it is thought that sailing with EALs causes a

higher oil spillage while shortening the service life of stern tube seals. Regardless of the technical complexity of obtaining data on the stern tube of sailing vessels, running conditions differ from ship to ship, making it impossible to reliably compare the impacts of specific lubricants alone. Computational models for rotary lip seals are available in the literature; however, those models commonly assume Newtonian behaviour of the lubricant [9,10]. It is unknown if the results from these models still apply when the seals operate with EALs instead, as the rheological properties are not well characterized.

For rotary lip seals, the optimal friction, leakage, and wear rate are determined during the transition from mixed to the full-film lubrication regime [11]. For a fixed gap geometry (including roughness), load W, and velocity u on a certain contact, the lubrication regime only depends on viscosity η. The viscosity of a lubricant relates the shear stress τ to the shear rate $\dot{\gamma}$·. The viscosity of a fluid depends on the following: composition, temperature, shear rates, pressure, and time.

The importance of EAL composition is self-explanatory. The nature of both the base oil and the additive package play an important role in chemical incompatibility [12] with the surrounding hardware and harmful fluids (i.e., water). The possible ingress of water into the stern tube would lead to an emulsion that would affect the original properties of the lubricant. The impact of water on EALs is beyond the scope of this paper. It is difficult to break apart the formulation of a lubricant; however, the presence (or lack) of certain components can be identified using Fourier transform infrared (FT-IR) or Raman spectroscopy [13].

Lubricant formulations often use viscosity index modifiers (VII), which increase the overall viscosity of the base-lubricant blend [8]. These are usually long polymeric chains that help transmit tangential loads between the different lubricant layers. As a result of high loading, high temperature, or long running periods, the rupture of those VIIs can lead to a permanent loss of viscosity. Even if the polymeric chains show a high shear stability, they can be oriented in the direction of the flow due to shear stress, leading to a temporary loss of viscosity. In extreme

situations (at higher shear rates), the lubricant takes the viscosity of its base oil or blend of base oils [7].

The viscosity index (VI) is a measure of the viscosity dependence on temperature T. Temperature-viscosity data are usually provided by the lubricant supplier. The shear stress of mineral oil-based lubricants is generally considered to be directly proportional to the shear rate applied to it (i.e., Newtonian behaviour). However, when additives (e.g., VIIs) and contaminants increase the viscosity of the fluid at low shear rates, the lubricant can become susceptible to shear thinning. In stern tube seals, the shear rate of the lubricant is high. The ratio between the shaft liner velocity and the oil film thickness on the elastomeric seals leads to shear rates up to 106 s^{-1}. Shear thinning can be measured via specialized rheometers that allow reaching such high shear rates. The pressure-viscosity coefficient α relates the increase in the viscosity of a lubricant with pressure. Neither the pressure on the stern tube chamber nor the hydrodynamic pressure between the stern tube seals and the liner exceed 10 MPa [14]. It can be estimated that the impact of pressure on the lubricant viscosity, even with the highest pressure-viscosity coefficients, is relatively small and can be thereby disregarded in stern tube seals.

The capability of a liquid to spread on a surface is known as wettability. Wettability cannot be disregarded in the case of stern tube seals since it determines if the fluid enters the contact zone. The affinity of the lubricant to the surrounding surfaces is a system variable and therefore it is not exclusively dependent on the fluid but also on the contacting surfaces [15]. Properties like foaming depend on viscosity and surface tension of the lubricant [7]. Both chemical incompatibilities and rheological differences with a mineral oil-based can cause EALs to perform differently.

This paper focuses on the viscosity and wettability of the lubricant, as these factors determine the properties for the lubrication and sealing performance. The viscosity of new Environmentally Acceptable Lubricants under the high shear rates found in the stern tube applications has been well characterized. In detail, a set of EALs are compared to a mineral oil-based lubricant in terms of viscosity, density, and wetting characteristics under demanding conditions.

Rheological models are fitted to the measurements so these can be used in more complex lubrication models.

2. Materials and Methods

One traditional mineral oil-based marine lubricant as well as five readily available EALs were selected and are listed in Table 1. Each lubricant contains a base oil (or a blend) mixed with an additive package. Lubricant 1 is not an EAL. Lubricants 2 and 3 are synthetic esters from the same supplier as Lubricant 1. Lubricants 4 and 5 are PAOs from a second supplier and Lubricant 6 is a synthetic ester obtained from a third supplier.

Table 1. *Set of lubricants tested.*

	Lubricant		Base oil	Viscosity @ 40˚C (mm^2/s)	Viscosity @ 100˚C (mm^2/s)	VI
Lubricant 1	Supplier A	no EAL	Mineral	133	13.5	95
Lubricant 2	Supplier A	EAL	Synthetic Ester	70	13.3	195
Lubricant 3	Supplier A	EAL	Synthetic Ester	103	16.9	178
Lubricant 4	Supplier B	EAL	PAO	68	13.5	205
Lubricant 5	Supplier B	EAL	PAO	100	20.0	225
Lubricant 6	Supplier C	EAL	Synthetic Ester	68	14.0	215

The lubricants tested are used in the stern tube lubrication of big vessels. Typical operation conditions of the lubricant placed between the seals and the shaft liner (Figure 1) are shown in Table 2.

Table 2. *Stern tube seals running conditions.*

Lubricant	Minimum	Maximum
Temperature	20˚C	100˚C
Shear Rate	0 s^{-1}	10^7 s^{-1}
Pressure	cavitation pressure	10 MPa

Under operational conditions, the stern tube lubricant temperature is strongly related to the sea water temperature. The ship shaft acts as a heat pipe releasing most of the heat dissipated in the stern tube bearings and seals. However, the temperature close to the running surface between the seals and liner can exceed 100 °C at the highest shaft angular speeds. A wide range of shear rates can occur depending on the operational conditions in different stern tubes. Consequently, different viscometers were used to cover a wide range of shear rates. The measurements at different temperatures and low shear rates were carried out using a low-shear rate viscometer Brookfield Pro+II (Brookfield, Middleboro, MA, USA) shown in Figure 2a. An Ultra Shear Viscometer (PCS Instruments, London, UK) was used to reach shear rates between 10^6 and 10^7 s^{-1} (Figure 2b). To find out if a permanent loss of viscosity developed in the lubricant, the measurement at 10^6 s^{-1} was repeated after testing a sample at the highest shear rates. The average of five measurements was calculated at each operational condition (temperature and shear rate). The high shear rate viscometer typically achieved a repeatability of 2% of the viscosity value.

The density of each lubricant was measured using a high precision Stabinger viscometer SVM 3000 (Anton Paar, Graz, Austria), which additionally works as a densitometer. The device accurately measures the viscosity at low shear rates, so the measurements obtained with the Brookfield viscometer could be validated.

The Wilhelmy plate method on a DCAT11 tensiometer (DataPhysics, Filderstadt, Germany) was used to measure the surface tension γ_L of the different lubricants (Figure 3). A platinum plate was immersed on the lubricant sample and the necessary load to pull it out was recorded. Once the plate properties and the length of the wetted perimeter of the plate L were known, it was possible to deduce the surface tension of the liquid from that pulling load F, as shown in Equation 1. The lubricants tested showed a good wettability on metal surfaces with contact angles below 10° and hence complete wetting can be assumed ($cos\theta = 1$).

$$F = \gamma_L \, L \, cos(\theta) \tag{1}$$

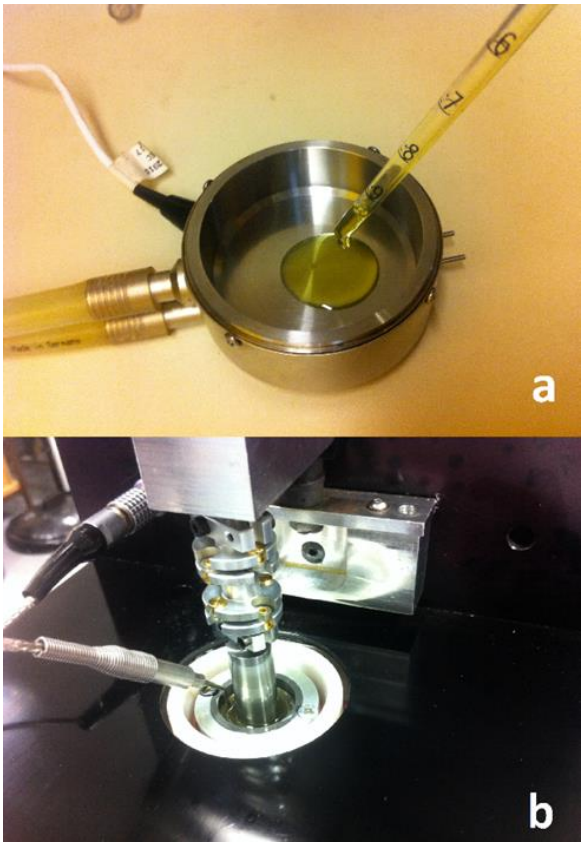

Figure 2. *(**a**) Measurement of the viscosity at low shear rates; (**b**) Measurement of the viscosity at high shear rates.*

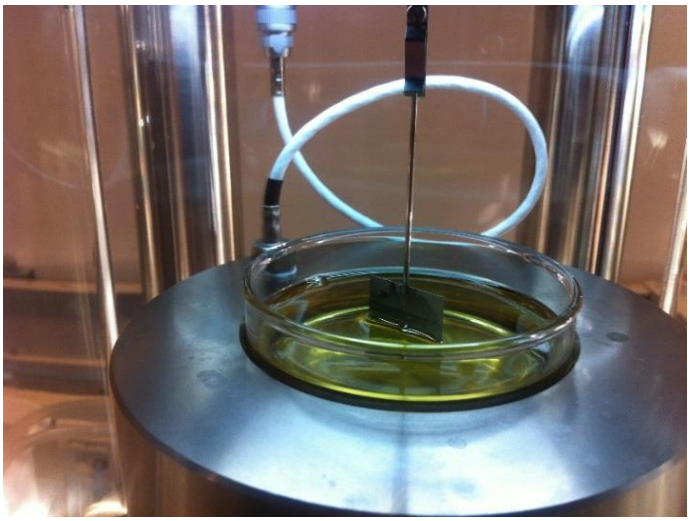

Figure 3. *Measurement of surface tension using the Wilhelmy plate method.*

The test was repeated three times per lubricant and the plate was thoroughly cleaned each time with a fire gun.

All the lubricants were analysed using a Spectrum 100 FT-IR Spectrometer (PerkinElmer, Waltham, MA, USA) with attenuated total reflection (ATR) sampling technique. Although the FT-IR technique does not reveal the specific formulation of each lubricant, the main components of the different lubricants can be identified and compared.

Gel Permeation Chromatography (GPC) was used to measure the molecular weight distribution of the different lubricants. The device used was an Agilent 1200 series (Agilent, Santa Clara, CA, USA) with a refractive index and an ultraviolet (UV) detector at 254 nm with three GPC PLgel 3 µm MIXED-E columns in series. The column was operated at 23 °C with tetrahydrofuran as solvent with a flowrate of 1 mL/min. Polystyrene solutions ranging from 162 to 27,810 Da were used to calibrate the device.

3. Results

3.1. Viscosity

The impact of temperature and shear rate on the viscosity of each lubricant was measured. The viscosity measurements of Lubricant 1 (Figure 4) and Lubricant 5 (Figure 5) show the impact of the shear rate for a Newtonian mineral oil and a non-Newtonian EAL, respectively. The lower shear rate measurements up to 10^2 s^{-1} were obtained with the Brookfield (Figure 2a) and Stabinger viscometers, whereas the high viscosity measurements were taken recorded the Ultra Shear Viscometer (Figure 2b).

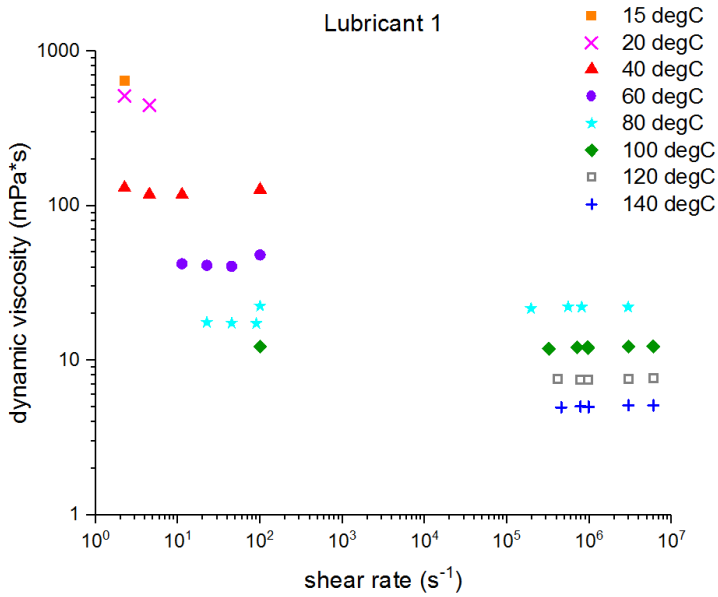

Figure 4. *Viscosity measurements at different temperatures and shear rates for the reference mineral-based oil (Lubricant 1).*

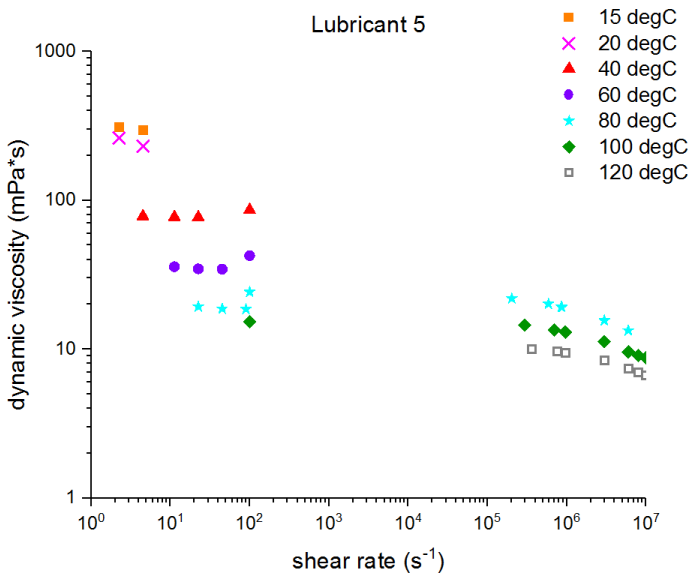

Figure 5. *Viscosity measurements at different temperatures and shear rates for a PAO-based lubricant (Lubricant 5).*

Within the testing temperature range, there was no significant difference between EALs with a similar viscosity grade. The viscosity measurements at low shear rates of the lubricants listed in Table 1 are plotted together in Figure 6. The mineral oil-based lubricant (Lubricant 1) had the highest viscosity of 133 mPa·s at 40 °C and a greater variation with temperature as denoted by its low VI of 95. Lubricants 2, 4, and 6 had viscosities around 68 mPa·s at 40 °C. Lubricants 3 and 5 were the thicker EALs tested and had viscosities close to 100 mPa·s at 40 °C. Both kinds of EALs, synthetic ester- and PAO-based, show a lower change in viscosity with temperature compared to the mineral oil-based lubricant; this was expected due to their higher VI (Table 1).

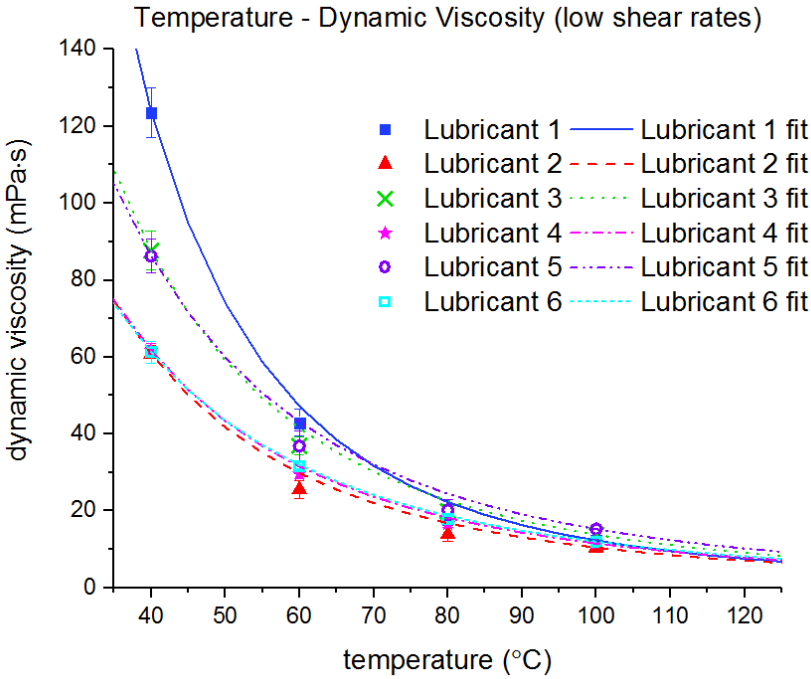

Figure 6. *Comparison of the low shear rates viscosity at different temperatures for lubricants based on mineral oil (Lubricant 1), synthetic esters (Lubricants 2, 3, and 6) and poly-α-olefins (Lubricants 4 and 5) listed in Table 1. Results obtained with Brookfield and Stabinger viscometers.*

Some rheological models were fitted to the measurements obtained so these could be incorporated to more advanced computational models [16]. For Newtonian fluids, the Walther formula [17] with a shift constant $\Psi = 0.7$ is frequently used to relate the kinematic viscosity and temperature for liquid petroleum products [18]:

$$log(log(\nu_T + \Psi)) = A - B\, log(T) \tag{2}$$

ν_T is the kinematic viscosity at a temperature T and the material constants A and B are empirical parameters obtained from fitting the function to measurements (Table 3). The Walther formula, between 40 °C and 100 °C, accurately captured the viscosity variation with temperature for all the lubricants. As expected from its lower viscosity

index (Table 1), the viscosity of the mineral oil was more susceptible to temperature variations than the EALs tested. The dynamic and kinematic viscosities of the lubricants are related by their densities as shown in the next section.

Table 3. *Fitting parameters according to Walther formula (Figure 6).*

	A	B	R^2
Lubricant 1	8.898	3.433	0.98
Lubricant 2	7.447	2.879	0.98
Lubricant 3	7.270	2.794	0.97
Lubricant 4	6.858	2.639	0.99
Lubricant 5	6.608	2.526	0.96
Lubricant 6	6.745	2.597	0.99

At high shear rates, Lubricants 2 and 3 showed a shear rate-independent behaviour, similar to the reference mineral oil, whereas Lubricants 4, 5, and 6 underwent a significant viscosity decrease due to shear thinning (Figure 7). We then deduced that Lubricants 4, 5, and 6 contain VIIs. The rate at which the viscosity decreases with shear rate is related to the specific VIIs used in their formulation. For Lubricant 6, the shear thinning initiated at low shear rates (10^2 s^{-1}), whereas for Lubricants 4 and 5, this developed at higher shear rates (10^5 s^{-1}). Contrary to the steep viscosity drop observed in Lubricants 4 and 5, the viscosity decrease of Lubricant 6 was rather slow, allowing it to carry relatively higher loads at the higher shear rates than the other two shear thinning lubricants.

Different cases of the Generalized Carreau-Yasuda law are commonly used to model the viscosity dependence on shear [19]:

$$\eta_{\dot{\gamma}} = \eta_{\infty} + (\eta_0 - \eta_{\infty})[1 + (\dot{\gamma}\lambda)^a]^{\frac{n-1}{a}} \quad (3)$$

where $\eta_{\dot{\gamma}}$ is the dynamic viscosity at shear rate $\dot{\gamma}$, η_0 is the low shear rate viscosity, η_{∞} is the high shear rate viscosity, n is the power index, λ is the relaxation time (inverse of the critical shear rate $\dot{\gamma}_c$), and a is the index controlling the transition from the Newtonian plateau to power-law region.

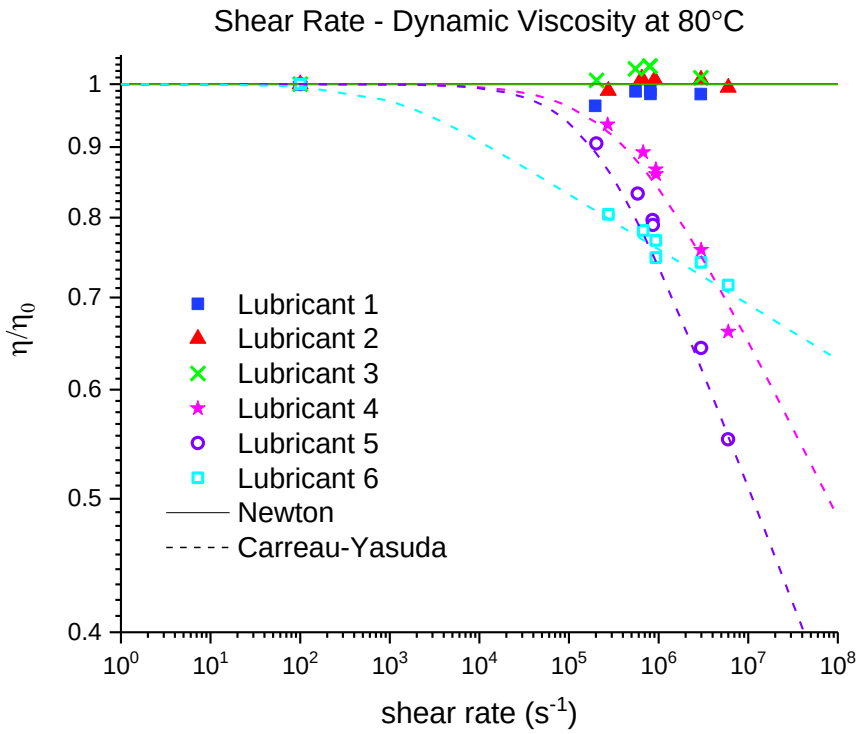

Figure 7. *Normalized viscosity measurements at 80°C and fitting of the Generalized Carreau-Yasuda model.*

For the results at 80 °C, the Generalized Carreau-Yasuda model was fitted and the results are shown in Figure 7. None of the lubricants tested reached the infinite viscosity plateau so this test was been considered null. As can be seen in Table 4, this model showed a high accuracy with correlation coefficient (R2) values close to unity.

Table 4. *Fitting parameters Generalized Carreau-Yasuda model at 80 °C for the lubricants showing shear-thinning. The results are depicted in Figure 7.*

	η_0	η_∞	a	n	$\dot{\gamma}_c = \lambda^{-1}$	R^2
Lubricant 4	18.06	0	0.90	0.87	3.84 x 10^5	0.97
Lubricant 5	24.21	0	1.06	0.83	1.92 x 10^5	0.98
Lubricant 6	18.54	0	1.00	0.96	0.10 x 10^4	0.99

There are different methods to account for both the shear rate and temperature dependencies on viscosity [7]. The simplest method is to multiply a temperature-dependent factor $H(T)$ to the viscosity obtained from a non-Newtonian model $F(\dot{\gamma})$.

$$\eta_{T,\dot{\gamma}} = H(T)F(\dot{\gamma}) \tag{4}$$

However, due to the shift of the shear thinning slope at different temperatures, it was observed that the lubricant viscosity was not accurately captured by simply scaling the results obtained with the models previously presented. Consequently, an Arrhenius-shaped temperature-dependent term $H(T)$ was included to the Generalized Carreau-Yasuda model [20, 21]. The results are shown in Figure 8 and 9, together with extrapolated results for temperatures between 15 °C and 140 °C, which is the typical range of expected operational temperatures.

$$\eta_{T,\dot{\gamma}} = \eta_{T,\infty} + \left(\eta_{T,0} - \eta_{T,\infty}\right)\left[1 + \left(\dot{\gamma}\lambda e^{\frac{T_0}{T}}\right)^{a}\right]^{\frac{n-1}{a}} \tag{5}$$

where $\eta_{T,\dot{\gamma}}$ is the dynamic viscosity at temperature T and shear rate $\dot{\gamma}$, λ is the relaxation time, n is the power-law index and T_0 is the temperature constant in Kelvin. The $\eta_{T,\dot{\gamma}}$ is obtained from combining Eq. 2 and Eq. 6. The fitting parameters for Eq. 5 for the lubricants presenting shear thinning are shown in Table 5.

Table 5. *Fitting parameters of the temperature-dependent Generalized Carreau-Yasuda model for the lubricants showing shear-thinning.*

	$\eta_{T,0}$	$\eta_{T,\infty}$	a	n	$\dot{\gamma}_c = \lambda^{-1}$	T_0	R^2
Lubricant 4	$\eta_{T,0}$	0	0.9	0.70	2.9e11	4200	0.96
Lubricant 5	$\eta_{T,0}$	0	0.8	0.75	2.6e11	4500	0.98
Lubricant 6	$\eta_{T,0}$	0	1.0	0.95	5.0e9	4800	0.92

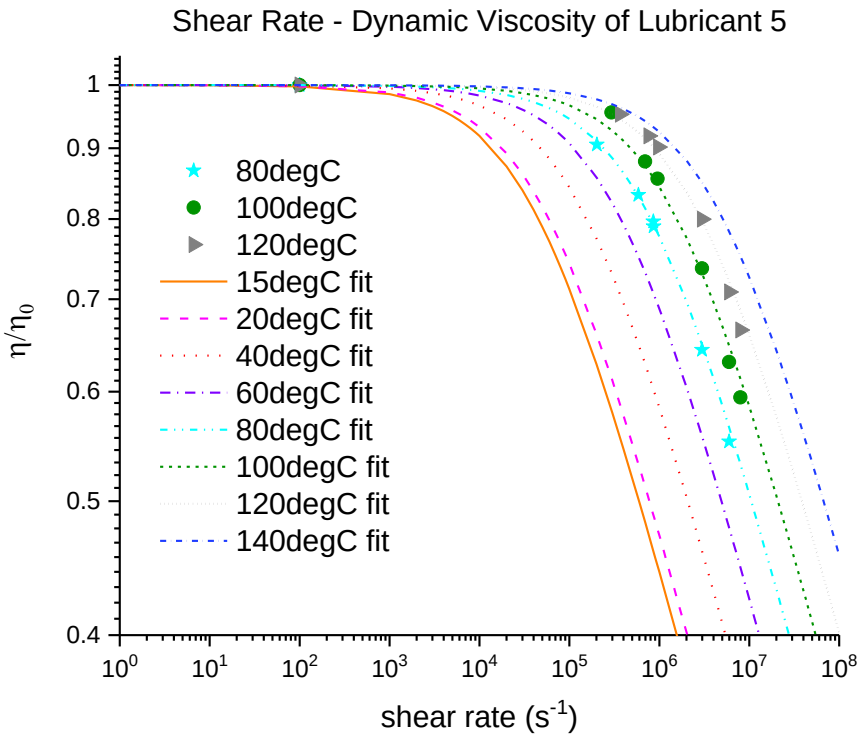

Figure 8. *Normalized viscosity of Lubricant 5 as a function of the shear rate and temperature-dependent Generalized Carreau-Yasuda fit.*

After the high shear rates were applied to a sample, a last final measurement point was performed to account for the potential permanent loss of viscosity due to the high shear rates to which the lubricant was exposed during testing. Notably, a certain part of the oil tested was replaced in every measurement to prevent running under starved conditions. Although the same amount of fresh lubricant was added, the amount of fresh oil entering the shearing zone could not be quantified. The average loss of viscosity per lubricant is shown in Table 6, and was small, except for Lubricant 6. This indicates a potential polymer-cracking by shear of Lubricant 6. Further specialized tests must be carried out in order to confirm this finding.

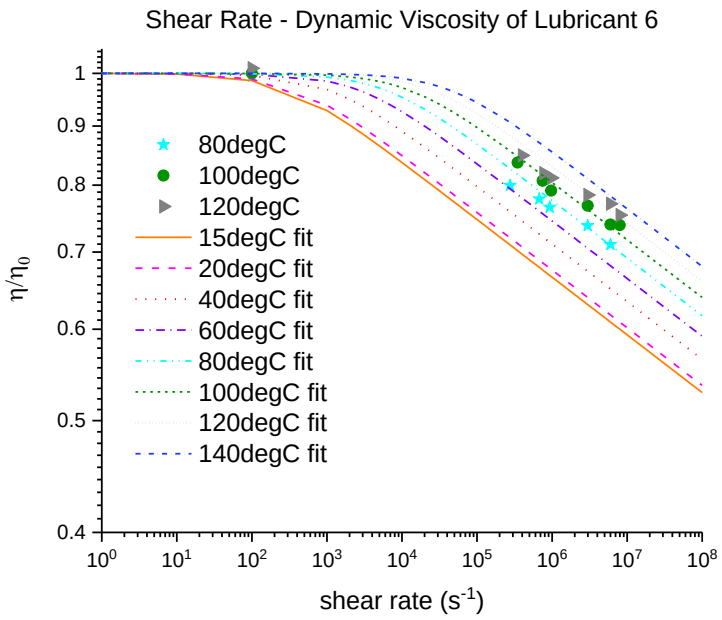

Figure 9. *Normalized viscosity of Lubricant 6 as a function of the shear rate and temperature-dependent Generalized Carreau-Yasuda fit.*

Table 6. *Permanent viscosity loss at low shear rates of the lubricants after being tested at the higher shear rates.*

	Viscosity Change
Lubricant 1	-0.75%
Lubricant 2	0.09%
Lubricant 3	-0.17%
Lubricant 4	-1.02%
Lubricant 5	-0.54%
Lubricant 6	-3.60%

3.2. Density

The density measurement results of the lubricants at different temperatures are presented in Figure 10. The common linear relationship between temperature and density was measured for all the lubricants. We observed that PAO-based EALs have a lower

density whereas the synthetic esters and the mineral oil-based lubricants had similar results (Figure 10).

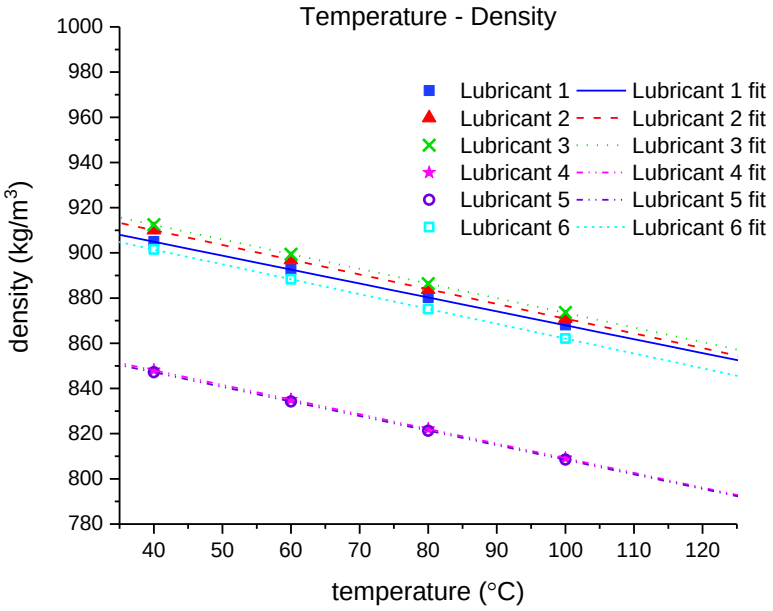

Figure 10. *Comparison of the density at different temperatures.*

Within the operating temperature range, the density varies linearly with temperature [22]. The slopes and the expected density at zero degrees for all the lubricants are shown in Table 7.

$$\rho_T = \rho_{T_0} + k(T - T_0) \tag{6}$$

where ρ_T is the density at temperature T, k is the slope depending on the fluid and ρ_{T_0} is the reference density at temperature T_0.

Table 7. Coefficients from linear fitting density and temperature.

	k	$\rho_{T_0=0°C}$	R^2
Lubricant 1	-0.616	929.56	0.99
Lubricant 2	-0.652	936.09	0.99
Lubricant 3	-0.649	938.37	0.99
Lubricant 4	-0.649	874.02	0.99
Lubricant 5	-0.645	872.95	0.99
Lubricant 6	-0.657	927.74	0.99

3.3. Surface tension

The surface tension γ_L measurements at room temperature obtained with the Wilhelmy plate method were similar for all the liquids, as shown in Figure 11. The nature of the intermolecular forces of the lubricants could not be determined from this data; however, the overall surface tension values measured were relatively low compared to more polar liquids (e.g., water). The induced polarity from the ester groups was not significantly reflected in the overall surface tension.

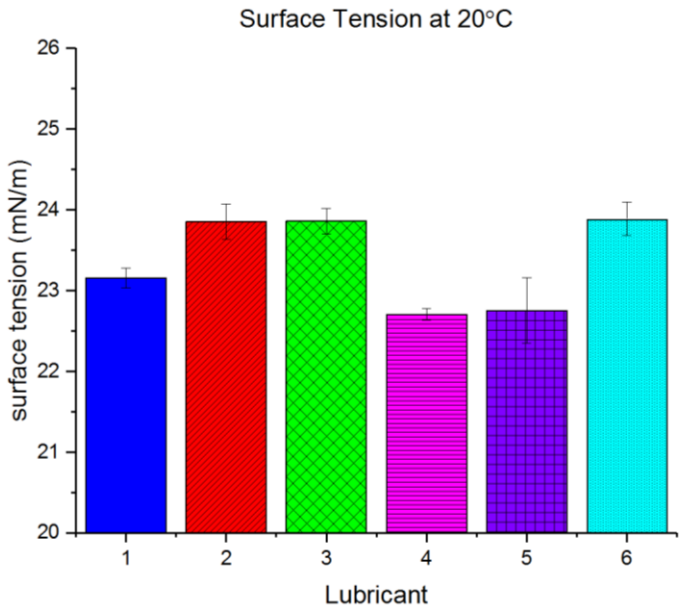

Figure 11. *Comparison of surface tension of the lubricants at room temperature.*

3.4. Fourier-transform infrared spectroscopy (FT-IR)

Figure 12 and Figure 13 show the FT-IR spectra of the synthetic esters-based and PAO-based lubricants measured together with the mineral oil-based one, respectively. The absorbance spectra were normalized to the same value of the 1460 cm^{-1} band. All the lubricants analysed showed the symmetric and asymmetric stretch of methylene at 2842 and 2920 cm^{-1} characteristic of hydrocarbons. The bands related to the ethylene and propylene segments, methylene/methyl

bending and methyl bending bands, at 1464 and 1378 cm^{-1}, respectively [23], appeared for all the lubricants tested. The C–H out of plane bending vibration and the C–H in-plane bending vibration at 726 and 1157 cm^{-1} were also present [13]. The latter is highly pronounced on the carbonyl group containing lubricants. The small peak at band 3005 cm^{-1} for all the ester-containing lubricants probably belongs to the methyl ester. The lubricants lack the absorption bands from the double carbon-to-carbon bonds at 1650 cm^{-1} [13]. At the highest absorption bands, nothing was displayed denoting the lack of aromatic structures, oxygen-hydrogen bonds, and consequently a lack of water content. The carbonyl group absorption bands around the 1740 and 1151 cm^{-1} [13] were present in both the synthetic esters and poly-α-olefin-based lubricants, whereas they were not present in the mineral oil-based one. The presence of these peaks in both Lubricants 4 and 5 suggests that the PAOs were blended with synthetic esters or the use of poly alkyl methacrylate VIIs.

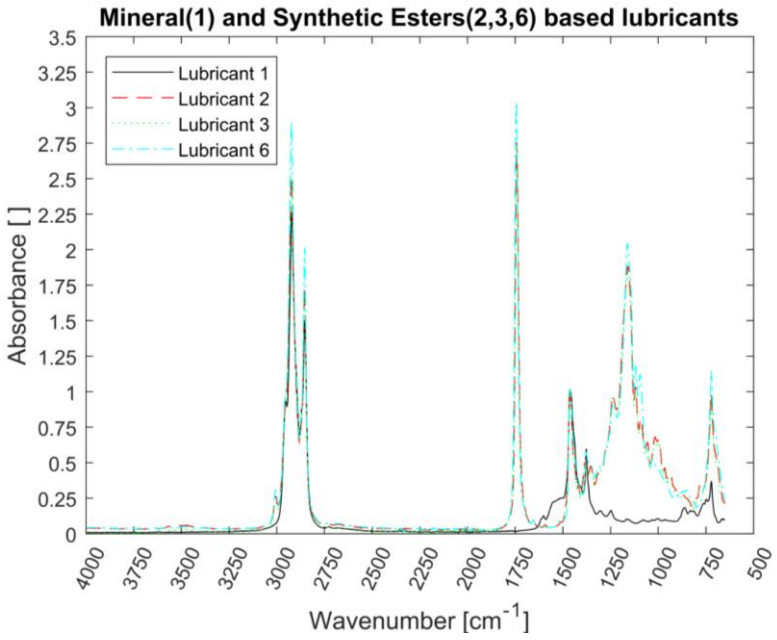

Figure 12. *Comparison of infrared (IR) spectra of synthetic esters-based lubricants (Lubricants 2, 3, and 6) and a mineral oil-based one (Lubricant 1). The spectra is normalized to the value of the 1460 cm^{-1} band.*

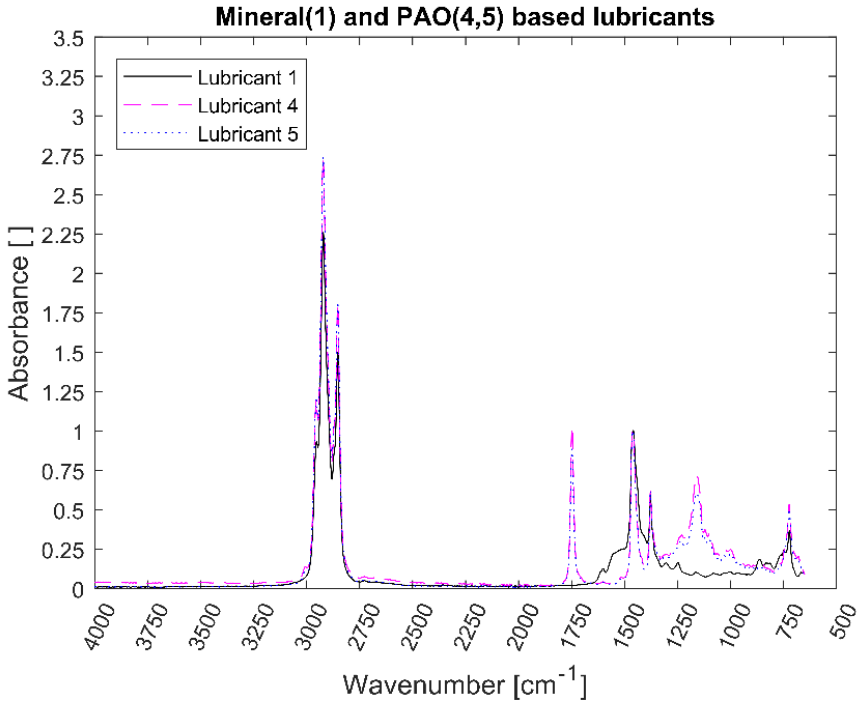

Figure 13. *Comparison of IR spectra of PAO-based lubricants (Lubricant 4 and 5) and a mineral oil-based one (Lubricant 1). The spectra is normalized to the value of the 1460 cm^{-1} band.*

3.5. Gel permeation chromatography (GPC)

UV detector measurements were used to plot the normalized distributions shown below. Only Lubricant 1, the mineral oil-based lubricant, showed a monodisperse broad distribution whereas the rest of synthetic lubricants showed a multimodal distribution (Figure 14 and Figure 15). The different peaks correspond to the different oils blended and the additives. Unfortunately, the polystyrene calibration charts used were not fit for the compounds measured and heavy polymeric chains might be ignored. The results presented below mainly cover the low-weight lubricant compounds.

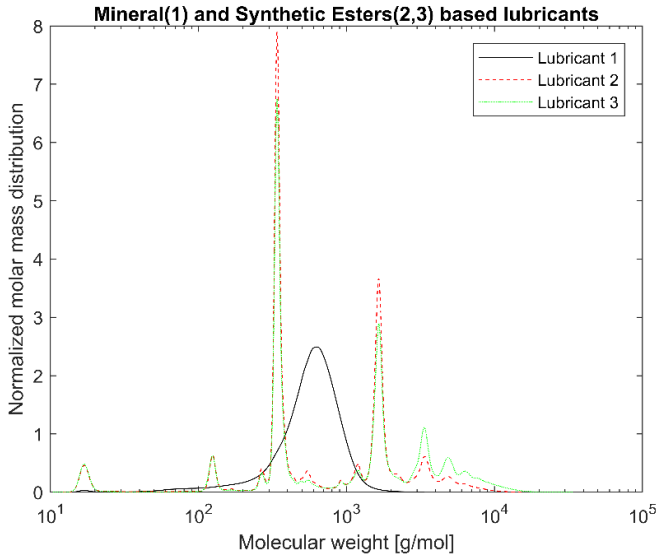

Figure 14. *Comparison of the normalized molar mass distribution of synthetic esters-based lubricants (Lubricant 2 and 3) and a mineral oil-based one (Lubricant 1).*

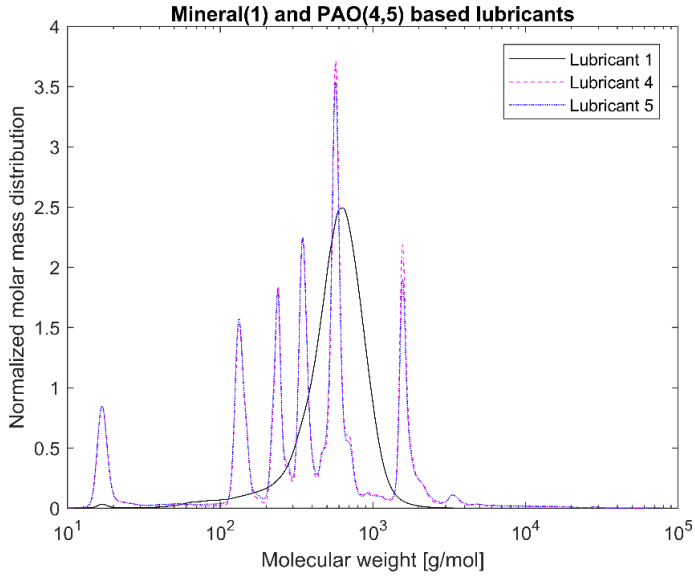

Figure 15. *Comparison of normalized molar mass distribution of PAO-based lubricants (Lubricant 4 and 5) and a mineral oil-based one (Lubricant 1).*

4. Discussion

Three out of five EALs tested showed shear thinning at shear rates above 10^5 s^{-1}. Shear thinning was observed in both synthetic ester as well as poly-α-olefin-based EALs. Whether or not shear thinning occurs in a stern tube depends, to a large extent, on the operational conditions in the stern tube. Assuming stern tube seals operate under their optimal point, i.e., lowest friction and wear rate values, the lubricant film thickness must be around the average roughness of the liner surface. With this educated guess, we deduced that the shear rate operational values of a ship fall within the range where shear thinning was observed.

It has been suggested that the presence of shear thinning is related to the amount and type of viscosity index improvers (VIIs) used within the lubricants formulation [24]. The IR spectra of Lubricants 2, 3, and 6 were similar; however, Lubricant 6 shear thinned at the shear rates tested whereas 2 and 3 did not. The shear thinning curves in Figure 7 show a completely different shear thinning development for the ester- and PAO-based lubricants. The PAO-based lubricants (4 and 5) presented a sudden decrease in viscosity beyond a certain critical shear rate; the viscosity of lubricant 6 started at a lower shear rate and experienced a steady viscosity decrease. The shape of the polymer chains and intermolecular forces determine their ability to stretch and align themselves in the direction of flow causing a decrease in viscosity. Therefore, the different lubricant responses to shear stress shown in Figure 7 are a result of the shape, size, and interactions of the VIIs used in their formulations. A permanent loss in viscosity is attributed to the scission of the larger hydrocarbon chains of the VIIs due to mechanical loading. Lubricant 6 showed a certain polymer-cracking by shear as a result of being tested at 10^7 s^{-1} (Table 6).

The measured surface tension was shown to be within the same range for all the lubricants tested, independent of the nature of the base oil used in its formulation. The polarity of a synthetic ester is determined by the alcohols and carboxylic acids used in their formulation. Pure poly-α-olefins have a surface tension around 20 mN/m [25], which is within the range of the final PAO-based lubricants measured. The use of certain additives, like foam inhibitors, act as surface tension

depressants and could mask the surface tension of the final lubricants [7]. Surface tension depressants are also commonly used to decrease the amount of swelling or shrinkage of elastomers immersed in hydrocarbon fluids [7], which is an undesirable effect in dynamic seals.

FT-IR analysis revealed that all the EALs tested contained ester-based components. Synthetic esters are frequently used in PAO-based formulations as additives carriers due to their more-polar nature [7]. Consequently, the PAO-based EALs tested can be susceptible to hydrolytic degradation due the certain amount of present esters. Lubricants 2 and 3 are synthetic esters-based from the same manufacturer. Although they have different viscosities, they displayed the same IR spectra because the functional groups are the same. The same phenomenon occurred with Lubricants 4 and 5. The GPC allowed us to distinguish the lubricants from the same manufacturer. The blend of base oils became clear for both the synthetic esters- and the PAO-based lubricants. The amount of higher molecular weight components could explain the higher viscosity of Lubricant 3 with respect to Lubricant 2. This was not as evident for the PAO-based lubricants (Lubricants 4 and 5); however, the degree of branching of different oligomers and the affinity with the solvents also plays a role in the overall viscosity. As mentioned, by polystyrene calibration standards, polymeric chains that significantly contribute to the rheology of the lubricant might unfortunately be ignored. In other words, the GPC mainly covered low molecular weight lubricant compounds. No correlation between the molecular weight distribution and the shear thinning could be established because the high molecular weight range that could confirm the presence of VIIs was neglected.

From this research, we concluded that EALs cannot directly be treated as common mineral oil-based lubricants. Although EALs perform fairly similarly with temperature as the traditional stern tube mineral oils, at high shear rates, a viscosity drop is observed for certain EALs (i.e., shear thinning). Under the same high shear running conditions, the thickness of the film between the seals and the shaft liner will be reduced when using certain EALs. By running at lower viscosities, an increase in temperature can occur if the mixed-lubrication regime is entered. Although shear thinning is not a negative characteristic per

se, if the viscosity drops below a certain value, higher wear rates, temperatures, and friction loads are expected, which would consequently shorten the lifespan of the stern tube seals.

Rheological models were fitted to the measurements and accurately predicted the density, viscosity and surface tension of these lubricants for conditions as they occur in stern tube seals. Therefore, it is now possible to predict the impact of EALs in more complex mechanical models.

5. Conclusions

A set of readily available Environmentally Acceptable Lubricants (EAL) were compared under stern tube seals operational conditions. All EALs presented surface tension values between 22 and 24 mN/m. EALs and traditional mineral oil-based lubricants performed similarly within the stern tube temperature range from 20 °C to 100 °C. However, under shear rates of 10^6 s^{-1}, a distinctive viscosity decrease up to 40% of its initial viscosity value was observed in some EALs.

The decrease was measured in both synthetic ester- and poly-α-olefin based lubricants. The steep decrease in viscosity at shear rates of 10^5 s^{-1} of Lubricants 4 and 5 was significantly different to the earlier (10^2 s^{-1}) steady viscosity decrease observed in Lubricant 6. The specific type of VIIs used in the formulation of the lubricants might explain the different shear thinning developments. We concluded that the operational shear rate value of the ship, by means of fluid film thickness and shaft velocity, must be considered when selecting its stern tube lubricant.

Acknowledgments: Nigel Marx and Marc Masen from the Imperial College of London to grant access to their facilities to carry out some of the tests. Robbie Venderbosch from the Biomass Technology Group for his guidance on organic chemistry. Ruiz Ramiro and Smink from the SPT research group for their contribution with the GPC. De Beer for her advice in polymer physics.

References

[1] I. Madanhire and C. Mbohwa, "Mitigating environmental impact of petroleum lubricants," *Mitigating Environ. Impact Pet. Lubr.*, no. Freedonia 2013, pp. 1–239, 2016.

[2] D.S. Etkin, "Worldwide analysis of in-port vessel operational lubricant discharges and leakages," Cortlandt Manor, NY 10567-1160 USA, 2008.

[3] United States Environmental Protection Agency, "Environmentally Acceptable Lubricants," Washington, 2011.

[4] A. Jarabo, "Choosing optimum lubricant solutions for your operation," *Fathom Focus*, 2014.

[5] European Commission, "European Union Ecolabel application pack for lubricants," Den Haag, The Netherlands, 2014.

[6] J.V. Sherman, "Water soluble, environmentally acceptable lubricants for stern tube applications," in *Society of Naval Architects and Marine Engineers (SNAME) 14th Propeller and Shafting Symposium*, 2015, pp. 1–10.

[7] G. Totten, S. Westbrook, and R. Shah, *Fuels and lubricants handbook: technology, properties, performance, and testing*. 2003.

[8] L.A. Quinchia, M.A. Delgado, T. Reddyhoff, C. Gallegos, and H.A. Spikes, "Tribological studies of potential vegetable oil-based lubricants containing environmentally friendly viscosity modifiers," *Tribiology Int.*, vol. 69, pp. 110–117, 2014.

[9] R.F. Salant and A.H. Rocke, "Hydrodynamic Analysis of the Flow in a Rotary Lip Seal Using Flow Factors," *J. Tribol.*, vol. 126, no. 1, p. 156, 2004.

[10] A. Maoui, M. Hajjam, and D. Bonneau, "Analysis of three-dimensional non-axisymmetric elastic effects of the lip on the thermoelastohydrodynamic radia lip seal behaviour," *Proc. Inst. Mech. Eng. Part J J. Eng. Tribol.*, vol. 221, no. 8, pp. 859–868, 2007.

[11] R.F. Salant, "Theory of lubrication of elastomeric rotary shaft seals," *Proc. Inst. Mech. Eng. Part J J. Eng. Tribol.*, vol. 213, no. 3, pp. 189–201, 1999.

[12] J. Carrell, R. Lewis, and T. Slatter, "The Interaction of Bio-lubricants with Elastomers , Tested Through Hanson Solubility Parameter and Stress Relaxation Tests," in *The 17th Nordic Symposium on Tribology*, 2016, pp. 1–10.

[13] J. Coates, "Interpretation of Infrared Spectra, A Practical Approach," *Encycl. Anal. Chem.*, pp. 1–23, 2006.

[14] R. Flitney, *Seals and Sealing Handbook*, vol. 52. 2014.

[15] W. Leszek and W.J. Leszek, "The influence of lubricant polarity on the boundary lubrication of sliding steel contacts," *Wear*, vol. 73, pp. 87–93, 1981.

[16] M. Vingaard, B. Endelt, and J. Christiansen, "Implementation of a material model with shear rate and temperature dependent viscosity," *Proc. 6th Eur. LS-DYNA*, pp. 213–222, 2007.

[17] C.J. Seeton, "Viscosity-temperature correlation for liquids," *Tribol. Lett.*, vol. 22, no. 1, pp. 67–78, 2006.

[18] The American Society for Testing and Materials, "Petroleum Products and Lubricants (I)," in *Annual Book of ASTM Standards*, no. Part 23, 1981.

[19] P. Kennedy and R. Zheng, *Flow Analysis of Injection Molds*, 2nd Editio. Carl Hanser Verlag, 2013.

[20] E.R.G. Eckert and J. N. Shadid, "Viscous heating of a cylinder with finite length by a high viscosity fluid in steady longitudinal flow -II. Non-Newtonian Carreau model fluids," *Int. J. Heat Mass Transf.*, vol. 35, no. 10, pp. 2739–2749, 1992.

[21] "Viscosity for Non-Newtonian Fluids," in *Fluent 6.1. User's Guide*, Fluent Inc., 2003, pp. 7–24.

[22] P.L. Wong, R. Wang, and S. Lingard, "Pressure and temperature dependence of the density of liquid lubricants," *Wear*, vol. 201,

no. 1–2, pp. 58–63, 1996.

[23] E. Torres, “Molecularly designed Viscosity Index Improvers for lubricants,” University of South Australia, 2003.

[24] T.J. Zolper, Y. He, M. Delferro, P. Shiller, G. Doll, B. LotfizadehDehkordi, N. Ren, F. Lockwood, T.J. Marks, Y.W. Chung, A. Greco, A. Erdemir, and Q. Wang, “Investigation of Shear-Thinning Behavior on Film Thickness and Friction Coefficient of Polyalphaolefin Base Fluids With Varying Olefin Copolymer Content,” *J. Tribol.*, vol. 139, no. 2, 2016.

[25] M. Fiedler, R. Sánchez, C. Valencia, C. Leopold, E. Kuhn, and J. Franco, “Influence of Base Oil Polarity on the Transient Shear Flow of Biodegradable Lubricating Greases,” *Lubricants*, vol. 3, pp. 611–627, 2015.

Paper B

(This page is intentionally left blank)

Stern tube seals under static condition: A multi-scale contact modelling approach

F.X. Borras[1], M. Bazrafshan[1], M.B. de Rooij[1] and D.J. Schipper[1]

[1]University of Twente, Surface Technology and Tribology, Enschede, The Netherlands

(This page is intentionally left blank)

Abstract: A thermomechanical model of a stern tube seal has been developed, paying particular attention to the contact between the seal and the shaft. The finite element method was used to capture the macroscopic behaviour of the seal while roughness was evaluated at a microscopic level by applying the boundary element method. The seal material was independently characterized and the results were used to calibrate the material constitutive model used for the seal. Two specialized setups were built to validate the model in terms of radial force, contact width and percolation threshold. By combining the two models, the strains, stresses, temperature, and limits of static tightness can be predicted with high accuracy for a wide range of operating conditions.

Keywords: Lip seal, sealing, stern tube, modelling.

Nomenclature

S	Spring stiffness	$[N/mm]$
P_I	Pretension of the spring	$[N]$
P_c	Spring circumferential load	$[N]$
P_r	Spring radial load	$[N/mm]$
D_{ri}	Inner diameter of the garter spring before assembled	$[mm]$
D_s	Shaft diameter	$[mm]$
F_m	Load exerted by the stepper motor	$[N]$
F_r	Radial inwards force per unit length $F_r = F_{r_{tot}}/(\pi D_s)$	$[N/mm]$
μ_s	Coefficient of static friction between seal and liner	$[-]$
ϵ	Engineering strain $\epsilon = (L - L_0)/L_0$	$[-]$
λ_i	Principal stretches $\lambda = 1 + \epsilon$	$[-]$
ψ	Elastic strain energy density	$[(N \cdot m)/m^3]$
σ	Cauchy stress (nominal stress)	$[MPa]$
I_1^*	Distortional part of the first invariant of the right Cauchy-Green tensor	$[-]$
$\mathbf{b}^*$	Distortional part of left Cauchy-Green tensor	$[-]$
J	Jacobian: determinant of the deformation gradient	$[-]$

C_{i0}	Yeoh hyper-elastic model parameters	$[MPa]$
κ	Bulk modulus of the seal material	$[MPa]$
T_g	Glass transition temperature	$[K]$
E	Young modulus	$[MPa]$
ν	Poisson ratio	$[-]$
C_p	Specific heat capacity	$[J/(kg \cdot K)]$
ρ	Density	$[kg/m^3]$
k	Thermal conductivity	$[W/(m \cdot K)]$
α	Thermal expansion coefficient	$[1/K]$
u_e	Elastic deformation from Boussinesq solution	$[\mu m]$
p	Contact pressure from Boussinesq solution	$[MPa]$
E'	Storage modulus	$[MPa]$
E''	Loss modulus	$[MPa]$
E^*	Complex elasticity modulus	$[MPa]$
δ	Phase lag between stress and strain	[°]
x, y, x', y'	Coordinates of the surface in Boundary Elements model	$[mm]$
r, z, ϕ	Radial, axial and circumferential cylindrical coordinates	$[mm, mm, rad]$
α	Spring-side lip seal angle (scraper angle)	[°]
β	Back-side lip seal angle (barrel angle)	[°]
ω	Shaft angular velocity	$[rad/s]$
L_c	Contact width (axial direction)	$[mm]$
S_a	Average surface roughness	$[\mu m]$
S_q	Root Mean Square (RMS) of the surface roughness	$[\mu m]$
S_p	Height of the tallest surface roughness peak	$[\mu m]$
S_v	Height of the deepest surface roughness valley	$[\mu m]$
S_{z_5}	Average maximum surface height difference	$[\mu m]$
S_k	Skewness of the surface roughness	$[-]$
K_s	Kurtosis of the surface roughness	$[-]$

1. Introduction

The effective sealing of the stern tube has always been a challenge for marine engineers. The lubricant filling the stern tube needs to stay in the stern tube. The most common method is to fit a series of rubber rings between the rotating shaft and the stern tube as shown in Figure 1. These components prevent the ingress of seawater into the stern tube while, at the same time, limiting the spillage of the lubricant from the stern tube into either the sea or the engine chamber. Two sets of stern tube seals are positioned at each end of the stern tube: the aft package (oil-seawater interface) and the forward package (oil-air interface). Separate lubricant tanks feed the compartments left between the various seals, allowing control of the hydrostatic oil pressure acting on each sealing step [1]. The pressure difference between seals is specific to the seal-specific position and the ship design.

Stern tube seals are usually made of highly inert elastomers that are capable of withstanding elevated temperatures, lubricants and seawater. Specially tailored FKM compounds are the common choice for such seals, with the fluorine content defining their inertness and mechanical properties [2]. Additional compounds are used in the final formulation to ease its processing, stiffness, chemical compatibility and to improve the tribological characteristics. Stern tube seals often include a fabric reinforcement to stiffen the elastomeric component.

Stern tube seals are one of the largest types of lip seals. These components are widely used in static, rotary and reciprocating sealing applications. Rotary lip seals are designed so that a sharp tip at the edge of the lip acts as a physical barrier to prevent leakage through the seals. Stern tube seals are mounted on the a metallic shaft sleeve bolted to the shaft, and are often referred as shaft liners (see Figure 1).

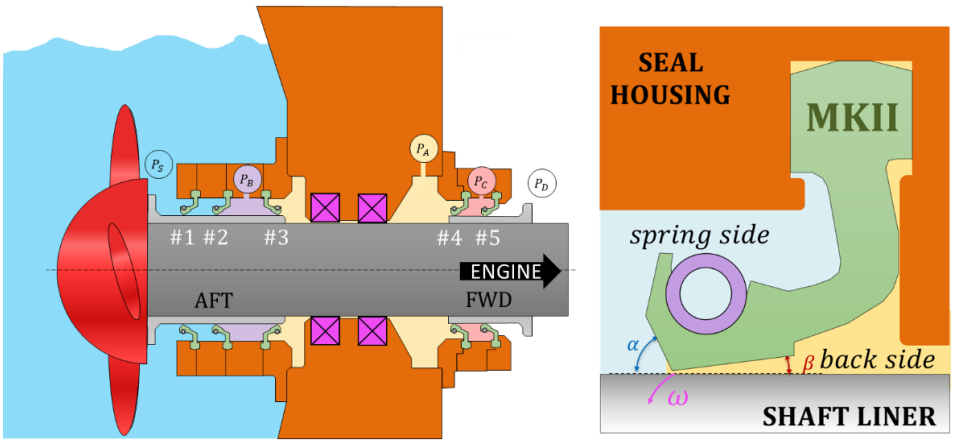

Figure 1. *Sketch of a stern tube of a ship (left) and seal detail (right).*

Rotary lip seals have been used for almost a century and extensive research has been carried out on the underlying technology. Surprisingly, their working mechanism is not yet fully understood [3]. Various working principles have been identified by Jagger [4], Horve [5], van Bavel [6], Salant [7], Stakenborg [8] and Wennehorst [3] among others. However, there is not a generally accepted theory that can accurately predict the performance of rotary lip seals. The authors consider it probable that several mechanisms develop simultaneously and, depending on the application and running conditions, one or another mechanism becomes dominant. Notice that the static and the dynamic sealing mechanisms are completely different [4]. Their large size and the severe running conditions under which they operate make stern tube seals a particularly challenging type of rotary seal in terms of manufacturing, consistency and laboratory testing.

This paper focuses on a key variable that largely determines the lubrication regime of lip seals and the prevention of leakage when the shaft at rest: the contact force between seal and shaft liner. Lip seals generally work under compression in the radial and axial directions while elongated in the circumferential direction. The resultant radial load determines the minimum load-carrying capacity that the thin film of lubricant running between the liner and the seal needs to operate within the wear-less full-film lubrication regime. Consequently, the sealing load determines the frictional torque, the leakage, the wear

rate, the power consumption and the lifespan of a stern tube seal [1], [9]. The static contact pressure profile, and hence the total contact force, depends on the following five aspects: seal geometry, seal material properties, Garter spring, pressure difference and temperature. Each is discussed below.

The seal-shaft contact force is a radially uniformly distributed load along a circumference of several hundreds of centimetres and hence it is not straight forward to measure. A specific method is repeatedly reported in the literature: the split-shaft setup [8], [10], [11]. Such test rig consists of a two semi-cylindrical jaws arrangement. One of the jaws is fixed to the bench table while the other semi-circular jaw seats on leaf springs and it is able to slide along a rail. When the two jaws are set apart a specific distance, they form an almost-complete cylinder representing the shaft. When the a seal is mounted on the jaws, a certain load results that pushes the jaws together (see Figure 4). This unidirectional load is measured and is related to the distributed radial load between the seal and the shaft. The split-shaft setup can be placed in a temperature-controlled chamber so that both the impact of the thermal expansion of the components and the softening or hardening of the elastomer are measured [12]. Chung-Ying presented an alternative method to measure the contact force, based on the use of an inflatable mandrel [13]. That approach has the advantage of allowing the diameter of the shaft to be varied. A non-destructive approach was presented by Tasora [14] in which the seal could be directly characterized by measuring its response to the misalignment of the shaft.

The contact area between the seal and the shaft is often measured by mounting the seal on a hollow shaft made of a transparent material [8], [12]. Under ambient conditions, the contact pressure profile spans only along a few tenths of millimetres, thus complicating the measurement of local pressures. Chun-Ying used a pressure-sensitive foil to determine the pressure profile at the contact [13]. One indirect way to reveal the contact distribution involves measuring the displacement of the seal tip in the circumferential direction after a slight rotation of the shaft. Although inaccurate due to the unknown friction coefficient, a non-uniform displacement that is in agreement

with the expected parabolic pressure profile has often been reported [6], [8].

Finite Element (FE) models are used to predict the contact pressure profile of seals. It is often assumed [11] that the pressure profile does not vary along the circumferential direction so the seals are modelled assuming axisymmetry. A non-uniform pressure, non-uniform temperature distribution and shaft-seal misalignment are therefore disregarded. The elastomer is often modelled by linear elastic [15] or hyperelastic constitutive models such as the Neo-Hookean [3] or the Mooney-Rivlin [8], [14], [16]. The Garter spring is usually modelled as a distributed radial load [17], as an independent body with a fitted stiffness [14] or using a concentrated spring load [8], [13]. Wenk presented a multi-scale FE model that included the surface roughness [18] that until then had been disregarded.

Although much research has been conducted on lip seals, most of the research focuses on smaller non-pressurized seals and its applicability to stern tube seals has not yet been demonstrated. This investigation contributes to the scarce literature on large-sized elastomeric seals operating under pressurized conditions. Additionally, seal models usually restrict the displacement of the outer boundaries of the seal [13], [17], [19]. While this is beneficial to the convergence of the model, it is inaccurate for seals which are clamped to housing parts, e.g. stern tube seals and O-rings. The lack of published research on this application led to a step-by-step approach of reviewing the common assumptions applied when modelling sealing components. Such an approach outlines the specific contribution of each of the components of the system which presents a significant advantage when tuning the seal design. Three different validation methods are presented to corroborate the fidelity of the stern tube seal model developed. Dedicated test rigs were developed so the seals were validated under actual pressurized conditions which is, to the best of the authors knowledge, not been reported in the literature. The novel coupling between the macroscale and microscale allowed satisfactory prediction of the sealing limit of the components, i.e. the pressure difference at which a seal starts to leak. This research aims to determine the contact pressure and area of stern tube seals, thereby creating a solid base on which to build more advanced models.

2. Materials and Methods

The model presented requires the characterization of the elastomeric compound, the Garter spring and the surface topography of the contact. Further experiments were later carried out to validate the model against the joint performance of the various parts of the stern tube seal. Table 1 summarizes the tests conducted and the computational models developed.

Table 1. *Summary of the tests and computational models developed.*

Characterization	Computational models	Validation
Elastomer	Yeoh hyperelastic material	Contact area
Garter spring	Axisymmetric FE model	Percolation threshold
Surface roughness	Contact BE model	Radial force

An axisymmetric Finite Elements (FE) model was developed to capture the macroscopic behaviour of the seal. Next, the FE model was coupled to a Boundary Elements (BE) surface contact model to link the macroscale and microscale. That model is able to reliably predict the radial force, static strains, stresses and sealing limits over a wide range of pressures. Figure 2 shows the general structure of the model developed. The results were validated under an operating pressure range that is typical for a stern tube seal, i.e. up to 1.5 bar pressure difference.

2.1. Material characterization

Although the properties of the shaft liner and housing parts were obtained from datasheets, those of both the seal and the Garter spring were mechanically characterized. The results will be used as input parameters to the multiscale contact model.

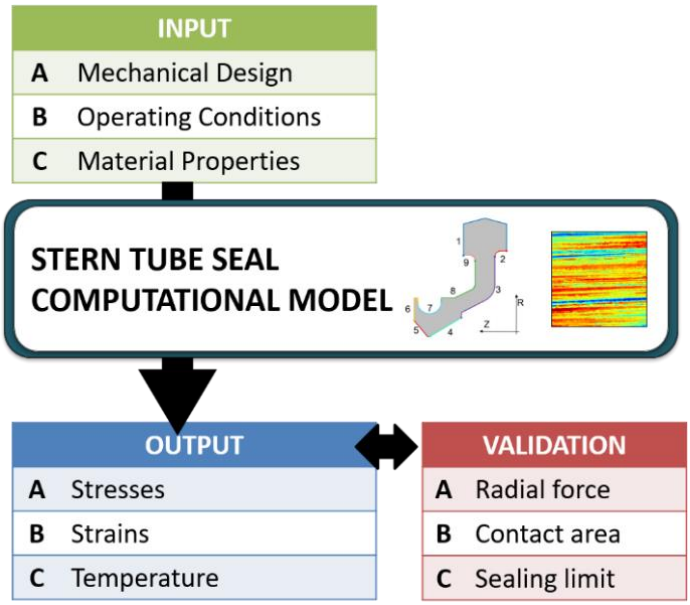

Figure 2. *Schematic of the thermomechanical multi-scale static stern tube seal computational model.*

Stern tube seals are commonly made of fluoroelastomer compounds often of the Viton® brand. The high fluorine content allows for elevated running temperatures while providing exceptional inertness against the mineral oils used in the stern tube seals [20]. Fluoroelastomers are a mixture of several monomers tailored for a particular application and they are generally cured by bisphenol. However, for the highest fluorine contents (as those studied in this research), cure-site-monomers are added to the formulation so peroxides are used for its vulcanization [2]. The diverse compositions of such elastomeric compounds requires independent characterization of each formulation.

It is common to test the seal material using samples cut directly from the final component. In this way there should be no difference between the curing states of the definitive parts and of the testing slabs. Unfortunately, this method showed a significant spread of results which was attributed to dimensional inaccuracies and the presence of micro-cracks generated when extracting the samples from the finished parts. Therefore, independently cured material slabs were used. Elastomers are viscoelastic materials characterized by mechanical

properties that vary over time when strained or loaded, leading to stress relaxation and creep. Furthermore, elastomers present a different response when tested under tension, compression or shear strains. Due to the Mullins effect, the initial stretches are unique events and, after a few loading cycles, the material response stabilizes to a repeatable stress-strain curve [21]. As a result, the maximum strain ever reached by the specimen determines the response of the elastomer. In addition to a certain strain rate dependency, the material behaviour when loading is usually different to the response when unloading, i.e. elastomers usually exhibit hysteresis. Temperature also influences the fluoroelastomer, leading to possible hardening or softening of the material [22] and, together with the excitation frequency [21], determining the viscoelastic characteristics of the material.

The fluoroelastomer compound used for moulding the seals was characterized under a set of loading modes, strain rates and temperatures to calibrate the constitutive material model. Tensile tests (Zwick Roell, Ulm, Germany), namely uniaxial extension, were carried out to examine the most relevant elastomer properties for the application: components orientation, strain rate dependence or relaxation. Stern tube seals operate for long periods of time; therefore, the stress-strain combinations of interest are the ones obtained after most of the stress relaxation is undergone. Evidence of varying stress relaxation behaviours under tension and compression has previously been reported for fluoroelastomers [23]. The viscoelasticity of the elastomer was studied following the procedure described by Dalrymple [24].

The sea temperature governs the stern tube lubricant temperature and consequently the seal temperature. However, due to friction heating, significantly higher temperatures develop on the tip of the seal [1]. The temperature-dependent viscoelasticity and the high thermal expansion of elastomers also need to be accounted for. The effects of bolt temperature (and viscoelasticity) on the mechanical properties between -80 °C and 120 °C was obtained by performing dynamic mechanical analysis using a DMA Gabo Eplexor 2000N (Netzsch, Selb, Germany).

2.2. Two-scale model of the seal-shaft contact

The COMSOL Multiphysics® commercial Finite Elements package was used to develop the thermo-mechanical model of the stern tube seal. The model is axisymmetric so perfect alignment, concentricity and roundness of the seal, shaft and housing components is assumed. The initial geometry of the seal was provided by a seal supplier and is shown in Figure 3. After moulding the seals, the remaining burr on the tip edge is manually removed. The curvature after this step was measured using a confocal microscope and it is included in the initial geometry of the model.

Boundary designation	Location
1	A-B
2	B-C
3	C-D
4	D-E
5	E-F
6	F-G
7	G-H
8	H-I
9	I-A

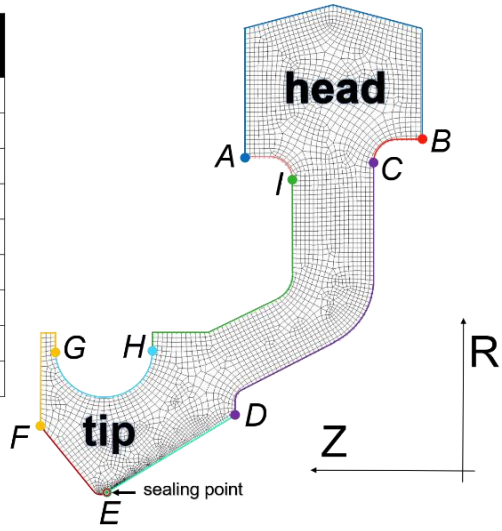

Figure 3. *Mesh of the selected stern tube seal model with boundaries.*

Both housing parts, the liner and the seal are each modelled as independent bodies. The seal head of stern tube seals is tightly clamped between the housing parts leading to a stressed situation. As a result, the seal head is not fixed but a certain displacement is allowed as listed in Table 2. The grooves clamping the seal head were removed after observing that they did not significantly impact the contact force between seal and liner once the thickness of the seal head was decreased.

The Garter spring is implemented on the model as an inwards radial boundary load acting on the seal circular groove. The magnitude can be deduced from the spring elongation and the spring characteristics (Eq. *8*) or from the radial force measurements obtained from the split-shaft setup.

The pressure on each side of the seal is modelled as a true follower load by varying the nodal forces according to the deformed configuration. The sealing point is assumed to be located at the tip of the seal which is where the highest local contact pressure develops. Consequently, the pressures on each side of the seal are applied to the whole seal surface up to the tip of the seal.

Table 2. *Boundary conditions for solving the virtual work equation (see Figure 3).*

Position	Boundary number	Boundary condition
Seal head and back-up wall	1, 2, 3, 9	Contact model (Penalty Term)
Seal tip	4, 5	Contact model (Augmented Lagrangian) Coulomb friction
Spring groove	7	Spring radial load
Spring-side of the seal	5, 6, 7, 8, 9	Pressure load
Back-side of the seal	2, 3, 4	Pressure load

The Coulomb friction model was defined between the seal and the liner with a constant coefficient of friction μ_s. Under normal operating conditions, namely fully lubricated and rotating, the resultant tangential load in the axial direction is expected to be minor. Note that the circumferential friction force (out-of-plane) is neglected in axisymmetric models.

The Yeoh hyper-elastic model (Eq. *1* to *3*) was selected for its ability to capture the fluoroelastomer stress-strain response together with its simplicity [25], i.e. the strain energy density only depends on the

distortional part of the first invariant I_1^* of the right Cauchy-Green tensor. A mixed formulation was used to prevent volumetric locking of the mesh. The mixed formulation, also referred as u-P formulation, consists in introducing the mean pressure as an extra degree of freedom avoiding in this way numerical problems and overly stiff models. The relaxed stress-strain curves together with the split-shaft measurements were used to calibrate the model.

$$\psi(I_1^*) = \sum_{i=1}^{3} C_{i0}(I_1^* - 3)^i + \frac{\kappa}{2}(\mathrm{J} - 1)^2 \tag{1}$$

$$I_1^* = \mathrm{J}^{\frac{3}{2}}(\lambda_1^2 + \lambda_2^2 + \lambda_3^2) \tag{2}$$

$$\sigma = \frac{2}{\mathrm{J}}[C_{10} + 2C_{20}(I_1^* - 3) + 3C_{30}(I_1^* - 3)^2]\mathrm{dev}[\mathbf{b}^*] + \kappa(\mathrm{J} - 1)\mathbf{I} \tag{3}$$

The heat equation was also solved together with the virtual work equation. Regardless of whether the material characteristics are considered temperature-dependent or not, the thermal expansion of the parts still occurs, necessitating a double direction coupling between the virtual work and heat balance equations.

Table 3. *Boundary conditions for solving the energy balance equation.*

Position	Boundary number	Boundary condition
Seal head and back-up wall	1, 2, 3, 9	Temperature
Seal tip	4, 5	Thermal contact: continuity
Spring-side of the seal	5, 6, 7, 8, 9	Convection
Back-side of the seal	2, 3, 4	Convection

The heat convection between the seal and the fluid was modelled using a set oil bath temperature and a constant convective heat transfer coefficient [8], [17]. When the system is static, no frictional heating develops; therefore the temperature of the parts and fluids together with material properties determine the temperature gradient along

the stern tube seal (Table 3). The continuity boundary condition was used to model the heat transferred between seal and liner.

The model described is clearly geometrically nonlinear. Although the magnitude of the strains is not significant, Green-Lagrange strains were used to account for the rotation of the seal body. COMSOL Multiphysics® solves the virtual work and energy equations (fully-coupled) using the Total Lagrangian approach.

Table 4. *Material properties used for the stern tube seal hardware (for linear elastic seal material).*

		Stern tube seal	**Shaft liner**	**Seal housing**
$\boldsymbol{E}$	$[MPa]$	14.0	200×10^{3}	106.5×10^{3}
$\boldsymbol{\nu}$	$[-]$	0.49	0.27	0.35
$\boldsymbol{\rho}$	$[kg/m^3]$	1900	7700	8800
$\boldsymbol{C_p}$	$[J/(kg \cdot K)]$	1670	1909.7	376
$\boldsymbol{k}$	$[W/(m \cdot K)]$	0.25	25	60
$\boldsymbol{\alpha}$	$[1/K]$	275×10^{-6}	10^{-6}	18.5×10^{-6}

Once the macroscopic FE model is validated against the radial force and contact width measurements, it is possible to reliably estimate the specific loading of the real contact area. For this reason the loading of the seal surface topography was modelled using a Boundary Element-based (BE) contact model assuming a semi-infinite half-space and homogeneous mechanical properties [26]. For that the surface patch is assumed to repeat itself along the circumferential direction of the contact, i.e. cell periodicity. The contact model uses the Conjugate Gradient Method (CGM) to estimate the local deformation and the pressure distribution resulting from the loading situation. The seal material stress was shown to be fairly linear to strains up to 0.5 (see Figure 6). For that and for simplicity, the seal asperities were assumed to be linearly elastic using the properties listed in Table 4. The soft seal material conforms to the shaft surface increasing the real contact area, adhesion is nevertheless assumed negligible due to surface contamination effects. Thereby the Boussinesq solution for elastic

deformation was used (see Eq. *4*). A smooth glass surface was considered so the initial gap was exclusively defined by the surface topography of the seal.

$$u_e(x,y) = \frac{1-\nu^2}{\pi E}\int_{-\infty}^{+\infty}\int_{-\infty}^{+\infty}\frac{p(x',y')}{\sqrt{(x-x')^2+(y-y')^2}}dx'dy' \qquad (4)$$

The model allowed variation of the total contact force so allowing the minimum load required for sealing the contact to be found. A conservative approach was adopted by assuming zero flow only when contact was detected, i.e. regardless of the characteristics of sealed fluids. A pair of surfaces were considered to be gas tight when no leakage path (in the axial direction) spanned from side-to-side of the contact when loaded (see Figure 19). The minimum pressure providing a tight contact, i.e. the quotient of the force and the contact area, is referred as the sealing limit of the contact.

2.3. Validation

A large-dimensions split-shaft test rig was designed and built to measure the radial force between the stern tube seal and the shaft liner (see Figure 4). However, the versatility of such a test rig is limited: each seal size requires its matching jaws to act as the shaft liner. Therefore, for this research, the stern tube seal model previously presented that had a nominal diameter of 200 millimetres was used.

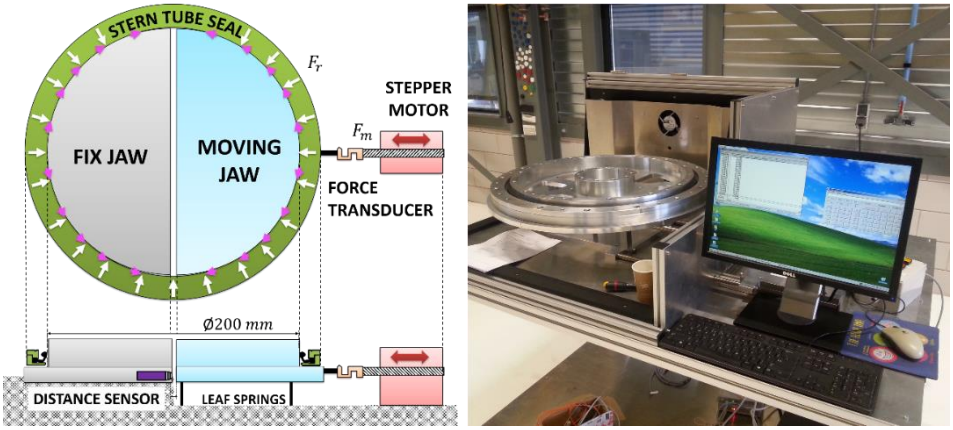

Figure 4. *Split-shaft test setup to measure the radial force between stern tube seals and shaft liner.*

The load required to keep the correct separation between the jaws when a seal is mounted on them is dependent on the inwards radial force between the seal and the liner $F_{r_{tot}}$ via Eq. *5*. Note that the moving jaw is not pulled further than its position conforming a circumference, i.e. the 200 millimetres shown in Figure 4. Once the circumference is conformed, the separation between the fixed and the moving jaws may allow that part of the seal material flow into it. However, the jaws and the control system are designed so that the separation between the jaws is minimum, i.e. few tenths of a millimetre. The tangential load between seal and jaws shown in Figure 4 is included, assuming Coulomb friction μ_s, so that:

$$F_{r_{tot}} = \frac{F_m \pi}{(1 + \mu_s)} \tag{5}$$

A capacity-distance sensor (Micro-Epsilon, Ortenburg, Germany) is used to measure the separation between the jaws. A control loop is implemented in LabView so that a stepper motor (Haydon Kerk Motion Solutions, Waterbury, USA) keeps the jaws a set distance apart. The S2M load cell (HBM, Darmstadt, Germany) mounted between the stepper motor and the moving jaw measures the pulling force exerted by the motor F_m. The stress relaxation of the elastomer and the spring force is measured over time. The setup was validated by measuring standard O-rings the material properties of which were independently measured using a tensile tester. Analogously to the procedure used for Garter springs (Eq. 7), the circumferential and radial forces of an O-ring can be related to the stress measured when pulling it on a tensile tester. The tensile stress results were found to be in good agreement with the measurements conducted when mounting the O-ring on the split-shaft setup. Lubrication of the seal-shaft liner contact did not significantly impact the results.

Four different configurations were tested on the split-shaft setup (see Table 5). Such an approach allowed the progressive validation of the computational model and to spot the source of inaccuracies. As expected, the characteristic stress relaxation of viscoelastic material makes the radial load between seal and shaft decrease over time. It was observed that most of the force decay occurs after 300 seconds; therefore this is set to be the measurement time of each test.

Table 5. *The four configurations tested in the split-shaft test rig.*

Configuration	Stern tube seal	Garter spring	Housing
A	YES	NO	NO
B	YES	YES	NO
C	YES	NO	YES
D	YES	YES	YES

A major contribution to the radial load between the stern tube seal lip and the shaft liner arises from the pressure difference between the sealing fluids. The split-shaft arrangement cannot measure the radial load under pressurized conditions, so an additional setup was developed allowing measurement of the width of the contact between seal and liner under actual operating pressures (Figure 5). The test rig is configured to include a hollow glass shaft on which the seal is mounted. Through the glass, the contact area between the transparent shaft and the seal can be directly observed. Using the Frustrated Total Internal Reflection technique [27], [28], the contact area is considered to be the location at which the evanescent wave is reflected by the seal. Both sides of the seal were independently pressurized and the seal tip displacement was captured by a precision camera (Dino-Lite, Taiwan, China).

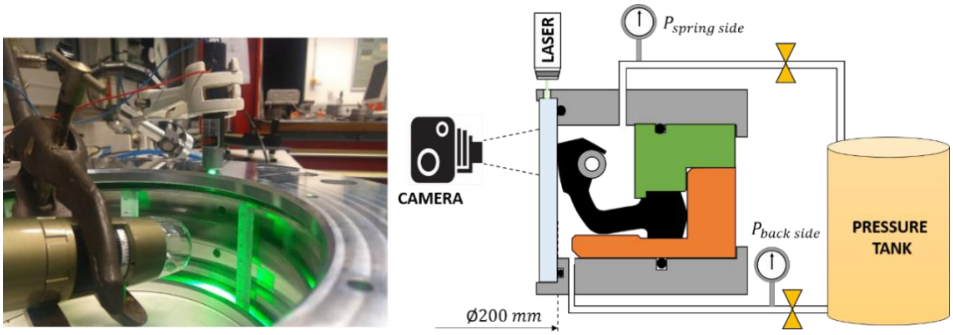

Figure 5. *Test bench with a hollow glass shaft to measure the contact area and leakage rate under actual operating pressure conditions.*

The contact width and its position were measured along the circumference and the results were used to validate the estimations produced by the seal FE computational model. The impact of uniformly

pressurizing the seal was also studied. As stress varies over time, so does the displacement of the seal, implying that the contact area is time-dependent.

The same setup allowed determination of the minimum pressure needed to keep the seal airtight (defined as the air percolation threshold). The flow rate (leakage) through the seal contact was measured using a ball flowmeter (EM-Technik, Maxdorf, Germany). The threshold was found by increasing the pressure at the back-side of the seal until a flowrate was observed. Additional measurements were taken at various leakage rates so that a trend could be observed.

3. Results

In this section, the experimental results obtained are presented along with the matching model predictions.

3.1. Seal material

Dumbbell B-type specimens were acclimatized for 10 minutes beforehand at the set temperature before testing them on the tensile tester. The strain was measured using contacting extensometers; the tensile tester load was zeroed before clamping the sample and an initial pre-tension of 0.1 MPa was imposed. The specimens were cycled as described by Dalrymple [24] to obtain the stress-strain curves together with the stress relaxation characteristics for each strain (see Figure 6). The initial length and section of the specimens were updated after each strain cycle and each test was repeated at least three times.

The strain rate at which the material is set for relaxation was swept from 2 to 250 mm/min showing a certain strain-rate dependency that was only significant at the highest strain rates. Therefore the material was considered strain-independent. Although the strain rate is irrelevant under static seal conditions, it will influence the seal when varying the shaft speed or when operating under misaligned shaft-seal conditions. The material showed a weak anisotropy when compared to dumbbell specimens that had been stamped in perpendicular directions. Additional compression tests were carried out up to -30% strain showing a higher stiffness under compression than under tension. The relative stress decay is plotted in Figure 7, evidencing the non-linear viscoelasticity of the material. Hence, the stern tube seals

which operate under a higher pressure difference (resulting in higher strains), will experience a greater stress decay than the seals operating under lower strains. The amount of relative relaxation decay is dependent on the strain rate at which the strain is set. However after 300 seconds the final stress becomes independent of the loading strain rate.

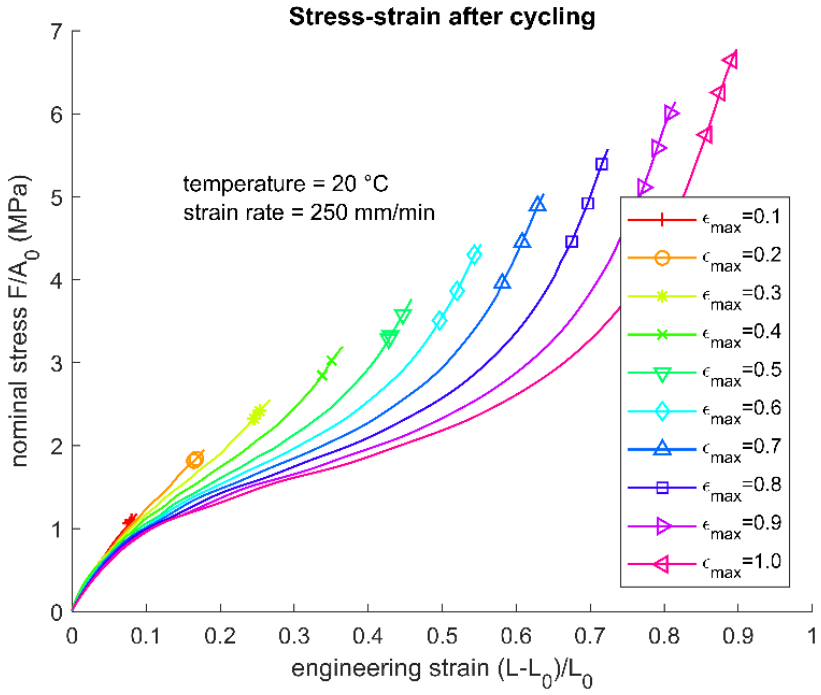

Figure 6. *Stress-strain curves after Mullins and recovery at 20 °C (loading strain rate of 250 mm/min).*

The effect of temperature on the elastomer was studied by applying dynamic mechanical analysis (DMA). The result of a temperature sweep from -80 °C to 120 °C at a frequency of 2 Hz and 1% strain is shown in Figure 8. The DMA confirmed that the elastomer undergoes a certain amount of temperature softening until reaching 40 °C at which a temperature-independent rubber plateau is reached.

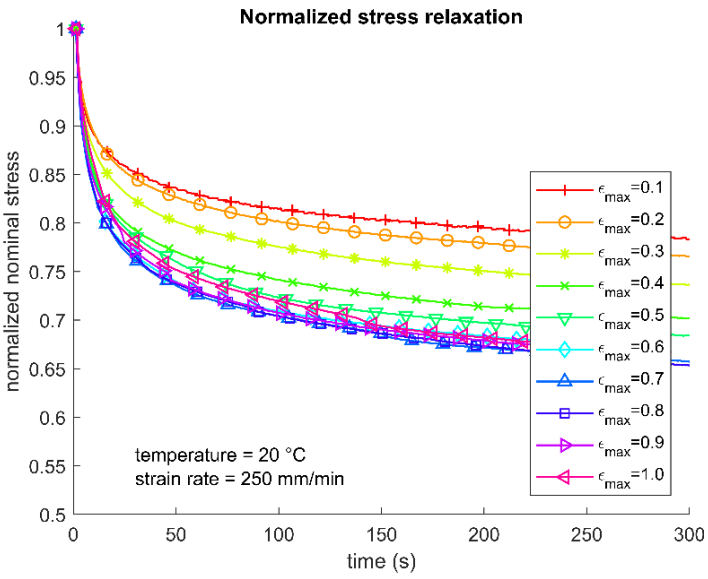

Figure 7. *Normalized stress relaxation at various strains at 20 °C (loading strain rate of 250mm/min).*

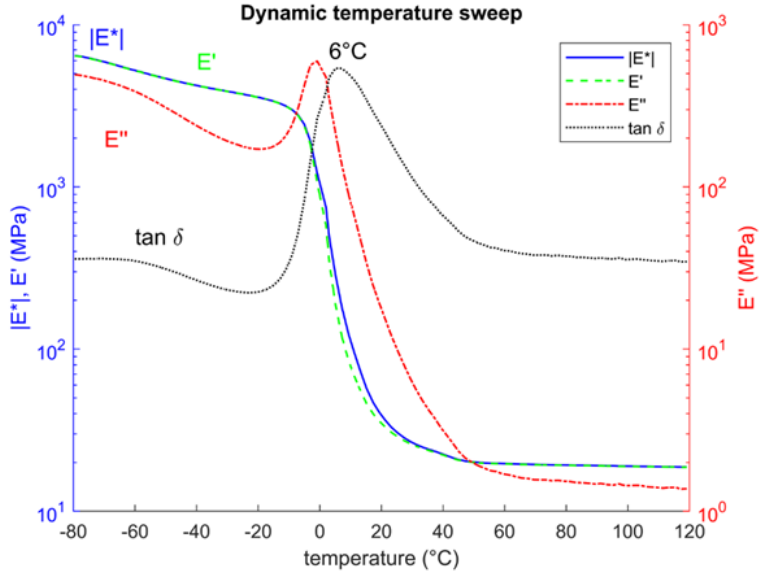

Figure 8. *Dynamic mechanical analysis (DMA) temperature sweep.*

The Yeoh hyper-elastic constitutive material model is fitted to the relaxed stress-strain curves [24] yielding the Yeoh parameters C_{10}, C_{20} and C_{30}. The seal material was left temperature-independent as the model validation was conducted at room temperature. The fitting of the tension and compression curves at 20 °C was performed using Abaqus/CAE® software and compared with the results obtained using the split-shaft measurements. Results will be discussed later and shown in Figure 11.

Table 6. *Parameters used for the Yeoh hyperelastic model.*

Hyperelastic Yeoh parameters (MPa)		
Yeoh parameter	C_{10}	2.50
Yeoh parameter	C_{20}	-0.61
Yeoh parameter	C_{30}	0.54
Bulk modulus	κ	1e4

3.2. Garter spring

The Garter spring characteristics were measured using a tensile tester [5] to measure the pre-tension ($P_I = 11.61\ N$) and the spring stiffness ($S = 0.32\ N/mm$). When the spring is assembled and mounted on a shaft of diameter D_s (see Figure 9), the linear response deduced from the measurements can be decomposed into the circumferential and radial directions [29] as shown in Eq *6* to *8*.

$$P_c = P_I + S(\pi D_s - \pi D_{ri}) \tag{6}$$

$$P_r = \frac{2P_c}{D_s} \tag{7}$$

$$P_r = 2\left[\frac{P_I}{D_s} + \pi S\left(1 - \frac{D_{ri}}{D_s}\right)\right] \tag{8}$$

This formulation assumes the spring's linear behaviour in the circumferential direction; this applies if the lateral bending stiffness is neglected and the coils are considered to be fully separated. It is also assumed that the radial load contribution to the shaft-seal contact is uniformly distributed along the perimeter of the contact.

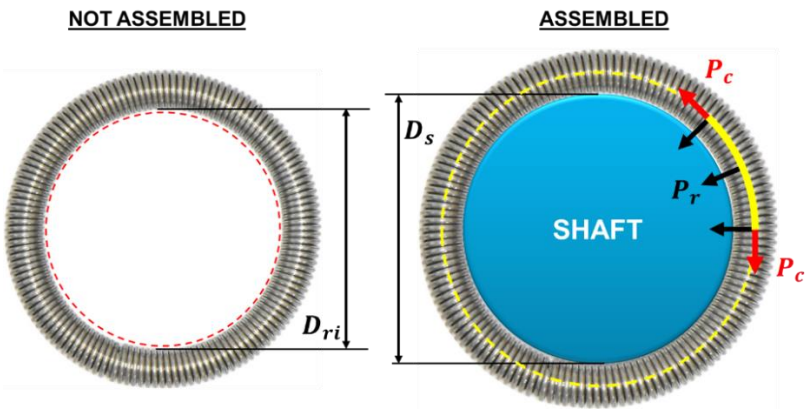

Figure 9. *Garter spring force decomposition.*

3.3. Surface roughness

The surface topography of a new seal was measured using a confocal microscope (Sensofar, Barcelona, Spain). A replicating compound was used to obtain the seal surface topography suitable for microscopy (Microset, Leicestershire, United Kingdom) and that topography is shown in Figure 10.

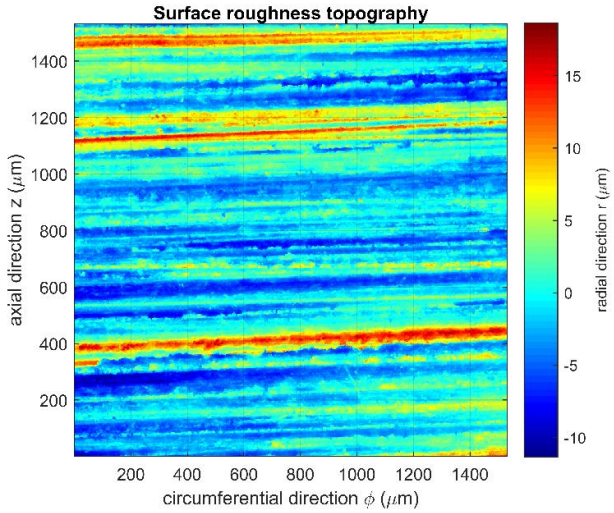

Figure 10. *Surface roughness topography of the tip of a new stern tube seal. Note the turning marks of the mould spanning on the circumferential direction.*

The surface roughness presents a clear wave pattern oriented in the axial direction. Such an undulated profile comes from the turning marks of the metal mould. The statistical roughness parameters are listed in Table 7.

Table 7. *Statistical surface roughness parameters.*

	new seal
S_a	3.52 μm
S_q	4.61 μm
S_p	30.46 μm
S_v	13.14 μm
S_{z_5}	43.44 μm
S_k	0.87
K_s	4.39

3.4. Radial force

Four seals were measured on the split-shaft setup at least five times per configuration (see Table 5), leading to the radial force values shown in Figure 11. The results are compared to the FE model predictions both with and without the spring and housing parts constraints.

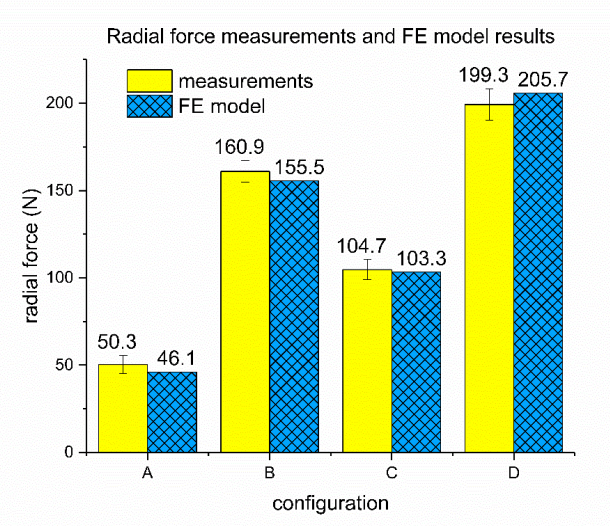

Figure 11. *Radial force under the four configurations tested (see Table 5) and the loads predicted by the FE model.*

The dimensional accuracy of the jaws and seals, the elastomeric compound composition, differences in the curing state, post-curing shrinkage, the amount of strain each seal had undergone, the testing temperature, the assembling of the seal within the housing parts and the housing-shaft alignment will all lead to a certain spread in the measurements. As reported by Gabelli [19], the model predictions underestimate the radial load of the seal by 5%. Parameter C_{10} was slightly increased so the aforementioned inaccuracies – together with the limitations of hyperelastic models – were compensated for. Note that although the only difference between configurations A-B and C-D is the presence of the Garter spring, the contributions differ. This shows that the spring load is partially supported by the housing parts in configuration D. The load difference between configurations A and B is in agreement with that estimated by Eq. *8*. It is interesting to observe that the radial force in configuration A (no spring and no housing parts) arises from the circumferential stretch of the material and this amount is doubled when the seal housing components are present in configuration C.

3.5. Contact width

Using the glass cylinder setup, captions of the seal tip were taken at pressure differences from 0 to 1.5 bar (see Figure 12). To show the almost-incompressible nature of the elastomer compound, the top and bottom chambers of the setup in Figure 5 were connected by a pipe equalizing the pressure on both sides of the seal. Next, using the precision camera, the overall pressure was increased up to 2 bar showing no difference between the surface captions at the minimum and maximum pressures.

The wavy pattern observed on the seal topography becomes evident on the back-side of the seal where the contact only occurs on the roughness peaks (Figure 10). Measurements and model predictions are plotted together in Figure 13. The contact width was measured at four different points of the contact after 300 seconds. The FE model underestimates the contact width because a smooth contact between the seal and the shaft is assumed [19]. The measurements and the model predictions showed good agreement when the surface roughness was accounted for by adding $S_{z_5}/2$ to the seal profile as shown in Figure

17. The friction between the seal and the glass prevents the sliding of the seal tip as pressure increases. The increase of the standard deviation in response to pressure difference shown in Figure 13 is attributed to the larger loads imposed on the seal.

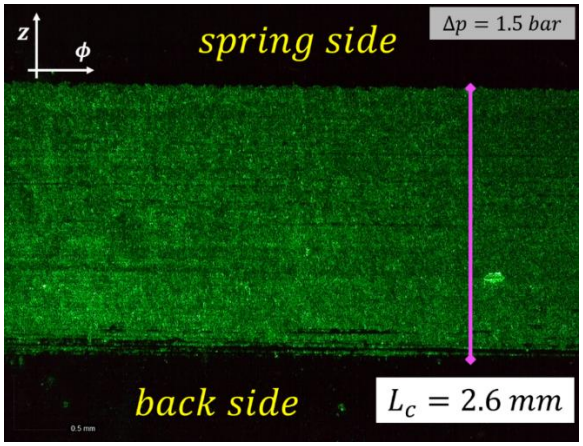

Figure 12. *Caption of the contact area on the glass shaft setup (*$\Delta P = 1.5\ bar$*). The turning marks of the mould are shown along the contact and become evident at the back-side of the seal.*

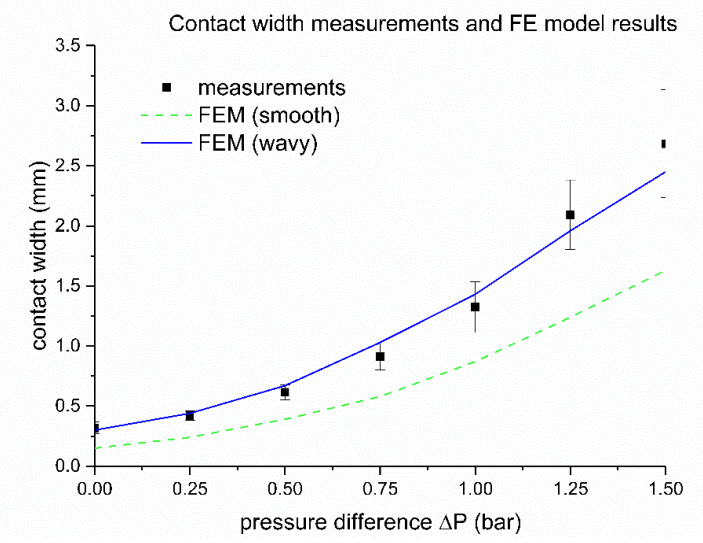

Figure 13. *Contact width measurement under various pressure differences using the hollow glass shaft setup. The prediction of the FE model (smooth) and the impact of adding* $S_{z_5}/2$ *(wavy).*

3.6. Leakage and sealing pressure

Using the same glass setup, the seal was inversely pressurized, i.e. with a greater pressure on the back side than on the spring-side. The pressure at the back-side of the seal was steadily increased until the flowrate (leakage) along the seal could be measured. Some time was left between intermediate measurements so that the seal material had time to adjust to the new strain conditions. That procedure was repeated in both loading and unloading situations and the results are plotted in Figure 14. The lowest pressure difference leading to leakage is referred as the opening pressure of the seal. Since the resolution of the flowmeter is 0.01 L/min, extra measurements were taken so the opening pressure can be extrapolated as shown in Figure 14.

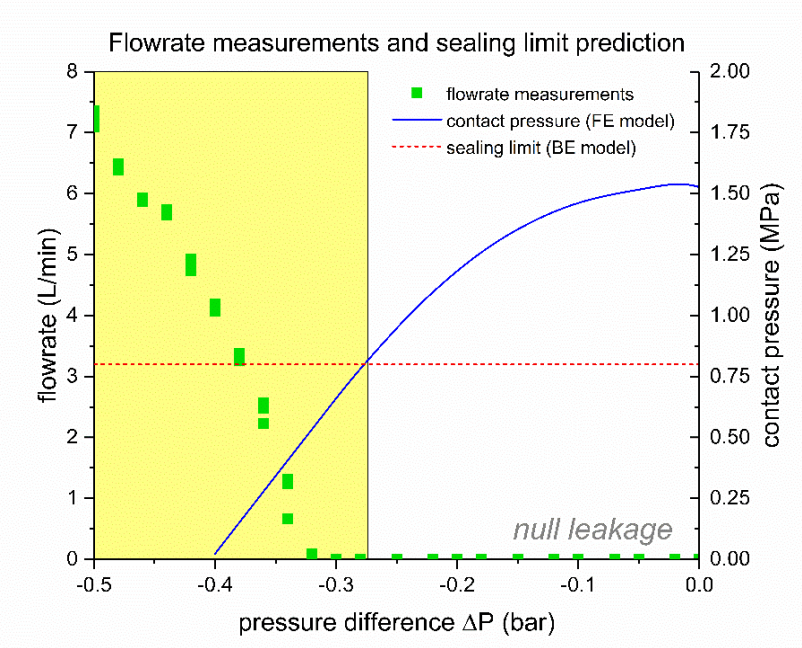

Figure 14. *Flowrates measured on the glass shaft setup under various pressure differences (dots). The maximum contact pressure predicted by the FE model when the seal is inversely pressurized (solid line). The dashed line shows the minimum contact pressure required for a tight surface, i.e. sealing limit, predicted by the BE model (see Figure 19). The shaded part corresponds to the pressure differences where leakage is expected.*

3.7. Finite Element (FE) model

The final position of the seal is shown to be highly dependent on pressure difference ΔP, i.e. the sealing pressure. As the pressure difference increases the tip of the seal moves closer to the seal head. The contact area steadily increases in response to increasing pressure as the back-side angle decreases. The role of the back-up ring becomes clear when the pressure difference ΔP reaches 1.0 bar (see Figure 15).

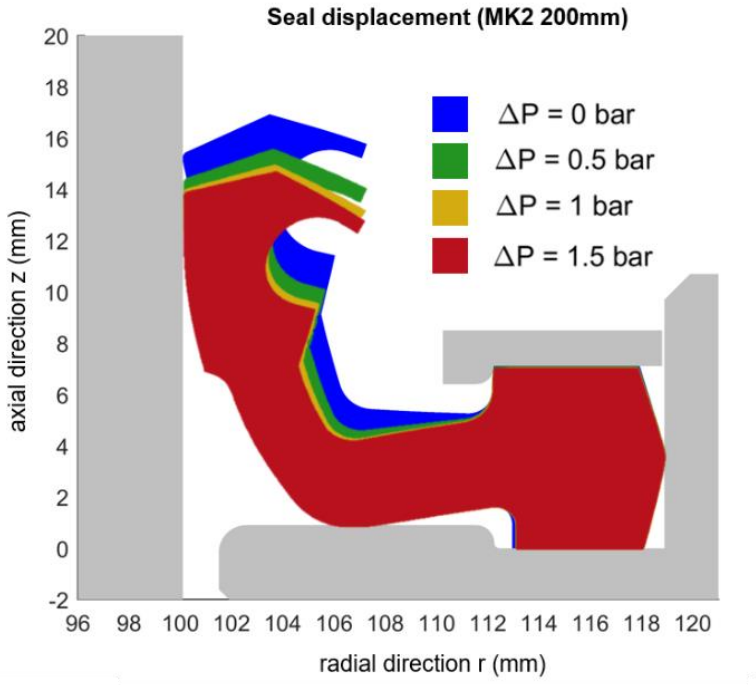

Figure 15. *Seal displacement estimation obtained with the stern tube seal FE model.*

Once the seal contacts the back-up ring, the contact area rapidly increases leading to the characteristic bell mouth-shaped pressure distribution (see Figure 16 and Figure 17). The distribution of the contact load on a wider contact area leads to a decrease in the maximum contact pressure. The maximum contact pressure for all the cases is located at the edge of the spring-side, thereby validating the sealing point assumption shown in Figure 3.

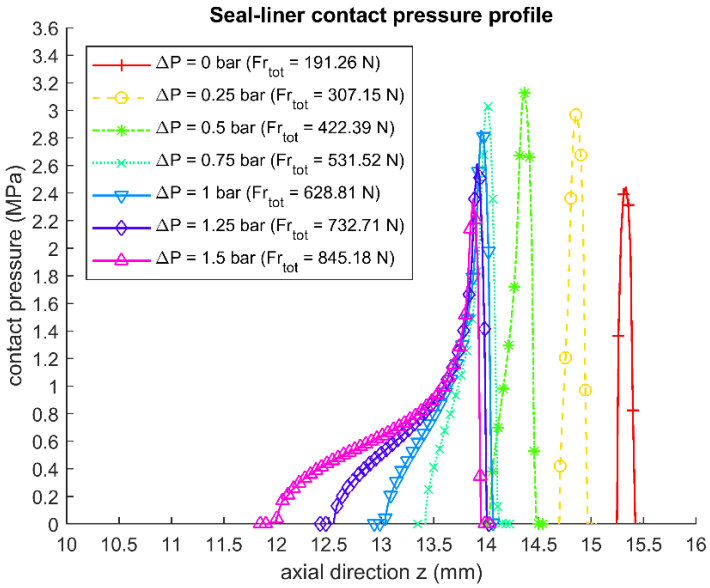

Figure 16. *Contact pressure profiles under a range of pressure differences ($\mu_s = 0.0$).*

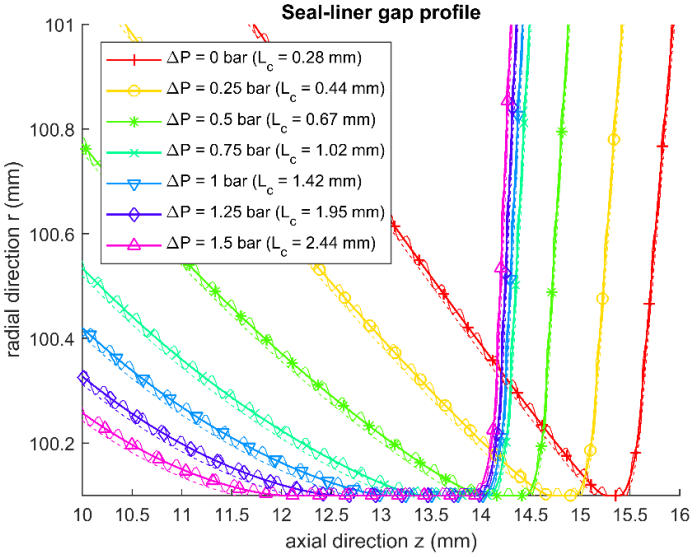

Figure 17. *Gap profile under a range of pressure differences ($\mu_s = 0.0$). A wavy profile with an amplitude of $S_{z_5}/2$ is overlapped on the seal tip profile showing the magnitude of the elastomer roughness.*

Figure 18 shows the contribution of the elastomer, the spring and the pressure difference to the seal-shaft contact force under various levels of pressurization. The elastomer force is a result of the inherent beam force of the seal lip and the hoop force. Note that the contribution of the pressure difference is only higher than the combined contribution of the spring and the material once the pressure difference ΔP exceeds 0.5 bar. As shown in Figure 1, each seal in the stern tube operates under a particular pressure difference which results in a seal-specific shaft-liner contact force and, consequently, in a specific tribological pair for each of the stern tube seals.

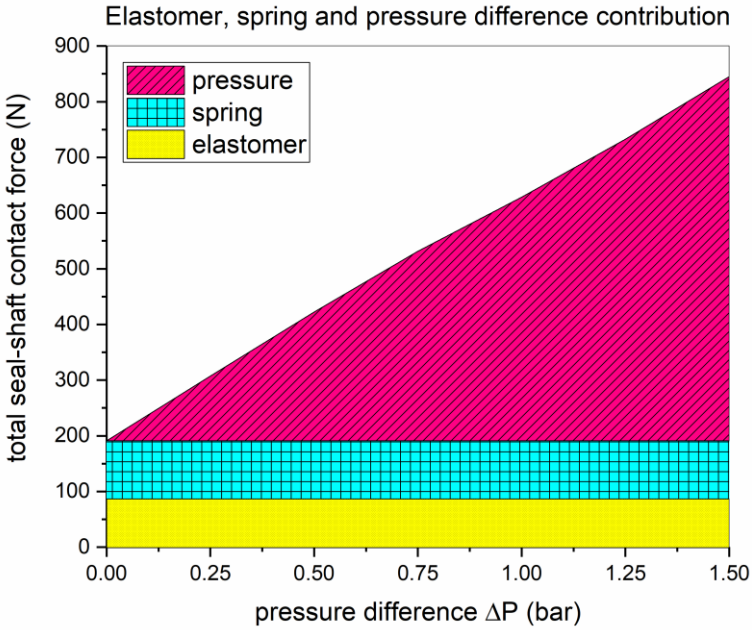

Figure 18. *Contribution to the total seal-shaft contact force by the elastomer, the Garter spring and pressure difference at various pressure levels.*

3.8. Surface contact Boundary Elements (BE) model

The contact between the seal and the shaft was modelled using a BE surface contact model under various loads. In this way the contact force threshold at which leakage occurs could be spotted and compared

with the flowrates measured on the glass shaft test rig. The seal topography measurements (Figure 10) and the material properties listed in Table 4 were used to identify the sealing threshold of the contact and that threshold is shown in Figure 19. The sealing limit is also shown as a dotted red line in Figure 14.

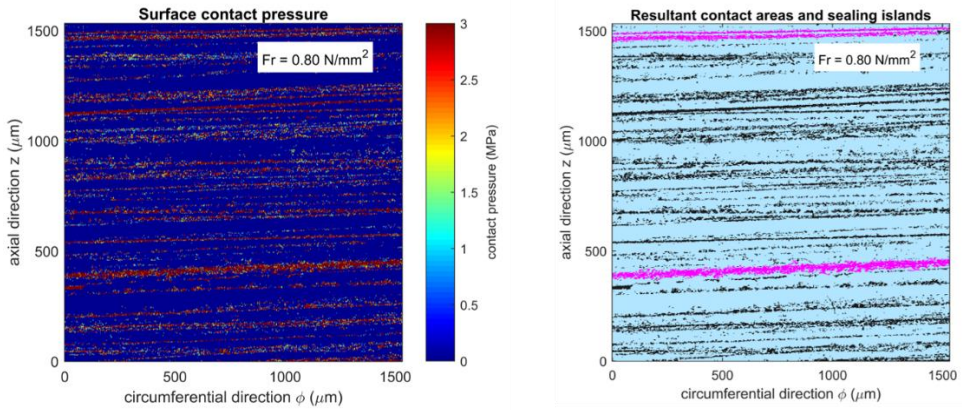

Figure 19. *Pressure distribution (left) and resultant contact areas depicted in black and pink (right). The areas in pink are the first sealing islands spanning from side-to-side in the circumferential direction, i.e. where a gas tight situation is considered.*

4. Discussion

The fluoroelastomer compound used for the stern tube seal studied was tested under various strains and loading conditions. A strong Mullins effect was observed, so the maximum strain ever reached by the elastomer determines its stress response. The relative stress relaxation was shown to be dependent on the strain, i.e. it exhibited non-linear viscoelastic behaviour. A strong viscoelastic component was identified at ambient temperature which, as expected, reduces as the distance between the current and glass transition temperature T_g increases. Consequently, the temperature-dependent material behaviour observed at 20 °C vanished at 40 °C leading to a temperature-independent rubbery plateau. Note that under dynamic loading conditions, the damping due to the viscoelasticity of the material would be completely different at 20 °C to what it would be at 40 °C, affecting the followability of the seal. The maximum strain level

that a particular seal reaches is not easily determined. The radial load measurements of brand-new seals is slightly higher than those for seals which had been previously stretched (to larger strains) and then tested. In addition, to avoid disassembling the whole propeller, stern tube seals are cut, stretched around the shaft and later re-joined, thereby achieving this way an even higher maximum strain. Therefore, the specific seal assembling procedure partially determines the resultant seal-shaft contact force when mounted.

The constitutive hyperelastic Yeoh model was chosen for its simplicity and was calibrated against the stress values obtained once the greatest part of the stress relaxation decay had occurred. By using an hyperelastic constitutive material model, the seal is treated as perfectly elastic so there is no provision for permanent strain deformation (zero stress leads to zero strain). Hyperelastic models disregard the maximum strain dependence and assume that the material response is the same under loading and unloading situations. However, such simplifications will inevitably add to the inaccuracy of the model.

The contribution of the Garter spring to the total seal-shaft contact force was obtained by measuring the spring characteristic and estimating its radial force once assembled and mounted on the shaft. The spring load estimation obtained by applying Eq. *8* was in agreement with the measurements carried out on the split-shaft setup.

The validation of the static FE model presented several challenges. A large-dimensions split shaft test bench was built so the radial force could be measured. The method presented consists of measuring the radial load for four different configurations. Such approach firstly allowed the validation of the constitutive material model, then the Garter spring contribution and finally the seal-housing clamping boundary conditions. However, the ability to predict the correct radial force under ambient conditions does not guarantee that the model is representative of the seal. An alternative validation method is presented which involves mounting the seal on a hollow glass shaft so the contact width between seal and liner can be measured. However, under ambient conditions, the contact width of most seals is of the order of a few hundred micrometres, hampering accurate

measurement. Furthermore, at a such scale, the roughness of the seal or marginal misalignments influence the measurement. For that reason, a specialized setup consisting of a transparent shaft and two sealing chambers was built. That setup allowed testing under actual application conditions under which larger stresses and strains develop due to the imposed external pressure. The position and the width of the contact at a range of operating pressures could be readily measured and showed good agreement with the predictions of the FE model.

A third novel method was introduced to further validate the two-scale model developed. The percolation threshold of the stern tube seal, i.e. the pressure difference required for the seal to leak, was measured by pressuring the seal on the glass shaft setup. Hereby, this time a higher pressure was imposed in the back-side than in the spring-side (inverse pressurization).

Using the perfectly smooth macroscopic FE model, the decrease in contact pressure resulting from inversely pressurizing the seal was predicted and is shown in Figure 14 in blue. Notice that, due to roughness, leakage occurs before the -0.4 bar pressure difference that is required to completely lift the seal. The estimated contact pressure was found to be in good agreement with that required for the microscale BE contact model to achieve an effective sealing barrier (shown by a red dashed line in Figure 14). The shaded area corresponds to the pressure differences that lead to a contact pressure that is inferior to that required for a tight contact, i. e. the pressure differences causing leakage.

A variation of ± 10 N in the radial force measurements was observed when measuring seals even from the same batch. As well as the inherent model simplifications, the seal dimensional accuracy, elastomer curing state or the strain history of the seal can explain this difference. The dimensional accuracy of the components of both the split-shaft and glass setups will also influence the results. Furthermore, the assembly of the stern tube seal to the housing components does not guarantee an accurate centring. It was decided to present frictionless results since stern tube seals most frequently

operate under fully flooded conditions (near the transition of mixed to full-film lubrication).

Extrapolation of the results presented for the dynamic operation of a stern tube seal must be carried out with care. Even if boundary lubrication conditions are assumed, i.e. the shaft-seal load is fully supported by the shaft and seal asperities, neither the seal tip displacement in the circumferential direction nor the friction heating of the seal tip have been included in this study. These could otherwise influenced the results.

5. Conclusions

A multi-scale model of a stern tube seal has been developed. The model couples the macro and microscales, allowing the prediction of strains, stresses, temperature distribution and percolation threshold under a wide range of pressures and temperatures.

Special attention was paid to the validation of the model. Two specialized setups were developed so that the model was validated under pressurized conditions via radial force, contact width and leakage rates, and showed a high degree of accuracy. Following the steps presented, the seal constitutive material model, the Garter spring and the implementation of the seal housing can be independently addressed. This approach increases the reliability of the overall model while granting its full understanding when improving its design. The strategy presented for modelling the contact on a lip seal constitutes a solid milestone towards developing more advanced, accurate and reliable models of sealing components.

Acknowledgments

Andries van Swaaij, Eric de Vries, Henk-Jan Moed, Walter Lette, Hans van Hoek and Jonne Postmes for their technical advice. Rob Dierink, Roy Kooijman, Bart Rooijmans and Sebastian Schipper for their assistance with the development of the testing setups. François Perseil-Rouillard, Gijs Boerrigter and Mauryn de Graaf for their contribution to the two-scale model.

References

[1] R. Flitney, "Rotary Seals," in *Seals and Sealing Handbook*, 6th ed., Waltham: Butterworth-Heinemann, 2014, pp. 105–288.

[2] J.G. Drobny, "Fluoroelastomers Handbook: The Definitive User's Guide," 2nd Ed., Elsevier, 2016, pp. 17–40.

[3] B. Wennehorst, "On Lubrication and Friction in Soft Rough Conformal Sliding Contacts," Ph.D. dissertation, Leibniz Universität Hannover, 2016.

[4] E.T. Jagger, "Rotary Shaft Seals: The Sealing Mechanism of Synthetic Rubber Seals Running at Atmospheric Pressure," *Proc. Inst. Mech. Eng. Part J J. Eng. Tribol.*, vol. 171, no. 1, pp. 597–616, 1957.

[5] L.A. Horve, *Shaft seals for dynamic applications*. New York: Marcel Dekker Inc., 1996.

[6] P.G.M. van Bavel, "The Leakage-Free Operation of Radial Lip Seals," Ph.D. dissertation, Eindhoven University of Technology, 1997.

[7] R.F. Salant, "Theory of lubrication of elastomeric rotary shaft seals," *Proc. Inst. Mech. Eng. Part J J. Eng. Tribol.*, vol. 213, no. 3, pp. 189–201, 1999.

[8] M.J.L. Stakenborg, "On the sealing mechanism of radial lip seals," Ph.D. dissertation, Eindhoven University of Technology, 1988.

[9] G. Marek, "On friction reduction in rubber lip seals for rotating shafts," *Seal. Technol.*, vol. 40, pp. 8–11, 1997.

[10] W. Sinzara, I. Sherrington, E.H. Smith, H. Brooks, and A. Onsy, "Effects of Eccentric Loading on Lip Seal Performance," in *6th European Conference on Lubrication Management and Technology*, 2018.

[11] D. Frölich, B. Magyar, and B. Sauer, "A comprehensive model of wear, friction and contact temperature in radial shaft seals," *Wear*, vol. 311, no. 1–2, pp. 71–80, 2014.

[12] T. Engelke, "Einfluss der Elastomer-Schmierstoff-Kombination auf das Betriebsverhalten von Radialwellendichtringen (in

German)," Ph.D. dissertation, Leibniz Universität Hannover, 2011.

[13] C.Y. Lee, C.S. Lin, R.Q. Jian, and C.Y. Wen, "Simulation and experimentation on the contact width and pressure distribution of lip seals," *Tribol. Int.*, vol. 39, no. 9, pp. 915–920, 2006.

[14] A. Tasora, E. Prati, and T. Marin, "A method for the characterization of static elastomeric lip seal deformation," *Tribol. Int.*, vol. 60, pp. 119–126, 2013.

[15] B. Pinedo, J. Aguirrebeitia, M. Conte, and A. Igartua, "Tri-dimensional eccentricity model of a rod lip seal," *Tribol. Int.*, vol. 78, pp. 68–74, 2014.

[16] M. El Gadari, A. Fatu, and M. Hajjam, "Shaft roughness effect on elasto-hydrodynamic lubrication of rotary lip seals: Experimentation and numerical simulation," *Tribol. Int.*, vol. 88, pp. 218–227, 2015.

[17] Chung K.K. and Woo J.S., "Analysis of contact force and thermal behaviour of lip seals," *Tribol. Int.*, vol. 30, no. 2, pp. 113–119, 1997.

[18] J.F. Wenk, L.S. Stephens, S.B. Lattime, and D. Weatherly, "A multi-scale finite element contact model using measured surface roughness for a radial lip seal," *Tribol. Int.*, vol. 97, pp. 288–301, 2016.

[19] A. Gabelli, F. Ponson, and G. Poll, "Computation and Measurement of the Sealing Contact Stress and its Role in Rotary Lip Seal Design," in *Fluid Mechanics and its Applications*, Dordrecht: Springer Netherlands, 1992, pp. 21–39.

[20] F.X. Borras, M.B. de Rooij, and D.J. Schipper, "Rheological and Wetting Properties of Environmentally Acceptable Lubricants (EALs) for Application in Stern Tube Seals," *Lubricants*, vol. 6, no. 4, p. 100, Nov. 2018.

[21] J. Bergström, "Elasticity/Hyperelasticity," in *Mechanics of Solid Polymers*, 1st Ed., vol. 76, no. 3, Elsevier, 2015, pp. 209–307.

[22] C. Ovalle Rodas, F. Zaïri, M. Naït-Abdelaziz, and P. Charrier, "Temperature and filler effects on the relaxed response of filled

rubbers: Experimental observations on a carbon-filled SBR and constitutive modeling," *Int. J. Solids Struct.*, vol. 58, pp. 309–321, 2015.

[23] A. Vandenbroucke, H. Laurent, N. Aït Hocine, and G. Rio, "A Hyperelasto-Visco-Hysteresis model for an elastomeric behaviour: Experimental and numerical investigations," *Comput. Mater. Sci.*, vol. 48, no. 3, pp. 495–503, 2010.

[24] T. Dalrymple, J. Choi, and K. Miller, "Elastomer rate-dependence : A testing and material modeling methodology," in *172nd Technical Meeting of the Rubber Division of the American Chemical Society, Inc.*, 2007.

[25] M. Shahzad, A. Kamran, M.Z. Siddiqui, and M. Farhan, "Mechanical Characterization and FE Modelling of a Hyperelastic Material," *Mater. Res.*, vol. 18, no. 5, pp. 918–924, 2015.

[26] M. Bazrafshan, M.B. de Rooij, M. Valefi, and D.J. Schipper, "Numerical method for the adhesive normal contact analysis based on a Dugdale approximation," *Tribol. Int.*, vol. 112, no. April, pp. 117–128, 2017.

[27] C.H. Hidrovo and D.P. Hart, "Development of a dual purpose visualization technique for the study of rotating shaft seals," in *3rd ASME/JSME Joint Fluids Engineering Conference*, 1999, pp. 1–6.

[28] A. Gabelli and G. Poll, "Formation of Lubricant Film in Rotary Sealing Contacts: Part I—Lubricant Film Modeling," *J. Tribol.*, vol. 114, no. 2, pp. 280–287, 1992.

[29] "Chapter 8: Garter Springs," in *Design handbook: engineering guide to spring design*, Barnes Group Inc, 1981, pp. 56–59.

(This page is intentionally left blank)

Paper C

(This page is intentionally left blank)

Misalignment-Induced Micro-Elastohydrodynamic Lubrication in Rotary Lip Seals

F.X. Borras[1], M.B. de Rooij[1] and D.J. Schipper[1]

[1]University of Twente, Surface Technology and Tribology, Enschede, The Netherlands

(This page is intentionally left blank)

Abstract: In the literature, the lubrication of rotary lip seals is explained by hydrodynamic action on a microscopic scale. This theory assumes perfect concentricity between the seal and the shaft, which in reality seldom occurs. Focusing on the stern tube seals application, an analysis is performed on the phenomena distorting the axisymmetric operation of rotary lip seals. Radial and angular shaft misalignments together with pressure and temperature gradients have been modelled. The model predictions are validated using a dedicated setup. Additionally, applying the soft-EHL film thickness expressions at the asperity level, an equivalent film thickness along the circumferential direction is estimated. The Reynolds PDE is solved to predict the misalignment-induced hydrodynamic pressure build-up. The derived film thickness variation and accompanying non-uniform contact pressure distribution were shown to be sufficient for hydrodynamic action and, depending on the minimum film thickness, the hydrodynamic pressure build-up can exceed the static contact pressure. Additionally, significant differences were observed between the radial and angular misalignment configurations.

Keywords: EHL, film thickness, rotary, lip seal, misalignment, stern tube, seal.

Nomenclature

ω	Shaft angular velocity	[rad/s]
ε	Radial misalignment (offset)	[m]
θ	Angular misalignment (slant)	[°]
x, y	Coordinate system in the circumferential and axial directions	[m]
S_q	Root mean square roughness	[m]
$\lambda_{x/y}$	Root mean square wavelength in the circumferential and axial directions	[m]
$\Delta_{x/y}$	Root mean square slope in the circumferential and axial directions	[−]
$R_{x/y}$	Effective radius of curvature in the circumferential and axial directions	[m]
A	Amplitude of the equivalent sinusoidal roughness profile	[m]
$N_{x/y}$	Number of asperities in the circumferential and axial directions	[−]

u_x	Mean surface velocity in the circumferential direction	[m/s]
w_z	Average normal load per asperity	[N]
E'	Equivalent elastic modulus	[Pa]
W_x	Dimensionless load parameter	[−]
U_x	Dimensionless velocity parameter	[−]
h_{cen}	Central film thickness	[m]
h_{min}	Minimum film thickness	[m]
F	Normal load (radial seal load)	[N]
E	Young modulus	[Pa]
ν	Poisson ratio	[−]
ρ	Density	[kg/m^3]
C_p	Specific heat capacity	[J/(kg · K)]
k	Thermal conductivity	[W/(m · K)]
α_T	Thermal expansion coefficient	[1/K]
η	Dynamic viscosity of the lubricant	[Pa · s]
h	Fluid film thickness	[m]
p	Hydrodynamic pressure	[Pa]
p_c	Cavitation pressure	[Pa]
ρ_c	Density of the lubricant in the cavitation region	[kg/m^3]
β	Bulk modulus of the lubricant	[Pa]
ϕ	Dimensionless cavitation variable	[−]
g	Cavitation index	[−]
L_c	Width of the contact	[m]
T	Temperature	[°C]
t	Time	[s]

1. Introduction

The working mechanism of lubricated rotary lip seals have been the subject of discussion for the past decades. The presence of some sort of hydrodynamic action is repeatedly reported in literature. Jagger [1] was the first one to notice that the frictional torque of rotary lip seals included a viscous component, i.e., the friction between the shaft and the seal was inherently coupled to the turning velocity. His findings could explain the extremely low wear rates observed in some rotary lip seals [2]. Later Stakenborg [3] observed air bubbles arising from the sealing contact when running. The location of the cavitation area varied with the shaft angular speed. Wennehorst [4], among others,

measured the lift-off of the seal lip with increasing shaft speed. While it is a given that a hydrodynamic film (partial or full) is present, the following two questions posed by Salant [5] prevail: what is the origin of the fluid hydrodynamic pressure built-up? If surface separation partially or fully develops, why does the seal not leak?

Contrasting with journal bearings and thrust bearings, lip seals do not present a convergent gap profile, i.e., a wedge, in the direction of motion in the absence of misalignment. Therefore, no pressure build-up is expected from the operation of a perfectly concentric seal [4]. Lip seals resemble mechanical shaft seals in the sense that both require deviations from nominal parallelism to generate an hydrodynamic load support. Ever since the presence of hydrodynamics was first documented, researchers have theorized about the mechanism behind rotary lip seals. Several theories, both macroscopic and microscopic [6], able to explain the almost leak-less and wear-less operation of lubricated rotary lip seals have been presented in literature.

Up to now, the generally accepted theory relies on the hydrodynamic action on the microscopic level to explain the performance of rotary lip seals. When the shaft rotates, the microscopic wedges between the seal and shaft surface asperities generate a hydrodynamic fluid load carrying capacity capable of partially or fully supporting the radial force of the seal lip. Furthermore, the compressed asperities are tangentially distorted in the circumferential direction due to friction leading to a shaft-seal topography resembling a micro-screw pump [5] (see Figure 1). Consequently, in a similar fashion as a visco-seal, the rotation of the shaft induces a flow in one direction preventing the leakage in the opposite direction. This sealing mechanism is known as the reverse, upstream or back pumping of rotary lip seals [6]. When running on an oil–air interface, the ingress of air is often described in literature [7].

Although the microscopic theory can explain many of the phenomena observed in rotary lip seals [5], it disregards the shaft-seal misalignment which has repeatedly shown to play a significant role when it comes to wear rate, contact temperature, and the lifespan of sealing components [8]. The loss of the seal–shaft concentricity is usually classified between radial and angular misalignments [9].

Radial misalignment refers to the offset between the bore and shaft axes (parallel misalignment), i.e., keeping the axes parallel. The second type of misalignment, also known as skewness, cocking, cant or slant, refers to the difference in orientation between the shaft and bore axes. Both radial (ε) and angular (θ) misalignments can be constant (static) or variable in time (dynamic). The four possible configurations are shown in Figure 2. The loss of nominal parallelism between the seal and the shaft can result from the bearings internal and mounting clearances, the shaft out-of-roundness, the manufacturing tolerances, the radial vibrations, the shaft loading or the speed-induced wobbling of the shaft [10]. The viscoelasticity of the seal material affects the followability of the seal [11] and it will also lead to a misaligned operation [12]. Poll [13] presented torque measurements of a seal oscillating at the rotation frequency of the shaft. This is a clear consequence of dynamic misalignment between the seal and the shaft.

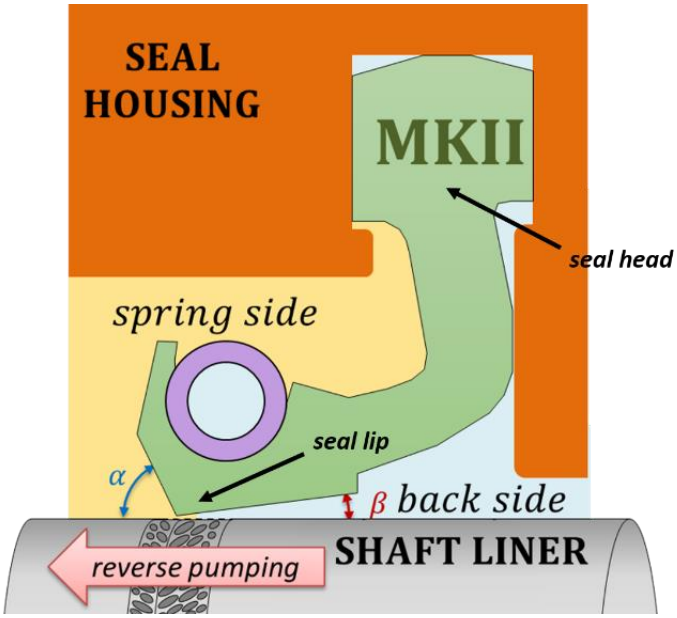

Figure 1. *Reverse pumping mechanism of rotary lip seals.*

While there are methods to measure the sealing force of a radial seal [14], there is not a standard way to measure it when the seal and the shaft are offset. The overall reaction force to a set of radial misalignments were measured by Tasora [15] and Pinedo [16]. Their

measurements show good agreement with the loads obtained using the Finite Elements (FE) models. Van Babel [17] sketched the resultant contact area from both radial and angular misalignments showing that, the tip of the seal is axially displaced as a result of it. This phenomenon is shown in Figure 3.

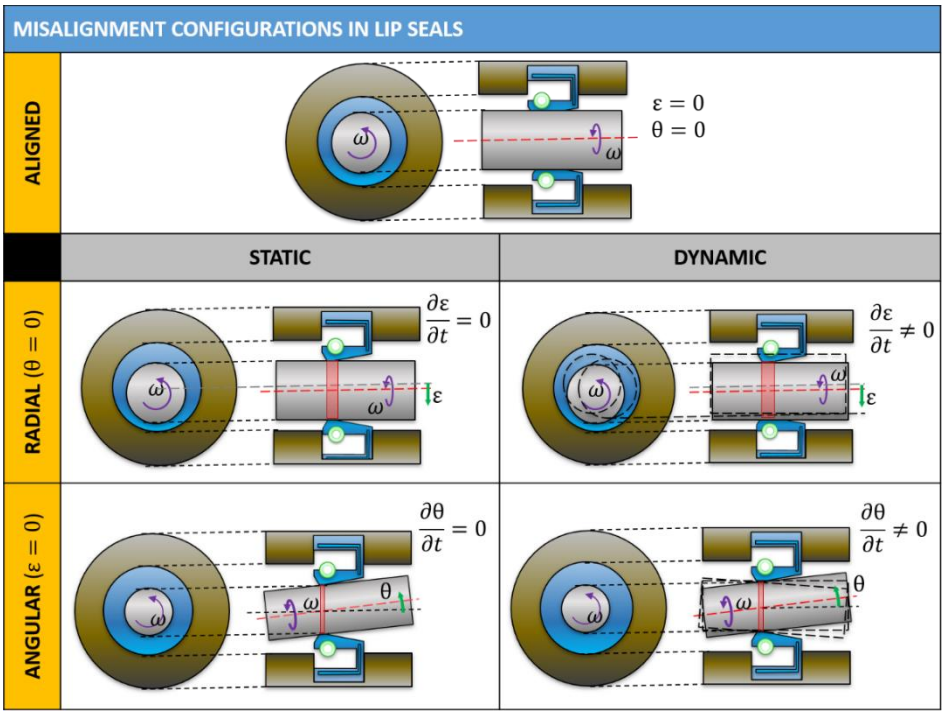

Figure 2. *Classification bore-to-shaft misalignment in lip seals.*

Here a particular type of a stern tube seal of 200 mm nominal diameter is analysed. For this application, the large dimensions of the components of the propulsion system, the manufacturing accuracy of the elastomeric parts together with the inherent offset with the shaft bearings [18] make the bore-seal misalignment more than probable. Nevertheless, less obvious effects might also lead to a non-concentric shaft operation. Stern tube seals operate below the seawater level thereby subjected to hydrostatic pressure. Furthermore, as the seals are vertically positioned, there is a hydrostatic pressure gradient from the highest to the lowest point of each seal. The pressure difference is directly related to the diameter of the seal. As a result of it, stern tube seals can present a skewed contact profile. Ultimately, Arai [10]

showed the sensitivity of the seal to temperature variations due to the large thermal expansion of elastomers. He reported about seals which were only tight beyond a particular temperature. Sinzara [19], using an IR camera, showed a significant temperature gradient along the perimeter of the seal contact when the shaft was intentionally offset.

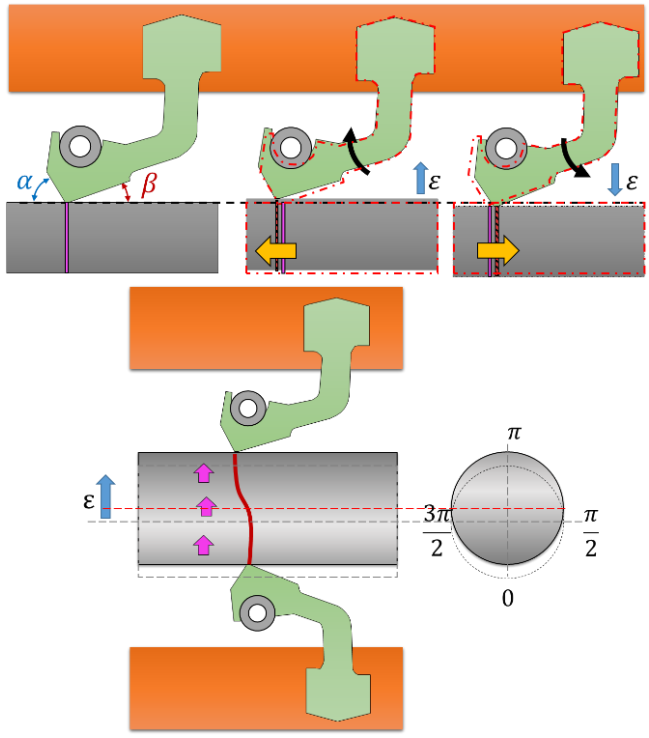

Figure 3. *Tip axial displacement induced by the shaft offset.*

The actual film thickness of rotary lip seals, which would clarify their actual lubrication regime, still remains difficult to measure. The film thickness values shown in literature span from 0.1 to 10 μm and significant changes to the tribo-system are required to make the measurements feasible. Organisciak [20] fitted a function to the lubricant film thickness measurements of radial shaft seals for gearboxes showing a fair resemblance to the iso-viscous elastic film thickness expressions (soft-elastohydrodynamic lubrication [21]). Fowell [22] measured the film thickness of fluoroelastomer specimens using the laser induced fluorescence (LIF) technique and these showed to be in good agreement with Hamrock [21] and Nijenbanning [23]

elastohydrodynamic lubrication (EHL) models. First Gabelli [24] and then Wennehorst [4] made use of the Chittenden expressions [25] to predict the minimum film thickness on rotary lip seals by applying it at the microscopic level, i.e., for a single asperity contact. Wennehorst recently managed to measure the film thickness on a rotary lip seal using the LIF technique [4].

The contact pressure and area resulting from different misaligned configurations are obtained. Next, the effects of the temperature difference over the seal as well as the presence of a hydrostatic pressure gradient will be analysed. Further, the authors applied the soft-EHL theory to estimate the equivalent gap profile between the shaft and the seal. Ultimately, the seal is modelled as a journal bearing to estimate the hydrodynamic pressure expected from a misalignment-induced gap profile.

2. Materials and Methods

The strategy for modelling the hydrodynamics developing under a non-concentric shaft-seal configuration counted with the three steps shown in Figure 4. The first step consisted in estimating the contact pressure and contact area on a misaligned configuration. Subsequently, specifying a shaft angular velocity and a lubricant viscosity, the soft-EHL theory was applied resulting in a lubricant film thickness along the circumferential direction. Ultimately, by solving the Elrod–Adams algorithm in the film thickness profile obtained (i.e., under the same operating conditions), the hydrodynamic pressure build-up was predicted.

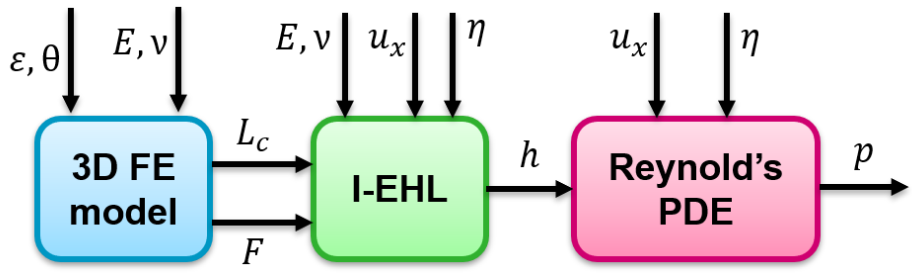

Figure 4. *Scheme of the modelling strategy (see Nomenclature).*

A stern tube seal FE model was developed to study the response of a lip seal to various kinds of misalignments. The commercial FE package COMSOL Multiphysics® was used to model a 200 mm stern tube seal. The contact force, contact area and pressure profile under the seal tip were predicted using the large strain theory and modelling the seal with the Saint Venant–Kirchoff constitutive material model with the properties listed in Table 1. The lack of axial symmetry of the loads required the use of a three-dimensional model [15,16]. Therefore, the axisymmetric approach presented in a previous publication of the authors [14] was extended along the circumferential direction. The initial configuration was considered to be the one with the seal head already clamped between the seal housing components (see Figure 1). It is essential to model the clamping stage as the inner diameter of the seal lip decreases as a result of it. The seal head boundary nodes were consequently fixed leading to a model with a single boundary contact (instead of four [14]).

Table 1. *Material properties used in the three-dimensional stern tube seal FE model.*

		Stern Tube Seal	**Shaft**	**Seal Housing**
E	[MPa]	14.0	2.0×10^5	1.065×10^5
ν	[−]	0.49	0.27	0.35
ρ	$[\mathrm{kg/m^3}]$	1900	7700	8800
C_p	$[\mathrm{J/(kg \cdot K)}]$	1670	1909.7	376
k	$[\mathrm{W/(m \cdot K)}]$	0.25	25	60
α_T	[1/K]	2.75×10^{-4}	10^{-5}	1.85×10^{-5}

The frictionless penalty term method was used easing the overall convergence of the model. This method allows for a certain body penetration leading to slightly lower maximum contact pressures than when using the augmented Lagrangian method. Due to that, the stiffness listed in Table 1 was obtained by matching the model predictions to the actual radial force measurements conducted using the split-shaft setup shown in Figure 5 [14]. The tangential load at the contact was shown to not significantly impact the contact pressure nor the contact width for a seal with the material properties as given in Table 1.

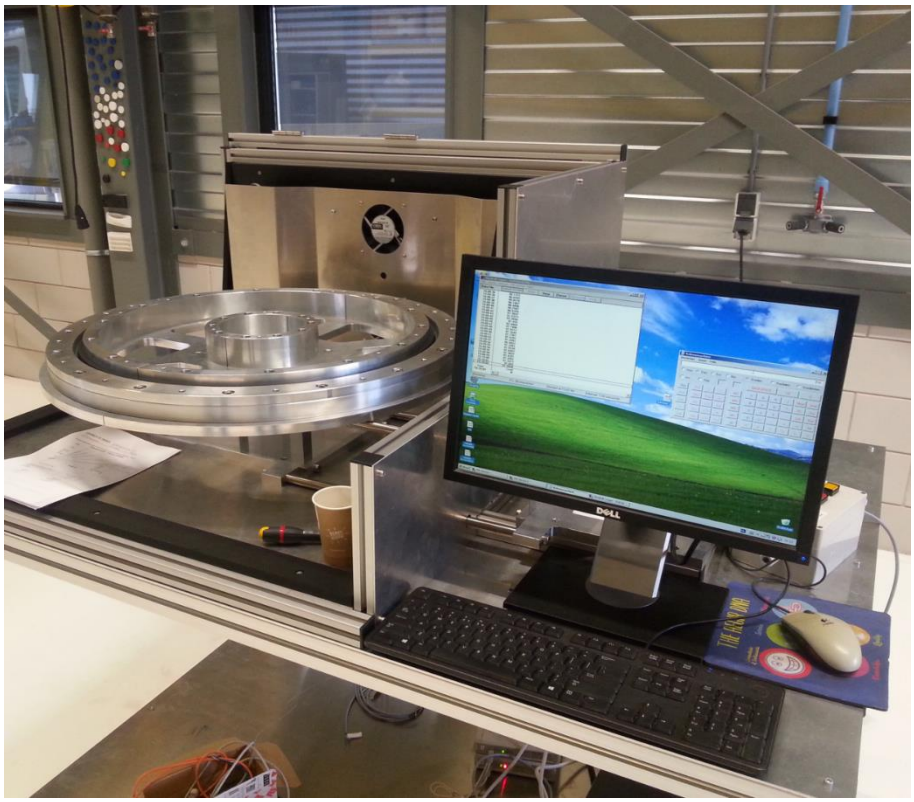

Figure 5. *Split-shaft setup used for measuring the radial force exerted by the stern tube seal.*

The radial and angular static misalignments were implemented by prescribing the displacement of a rigid shaft as depicted in Figure 2. The hydrostatic pressure was modelled as a true follower load coupled to the x direction in Figure 6. The symmetric nature of the components and the misalignments allowed to only model half the seal. For the study of hot spots, the temperature at the tip of the seal was prescribed as a boundary condition and the energy equation was solved using the same convective coefficients as used by Stakenborg [3] while the surrounding temperature was set to 20 °C. A quad element mesh was used for the seal and shaft sections. A high degree of mesh refinement on the circumferential direction was required so the pressure profile of the three-dimensional model matched with the one obtained when using an equivalent axisymmetric model.

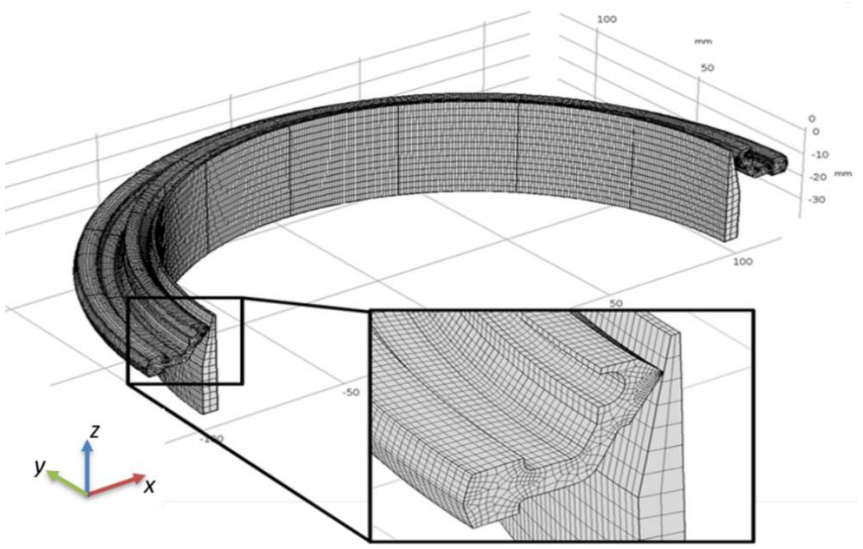

Figure 6. *Three-dimensional model of the seal. Note the taper shaft part required for its concentric assembly.*

The dedicated setup schematically shown in Figure 7 was developed allowing to measure the contact area between the seal and the shaft. The setup is equipped with a glass shaft which allows for the direct inspection of the contact area. A precision camera (Dino-Lite, Taiwan, China) and a 45 degrees mirror are assembled on a turning table allowing to directly observe the contact area along the complete perimeter of the seal. The Frustrated Total Internal Reflection technique is used to ease the visualization of the contact [4,14]. The setup also allows the housing parts (and the seal) to slide with respect to the glass shaft so a static offset can be simulated. The test rig was used to validate the predictions of the FE model.

Once the reliability of the model was ascertained and in agreement with Gabelli [24] and Wennehorst [4], the iso-viscous elastohydrodynamic film thickness expression (soft-EHL or I-EHL) introduced by Chittenden [25] was used to estimate the film thickness profile between the seal and the shaft under real operating conditions (Equations 1 to 4). The angle between the lubricant entraining vector and the major axis of the asperities was considered to be low enough to disregard its impact to the fluid film thickness.

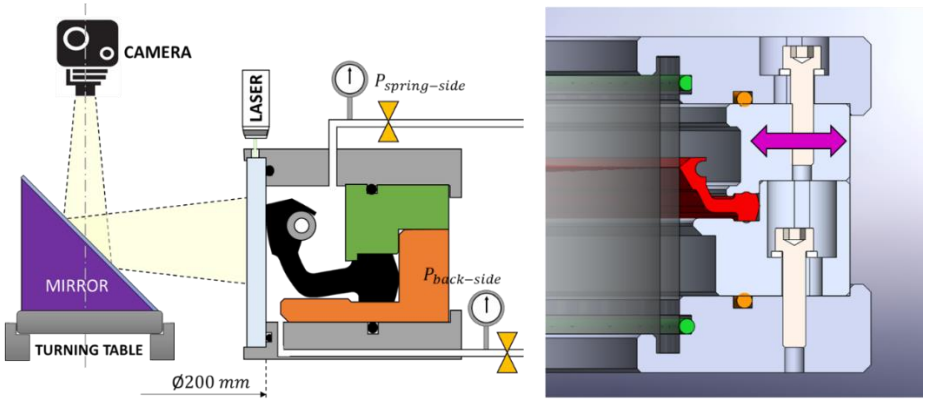

Figure 7. *Specialized seal setup to observe the seal contact under various misalignments and pressurized conditions.*

$$\frac{h_{cen}}{R_x} = 8.28\left(1 - e^{-0{,}86\left(\frac{R_y}{R_x}\right)^{2/3}}\right) U_x^{0{,}65} W_x^{-0{,}21} \tag{1}$$

$$U_x = \eta u_x / (E' R_x) \tag{2}$$

$$W_x = F / (E' R_x^2) \tag{3}$$

$$E' = \frac{2}{\frac{(1 - v_1^2)}{E_1} + \frac{(1 - v_2^2)}{E_2}} \tag{4}$$

Equation 1 predicts the central film thickness h_{cen} in elliptical conjunctions. Due to the lack of a radius of curvature in the entrainment direction of rotary lip seals, no pressure can be generated in circumferential directions. However, at the microscopic level, the radius of curvature can be defined. In order to model micro-hydrodynamic pressure generation, the I-EHL formula is applied at the asperity level. The seal surface roughness was scanned with lateral sampling intervals in both directions of 0.217 µm using a confocal microscope (Sensofar, Barcelona, Spain). From the surfaces roughness measurements, the effective wavelength $\lambda_{x/y}$ and the equivalent radius $R_{x/y}$ were obtained by applying Equations 5 and 6 in agreement with Wennehorst [4].

$$\lambda_{x/y} = 2\pi \frac{S_q}{\Delta_{x/y}} \tag{5}$$

$$R_{x/y} = \frac{1}{\sqrt{2}\, S_q} \left(\frac{\lambda_{x/y}}{2\pi} \right)^2 \tag{6}$$

Neither the contact pressure nor the contact area are uniformly distributed in the circumferential direction when the system is misaligned. Therefore, the number of asperities in the axial direction becomes the ratio between the contact width L_c and the effective wavelength λ_y. The loading of each asperity is obtained by uniformly distributing the contact pressure over the number of asperities in the axial direction (see Figure 8). The equivalent film thickness is defined as the I-EHL central film thickness h_{cen}. It is worth emphasizing that full film lubrication is assumed hence direct asperity contact does not occur and the so-called asperity load is fully carried by the micro-hydrodynamic pressure.

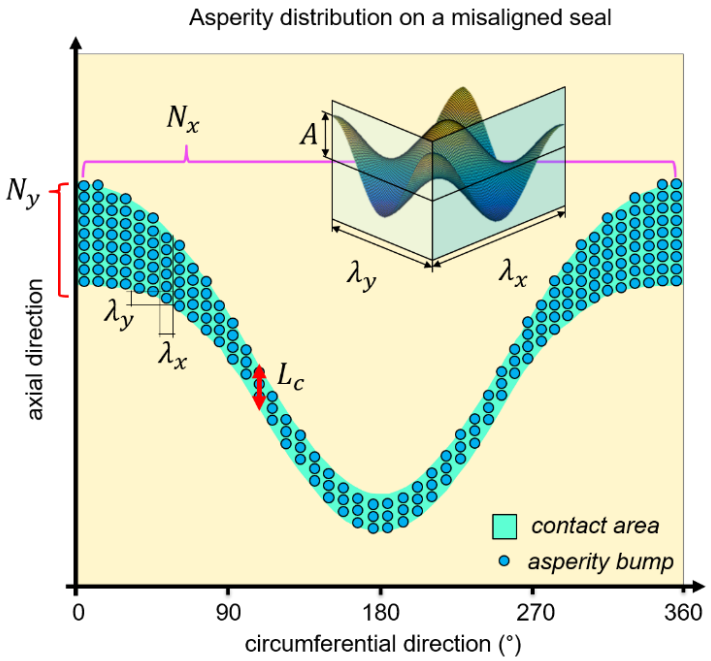

Figure 8. *Distribution of asperities on the contact area profile of a slanted seal (see Nomenclature).*

Ultimately, the two-dimensional mass-conservative Elrod–Adams Reynolds formulation (Equations 7 to 9) was solved on the gap profile obtained from the I-EHL film thickness expression. In the simulations, the contact width, the lubricant viscosity and density were kept constant in the computational domain. Further information on the strategy for solving the partial derivative equation can be found in [26]. The hydrodynamic pressure built-up induced by a non-uniform pressure distribution along the circumferential direction was then predicted. A sensitivity analysis of the minimum film thickness and the contact width is shown in the results section.

$$p = p_c + g\beta \ln(\phi) \tag{7}$$

$$\frac{\partial}{\partial x}\left(\frac{g\beta h^3}{12\eta}\frac{\partial \phi}{\partial x}\right) + \frac{\partial}{\partial y}\left(\frac{g\beta h^3}{12\eta}\frac{\partial \phi}{\partial y}\right) = \frac{u_x}{2}\frac{\partial(\phi h)}{\partial x} \tag{8}$$

$$full\ film\ zone \begin{cases} \phi > 1 \\ g = 1 \end{cases} \qquad cavitation\ zone \begin{cases} \phi < 1 \\ g = 0 \end{cases} \tag{9}$$

The strategy described allows to predict the impact of operating with a non-uniform contact pressure distribution in the circumferential direction for rotating conformal contacts. Note that the additional deformation of the seal tip due to the hydrodynamic action is disregarded in the approach discussed above and hence lower pressure values are expected in the real application.

3. Results

The deformed seal configurations as a result from the radial and angular misalignments are presented in Figure 9. On the top plots, the black arrows indicate the displacement of the shaft. In the figure, the seal is coloured according to the magnitude of the seal displacement. On the bottom plots the displacement of the seal in axial direction with respect to the assembled concentric situation is shown. Figure 10 shows the magnitude of the displacements under various misalignments.

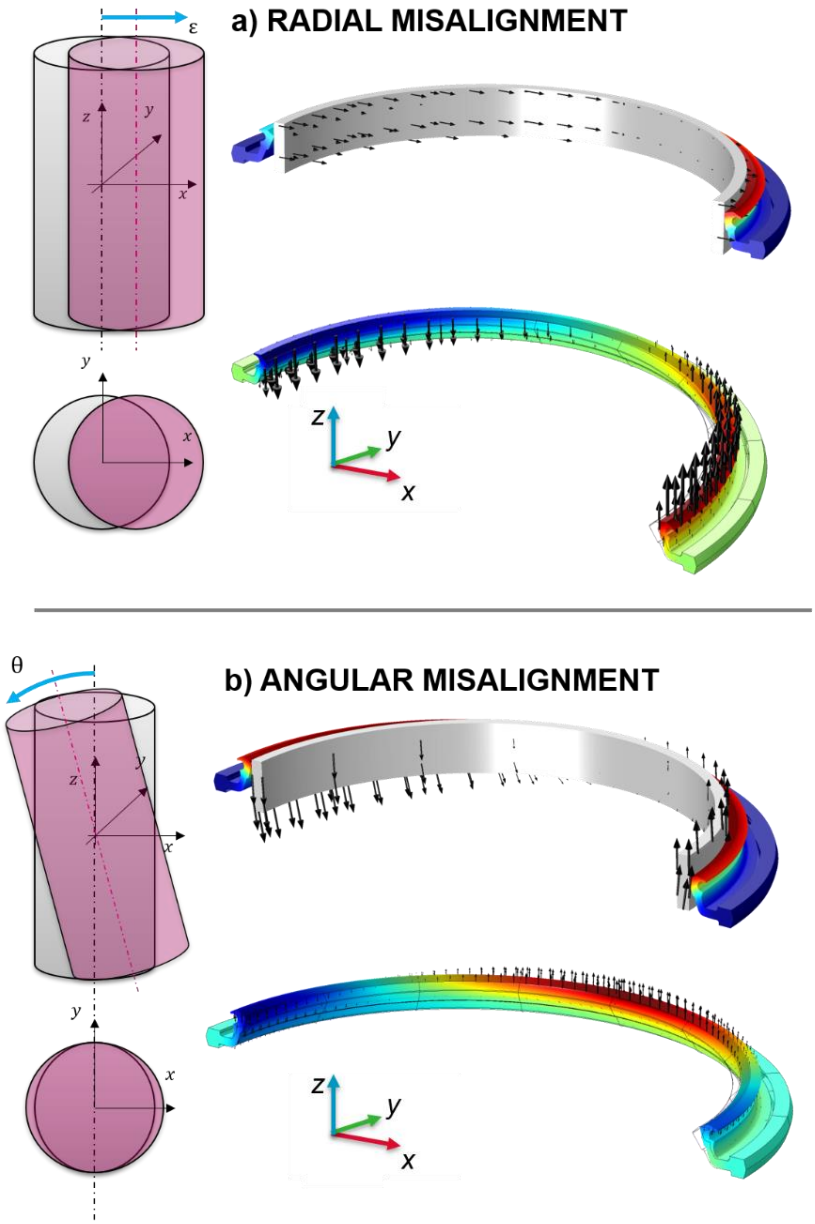

Figure 9. *Seal displacement due to radial (a) and angular (b) misalignments.*

The contact area profiles obtained under radial misalignment coincide with the schematic sketch presented by Van Bavel [17] however the contact area under angular misalignment does not. As it was observed with O-rings [27], under angular misalignment, the sealing section becomes oval increasing the diameter of the shaft on the direction of misalignment (see Figure 9). A negative axial displacement of the lip occurred where the diameter was enlarged and a displacement in the opposite direction developed where the diameter remained constant. As shown in Figure 10 the lip displacement under angular misalignment was smaller than under radial misalignment. Note that while a radial misalignment produced one sinus-shaped profile, an angular misalignment led to two sinus shaped profiles along the circumference. Using the setup shown in Figure 7 the contact area profile under radial misalignment was validated. The amplitude of the contact profile shows good agreement with the FE model predictions (see Figure 10). The calculated radial contact force along the circumferential direction is shown in Figure 11. It is shown that the pressure variation along the circumferential direction for the largest radial misalignment case ($\varepsilon = 1.5$ mm) oscillated by 20% with respect to its aligned position. For the largest angular misalignment modelled ($\theta = 2°$) the pressure variation only varied 1%.

When the hydrostatic pressure gradient was modelled as a boundary condition the displacements obtained were minimal even under frictionless conditions. Therefore, the seal–shaft misalignment due to the hydrostatic pressure gradient was found neglectable for this particular seal with a nominal diameter of 200 mm.

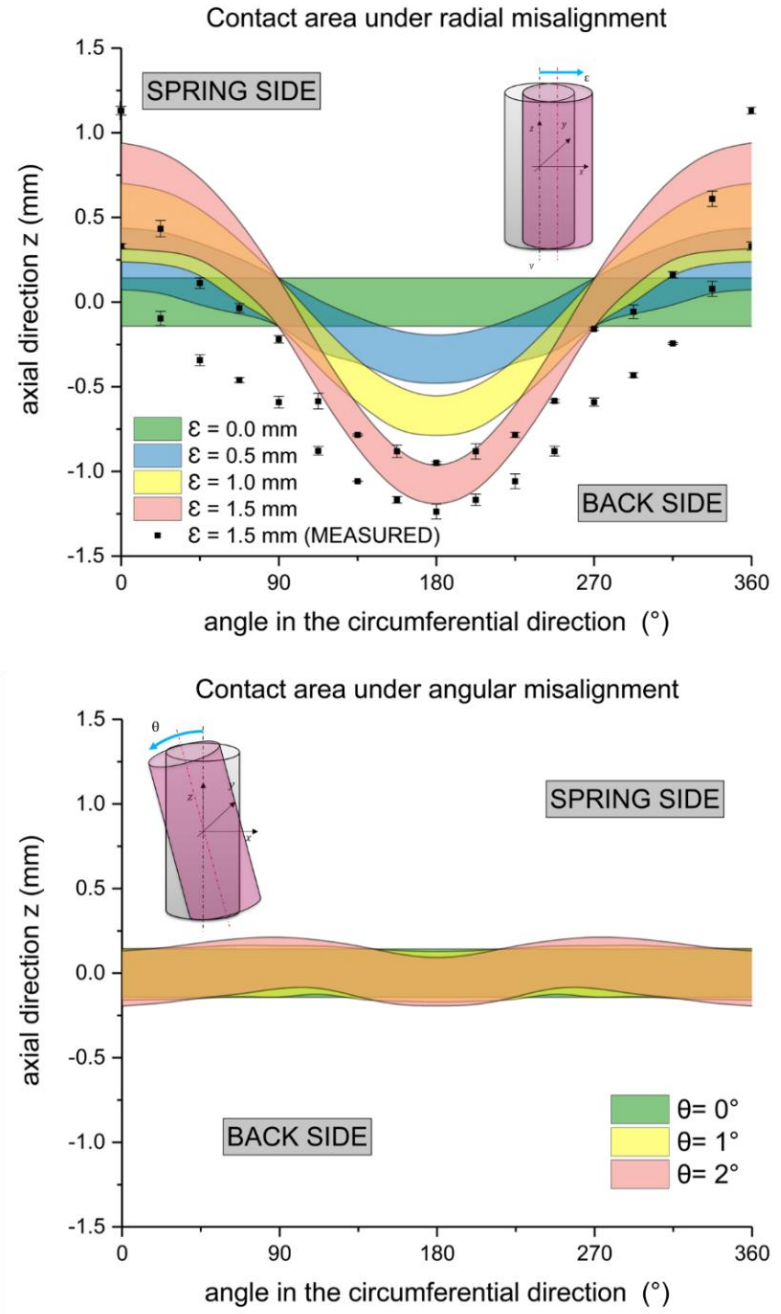

Figure 10. *Contact area around the shaft for various radial and angular misalignments.*

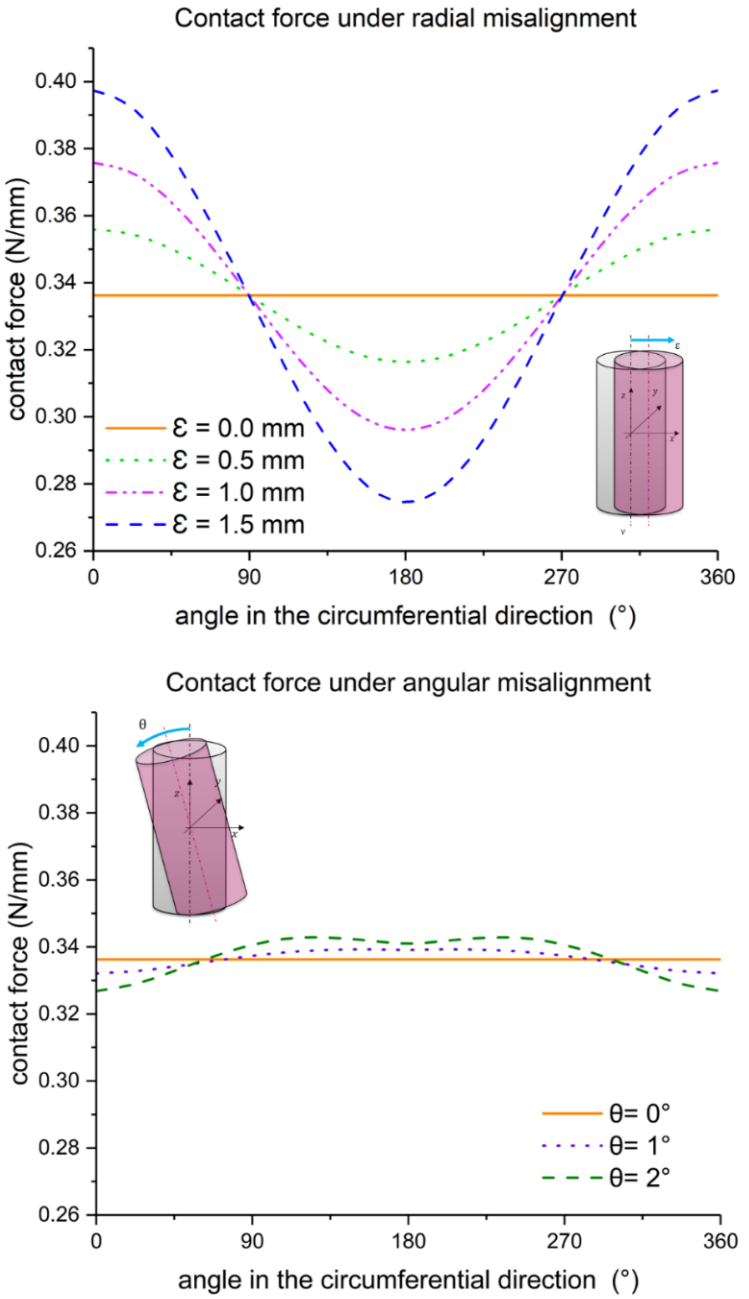

Figure 11. *Contact force around the shaft for various radial and angular misalignments.*

Lastly, the effect of temperature differences along the circumference is analysed. Such temperature difference can possible occur due to local frictional hot spots, leading to localized frictional heating. If temperature differences are present, the consequences will be magnified due to the large thermal expansion coefficients of elastomers. The presence of warmer points on the seal contact, i.e., hot spots, results into a non-uniform thermal expansion of the seal tip leading to a distorted gap profile [19]. The thermal distortion of the seal lip when a temperature gradient developed at the contact of a perfectly aligned seal was modelled. Hence the sole impact of temperature was captured and it is shown in Figure 12. The temperature gradient was defined along the contact area of the seal as a temperature boundary condition while a heat convection to a 20 °C surrounding was set for the rest of the seal boundaries. Figure 12 shows that with a temperature gradient of 20 °C along the seal contact the thermal expansion only slightly distorted the seal alignment, both the contact area and the contact pressure became larger at the warmest section of the seal.

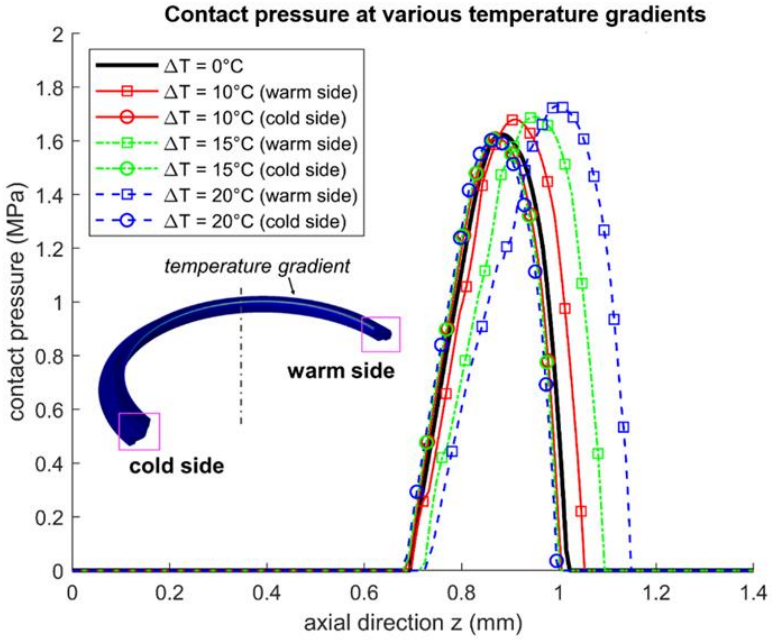

Figure 12. *Impact of a contact temperature gradient along the seal perimeter.*

Next, the film thickness along the circumferential direction was predicted for the 1.5 mm radial misalignment case. The worn surface topography scanned presented the following surface roughness parameters: $S_q = 1.24$ µm, $\Delta_x = 0.217$ µm and, $\Delta_y = 0.275$ µm (see Nomenclature). Figure 13 shows the average load that the micro-hydrodynamic pressure generated at each asperity together with the film thickness obtained by applying the I-EHL formulae (Equations 1–4). It is shown that the maximum hydrodynamic load was approximately three times the minimum one while the difference between the maximum and minimum film thickness was just of the order of 100 nanometres.

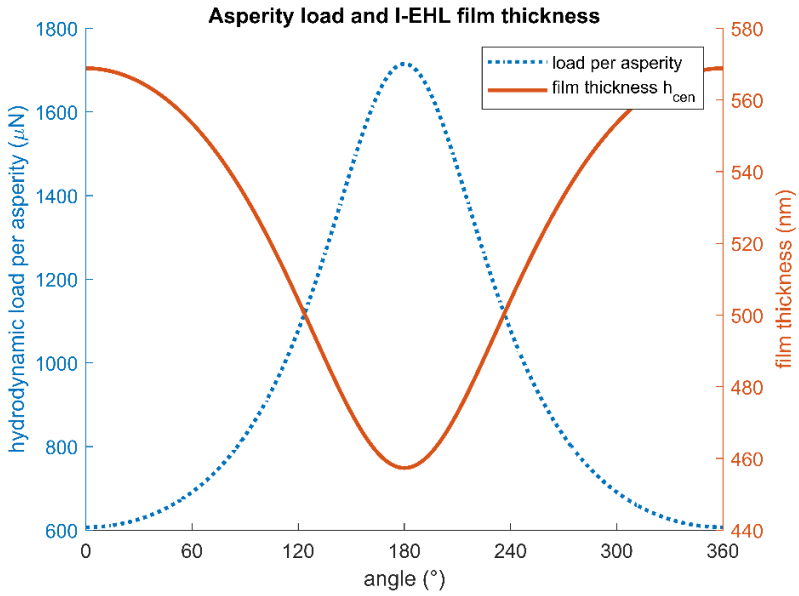

Figure 13. *Asperity loading and fluid film thickness for the seal with a 1.5 mm radial misalignment offset.*

Ultimately, the 2D Elrod–Adams equation (Equation 7) was solved on the I-EHL film thickness profile shown in Figure 13 so the hydrodynamic pressure build-up for the 1.5 mm radial misalignment situation was predicted. Figure 14 shows that the resultant hydrodynamic pressure profile was one order of magnitude smaller than contact pressure and hence it cannot be directly disregarded.

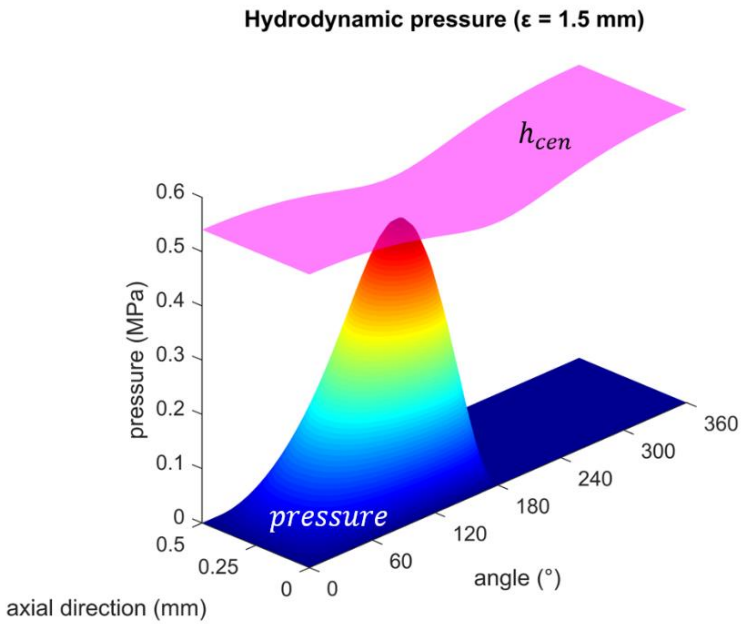

Figure 14. *Hydrodynamic pressure build-up under radial misalignment offset ($\varepsilon = 1.5\ mm$, $\eta = 100\ mPa \cdot s$, $\beta = 10^7\ Pa$, $u_x = 1\ m/s$, $L_c = 0.5\ mm$). The I-EHL film thickness from Figure 13 is magnified and shown in pink.*

To study the dependency of the lubricant film profile to the hydrodynamic pressure generation both the minimum film thickness (Figure 15) and the contact width (Figure 16) are varied while keeping the film thickness gradient deduced from I-EHL (see Figure 13). Both the minimum film thickness and the contact width were shown to be key parameters to the seal operation. It is observed that, for some cases, the hydrodynamic pressure build-up (disregarding the lip deformation) overcame the static contact pressure and hence it largely impacted the lubrication mechanism of rotatory lip seals.

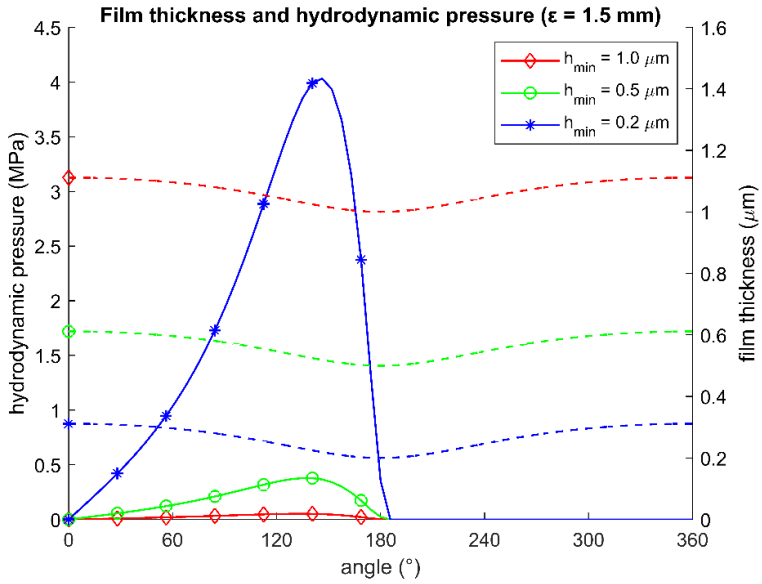

Figure 15. *Minimum film thickness sweep ($\varepsilon = 1.5\ mm$, $\eta = 100\ mPa \cdot s$, $\beta = 10^7\ Pa$, $u_x = 5\ m/s$, $L_c = 0.5\ mm$).*

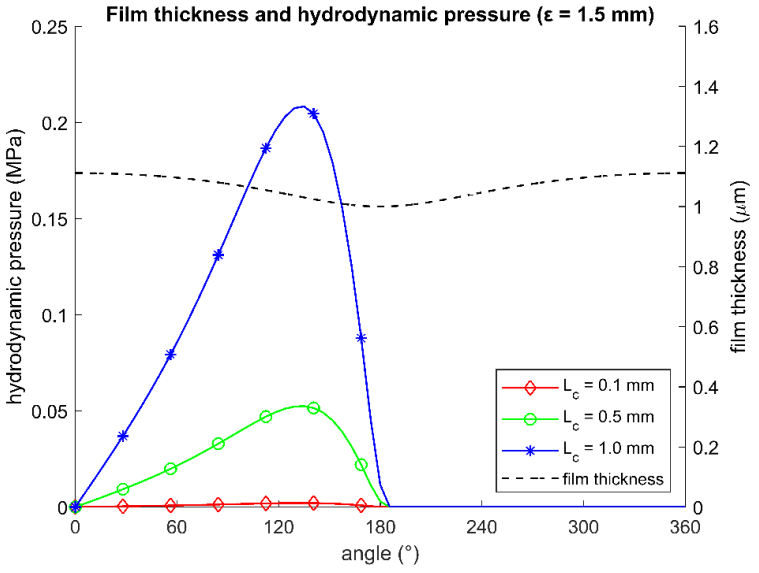

Figure 16. *Contact width L_c sweep with the I-EHL film thickness variation ($\varepsilon = 1.5\ mm$, $\eta = 100\ mPa \cdot s$, $\beta = 10^7\ Pa$, $u_x = 5\ m/s$, $h_{min} = 1\ \mu m$).*

4. Discussion

Various mechanisms leading to a non-concentric operation of stern tube seals were analysed. The radial misalignment was shown to distort the axial symmetry of the system more significantly than the angular one (skewness). Under real operating conditions a combination of both misalignments is to be expected. On the same line, the contact area and pressure did minimally vary for the canted seal. An angular misalignment of 2° is several times larger than the maximum slope mismatch expected in the aft stern tube bearing under free-sailing condition [28]. However, the length and diameter of the shaft is ship-dependent and the distance from the stern tube bearing to the sealing rings may lead to a larger angular misalignment. Additionally, assembling or manufacturing defects may also result in a shaft-seal non-concentric operation. The contact area measurements showed to be in good agreement with the FE model predictions. The use of a linear elastic model for the seal and the simplification of the seal boundary conditions can explain the slight differences observed between the model and the experiments. The sinusoidal and double-sinusoidal contact profiles along the circumference will lead to an axial flowrate promoting the lubrication of the seal. The swept contact area is in both cases increased so lower contact temperatures are expected. Although time-dependent effects were out of the scope of this research, the viscoelasticity of the material will play a significant role under dynamic misalignment, e.g., wobbling [11,12,29]. The difference in pressure between the top and bottom part of the 200 mm seal, i.e., around 0.02 bar pressure difference, did not significantly distort the alignment of the system. Note that the hydrostatic pressure difference increases with the shaft diameter and its contribution to the seal slant must be then re-evaluated when working with larger seals. The large thermal expansion coefficient of the seal material was shown to impact the position of the seal tip. Although the temperature of the seal is expected to even out on the long term, during its transient state, the temperature gradient promotes a wedge profile and therefore hydrodynamics.

The use of EHL film thickness expressions [21] for a conformal contact has its uncertainties and limitations [4]. Nevertheless, these formulae is used to evaluate the hydrodynamic potential arising from a

misaligned shaft-seal situation. Furthermore, the magnitude of the film thickness predicted is in fair agreement with the ones found in literature. For the largest case of radial misalignment, i.e., 1.5 mm offset, the maximum hydrodynamic load per asperity is 2.82 times larger than the minimum one. The maximum film thickness calculated with Equation 1 becomes only 1.24 times larger than the minimum one. That is because the loading of the junction does not significant impact the film thickness according to the I-EHL formulations revised [21,23,25]. Note that, in some particular cases, the contact area can increase further than the contact pressure on the loaded side of the seal. This leads to the counterintuitive situation where the asperities on the uncompressed side of the seal bear the largest loads.

The hydrodynamic pressures predicted from modelling a rotary lip seal as a slender journal bearing (Equation 7) showed to be of the same order of magnitude than the static contact pressures [14]. Note that such peak pressure values will not develop as the seal deforms as a result of it. Some authors [5] suggested that a varying contact pressure, whether due to the coils separation of the Garter spring or due to the moulding of hydrodynamic ribs, generates a secondary load pressure build-up mechanism. The same may occur due to the inherent viscoelasticity of the seal material [11,12]. The analysis shows that minute gap gradients suffice to generate a significant hydrodynamic action and that, together with the minimum film thickness and the contact width, impacts the normal operation of rotary lip seals. Furthermore, if such macroscopic hydrodynamic pressures develop, the micro-elastohydrodynamic working principle behind rotary lip seals will be distorted. As it occurs with visco-seals, the pumping ability vanishes with the alignment of the shaft. When it comes to modelling, the widely used approach presented by Salant [4,5] analyses a single patch (i.e., cell) of the seal surface and the results are extrapolated to the rest of the contact, i.e., these cells are assumed to be periodic along the circumferential direction. However, when the pressure is not uniformly distributed along the circumferential direction, each surface patch operates under unique operating conditions and hence each patch must be independently evaluated.

It is worth mentioning that the sinus-shaped contact area will further promote the hydrodynamic action. The slant of the contact area

unequivocally leads to a normal-to-the-contact shaft velocity component (hereby omitted). Although an early model accounting for this velocity component is available [8], a more advanced hydrodynamic model is required to accurately consider it.

5. Conclusions

Four different mechanisms distorting the axisymmetry of rotary lip seals were studied: radial and angular misalignments, the hydrostatic pressure gradient and the presence of hot spots at the seal contact. Both shaft misalignments and thermal expansion were found to contribute to hydrodynamic pressure build-up. On the other hand, the hydrostatic pressure differences between the top and the bottom of a stern tube seal do not significantly influence hydrodynamic effects for the stern tube seal studied. The radial and angular misalignments showed substantial different contact profiles. The misalignment-induced hydrodynamics arising from the equivalent film thickness profile were shown to be significant. This pressure build-up was shown to be extremely sensitive to the minimum film thickness and contact width. The results show that the assumption of periodic cells on the circumferential direction when modelling rotary lip seals must be reviewed for misaligned configurations.

Acknowledgments: Rob Dierink, Eric de Vries, Robert-Jan Meijer and Thomas Giorgio for their contribution to the development of the contact area glass setup. Philippe Vergne, Kees Venner and Bengt Wennehorst for their advice in I-EHL theory. Wojciech Litwin for providing data on the tail shaft dynamic behaviour.

References

[1] E.T. Jagger, “Rotary Shaft Seals: The Sealing Mechanism of Synthetic Rubber Seals Running at Atmospheric Pressure,” *Proc. Inst. Mech. Eng. Part J J. Eng. Tribol.*, vol. 171, no. 1, pp. 597–616, 1957.

[2] D.E. Johnston and R. Vogt, “Rotary shaft seal friction, the influence of design, material, oil and shaft surface,” *SAE Tech. Pap.*, no. 41 2, 1995.

[3] M.J.L. Stakenborg, “On the sealing mechanism of radial lip

seals," Ph.D. dissertation, Eindhoven University of Technology, 1988.

[4] B. Wennehorst, "On Lubrication and Friction in Soft Rough Conformal Sliding Contacts," Ph.D. dissertation, Leibniz Universität Hannover, 2016.

[5] R.F. Salant, "Theory of lubrication of elastomeric rotary shaft seals," *Proc. Inst. Mech. Eng. Part J J. Eng. Tribol.*, vol. 213, no. 3, pp. 189–201, 1999.

[6] H.K. Müller and B.S. Nau, "Rotary Lip Seals," in *Fluid Sealing Technology: Principles and Applications*, New York: Marcel Dekker Inc., 1998, pp. 73–110.

[7] Y. Kawahara, M. Abe, and H. Hirabayashi, "An Analysis of Sealing Characteristics of Oil Seals," *ASLE Trans.*, vol. 23, no. 1, pp. 93–102, 1980.

[8] L.A. Horve, *Shaft seals for dynamic applications*. New York: Marcel Dekker Inc., 1996.

[9] M.O.A. Mokhtar, M.A.A. Mohamed, M.E. El-Giddawy, and S.A.Y. Yassen, "On the effect of misalignment on the performance of U-type lip seal," *Wear*, vol. 223, no. 1–2, pp. 139–142, 1998.

[10] Y. Arai, "Sealing theory in oil seals - 1," in *JSLE-ASLE International Lubrication Conference*, 1976, pp. 830–839.

[11] M.J.L. Stakenborg, "Visco-Elastohydrodynamic (VEHD) Lubrication in Radial Lip Seals: Part 1 - Steady-State Dynamic Viscoelatic Seal Behavior," *Trans. ASME*, vol. 112, p. 578, 1990.

[12] B. van der Vorst and M. Organisciak, "Fast Analytical Model for Followability Prediction of Rotary Shaft Seals," in *19th International Sealing Conference*, 2016.

[13] G. Poll and A. Gabelli, "Formation of Lubricant Film in Rotary Sealing Contacts: Part II—Lubricant Film Modeling."

[14] F.X. Borras, M. Bazrafshan, M. B De Rooij, and D. J Schipper,

"Stern tube seals under static condition: A multi-scale contact modeling approach," *Proc. Inst. Mech. Eng. Part J*, May 2020.

[15] A. Tasora, E. Prati, and T. Marin, "A method for the characterization of static elastomeric lip seal deformation," *Tribol. Int.*, vol. 60, pp. 119–126, 2013.

[16] B. Pinedo, J. Aguirrebeitia, M. Conte, and A. Igartua, "Tri-dimensional eccentricity model of a rod lip seal," *Tribol. Int.*, vol. 78, pp. 68–74, Oct. 2014.

[17] P.G.M. van Bavel, "The Leakage-Free Operation of Radial Lip Seals," Ph.D. dissertation, Eindhoven University of Technology, 1997.

[18] W. Litwin, "Experimental Investigation on Marine Main Shaft," *Int. Jt. Tribol. Conf.*, pp. 1–3, 2010.

[19] W. Sinzara, I. Sherrington, E.H. Smith, H. Brooks, and A. Onsy, "Effects of Eccentric Loading on Lip Seal Performance," in *6th European Conference on Lubrication Management and Technology*, 2018.

[20] M. Organisciak, P. Baart, and A. Paykin, "Theoretical and experimental study of the frictional losses of radial shaft seals for industrial gearbox," *Power Transmission Engineering*, pp. 58–63, 2015.

[21] B.J. Hamrock, S.R. Schmid, and B.O. Jacobson, *Fundamentals of Fluid Film Lubrication*, 2nd ed. New York: CRC Press, 2004.

[22] M.T. Fowell, C. Myant, H.A. Spikes, and A. Kadiric, "A study of lubricant film thickness in compliant contacts of elastomeric seal materials using a laser induced fluorescence technique," *Tribol. Int.*, vol. 80, no. m, pp. 76–89, 2014.

[23] G. Nijenbanning, C.H. Venner, and H. Moes, "Film thickness in elastohydrodynamically contacts," vol. 176, pp. 217–229, 1994.

[24] A. Gabelli, "Micro-elastohydrodynamic lubricant film formation in rotary lip seal contacts," *Tribol. Ser.*, vol. 14, pp. 57–68, 1989.

[25] R.J. Chittenden, D. Dowson, and C.M. Taylor, "Paper VIII(ii) The lubrication of elliptical conjunctions in the isoviscouselastic regime with entrainment directed along either principal axis," *Tribol. Ser.*, vol. 11, no. ii, pp. 247–260, 1987.

[26] E. Koukoulopoulos and C.I. Papadopoulos, "Piston ring performance in two-stroke marine diesel engines: Effect of hydrophobicity and artificial surface texturing on power efficiency," *Proc. Inst. Mech. Eng. Part J J. Eng. Tribol.*, vol. 232, no. 8, pp. 940–963, 2018.

[27] M.S. Kalsi and G.A. Fazekas, "Feasibility Study of a Slanted O-Ring as a High Pressure Rotary Seal," *ASME*, p. 302, 1973.

[28] R. Roemen, "Calculations on the Oil Film Between a Propeller Shaft and the Aft Sterntube Bearing," in *Volume 1: Offshore Technology; Polar and Arctic Sciences and Technology*, 2011, pp. 815–821.

[29] M. Silvestri, E. Prati, and A. Tasora, "Numerical Analysis of Sealing Conditions in Elastomeric Rings," *AIMETA Int. Tribol. Conf.*, 2004.

(This page is intentionally left blank)

Paper D

(This page is intentionally left blank)

Misalignment-Induced Macro-Elastohydrodynamic Lubrication in Rotary Lip Seals

F.X. Borras[1], M.B. de Rooij[1] and D.J. Schipper[1]

[1]University of Twente, Surface Technology and Tribology, Enschede, The Netherlands

(This page is intentionally left blank)

Abstract: Typically, film formation in a rotary lip seal is explained by microscopic effects, but here it is explained from a macroscopic point of view. When the nominal parallelism between the shaft and the seal is lost, the contact area is distorted leading to a skewed sealing profile. The resultant slanted gap between the shaft and the seal presents a macroscopic wedge profile in the direction of rotation, hence constituting a source of hydrodynamics. An elastohydrodynamic model is developed predicting the implications of operating a rotary lip seal under misalignment. It is concluded that the non-concentric operation of rotary lip seals leads to a bidirectional fluid migration from the back to the spring side of the seal and vice versa.

Keywords: lip seal, film thickness, elastohydrodynamic, soft, lubrication, rotary, misalignment, stern tube seal, marine.

Nomenclature

ε	Radial misalignment (offset)	$[m]$
v_{shaft}	Shaft liner velocity	$[m/s]$
x, y, z	Cartesian coordinate system	$[m, m, m]$
r, z, ϕ	Cylindrical coordinate system	$[m, m, rad]$
n, t	Normal and tangential directions to the seal contact	$[m, rad]$
$v_{n/t}$	Linear velocity in the normal and tangential directions	$[m/s]$
$v_{z/\phi}$	Linear velocity in the axial and circumferential directions	$[m/s]$
$v_{x_{a/b}}$	Linear velocity in the x direction of surfaces a and b	$[m/s]$
$v_{y_{a/b}}$	Linear velocity in the y direction of surfaces a and b	$[m/s]$
$v_{z_{a/b}}$	Linear velocity in the z direction of surfaces a and b	$[m/s]$
η	Dynamic viscosity of the lubricant	$[Pa \cdot s]$
h	Fluid film thickness (gap between the seal and the shaft)	$[m]$
h_{min}	Minimum film thickness between the seal and the shaft	$[m]$
p	Hydrodynamic pressure	$[Pa]$
p_c	Cavitation pressure	$[Pa]$
ρ_c	Density of the lubricant in the cavitation region	$[kg/m^3]$
κ	Bulk modulus of the lubricant	$[Pa]$
ξ	Dimensionless cavitation variable	$[-]$
g	Cavitation index	$[-]$
B	Contact width	$[m]$

α	Angle on the back side when misaligned	$[rad]$
β	Angle on the spring side when misaligned	$[rad]$
α_0	Angle on the back side when aligned	$[rad]$
β_0	Angle on the spring side when aligned	$[rad]$
Λ	Rotation of the hinge model	$[rad]$
A, B, C	Constitutive points of the hinge model	$[m]$
L	Distance from point A to point B of the hinge model	$[m]$
T	Distance from point B to point C of the hinge model	$[m]$
$q_{s\to b}$	Flow rate from the spring side to back side of the seal	$[m^3/s]$
$q_{b\to s}$	Flow rate from the back side to spring side of the seal	$[m^3/s]$
d_r	Displacement in the radial direction	$[m]$
C_r	Radial direction compliance matrix, $N \times N$ (N = number of nodes)	$[m/Pa]$
i, k	Indices used in the compliance matrix method ($p_i, C_{r_{i,k}}, d_{r_i}$)	$[-]$
$\Delta n, \Delta t$	Resolution of the grid in the normal and tangential directions	$[m, m]$
t_s	Time	$[s]$

1. Introduction

In the 1950s a degree of hydrodynamic action was observed carrying some or all of the radial load of rotary lip seals [1]. The lack of an apparent wedge profile in the direction of the velocity, i.e. in the circumferential direction, means there is no driving force for hydrodynamic lubrication in the circumferential direction. Since the success or failure of a rotary lip seal was shown to be tightly coupled to the surface roughness of the contact, researchers relied on microscopic-scale hydrodynamics to explain the operation of rotary lip seals. The nowadays widely accepted theory is based on the micro-hydrodynamic pressure bumps generated between the seal and the asperities on the shaft. This allows the load to be carried, wholly or partially, in the seal-shaft contact [2]. Additionally, most rotary lip seals present an inherent pumping direction towards one side of the seal; this is known as the reverse, upstream or back pumping mechanism [3]. Still on the microscopic level, this effect is explained by the distortion of the seal asperities due to the shearing forces resulting from the shaft rotation (see Figure 1). The seal asperities deform in micro-ridges or vanes resembling a screw pump, a visco-seal or a herring-bone bearing, hence with the ability of pumping fluid

towards one of the sides of the seal [4]. This approach assumes perfect concentricity between the seal and the shaft. However, under real operating conditions nominal parallelism is hardly ever achieved [5].

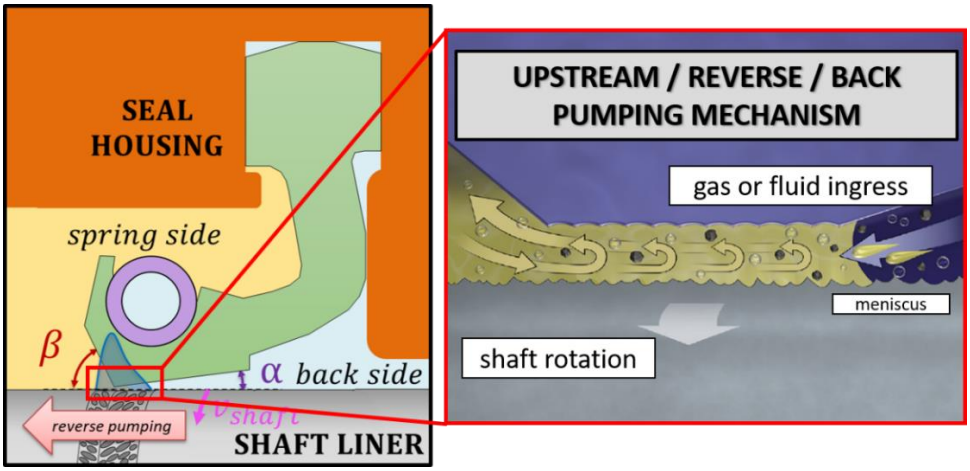

Figure 1. *Reverse pumping mechanism. Based on* [6].

Jagger [1] tested fully-immersed rotary lip seals. The lubricants on each side of the seal were dyed a different colour. He observed that after few minutes the lubricants mixed on both sides of the seal, hence no effective liquid separation could be achieved. Kalsi [7] showed that O-rings installed at a slant show a lower running temperature, a greater flow rate and a lower wear rate. Horve [8] observed the same behaviour as Kalsi on canted rotary lip seals. In addition to better lubrication, the cooling of the contact area of skewed seals is improved by spreading the friction heat over a wider area [9]. Müller [10] and Gawlinksi [11] realized that, under dynamic radial misalignment, the axial motion of the tip of the seal resembled a reciprocating seal. They concluded that the tip oscillation further promoted the reverse pumping capability of a seal. Horve engineered a smart setup capable of replicating the oscillating motion of the seal tip while preventing the drag of lubricant in the circumferential direction [12]. Almost no leakage developed because of the sole reciprocating motion of the seal tip.

Arai [5] studied the initial reverse pumping by observing the seal-shaft interface from the spring side. He noted that the first droplets

appeared at single positions of the contact instead of as a film uniformly distributed along the whole shaft perimeter. The points at which leakage was spotted varied periodically. According to Arai, the inevitable whirling of the shaft when turning shifts the position of the wider contact zone along the seal path, resulting in a periodic liquid migration towards the spring side. Mokhtar [13] tested U-type rotary lip seals under traditional operating conditions, i.e. oil in the spring side and air in the back side. He showed that the leakage on a failing seal decreases with angular misalignment while the leakage increases with radial misalignment. Sinzara [14] tested stern tube seals under radial misalignment, showing that the maximum admissible offset before leakage decreases with the shaft velocity. Sinzara observed that the contact temperature decreased with seal-shaft eccentricity while the torque was kept fairly constant for the offsets he tested. That can be explained by the better seal contact cooling mechanism when misaligned [2]. On the other hand, Maoui showed that the frictional torque decreased when the seal was radially offset [15].

The followability of seals, understood as the capacity of a seal to follow the shaft motion, has also been a subject of research. Ishiwata [16] assumed that a rotating shaft has – indispensably – dynamic eccentric motion. He showed the loci of displacements of singular points at the tip of the seal under various angular velocities, seal-shaft interferences (or fittings) and dynamic eccentricities. Ishiwata reported that eccentric seals leaked even when the lip followed the shaft accurately. Sansalone [17] and van der Vorst [18] modelled the followability of viscoelastic seals when subjected to radial misalignment. Sansalone and van der Vorst ignored the role of the lubricant film, considering instead the failure of the system when the contact pressure between the seal and the shaft becomes zero [19]. Arai [5] tested dry and lubricated seals and concluded that a better followability was obtained when the seal-shaft interface was lubricated. He attributed the difference in followability to the fact that the cavitation of the lubricant film compensates partially for the viscoelasticity of the seal. Stakenborg [20] observed cavitation at the seal-shaft interface and, together with van Leeuwen [21], [22], based the visco-elastohydrodynamic (VEHD) lubrication theory on the inability of the seal material to follow the shaft. As a result, convergent macroscopic wedges develop on the contact, leading to hydrodynamic action.

Schuck [23] tested rotary seals running on shafts with a circular profile and shafts with triangular polygonal-profile cross sections. The noncircumferential shaft profiles showed a lower frictional torque; however, they leaked at the lowest shaft velocities.

In a former publication by the authors, the variation of the contact pressure and contact area of a lip seal when misaligned was investigated [24]. The consequences of operating with a non-uniform contact pressure profile in the circumferential direction were approached via the EHL theory. It was also shown that when the contact becomes slanted an effective wedge is generated in the direction of motion. Horve [12] presented an analytical model based on the hydrodynamic action resulting from operating under misaligned conditions. Horve assumed that the flow rate along a rotary seal derived exclusively from the seal misalignment, i.e. the liquid dragged by the shaft in the circumferential direction. Although the seal was considered skewed, Horve's model assumes that both the contact pressure profile and the contact width are uniform along the circumferential direction and equal to the concentric static case.

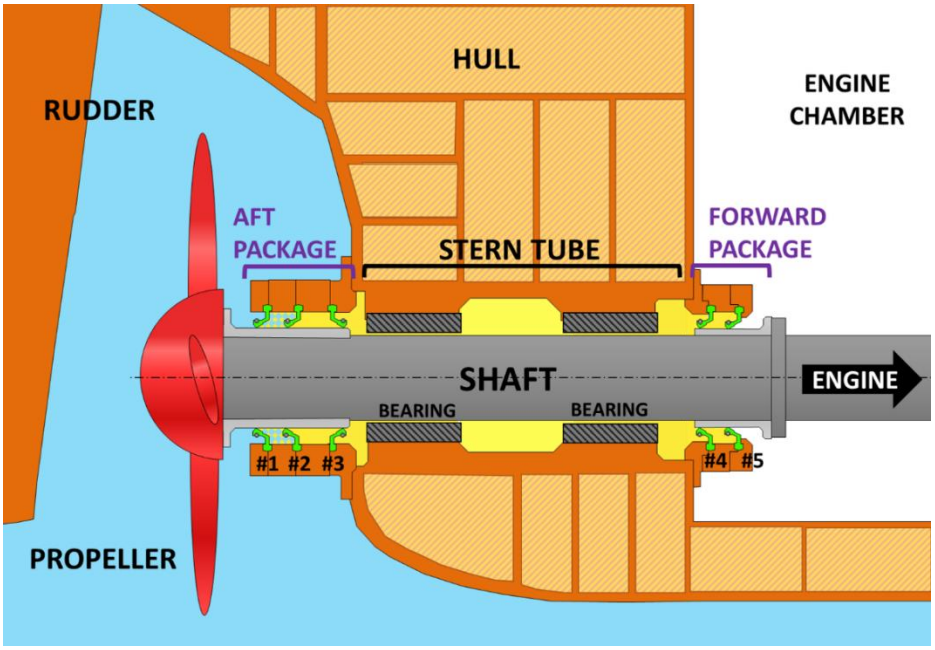

Figure 2. *Stern tube seal of a ship.*

Stern tube seals are one of the largest kinds of rotary lip seals. As shown in Figure 2, several sealing rings are assembled in-line to avoid the spillage of lubricant to the environment while preventing the ingress of water to the stern tube. The middle seals operate with lubricant on both sides while the outermost and innermost seals operate against a water-oil and an oil-air interface respectively. All the seals operate under fully flooded conditions on both the spring and the back sides except for the one facing the engine chamber. Generally, rotary lip seals pump liquid towards the spring side. Consequently, if this were the case with stern tube seals, the two outer-most seals would constantly force the lubricant out of the stern tube. In reality, a constant spillage of lubricant develops [25], often combined with the ingress of water to the stern tube. In that case, a water-in-oil emulsion forms in the chamber between seal #1 and #2, impacting the rheology of the lubricant and at the same time challenging its hydrolytic stability [26]. In this study, only the fluid viscosity is used to characterize a lubricant. The pressures reached in the rotary lip seal application rarely overcome few MPa [2] and hence the viscosity variation with pressure is usually neglected.

Although the literature on the misaligned running of rotary lip seals is scarce and often contradictory, special seal designs are readily available in the market: these boost the lubrication of the contact by promoting a slanted contact profile [8], e.g. Waveseal® [2] , Gerromatic® [9] and Kalsi® seals. In these types of seals the initial seal geometry already presents a convergent wedge profile in the circumferential direction, favouring a hydrodynamic lift-off.

This study analyses the flow rates resulting from operating with a slanted contact profile caused by misalignments. While the followability of the viscoelastic seal limits its range of operation [18], misalignment impacts the seal before the contact pressure between the shaft and the seal becomes null [19]. Building on Horve's early model [12], a macroscopic elastohydrodynamic lubrication model has been developed that is capable of predicting the misalignment-induced hydrodynamic pumping of the seal on a macroscopic level. The model assumes full film lubrication and both the seal material viscoelasticity and the surface roughness are ignored. The focus is placed on the hydrodynamics arising from operating with a slanted contact profile,

which is disregarded by the extensively used micro-EHL models [27] that assume the nominal parallelism between the seal and the shaft.

2. Materials and Methods

Previously, [19] analysed the displacement of the lip seal used in this study to various misalignments by modelling half a seal and applying symmetry boundary conditions at its ends. However, this simplification is not feasible when including hydrodynamics by solving the Reynolds partial differential equation (PDE) [28], i.e.

$$\frac{\partial}{\partial x}\left(\frac{\rho h^3}{12\eta}\frac{\partial p}{\partial x}\right)+\frac{\partial}{\partial y}\left(\frac{\rho h^3}{12\eta}\frac{\partial p}{\partial y}\right) = \frac{\partial}{\partial x}\left(\frac{\rho h\left(v_{x_a}+v_{x_b}\right)}{2}\right)+\frac{\partial}{\partial y}\left(\frac{\rho h\left(v_{y_a}+v_{y_b}\right)}{2}\right) + \rho\left(v_{z_a}-v_{z_b}-v_{x_a}\frac{\partial h}{\partial x}-v_{y_a}\frac{\partial h}{\partial y}\right)+h\frac{\partial \rho}{\partial t_s}. \quad (1)$$

The film thickness gradients $\partial h/\partial y$ along the circumferential direction are not symmetric and therefore a full three-dimensional seal model is required.

Experimental analyses showed that the versatility of a full three-dimensional seal model was limited due to the large number of elements required. Figure 3 shows an example of a pressure distribution obtained with a full three-dimensional finite element model. The section view shown in the same figure allows for a better understanding of the macroscale hydrodynamics that develop in a misaligned rotary lip seal.

As shown in Figure 3, the shaft misalignment leads to a sinusoidal contact profile [8] and this presents a macroscopic wedge profile in the circumferential direction. For the particular case of radial misalignment, two convergent gaps are formed, one at the spring side and the other at the back side. Analogously, two divergent gaps are formed. The morphology of both gaps depends greatly on the seal design and the amount of misalignment. As the gap is symmetric, the pressure distribution is mirrored when the direction of the shaft is

reversed. Consequently, the flow rate from spring-to-back and back-to-spring sides is independent of the direction of rotation.

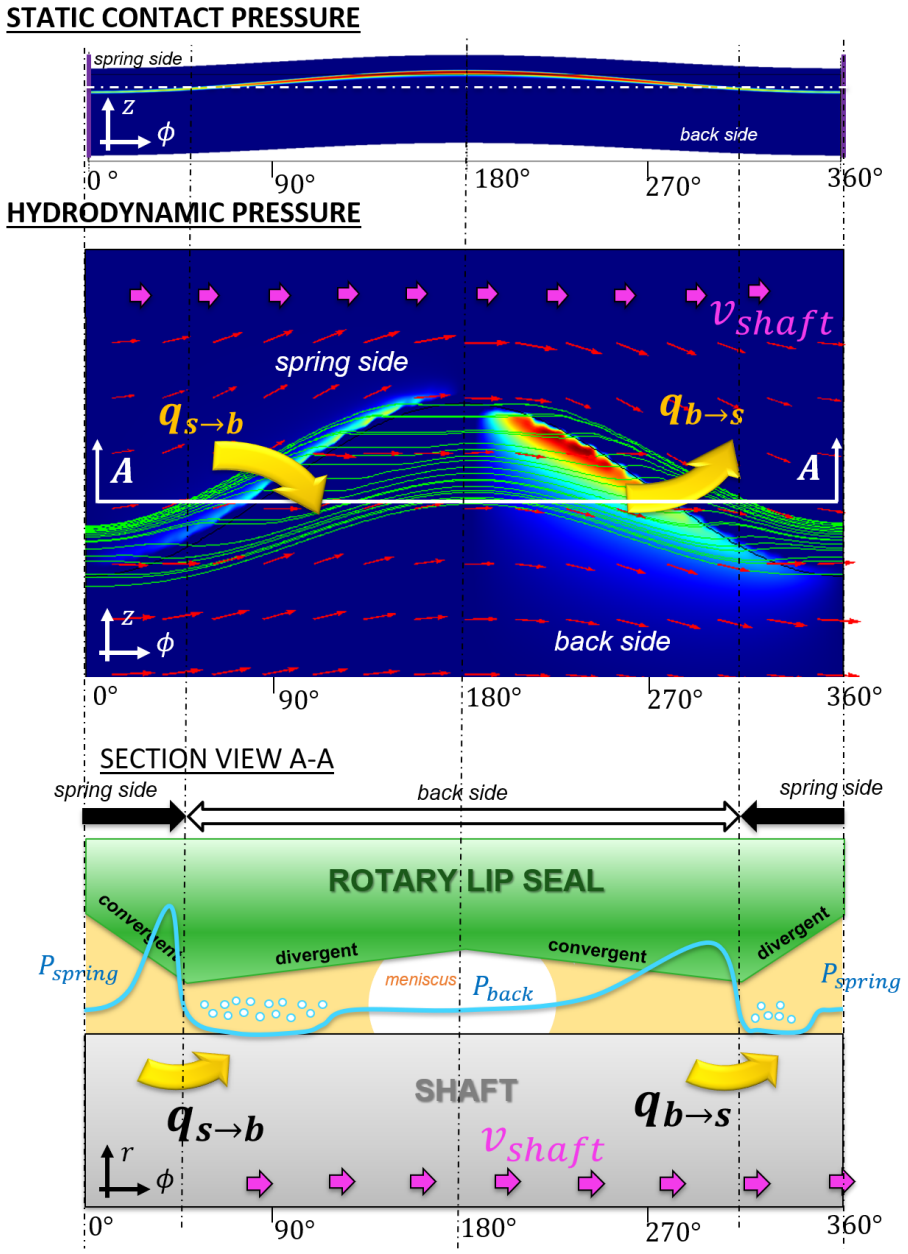

Figure 3. *Sketch of the hydrodynamic pressure build-up resulting from operating with a slanted contact profile.*

To gain insight into this phenomenon, a finite differences model has been developed in MATLAB® solving the Reynolds equation along the contact profile. Instead of using the axial and circumferential directions, the coordinate system is placed on the contact line in agreement with [12]. By using this alternative reference system shown in Figure 4, the contact becomes a straight line making the discretization of the gap and the results trivial. Consequently, the shaft velocity is decomposed in the normal and tangential directions as shown in Figure 4. The squeeze term and the shaft velocity in the z-direction are considered null. The stretch term of the Couette component of the Reynolds equation is also ignored since the tangential velocity hardly varies along the tangential direction $\frac{\partial v_t}{\partial t} \approx 0$ because the length in circumference direction is greater than the axial displacement.

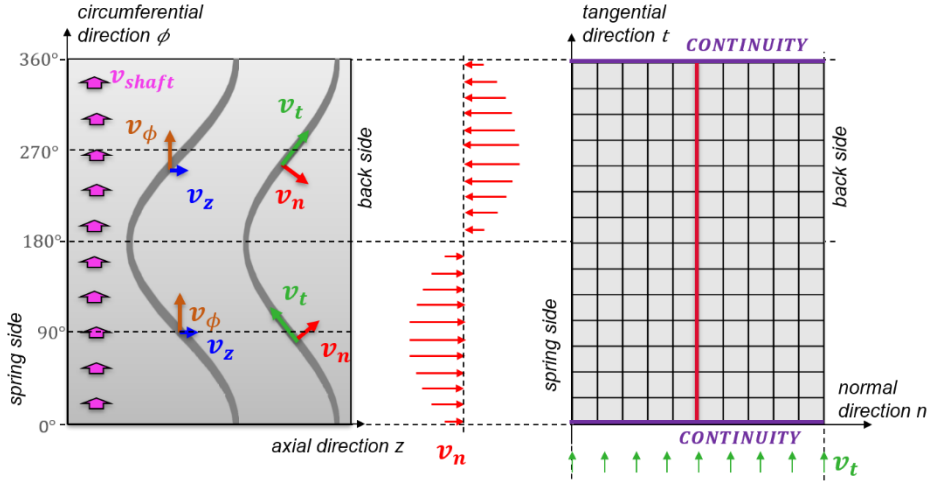

Figure 4. *Decomposition of the shaft speed in normal and tangential components.*

In this study, an analytical expression is prescribed for the seal-shaft separation, i.e. the gap. This facilitates the analysis of the misalignment-induced lubrication mechanism. In non-pressurized radially misaligned situations, the deformation of the seal was shown to be minimal [19] and the displacement experienced by the seal tip is basically a rigid body rotation as shown in Figure 5. In agreement with seminal lip seals theory which defines a hinge point as a design

parameter of lip seals [2], the simplified gap model shown in Figure 6 is used.

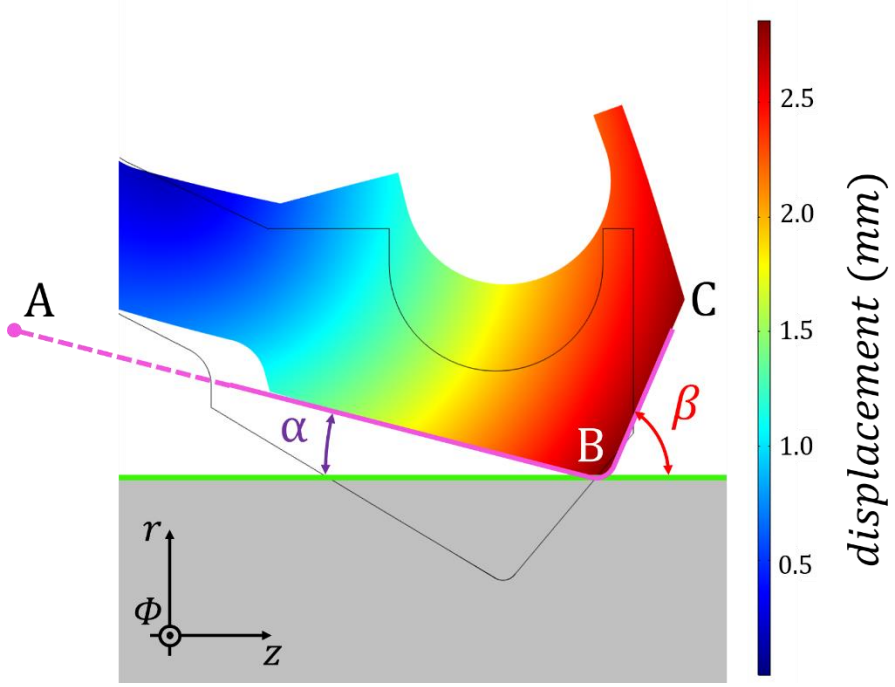

Figure 5. *Rotation of the seal head when assembled.*

While the convergent gap profile in the axial direction is self-evident, the wedge in the circumferential direction is not. The distance from the hinge point (point A) to the shaft liner is constant only when the misalignment is null (α_0 and β_0). The seal-shaft contact angles α and β vary along the circumferential direction according to the hinge rotation Λ as in

$$\Lambda = \alpha_0 - \alpha = \alpha_0 - asin\left(sin(\alpha_0) + \frac{\varepsilon}{L}\, cos(\phi)\right), \tag{2}$$

where Λ is determined by the amount of radial misalignment ε from geometrical considerations. The three points A, B and C shown in Figure 6 are described according to

$$\begin{aligned} A(n,r) = \Big\{ & -L\, cos\left(asin\left[sin(\alpha_0) + \frac{\varepsilon}{L} cos(\phi)\right]\right), \\ & L\, sin\left(asin\left[sin(\alpha_0) + \frac{\varepsilon}{L} cos(\phi)\right]\right)\Big\}, \end{aligned} \tag{3}$$

$$B(n,r) = \{0, \quad 0\}, \tag{4}$$

and

$$C(n,r) = \{T\,cos(\beta_0 + \Lambda)\,,\ T\,sin(\beta_0 + \Lambda)\}, \tag{5}$$

respectively. Eq. 3, 4 and 5 are obtained by applying a rotation Λ to the seal-shaft concentric position, i.e. the relative angle between the spring wall and the back wall is constant along the circumferential direction. The tip of the seal (point B) is smoothed using the expressions proposed by van Bavel [29]. Interestingly, the film thickness profile resembles the work of Hirani on misaligned bearings [30]. Notice that the radial misalignment influences the angles α and β. The colourmap in Figure 6b uses elevation fringes so the points at the same height are easily identified.

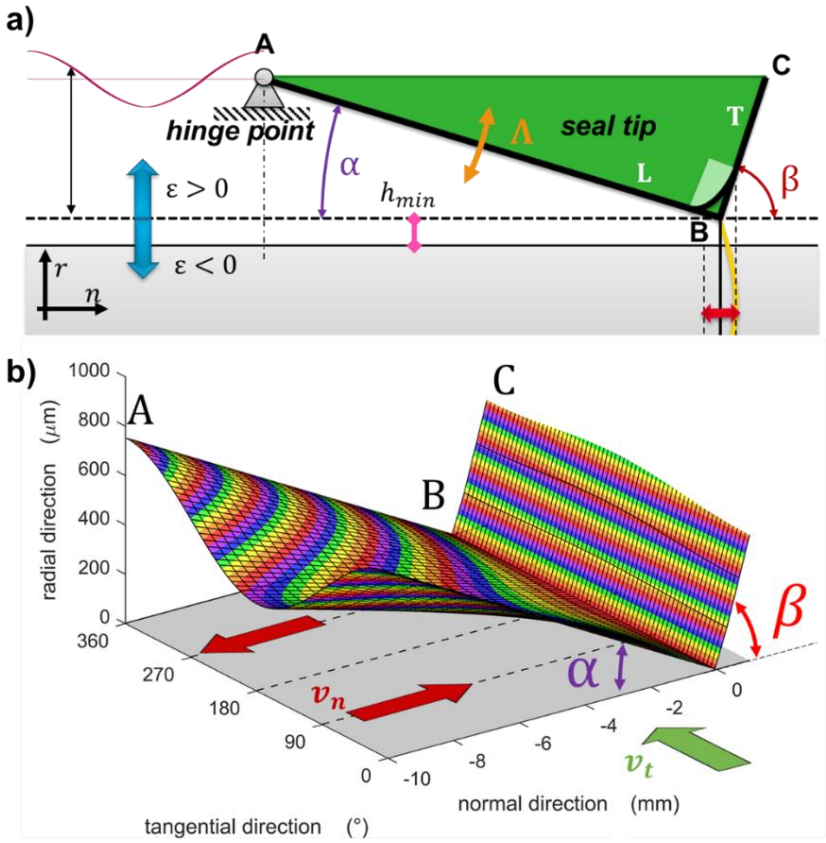

Figure 6. *Radially misaligned shaft-seal gap based on a hinge point.*

The gap profile shown in Figure 6 shows both convergent and divergent wedges in the direction of velocity. For instance, between 0 and 180 degrees, a hydrodynamic pressure build-up is expected at the back side of the seal (A-B), while cavitation is expected at the spring side (B-C). The Reynolds PDE shown in Eq. *1* does not account for the liquid cavitation and physically impossible negative pressures can be predicted. Cavitation plays an essential role in rotary lip seals [5] and hence an alternative form of Eq. *1* is required to properly incorporate it.

The Elrod-Adams algorithm [31] allows to resolve the full film zone and the cavitation zone in a mass conservative way in a single equation. Instead of p, the Elrod-Adams algorithm solves the partial differential equation for a dependent universal variable

$$\xi = \frac{\rho}{\rho_c} \tag{6}$$

where ρ_c is the density of the liquid at the cavitation region. Together with a switch function g, the full film and the cavitation regions are specified as follows:

$$full\ film\ zone \begin{cases} \xi > 1 \\ g = 1 \end{cases} \qquad cavitation\ zone \begin{cases} \xi < 1 \\ g = 0 \end{cases} \tag{7}$$

The model relates the lubricant pressure and density through the fluid bulk modulus $\kappa = \rho \frac{\partial p}{\partial \rho}$. Therefore, relating to ξ, within the full film region this relation can be written as

$$g\kappa = \xi \frac{\partial p}{\partial \xi}. \tag{8}$$

After integrating 8, this becomes

$$p = p_c + g\kappa\, ln(\xi). \tag{9}$$

When substituting Eq. 9 into Eq. *1* and considering the velocity v only in the x direction, the stationary Elrod-Adams partial differential equation reads

$$\frac{\partial}{\partial x}\left(\frac{g\kappa h^3}{12\eta}\frac{\partial \xi}{\partial x}\right) + \frac{\partial}{\partial y}\left(\frac{g\kappa h^3}{12\eta}\frac{\partial \xi}{\partial y}\right) = \frac{v}{2}\frac{\partial(\xi h)}{\partial x}. \tag{10}$$

Ultimately, algorithm was solved using the following dimensionless variables

$$\bar{x} = \frac{x}{B}, \quad \bar{y} = \frac{y}{L}, \quad \bar{h} = \frac{h}{\sigma}, \quad \Psi = \frac{6\mu u B}{\kappa \sigma^2}, \tag{11}$$

rendering to

$$\frac{\partial}{\partial \bar{x}}\left(g\bar{h}^3 \frac{\partial \xi}{\partial \bar{x}}\right) + \left(\frac{B}{L}\right)^2 \frac{\partial}{\partial \bar{y}}\left(g\bar{h}^3 \frac{\partial \xi}{\partial \bar{y}}\right) = \Psi \frac{\partial(\bar{h}\xi)}{\partial \bar{x}}. \tag{12}$$

The model was validated against the results presented by Giacopini [32] and Almqvist [33]. Note that the viscosity is left constant within the computational domain. The developed model assumes full film lubrication disregarding surface roughness and consequently micro-hydrodynamics. In other words, the model assumes that a continuous separation exists between the seal and the shaft. Since the minimum separation between the seal and the shaft is an input, the results must be read qualitatively and not quantitatively.

The seal material is soft and quickly deforms under hydrodynamic action, i.e. soft-elastohydrodynamic lubrication (soft-EHL) [28]. EHL models need a double direction coupling between the hydrodynamic and deformation algorithms. The use of a full three-dimensional finite elements seal model was shown to be inefficient, so the radial deformation of the seal is computed using the influence coefficient approach [27], [34]. The compliance matrices are obtained through the linear perturbation method. This technique consists of assembling a compliance matrix C_r by iteratively applying single unity loads to the surface nodes of the seal contact [35] as shown in Figure 7. All the nodal displacements resulting from each unity loading constitute the columns of the compliance matrix. According to the principle of superposition, the overall deformation of the seal can be predicted according to

$$(d_r)_i = \sum_{k=1}^{N} (C_r)_{ik} \, (p \Delta n \Delta t)_k. \tag{13}$$

For simplicity, the concentric three-dimensional model of the assembled seal is used. In the model it is thus assumed that the micro-hydrodynamic lubrication carries the radial force between the seal and the shaft and therefore no solid-solid asperity contact is present. In this specific case, where the model is axisymmetric, it is possible to

apply the nodal loads to a single section of the seal as the displacement would be the same when applied to any of the other sections. Furthermore, as both the seal and the loading are symmetric, a half seal model with a symmetry boundary condition can be used, as in [24]. The axial and circumferential displacements were hereby ignored, as they contribute very little to the hydrodynamic action of a perfectly smooth seal. Notice that the resolution of the hydrodynamic computational domain shown in Figure 4 is determined by the number of nodes considered when building the compliance matrix C_r.

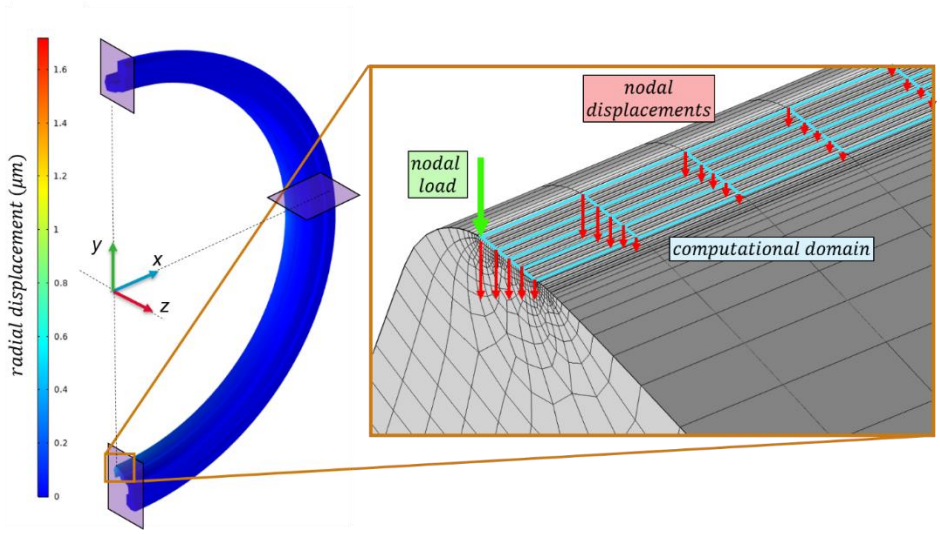

Figure 7. *Assembly of the compliance matrix by the linear perturbation method. Note that the resolution of the grid is reduced in this Figure.*

This elastohydrodynamic model is used to study the main variables governing the misalignment-induced lubrication induced by the normally oriented velocity component resulting from a slanted contact profile.

3. Results

The hydrodynamic model described above predicts the pressure distribution and consequently the flow rates on a misaligned seal-shaft gap profile. The model makes it possible to study the individual contribution of the shaft radial offset ε, the seal angles α and β, the

shaft liner velocity v_{shaft} and the lubricant dynamic viscosity η to the operation of a rotary lip seal under radial misalignment. As an example, a sinusoidal (hence symmetric) gap profile is input to the model, leading to the results shown in Figure 8.

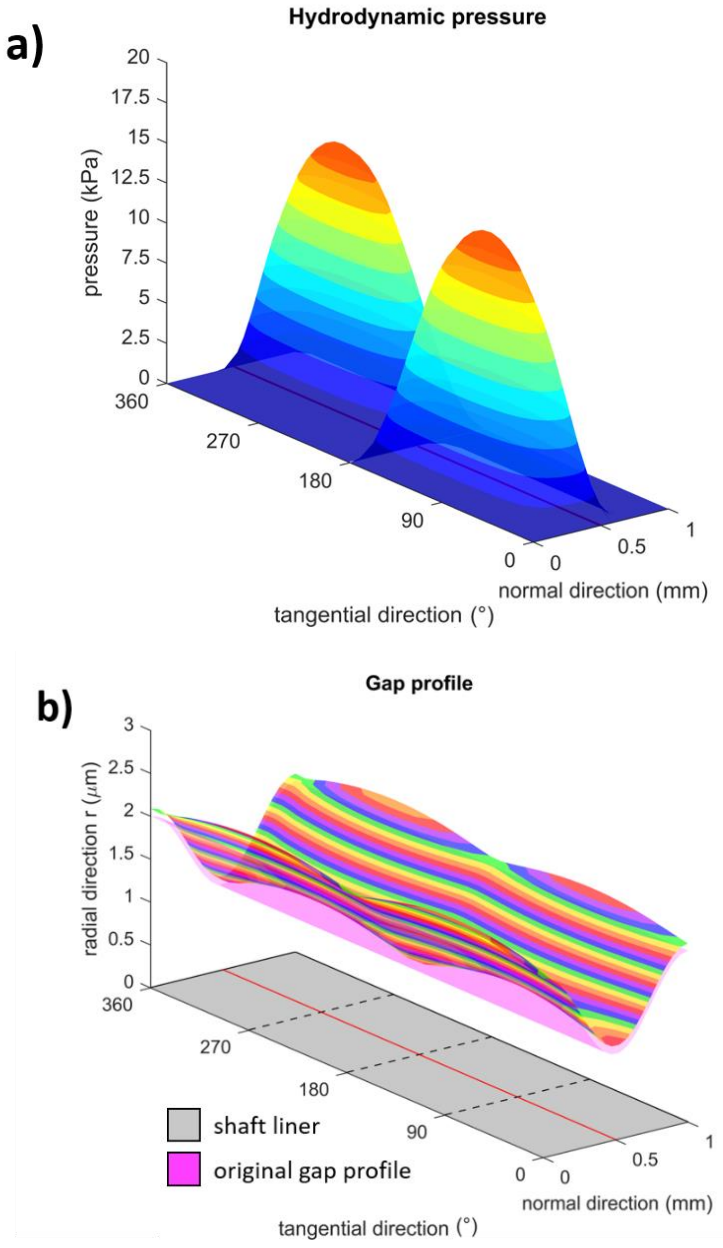

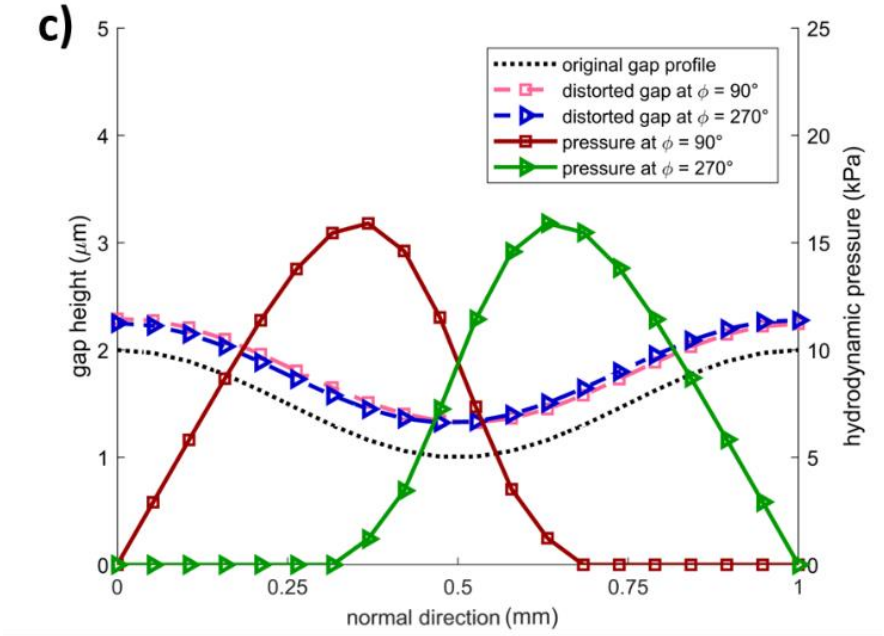

Flow rates	
$q_{b\to s}$	$0.44\ \mathrm{mm}^3/\mathrm{s}$
$q_{s\to b}$	$0.44\ \mathrm{mm}^3/\mathrm{s}$
$q_{b\to s} - q_{s\to b}$	$0.0\ \mathrm{mm}^3/\mathrm{s}$

Figure 8. *Results with a sinusoidal gap profile ($\varepsilon = 1\ mm$, $h_{min} = 1\ \mu m$, $v = 3\ m/s$, $\eta = 50\ mPa \cdot s$, $\kappa = 10^7\ P$).*

Figure 8b and Figure 8c show that the initial gap profile is distorted as a result of the given hydrodynamic pressure bumps developing in each side of the seal plotted in Figure 8a. The resultant gap profiles and pressure distribution in each direction are almost identical. Consequently, the resultant flow rate in each direction, back to spring sides $q_{b\to s}$ and spring to back sides $q_{s\to b}$, is the same, leading to a null net flow rate ($q_{b\to s} - q_{s\to b} = 0$). The initial minimum film thickness largely determines the magnitude of the pressure build-up, hence the distortion of the gap. As mentioned before, the results presented must be read qualitatively rather than quantitively.

The sole influence of the wedge profile on the back side of the seal is investigated and the results are shown in Figure 9. The gap profile is therefore fixed, i.e. rigid, and the influence of having a more aggressive or a softer back side angle α is analysed. The width of the computational domain B (in the axial direction) is adjusted to a maximum film thickness of 50 μm.

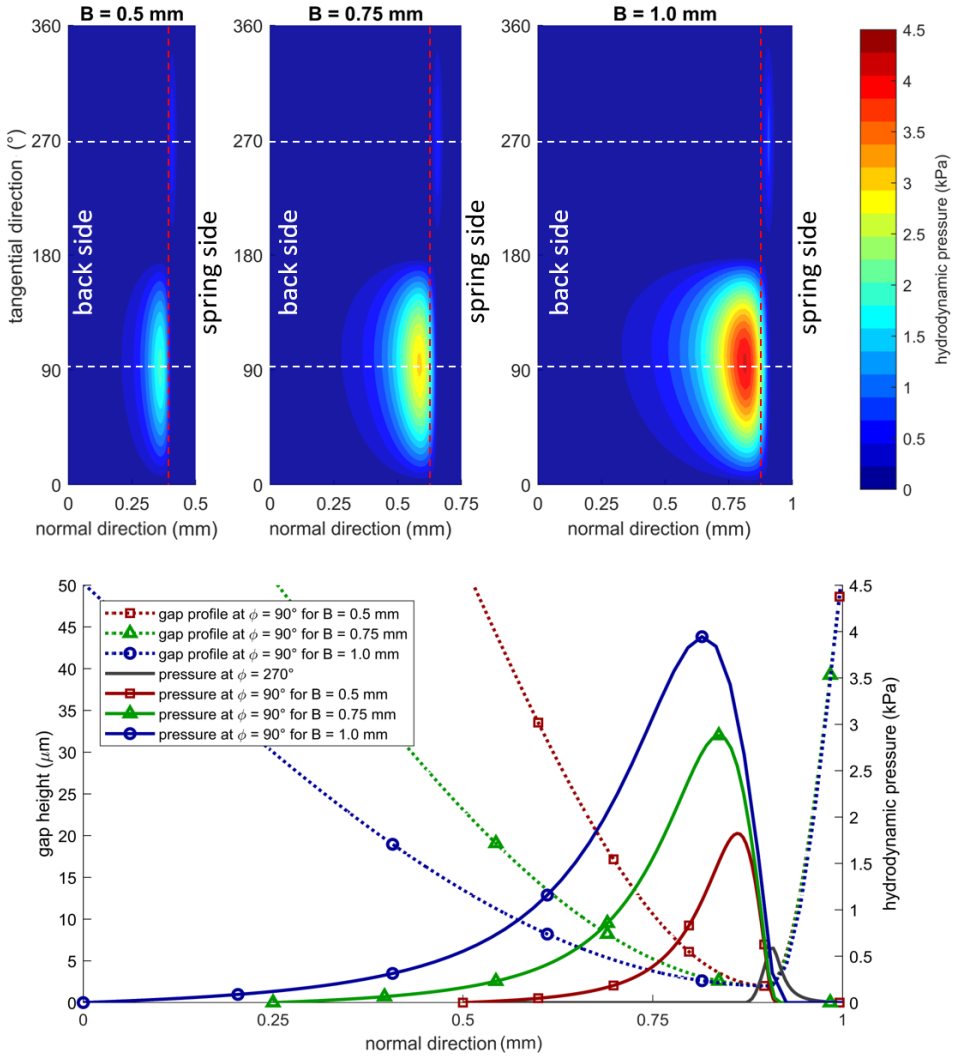

Figure 9. *Results with a various rigid gap profiles* ($\varepsilon = 1\ mm$, $h_{min} = 2\ \mu m$, $v = 3\ m/s$, $\eta = 50\ mPa \cdot s$, $\kappa = 10^7\ Pa$).

Figure 9 shows that, resembling a tilting-pad thrust bearing, the gap profile strongly influences the magnitude of the hydrodynamic pressure generation and therefore the load-carrying capacity of the lubricant film. The maximum pressure generated by the flow from the spring side (ϕ = 270°) was shown to be fairly independent of the pressure generated at the other side.

Ultimately, using the hinge point model the gap profile obtained in [19] under non-pressurized conditions is replicated and the results are shown in Figure 10. Once more, an elevation colourmap is used for Figure 10b so the microscopic distortion of the lip profile is clearly shown.

The original and distorted gap profiles are plotted in Figure 10c, showing that the two hydrodynamic bumps lead to a local deformation of the tip of a few micrometres at ϕ = 90°. As a result, the model predicts a net flow rate towards the spring side of the seal.

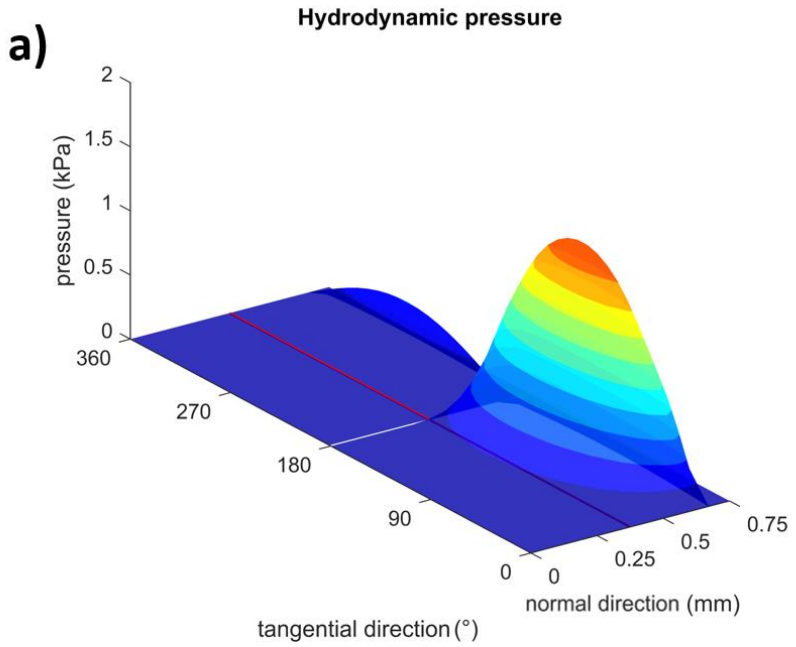

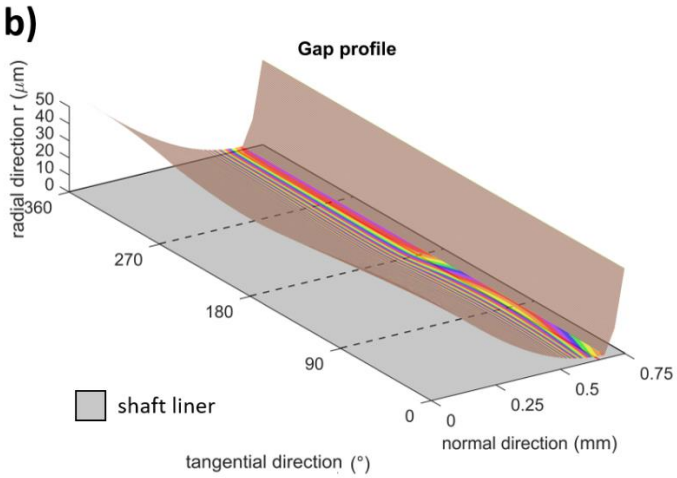

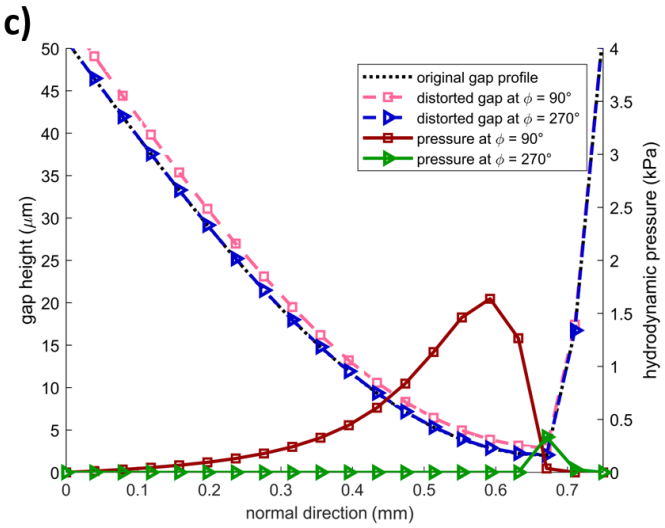

Flow rates	
$q_{b\to s}$	1.15 mm^3/s
$q_{s\to b}$	0.65 mm^3/s
$q_{b\to s} - q_{s\to b}$	0.5 mm^3/s

Figure 10. *Hydrodynamic pressure build-up the spring side gap profile between the seal and the shaft.* ($\varepsilon = 0.5\ m$, $h_{min} = 2\ \mu m$, $v = 3\ m/s, \eta = 50\ mPa \cdot s,$, $\kappa = 10^7\ Pa$).

4. Discussion

The main difference between the microscopic viscous seal theory and the misalignment-induced macroscopic theory presented in this study is the bidirectionality of the fluid migration. It was shown in Figure 3 that a radially misaligned lip seal leads to two convergent and two divergent wedge profiles in the circumferential direction. When the shaft rotates, two hydrodynamic pressure build-up and two pressure-decreasing regions develop. Consequently, the flow rate develops in both directions, i.e. spring-to-back and back-to-spring sides. When the hydrodynamic film formation conditions are not symmetric, i.e. different α and β angles or when sealing liquids of different viscosities, the flow rate in one direction becomes greater than the flow rate in the other one. The migration of fluid still occurs in both directions; however, a net flow rate is found towards one of the sides. The bidirectionality of the flow due to misalignment explains the inability of rotary lip seals to effectively separate two liquids [1], [10], [36].

Successful rotary lip seals present a steeper angle on the spring side than on the back side [2].The angle of the back side α generally presents better characteristics than the spring side angle β for generating a hydrodynamic pressure increase (and decrease). The consequent distortion of the lip leads to an asymmetric flow rate. Hence, although the migration of lubricant simultaneously occurs in both directions, the net flow rate is directed towards the spring side of the seal. Notice that, according to the model developed, the flow rate in each direction is independent of the direction of rotation. Stakenborg [20] observed the seal-shaft interface through a transparent rotating shaft. He described the occurrence of bubbling on the back side of the seal when the shaft rotated beyond a particular velocity. When the velocity of the shaft was further increased, cavitation also appeared on the spring side. Stakenborg's observations can be explained by the macroscopic misalignment-induced lubrication theory presented in this study.

This study focuses on the flow in the normal direction as in [12], while the flow in the tangential direction is disregarded. However, in a similar fashion as in [24], the variation of the distance between the seal and the shaft due to misalignment (Figure 6), together with the

deformation of the gap due to hydrodynamics (Figure 10), distort the nominal parallelism between the seal and the shaft in the tangential direction. This constitutes an additional source of hydrodynamics on a macroscopic level.

Furthermore, the misalignment-induced bidirectional flow rate may explain the early mixing of water and oil in the outermost chamber of a stern tube (seal #1 in Figure 2). Note that when sealing a water-oil interface the liquids present different viscosities which, together with the different angles α and β of the seal, results in different flow rates from the back to spring side and vice versa. The increased viscosity of a water-in-oil emulsion, for example, may change the net flow rate of a rotary lip seal. The role of the meniscus was not included in this study. However, as shown in Figure 3, when sealing against an air interface, the meniscus will limit the availability of lubricant at the back side of the seal and therefore the flow rate. Additionally, the misalignment-induced lubrication mechanism presented may contribute to the replenishment of the meniscus. When lip seals are pressurized, an increase of the contact load and a further deformation of the seal tip develop [19]. Therefore, to apply the model to a pressurized seal, both the pressure boundary conditions and the morphology of the gap profile must be updated. Special seal designs vary the direction of the pumping rate according to the pressurization level [2].

It is clear that the macroscopic hydrodynamic pressure resulting from the shaft radial misalignment does not lead to a uniform load-carrying capacity that is able to bear the seal radial load. Alternatively, when operating with a wobbling shaft, i.e. dynamic misalignment, the location of the pressure bumps because the misalignment periodically varies around the shaft. Depending on the magnitude of the misalignment-induced hydrodynamic load, part of the seal may (temporarily) operate under boundary, mixed or even full film lubrication. Consequently, although ignored in the presented model, the lubricant shear stress varies along the circumferential direction and may further slant the seal. The lubrication mechanism presented ignores any roughness effect, which has been proven to be key when it comes to directional pumping [3], [37]–[39]. Therefore, the misalignment-induced flow rate is thought to contribute to the already

existing microscale lubrication theory rather than replacing it. it is likely that various operating mechanisms are present in the operation of rotary lip seals [40] and the one investigated may become more significant in misaligned seals.

5. Conclusions

An elastohydrodynamic model able to predict the behaviour of rotary lip seals under misalignment has been presented. Once the contact profile is not in line with the perimeter of the shaft, part of the shaft velocity becomes normal to the sealing line, hence the fluid is dragged along a convergent wedge, inevitably leading to a hydrodynamic pressure build-up. Consequently, a bidirectional migration of lubricant develops when the nominal parallelism between the seal and the shaft is lost. Building on the work of Horve [12], the model presented predicts the flow rate of the seal as a function of the specific seal design, the lubricant rheology and its operating conditions. When two liquids of the same viscosity are sealed with a symmetrical seal-shaft liner profile, the model predicts equal flow rates in each direction, hence a null net flow rate develops.

Acknowledgments

Andreas Almqvist for his explanatory notes on solving the Reynolds partial differential equation accounting for cavitation. Aurelian Fatu and Richard Salant for their tips on the implementation of the stiffness matrix method.

References

[1] E.T. Jagger, “Rotary Shaft Seals: The Sealing Mechanism of Synthetic Rubber Seals Running at Atmospheric Pressure,” *Proc. Inst. Mech. Eng. Part J J. Eng. Tribol.*, vol. 171, no. 1, pp. 597–616, 1957.

[2] R. Flitney, “Rotary Seals,” in *Seals and Sealing Handbook*, 6th ed., Waltham: Butterworth-Heinemann, 2014, pp. 105–288.

[3] Y. Kawahara, M. Abe, and H. Hirabayashi, “An Analysis of Sealing Characteristics of Oil Seals,” *ASLE Trans.*, vol. 23, no. 1, pp. 93–102, 1980.

[4] R.F. Salant, “Theory of lubrication of elastomeric rotary shaft

seals," *Proc. Inst. Mech. Eng. Part J J. Eng. Tribol.*, vol. 213, no. 3, pp. 189–201, 1999.

[5] Y. Arai, "Sealing theory in oil seals - 1," in *JSLE-ASLE International Lubrication Conference*, 1976, pp. 830–839.

[6] Freudenberg Simrit GmbH & Co. KG, "Simmerrings and Rotary Seals," in *Simrit Catalog 2007*, 2007, pp. 15–166.

[7] M.S. Kalsi and G.A. Fazekas, "Feasibility Study of a Slanted O-Ring as a High Pressure Rotary Seal," *ASME*, p. 302, 1973.

[8] L.A. Horve, "Understanding The Sealing Mechanism Of The Radial Lip Seal For Rotating Shafts," in *Fluid Mechanics and its Applications*, Dordrecht: Springer Netherlands, 1992, pp. 5–19.

[9] Freudenberg Sealing Technologies, "Rotary seal with wave-shaped structure increases productivity in the process industry," *Sealing Technology*, pp. 1–13, 2019.

[10] H.K. Müller and B.S. Nau, "Rotary Lip Seals," in *Fluid Sealing Technology: Principles and Applications*, New York: Marcel Dekker Inc., 1998, pp. 73–110.

[11] M.J. Gawlinski, "Lip Motion and Its Consequences in Oil Lip Seal Operation," in *Ninth International Conference on Fluid Sealing*, 1981, p. D2 111-124.

[12] L. Horve, "A Macroscopic View of the Sealing Phenomenon for Radial Lip Oil Seals," in *10th Int. Conf. on Fluid Sealing*, 1984, p. K2 710-731.

[13] M.O.A. Mokhtar, M.A.A. Mohamed, M.E. El-Giddawy, and S.A.Y. Yassen, "On the effect of misalignment on the performance of U-type lip seal," *Wear*, vol. 223, no. 1–2, pp. 139–142, 1998.

[14] W. Sinzara, I. Sherrington, E.H. Smith, H. Brooks, and A. Onsy, "Effects of Eccentric Loading on Lip Seal Performance," in *6th European Conference on Lubrication Management and Technology*, 2018.

[15] A. Maoui, M. Hajjam, and D. Fribourg, "An experimental study on the temperature and the friction torque of rotary lip seal," in

8th EDF & LMS Workshop: "Dynamic Sealing in severe operating conditions," 2009, pp. 1–7.

[16] H. Ishiwata, "Effect of shaft eccentricity in oil seals," in *Second International Conference on Fluid Sealing*, 1964, pp. H2-17 to H2-32.

[17] M. Sansalone, S. Blachere, and M. Gohlke, "Onto fast, Automated and Advanced Viscoelastic Modelling of Rubber Materials for Sealing Applications," in *18th International Sealing Conference*, 2014, pp. 685–699.

[18] B. van der Vorst and M. Organisciak, "Fast Analytical Model for Followability Prediction of Rotary Shaft Seals," in *19th International Sealing Conference*, 2016.

[19] F.X. Borras, M. Bazrafshan, M. B De Rooij, and D. J Schipper, "Stern tube seals under static condition: A multi-scale contact modeling approach," *Proc. Inst. Mech. Eng. Part J*, May 2020.

[20] M.J.L. Stakenborg, "On the sealing mechanism of radial lip seals," Ph.D. dissertation, Eindhoven University of Technology, 1988.

[21] H. van Leeuwen and M.J.L. Stakenborg, "Visco-Elastohydrodynamic (VEHD) Lubrication in Radial Lip Seals: Part 2 - Fluid film formation," *Trans. ASME*, vol. 112, pp. 584–591, 1990.

[22] M.J.L. Stakenborg, "Visco-Elastohydrodynamic (VEHD) Lubrication in Radial Lip Seals: Part 1 - Steady-State Dynamic Viscoelatic Seal Behavior," *Trans. ASME*, vol. 112, p. 578, 1990.

[23] O. Schuck and H.K. Müller, "Rotary shaft seals at large dynamic eccentricities," in *9th International Conference on Fluid Sealing*, 1981, p. D1 103-110.

[24] F.X. Borras, M.B. de Rooij, and D.J. Schipper, "Misalignment-Induced Micro-Elastohydrodynamic Lubrication in Rotary Lip Seals," *Lubricants*, vol. 8, no. 2, p. 19, Feb. 2020.

[25] D.S. Etkin, "Worldwide analysis of in-port vessel operational lubricant discharges and leakages." Cortlandt Manor, pp. 2–9, 2008.

[26] F.X. Borras, M.B. de Rooij, and D.J. Schipper, "Rheological and Wetting Properties of Environmentally Acceptable Lubricants (EALs) for Application in Stern Tube Seals," *Lubricants*, vol. 6, no. 4, p. 100, Nov. 2018.

[27] R.F. Salant, "Soft elastohydrodynamic analysis of rotary lip seals," *Proc. Inst. Mech. Eng. Part C*, vol. 224, no. 12, pp. 2637–2647, 2010.

[28] B.J. Hamrock, S.R. Schmid, and B.O. Jacobson, *Fundamentals of Fluid Film Lubrication*, 2nd ed. New York: CRC Press, 2004.

[29] P.G.M. Van Bavel, T.A.M. Ruijl, H.J. Van Leeuwen, and E.A. Muijderman, "Upstream Pumping of Radial Lip Seals by Tangentially Deforming, Rough Seal Surfaces," *J. Tribol.*, vol. 118, no. 2, pp. 266–275, 1996.

[30] H. Hirani and M. Verma, "Tribological study of elastomeric bearings for marine propeller shaft system," *Tribol. Int.*, vol. 42, no. 2, pp. 378–390, 2009.

[31] E. Koukoulopoulos and C.I. Papadopoulos, "Piston ring performance in two-stroke marine diesel engines: Effect of hydrophobicity and artificial surface texturing on power efficiency," *Proc. Inst. Mech. Eng. Part J J. Eng. Tribol.*, vol. 232, no. 8, pp. 940–963, 2018.

[32] M. Giacopini, M.T. Fowell, D. Dini, and A. Strozzi, "A mass-conserving complementarity formulation to study lubricant films in the presence of cavitation," *J. Tribol.*, vol. 132, no. 4, 2010.

[33] A. Almqvist and P. Wall, "Modelling Cavitation in (Elasto)Hydrodynamic Lubrication," in *Advances in Tribology*, InTech, 2016, pp. 197–213.

[34] A. Maoui, M. Hajjam, and D. Bonneau, "Analysis of three-dimensional non-axisymmetric elastic effects of the lip on the thermoelastohydrodynamic radia lip seal behaviour," *Proc. Inst. Mech. Eng. Part J*, 2007.

[35] D. Bonneau, A. Fatu, and Dominique Souchet, "Elastohydrodynamic Lubrication," in *Hydrodynamic Bearings*, 1st ed., Wiley-ISTE, 2014, pp. 159–184.

[36] C. Burkhart, K. Peter, S. Thielen, and B. Sauer, "Online determination of reverse pumping values of radial shaft seals and their tribologically equivalent system," in *22nd International Colloquium Tribology*, 2020, pp. 1–2.

[37] L.A. Horve, *Shaft seals for dynamic applications*. New York: Marcel Dekker Inc., 1996.

[38] S. Bekgulyan, S. Feldmeth, and F. Bauer, "Influence of static and dynamic eccentricity on the pumping rate of radial lip seals," in *25th International Conference on Fluid Sealing*, 2020, pp. 79–91.

[39] D. Liu, S. Wang, C. Zhang, and M.M. Tomovic, "Numerical study of the effects of textured shaft on the wear of rotary lip seals," *Tribol. Int.*, vol. 138, pp. 215–238, 2019.

[40] H.K. Müller, "Concepts of sealing mechanism of rubber lip type rotary shaft seals," in *11th International Conference on Fluid Sealing*, 1987, p. K1 698-709.

Paper E

(This page is intentionally left blank)

Stern Tube Seals Operation: a Practical Approach

F.X. Borras[1], R. van den Nieuwendijk[2], V. Ramesh[2], M.B. de Rooij[1] and D.J. Schipper[1]

[1]University of Twente, Surface Technology and Tribology, Enschede, The Netherlands

[2]AEGIR-Marine, Wijk bij Duurstede, The Netherlands

(This page is intentionally left blank)

Abstract: Stern tube seals are a key component of the propulsion system of a ship. The purpose of these sealing rings is to ensure a reliable sealing condition, preventing the spillage of lubricant to the environment. The research on these large rotary seals is limited due to their complex accessibility: stern tube seals are located below the seawater level on a moving ship. A dynamic setup replicating the operating conditions of a stern tube seal is presented. The frictional torque, the operating temperature and the lubricant migration across the seal are measured under various shaft velocities and pressure differences. The existing theory for rotary lip seals is reviewed for the stern tube seal application.

Keywords: stern tube seal, rotary lip seal, elastohydrodynamic lubrication, marine.

Nomenclature

b	Contact width	$[m]$
h	Fluid film thickness	$[m]$
D_s	Shaft diameter	$[m]$
η	Dynamic viscosity of the lubricant	$[Pa \cdot s]$
μ	Overall coefficient of friction (COF)	$[-]$
μ_0	Dry friction coefficient resulting from asperity contact	$[-]$
Γ	Frictional torque $\Gamma = \Gamma_0 + \Gamma_\eta$	$[N \cdot m]$
Γ_η	Lubricant frictional torque (viscous term)	$[N \cdot m]$
Γ_0	Asperity contact frictional torque (dry term)	$[N \cdot m]$
G	Duty parameter $G = \eta u b / F_{r_{tot}}$	$[-]$
ω	Shaft liner angular velocity	$[rad/s]$
u	Shaft liner linear velocity	$[m/s]$
Δp	Pressure difference	$[Pa]$
τ_{xz}	Viscous shear	$[Pa]$
λ	Lambda ratio $\lambda = h/\sigma$	$[-]$
$\dot{\gamma}$	Shear rate	$[1/s]$
$F_{r_{tot}}$	Total radial seal force	$[N]$
σ	Combined root mean square roughness $\sigma = \sqrt{S_{q_1}^2 + S_{q_2}^2}$	$[m]$
S_q	Root mean square roughness	$[m]$
S_p	Roughness maximum peak height	$[m]$
Δz	Hydrostatic height	$[m]$
g	Gravity constant	$[m^2/s]$
ρ	Density	$[kg/m^3]$
q	Flow rate from the spring side to the back side	$[mm^3/s]$

$\bar{q}$	Normalized flow rate $\bar{q} = q/v$	$[mm^3/m]$
T_{sump}	Temperature of the oil sump	$[K]$
T_c	Temperature at the seal-shaft contact	$[K]$
$K_{\Delta T}$	Proportionality factor for predicting the contact temperature	$[mm^2 \cdot K/W]$
K_s	Suction parameter	$[mm^3/s]$
ϕ_s	Characteristic sealing proportionality parameter	$[-]$
Q_d	Heat dissipated density $Q_d = \Gamma\omega/(\pi D_s b)$	$[W/m^2]$
Q_f	Heat dissipated $Q_f = \Gamma\omega$	$[W]$

1. Introduction

The propulsion system of a vessel is a critical part of a ship because it is subject to maintenance and crucial for the operation of the ship. The propulsion shaft goes through a metal cylinder welded onto the hull connecting the engine chamber to the stern of the ship, namely the stern tube. Within this tube, the stern tube bearings carry the weight of the shaft while allowing for its rotation. The entire stern tube is flooded with lubricant in order to minimize the friction on the bearings, so the engine power is used primarily to overcome the water resistance. A set of rotary lip seals is placed at both ends of the stern tube to prevent lubricant leakage and the entrainment of water to the stern tube. The seal arrangement shown in Figure 1 is common to many ships and the seals are numbered from #1 to #5 as indicated. Three oil tanks are used to provide a particular pressure difference across each of the stern tube seals.

Until the 1950s engineers thought that lubricated rotary seals operated in a similar fashion to dry rotary lip seals, by compressing the elastomeric lip of the seal against the rotating shaft to ensure a tight contact. It was not until Jagger [1] that the lubrication regime of rotary lip seals was taken into consideration. Jagger realized that the friction force of a lip seal was not proportional to its loading, as would be expected from a Coulomb-like frictional behaviour. Additionally, some friction force was present even when the loading of the seal was almost null. Jagger stated that a continuous lubricant layer may separate the seal and the shaft, preventing direct asperity contact. Since then, researchers have tried to analyse the mechanisms promoting the separation between surfaces and, if the contact is not tight, why the lubricant does not leak through the seal.

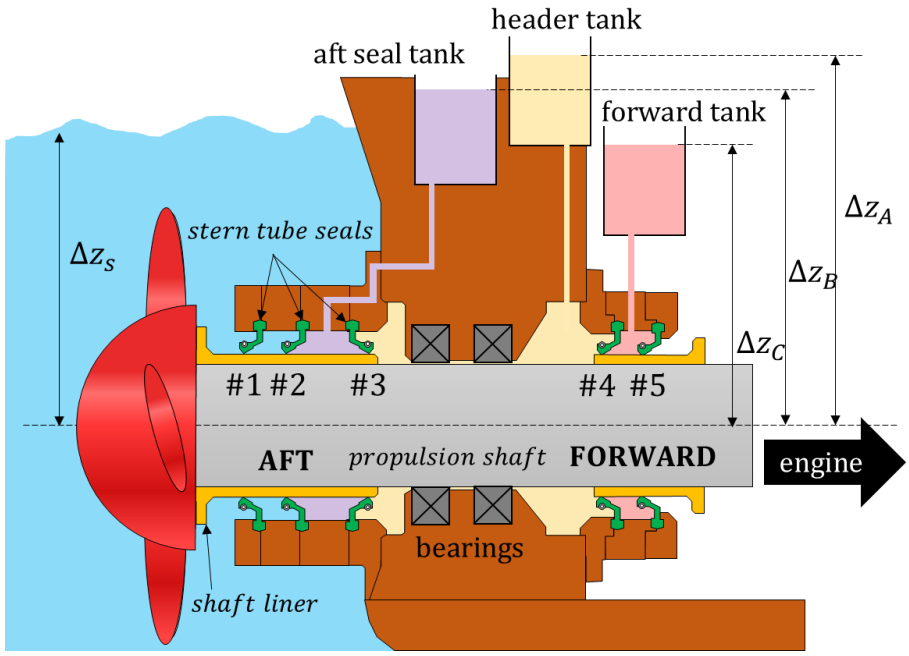

Figure 1. *Usual disposition of the stern tube seals and the oil tanks in a ship.*

Rotary lip seals are one of the most frequently used sealing components [2]; however, some mysteries still remain with respect to their working mechanism. The presence of hydrodynamics is repeatedly evidenced in rotary lip seal literature. Stakenborg [3] observed the cavitation of the lubricant through a sapphire glass shaft. The location of the bubbles shifted with the shaft angular velocity. Johnston [4] observed that, contrary to what it is expected from an Archard-like wear rate, rotary lip seals presented almost no wear after an initial running-in period. Kawahara, among others [5], [6], studied reverse pumping (also referred as upstream or back pumping). Reverse pumping is an inherent ability of rotary lip seals to pump liquid from the back side to the spring side of the seal, as shown in Figure 2. It is clear that reverse pumping could not develop in a tight seal-shaft interface. In contrast to journal bearings or thrust bearings, rotary lip seals do not present a convergent gap profile in the direction of rotation, hence there is no apparent source for hydrodynamic action. Nevertheless, in a similar fashion as journal or thrust bearings, rotary lip seals fail when the viscosity of the lubricant decreases excessively [7].

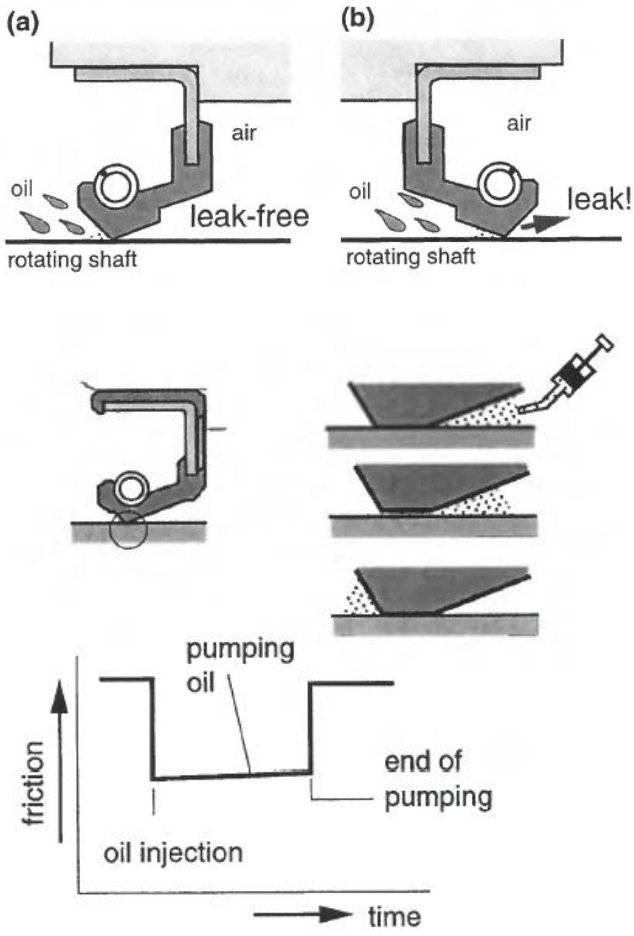

Figure 2. *Inwards pumping ability of rotary lip seals (top) and syringe pumping test (bottom)* [8].

Horve [9] noticed that seals with more micro-asperities on its surface showed better sealing characteristics, while excessively smooth seals showed a more erratic behaviour leading to leakage. Up to now, the behaviour of rotary lip seals has been explained by the presence of hydrodynamics at a microscopic level [10]. The micro-hydrodynamic pressure build-up between the surface asperities of the shaft and the seal leads to a load-carrying capacity which partially (or fully) replaces the seal-shaft radial load supported by direct asperity contact. The same micro-hydrodynamics can explain the reverse pumping

mechanism. The shearing load resulting from the rotation of the shaft shifts the tip of the seal, distorting the asperities on its surface. Since the radial pressure profile between the shaft and the seal is not uniform, neither is the tangential force in the circumferential direction nor the consequent distortion of the asperities. Consequently, the asperities on the seal surface become aligned, forming ridges resembling a viscous seal or a herring-bone bearing. The location of the maximum radial pressure determines the equator of the sealing contact, i.e. where the circumferential shearing force is the greatest. At that location, the two opposing microscopic screw pumps meet each other. Typically, in rotary lip seals it is ensured that the maximum contact pressure is located close to the spring side, thereby forcing a lubricant flow towards the spring edge. Alternative hypotheses for the film formation and sealing mechanisms are also found in the literature [10], [11], but the hypothesis based on the micro-hydrodynamics generating a micro-pump is the only one that can explain the presence of hydrodynamics, the pressure profile-dependent reverse pumping mechanism and the significant role of the surface roughness to the successful sealing of rotary lip seals [10]. It is thought that not a single unique lubrication mechanism but a combination of lubrication mechanisms is present in rotary lip seals [12].

Although the micro-hydrodynamic hypothesis described above may explain the operation of rotary lip seals, it is still not clear whether the separation of the seal and the shaft is partial or total. Micro-hydrodynamics may develop on the full film, mixed or boundary lubrication regimes [13], [14] (see Figure 3). Furthermore, as for any hydrodynamic component, it is likely that some designs lead to a complete lift-off while other designs do not. The parameters defining the boundary between the mixed and the full film lubrication regimes in rotary lip seals are yet to be determined. It is clear that leakage-free full film lubrication is convenient as the wear rate becomes virtually zero.

The separation between the seal and the shaft, fluid film thickness or gap has been the subject of extensive research as it provides a definitive answer to the lubrication regime in which rotary lip seals operate [15]. A wide range of techniques were implemented, including electrical resistance [12], capacitance with a conductive rubber compound [16], laser induced fluorescence (LIF) [17] and magnetic resistance [18], leading to film thickness values between 0.1 and 5 micrometres. Recently, Wennehorst [19] presented remarkable film

thickness measurements using the LIF technique under a wide range of operating conditions.

The lubrication regime is often inferred by comparing the film thickness with the composite standard deviation of undeformed surface heights of the two surfaces $\sigma = \sqrt{S_{q_1}^2 + S_{q_2}^2}$. This is known as the lambda ratio $\lambda = h/\sigma$. As shown in Figure 3, the lambda ratio can be used to determine the lubrication regime of contact. However, due to the soft nature of the elastomer compound used for the seal, the surface easily deforms when loaded, hence the surface topography of the seal varies. The lambda ratio λ becomes inexact when h becomes equal to or less than σ [13].

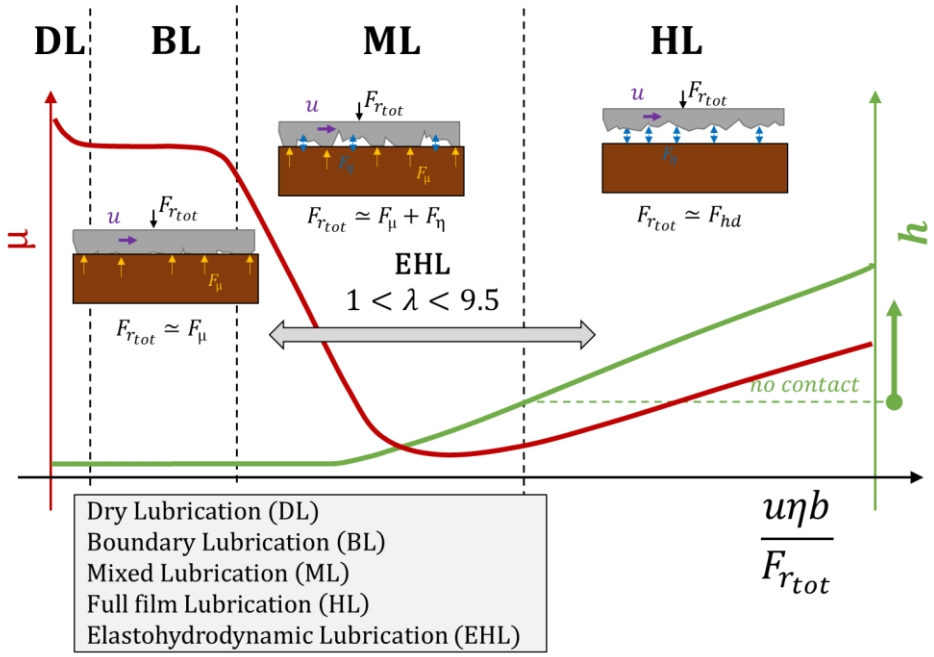

Figure 3. *Stribeck curve.*

Ogata [12] determined the boundaries of the lubrication regimes in the Stribeck curve by measuring the film thickness of several rotary lip seals under a wide range of operating conditions. The values for the dimensionless duty parameter $G = \eta u b / F_{r_{tot}}$ listed in Table 1 were presented in [10].

Table 1. *Boundaries of the lubrication regimes determined by Ogata* [12].

$G \leq 10^{-9}$	Dry
$10^{-9} < G \leq 10^{-8}$	Boundary
$10^{-8} < G \leq 7 \times 10^{-8}$	Mixed
$7 \times 10^{-8} < G$	Hydrodynamic

Johnston [20] tested a comprehensive amount of rotary lip seals showing that, while some seals follow the traditional Stribeck curve, other seals did not exhibit the typical boundary lubrication regime. Johnston concluded that the behaviour of rotary lip seals cannot be captured solely by the traditional Stribeck curve, hence additional variables such as the surface roughness or the seal material characteristics must be included [15].

The lubrication regime of rotary lip seals can also be deduced from fitting computational models to indirect measurements. Typically, the film thickness value is selected so the model shows good agreement with the frictional torque measurements. These models require from specific data that must be obtained beforehand, typically the contact width, the characteristics of the seal and shaft surfaces and radial load between the seal and the shaft. Specialized equipment is required for it this [21].

Setups for testing rotary lip seals under dynamic conditions are presented in the literature [3], [22]. Almost all the research on rotary lip seals focuses on seals where the lubricant is placed at the spring side, while the back side is filled with air as shown in Figure 2. These setups usually allow the seal to be installed conversely so as to measure the potential of the reverse pumping. The reverse pumping can be measured by the syringe test (Figure 2) or by measuring the oil flow rate when installed conversely, as shown in Figure 4 [23]. The metered tube method has the inconvenience of continuously varying the hydrostatic pressure conditions of the seal. Burkhart [24] recently measured the oil migration across the seal by monitoring precisely the hydrostatic pressure variation resulting from the oil level rise. Note that when the seal fails due to causes such as overheating, excessive wear or misalignment, the leakage develops in the other direction: from the spring side towards the back side. As in many applications, the oil level on the spring side is often set to half the shaft. The torque is typically measured via in-line torque sensors [25] or by measuring the reaction on the seal housing [5], [26]. Lubricated rotary lip setups generally arise from an auxiliary seal preventing the leakage of the oil in the chamber next to the driving shaft. Additionally, as in a

concentric cylinder rheometer, the viscous shearing of the lubricant hampers the rotation of the shaft too. The contribution of both the auxiliary sealing components and the lubricant shear must be subtracted from the torque readings. The temperature at the seal-shaft interface is usually deduced by placing a thermocouple near the seal-shaft contact zone. Thermocouples can be placed at the spring groove [16], within the seal [26] or inside the rotating shaft [27]. Infrared cameras have also been used [25], [28]. Finite Element (FE) models are often used to predict the temperature difference between the measurement point and the actual contact.

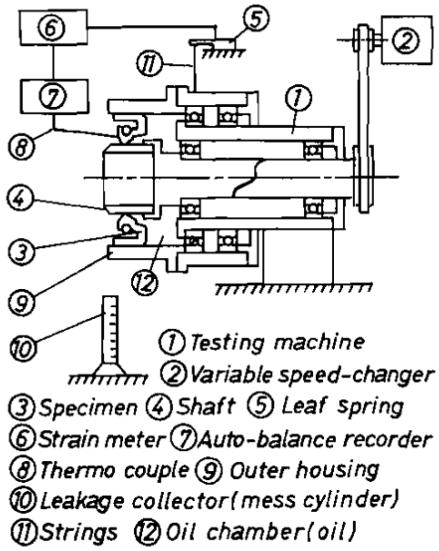

Figure 4. *Test apparatus used in [5] for measuring the reverse pumping of a rotary lip seal.*

The time required to reach stationary conditions increases with the seal diameter [26]. Furthermore, some setups are designed without a temperature control-loop of the bulk oil [25], hence the steady-state temperature of the liquid at each side of the seal depends on the operating conditions. Due to the poor thermal conductivity of elastomers, the overall seal temperature is determined to a large extent by the bulk oil temperature, so this must be taken into account in terms of the elastomer properties and the thermal expansion. Additionally, extensive research on the shaft and seal surface characteristics have been conducted as they have been shown to impact the migration of the lubricant across the seal [28]–[30].

Cylindrical grinding of the shaft, for example, can lead to a micron-scale screw thread on the shaft pumping oil from one side of the seal to the other. Plunge grinding is shown to minimize the shaft lead and, consequently, the liquid pump rates [31]. Studies on pressurized rotary lip seals are scarce. Jagger [1] studied at what maximum pressure difference a rotary seal could operate without leaking, given a specific shaft velocity and loading of the contact.

The simplest model used to describe the operation of rotary lip seals assumes a laminar flow between concentric rotating cylinders [9]. The frictional torque Γ derives exclusively from the viscous shear as shown in Eq. 1.

$$\Gamma = \Gamma_\eta = \tau_{xz}(\pi D_s b)\frac{D_s}{2} = \eta\,\dot{\gamma}(\pi D_s b)\frac{D_s}{2} = \frac{\pi b\,\eta\omega D_s^3}{4h} \tag{1}$$

Jagger [1] noticed that the frictional torque-shaft velocity curve shows a positive ordinate intercept. That suggests that direct asperity contact occurs, at least at low velocities, hence Eq. 1 is often generalized by including a dry friction term as in Eq. 2 [16], [22].

$$\Gamma = \Gamma_\eta + \Gamma_0 = \frac{\pi b\,\eta\omega D_s^3}{4h} + \mu_0 F_{r_{tot}}\frac{D_s}{2} \tag{2}$$

Consequently, the dry friction coefficient μ_0 can be measured [32] or deduced to fit the y-intercept of the torque-shaft velocity curve. Engelke [27] showed that a value of μ_0 of 0.3 often provides a good approximation for a wide range of oils and elastomers. Engelke also assumed the film thickness to be similar to the sum of the maximum profile peak height of the seal and the shaft ($h \approx S_{p_{shaft}} + S_{p_{seal}}$). Hirano [33] realized that the friction coefficient of rotary lip seals is proportional to the duty parameter G. A characteristic sealing proportionality parameter ϕ_s specific to each seal can be defined as shown in Eq. 3.

$$\mu = \phi_s G^{1/3} = \phi_s\left(\frac{\eta u b}{F_{r_{tot}}}\right)^{1/3} \tag{3}$$

The contact temperature increase with respect to the sump oil temperature is often predicted from the heat dissipated density Q_d using Eq. 4 [27]. The parameter $K_{\Delta T}$ describes the ability of releasing the heat generated at the contact and must be determined experimentally.

$$T_c = T_{sump} + K_{\Delta T}\frac{\Gamma\omega}{\pi D_S b} = T_{sump} + K_{\Delta T}Q_d \quad (4)$$

Kawahara [5] noticed that the flow rate across the seal when installed conversely, i.e. flooded seal back side, can be related to the duty parameter G as shown in Eq. 5. A dimensionless suction coefficient K_s can be specified for each particular seal.

$$q = K_s u D_s^2 G^{1/2} = K_s u D_s^2 \left(\frac{\eta u b}{F_{r_{tot}}}\right)^{1/2} \quad (5)$$

The first deterministic models for rotary lip seals appeared were developed in the 1990s by the hands of Gabelli [34], Pol [35] and Salant [36]. The hydrodynamic pressure generated on the microscopic level is modelled by solving the Reynolds partial differential equation on an equivalent gap profile representing the separation between the seal and the shaft. During the next decades a wide range of models of various complexities were developed. The distortion of the shaft asperities [37], the impact of operating with a non-Newtonian lubricant [38], the direct asperity contact [39], the viscoelasticity of the seal [40] or the presence of a meniscus [41] were added to these deterministic models.

Stern tube seals, together with the seals used for wind and water turbines, constitute one of the largest types of rotary lip seals [2]. The same type of seal is installed in both the aft and forward sealing packages as shown in Figure 1. Fluoroelastomer compounds are the preferred choice for the stern tube seals due to their inertness. The linear velocity of the shaft depends on the turning speed and the diameter of the shaft liner ($v = \omega D_s/2$). A shaft liner of 200 millimetres typically reaches linear velocities of up to 5 m/s. Stern tube seals are hydrostatically pressurized ($\Delta p = \rho g \Delta z$) by a set of oil tanks placed at a specific height, as shown in Figure 1. The draft of a vessel is specific to that vessel and depends on its loading condition. An example showing the pressure difference across each seal is given in Table 2. Pressurized rotary lip seals operate with a higher pressure on the spring side than on the back side. This way the pressure difference contributes to the overall loading of the seal contact. The specific lip seal profile determines the relationship between the pressure difference and the contact load. Consequently, the Poiseuille flow also increases as the pressure difference increases. Both the static and dynamic sealing must be guaranteed, leading to a compromise: a large

loading guarantees the seal tightness when the shaft is at rest but an excessive load is detrimental to its dynamic operation, leading to overheating and shortening of the lifespan of the seals.

Table 2. *Average pressure difference across each seal shown in Figure 1 under loaded and unloaded conditions. Densities of 1029 kg/m³ and 850 kg/m³ are assumed for the seawater and lubricant respectively.*

Pressure difference across each seal (bar) $\Delta p = p_{spring\ side} - p_{back\ side}$		
	Unloaded	**Loaded**
seal #1	0.00	0.00
seal #2	0.31	0.73
seal #3	1.00	1.03
seal #4	1.07	1.17
seal #5	0.08	0.08

The innermost seal, seal #5 in Figure 1, is the only ring sealing against an oil-air interface. The rest of the seals are fully flooded with liquid on both sides. In practice, the outermost seal facing the seawater, seal #1 in Figure 1, suffers wear quickly. An oil-water mixture is expected between seal #1 and seal #2. It is common practice to fill that space with grease. In fact, seal #1 acts as a dirt excluder, preventing the entrance of larger particles and marine life into the stern tube [29]. Seal #1 does not hold any pressure. Both an air-oil interface and a water-oil interface, i.e. two menisci, are found in the stern tube. Since the back side of stern tube seals is flooded with liquid it is anticipated that, if stern tube seals behave as common rotary lip seals (see Figure 2), they constantly leak lubricant to the environment, leading to a lower friction coefficient [1], [8]. The rheology of the lubricant of the stern tube plays an important role in the system. In [42] a strong temperature-dependence and occasional shear thinning were observed for stern tube lubricants. Additionally, the large dimension of the stern tube hardware challenges the dimensional accuracy, hence the nominal parallelism between the shaft and the seal [43]. The loading of the propeller, for example, may also lead to the misalignment of the shaft. Further, due to the dimensions, the surface finish becomes expensive and the lead [31] on the shaft liner surface is generally overlooked.

Cargo vessels and tankers, among others, travel around the world 365 days a year. The service time of these vessels has to be carefully

planned so the most profitable sailing time is achieved. Every two to five years such vessels are sent into dry dock for maintenance so the hull can be repaired and all the critical components replaced even if they are not significantly worn, e.g. the stern tube seals. Consequently, the stern tube seals must guarantee the reliable sealing of the stern tube until the next service of the ship. A failure of the sealing system of the stern tube generally leads to a costly unscheduled visit to the dry dock. When the seals are serviced after a few years of operation, the condition of the seals differ from each other. Seal #2, for example, is usually heavily worn while seal #5 looks as good as new. In fact, not only the shaft speed but also the pressure difference, the contact temperature, the lubricants and probably the shaft-seal alignment are specific to each seal position. This suggests that each seal may operate under a different lubrication regime.

The spillage of lubricant to the ocean is of great concern with respect to the marine environment; the use of mineral lubricants has therefore been limited in some countries [42]. Etkin [44] showed that the stern tubes of barge carriers, tankers and navy ships "consume"(i.e. spill) between 10 and 20 litres per day. In fact, lip seals are known to not reliably separate two liquids [45]. The back-to-back strategy with a vented chamber instead shows improving results, keeping the two liquids apart. This is already implemented in the propulsion system of some ships. Alternatively, few newbuild ships use seawater to lubricate the stern tube bearings.

The present work focuses on the operation of a particular stern tube seal of 200 millimetres nominal diameter. Combining both experimentation and modelling analyses, the behaviour of this large rotary lip seal is studied. A specialized setup was developed to measure the frictional torque, contact temperature and the under-lip flow rate under a wide range of velocities and pressure differences. The suitability of the already-available formulae for rotary lip seals is reviewed for the stern tube seal application. This study aims to create a solid foundation from which to tackle the large spillage of lubricant to the environment while extending its service time.

2. Materials and Methods

The test rig sketched in Figure 5 was developed to measure the frictional torque, the flow rate and the operating temperature of a

stern tube seal under various shaft velocities and pressure conditions. The pressure at each side of the seal is indirectly set by adjusting the pressure of the air space at the top of each tank. The system was designed to bear pressures of up to 2.5 bar. The driving motor allows the angular velocity of the shaft to be varied, reaching a maximum linear velocity of 10 m/s for a 200-millimetre shaft liner. The temperature of the sump oil in each side of the seal is independently controlled by circulating the liquid through two heat exchangers, as shown in the same Figure 5. Approximately 80 litres of lubricant are required to run the setup. All the tests were conducted using a mineral oil-based lubricant exhibiting a kinematic viscosity of 133 mm²/s and 14 mm²/s at 40 °C and 100 °C respectively. Further details on the rheology of the lubricant are presented in [42].

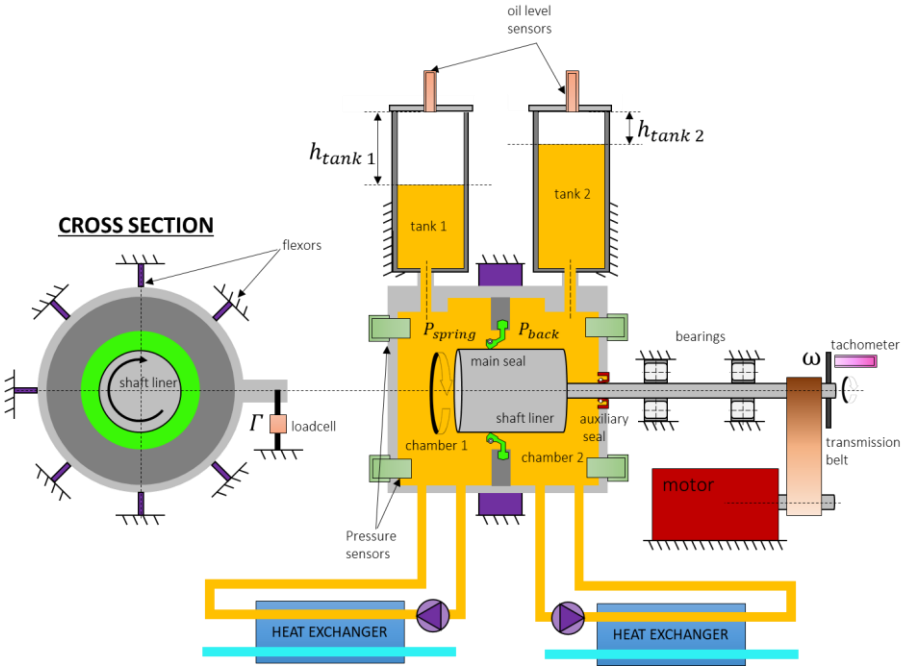

Figure 5. *Setup for measuring torque, seal temperature and flow rate of a stern tube seal under dynamic conditions.*

The measurement of the frictional torque is deduced from its reaction in the seal housing, i.e. the drum. The drum is suspended by several flexures carrying the weight of the drum while slightly constraining the rotation of the testing chamber. The rotation of the drum is exclusively prevented by a single rod connecting it to the ground. A

load cell is placed between the lever and the ground, as shown in Figure 5, from which the frictional torque is deduced. The contribution of both the lubricant and the auxiliary seal to the frictional torque are also measured by the load cell. However, the contribution of the auxiliary seal and the lubricant is low as it operates against a smaller shaft diameter and the space between the shaft and the drum is large, respectively. The residual torque, i.e. of the auxiliary seal and the lubricant, was mapped at various velocities and pressures by operating without the main seal and later subtracted from the measurements with the main seal assembled. For clarity, the main seal is mounted so the low pressure side, i.e. the back side, faces the chamber where the auxiliary seal seats (chamber 2 in Figure 5). This allows keeping the pressure constant on the back side so the auxiliary seal torque is dependent only on the shaft velocity.

The flow rate across the seal is obtained by measuring the oil height level in each tank using two distance sensors. Monitoring the oil height variation at both sides of the seal ensures that the oil volume migrating from one tank ends in the other one and does not leave the system, in other words it does not leak. Therefore, only measurements giving the same slope on both oil level sensors in time were accepted to ensure the mass of the oil is conserved. Notice that by increasing or decreasing the height of the lubricant the hydrostatic pressure on each side varies, affecting the operating conditions of the test [24]. To prevent that, a control loop is set at each side of the seal, adjusting the pressure of the air space above the tanks. This way, when the oil height increases the air pressure on the tank is decreased so the pressure on that side matches that prescribed for the test. Note that although this does not occur in the stern tube system of a ship, the section of the tanks on a ship is significantly larger, resulting in a minimal hydrostatic pressure variation with leakage. Air pockets formed occasionally while operating the setup. It is thought that the origin of the air bubbles in the system is a combination of gaseous cavitation, the reverse pumping of the auxiliary seal and the pumps used for controlling the oil sump temperature. The presence of an air bubble within the system drastically impacted the measurement of the oil level. It was shown imperative to provide an escape route for the air bubbles to the top of the tanks. Interestingly, breathers are present in the oil system on a stern tube of a ship [29]. Additionally, as described in [27], the thermal expansion of the lubricant was shown to impact the results strongly and the density-temperature relationship

presented in [42] was used. The surface finish of the shaft was grinded to the right outer diameter. No plunge ground surface operation was carried out. The final lead of the shaft was tested according to [46] showing no significant directionality.

The temperature of the stern tube system was monitored by a set of thermocouples distributed at various parts of the setup. The temperature of the oil at each side of the seal strongly determines the temperature of the seal and the housing parts. To account for the temperature at the contact, while avoiding having to drill a hole to the seal [26], a thermocouple was clamped between the garter spring coils providing the temperature on the spring groove as in [16]. The temperature at the contact was approximated by using the Finite Element (FE) model presented in [21]. Figure 6 shows the relationship between the temperature at the groove and the temperature at the contact. The lubricant viscosity was calculated from the contact temperature according to [42].

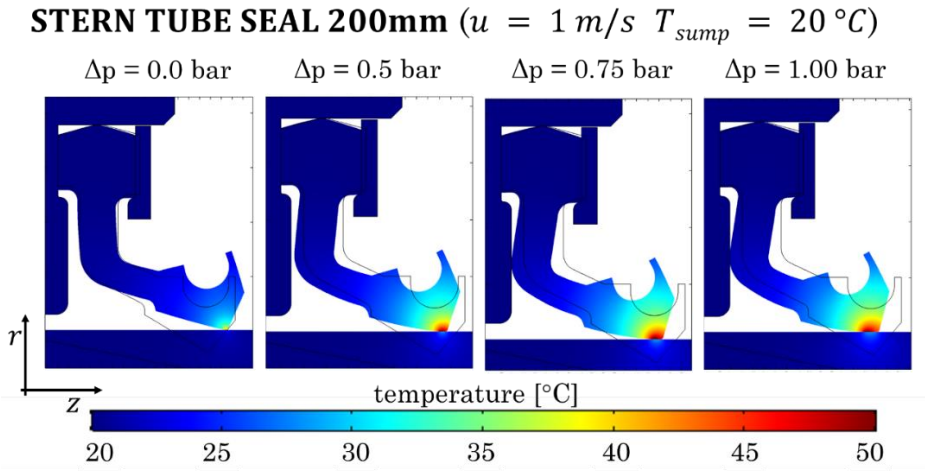

Figure 6. *The temperature at the contact is obtained from the FE model presented in* [21]. *Thermocouple measurements were placed close to the contact for validation.*

A 200-millimetre seal was tested under three shaft velocities and four pressure differences leading to twelve different operating points. This study focuses on the steady state operation of the stern tube seal, i.e. once it has undergone the initial running-in period. It is considered that the steady-state regime is reached once both the temperature and

friction torque readings stabilize, showing a variation of less than 5% for at least 1 hour. The sump oil temperature at both sides of the seal was set to 20 °C. The tests were repeated three times for each operational point and the average values are presented.

Table 3. *Operation conditions tested.*

	Pressure difference Δp [bar]	**Shaft velocity v [m/s]**	**Oil sump temperature T_{sump} [°C]**
1	0.0	1	20
2	0.0	3	20
3	0.0	5	20
4	0.5	1	20
5	0.5	3	20
6	0.5	5	20
7	0.75	1	20
8	0.75	3	20
9	0.75	5	20
10	1.0	1	20
11	1.0	3	20
12	1.0	5	20

The accuracy of the analytical expressions, Eq. 1, Eq. 2 and Eq. 4, for the stern tube seals application was reviewed. The static characterization of the same type of stern tube seal was presented in [21] showing a minimum accuracy of 4% and 8% for the radial load and the contact width respectively . The results are reproduced for commodity in Figure 7 and Figure 8. The surface roughness analysis of both the seal and the shaft and seal material characterization are also disclosed in the same publication. The surface roughness in the direction of rotation is 0.85 μm and 0.14 μm for the seal and the shaft liner respectively.

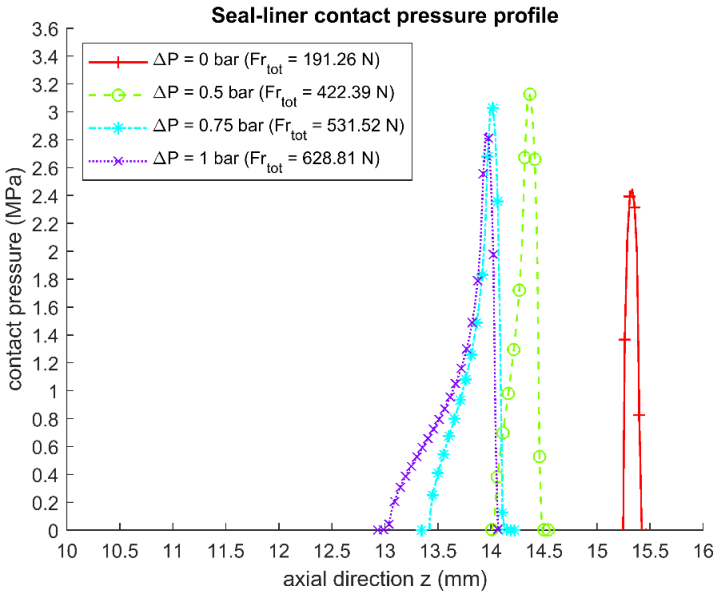

Figure 7. *Contact pressure at various pressure differences (see Figure 6). Reproduced from* [21].

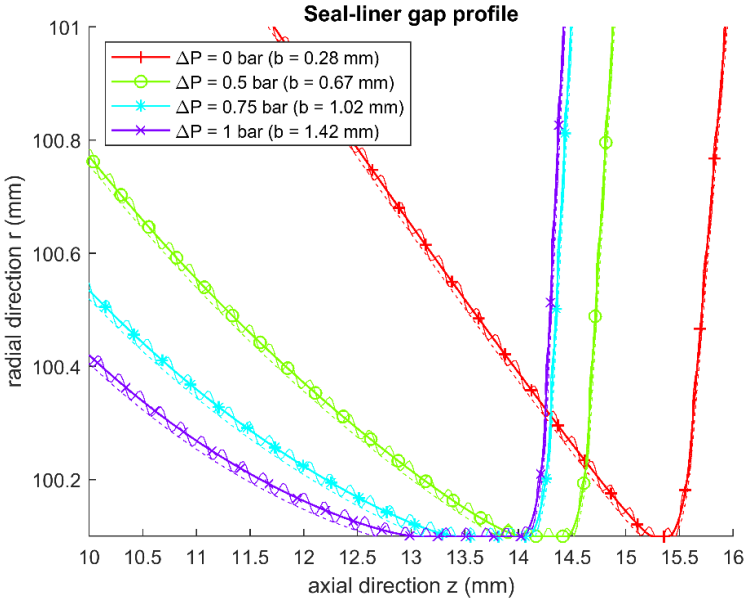

Figure 8. *Seal tip profile at various pressure differences (see Figure 6). Reproduced from* [21].

3. Results

A particular stern tube seal of 200 millimetres nominal diameter was tested under the operating conditions as listed in Table 3, i.e. four pressure differences and three shaft velocities. Figure 9, Figure 10, Figure 11 and Figure 12 show the frictional torque, the contact temperature, the flow rate and the heat dissipation of the seal respectively.

The torque decrease with an increase of velocity shown in Figure 9 is not often observed in rotary lip seals [19]. El Gadari [47] showed a friction-velocity curve presenting a maximum friction at 2500 rpm; beyond that velocity the torque decreased. That is explained by a larger viscosity decrease than the velocity increase. The same occurs with the stern tube seal tested and it is clearly evidenced when plotting the coefficient of friction μ over the duty parameter G as in Figure 13.

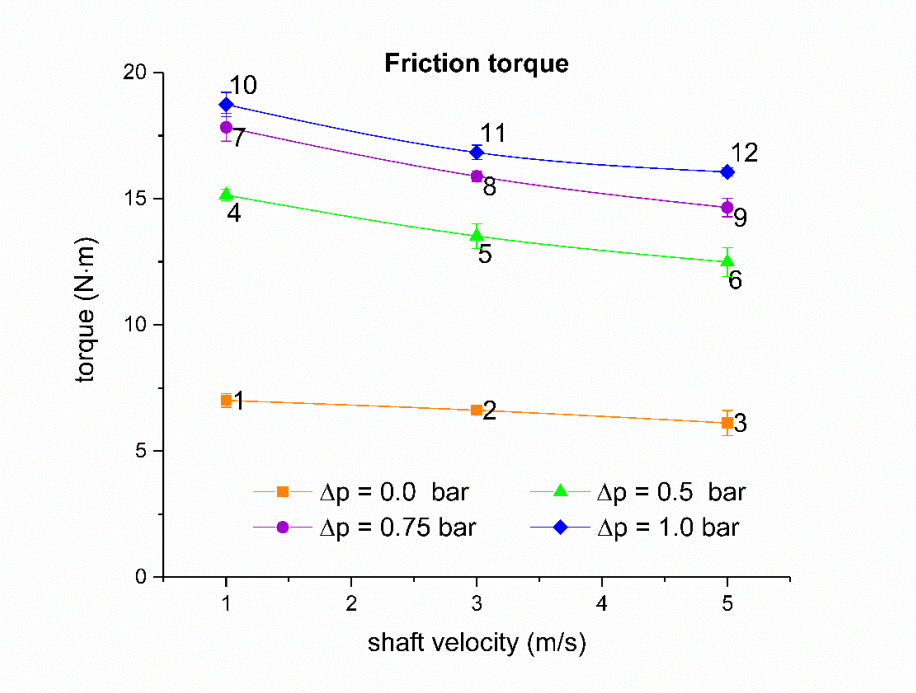

Figure 9. *Frictional torque measurements after subtracting the parasitic friction.*

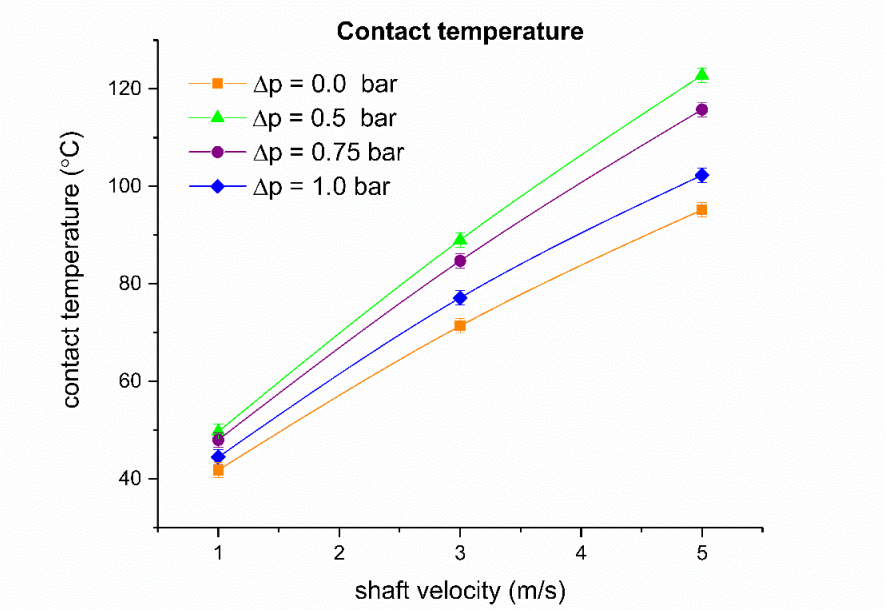

Figure 10. *Contact temperature predicted from the garter spring temperature measurements via the FE model presented in* [21].

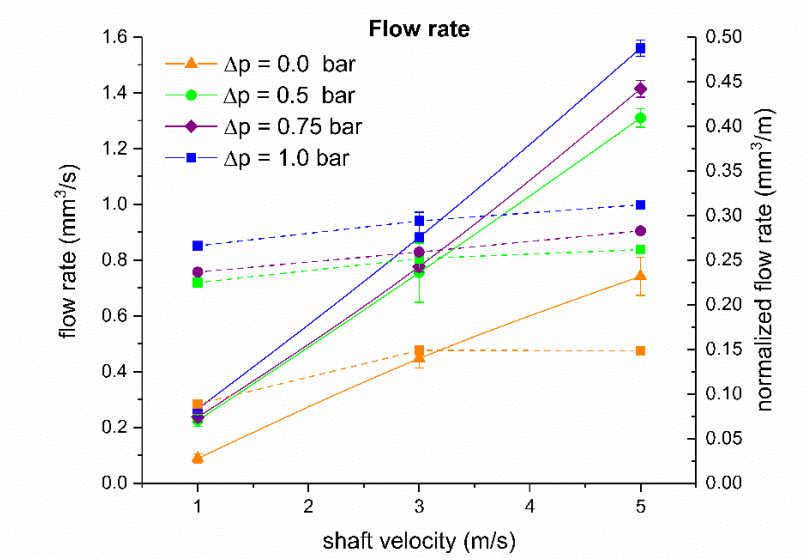

Figure 11. *Flow rate measurements from spring side to back side of the seal. The flow rate q and the normalized flow rate $\bar{q} = q/v$ are plotted in continuous and dashed lines respectively.*

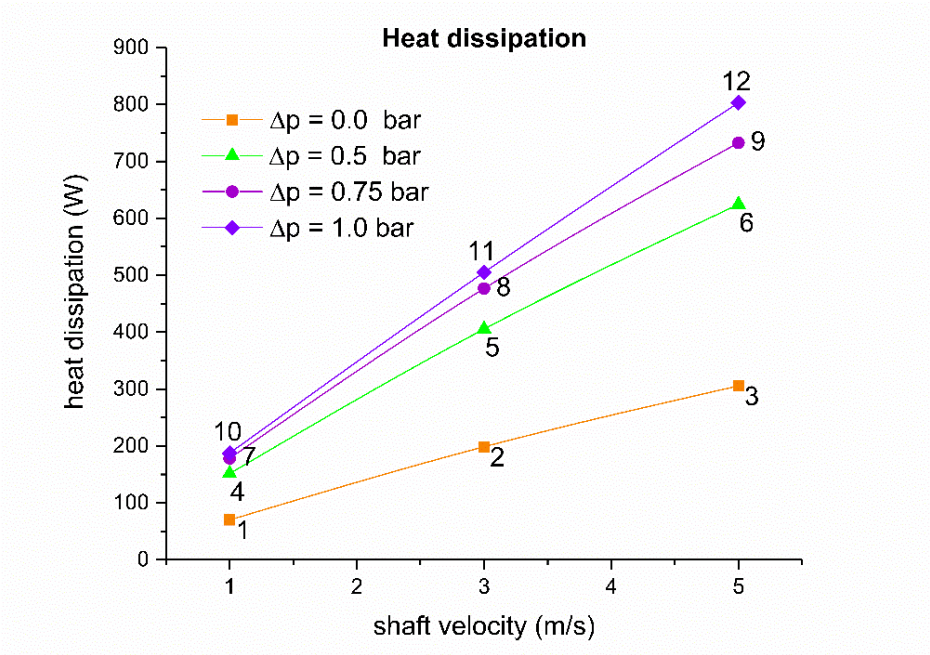

Figure 12. *Heat dissipated at the contact* $Q_f = \Gamma\omega$.

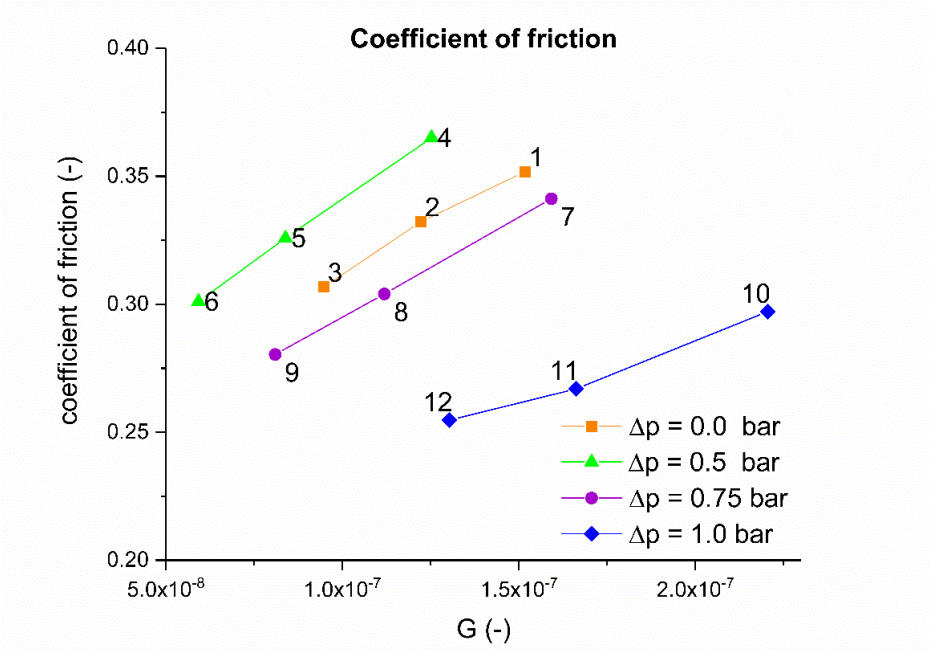

Figure 13. *Stribeck curve.*

Figure 13 suggests that the operating points tested belong to the transition between mixed and the full film lubrication regimes, i.e. at the right-side of the minimum friction coefficient value of the Stribeck curve. Figure 3 shows that EHL encompasses the minimum of the Stribeck curve, hence the slope of the μ-G is not as steep as in the full film hydrodynamic lubrication regime.

Also, previous studies showed a linear correlation between the friction coefficient and the cubic root of the duty parameter $G^{1/3}$ [33]. The linear regressions exhibit a coefficient of determination R^2 of at least 0.92. A characteristic friction proportionality factor specific to each pressure difference is obtained as shown in Figure 14.

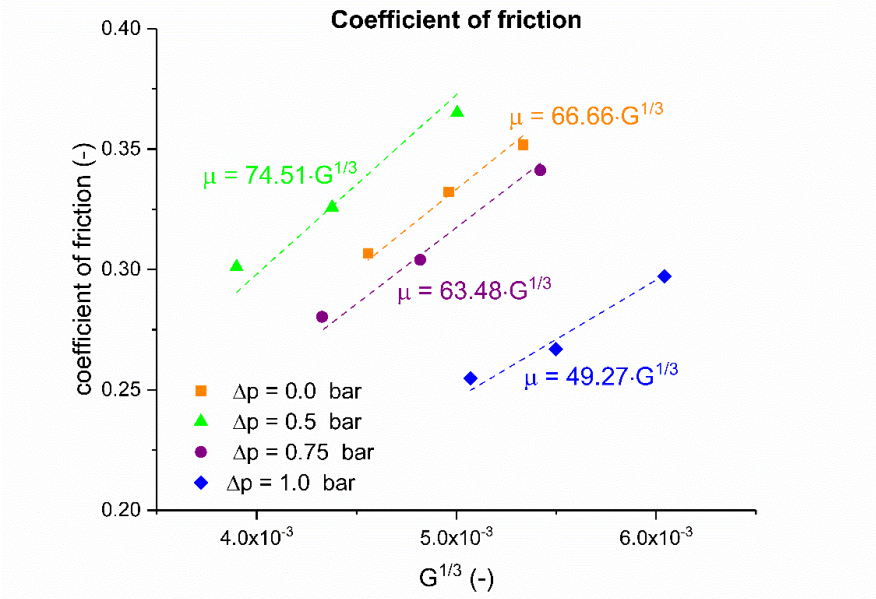

Figure 14. *Coefficient of friction as a function of $G^{1/3}$ as shown in* [33].

The temperature at the contact is shown to be proportional to the heat dissipation density Q_d. Therefore, using Eq. 4 as shown in Figure 15 the temperature parameter $K_{\Delta T}$ is deduced showing determination coefficients over 0.97.

The validity of Eq. 5 to relate the operating conditions of a rotary lip seal to the flow rate across its contact was analysed. Figure 16 shows that Kawahara's expression [5] is applicable to the stern tube seal tested exhibiting R^2 above 0.93.

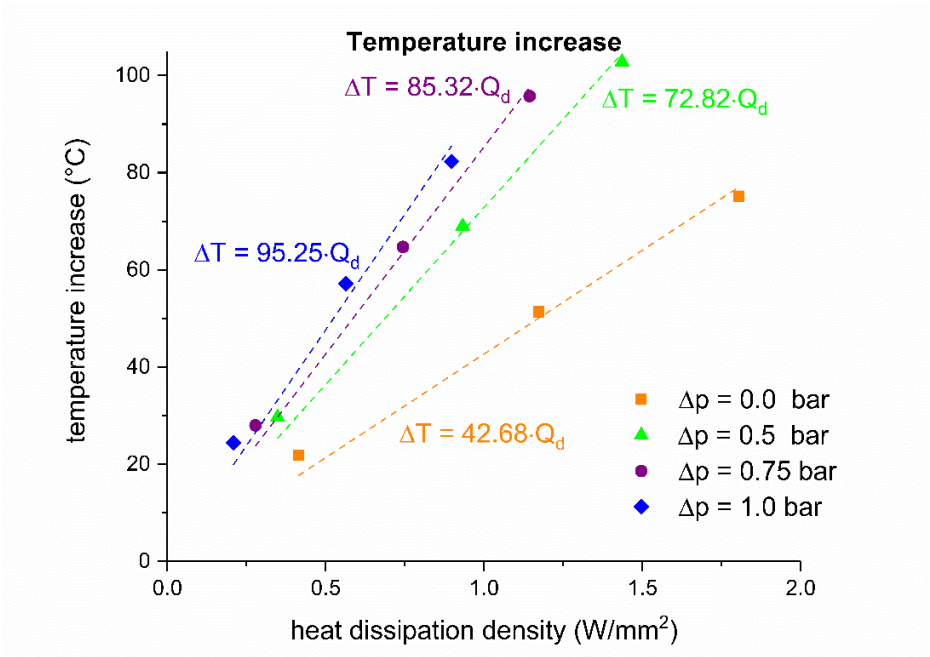

Figure 15. *Temperature increase at the contact.*

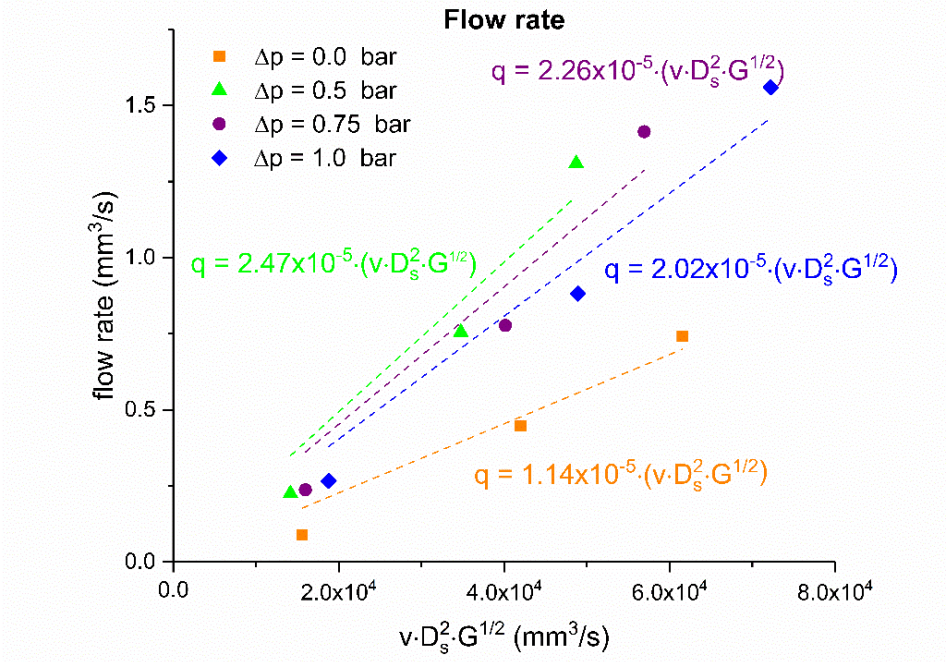

Figure 16. *Flow rate fitting as shown in* [5] .

The film thickness at the contact was not measured. However, an approximated value of the seal-liner separation can be indirectly obtained by fitting Eq. 2 to the frictional torque measurements as shown in in Figure 17. As expected, a larger film thickness results from assigning a lower viscous shear load ($\mu_0 = 0.1$).

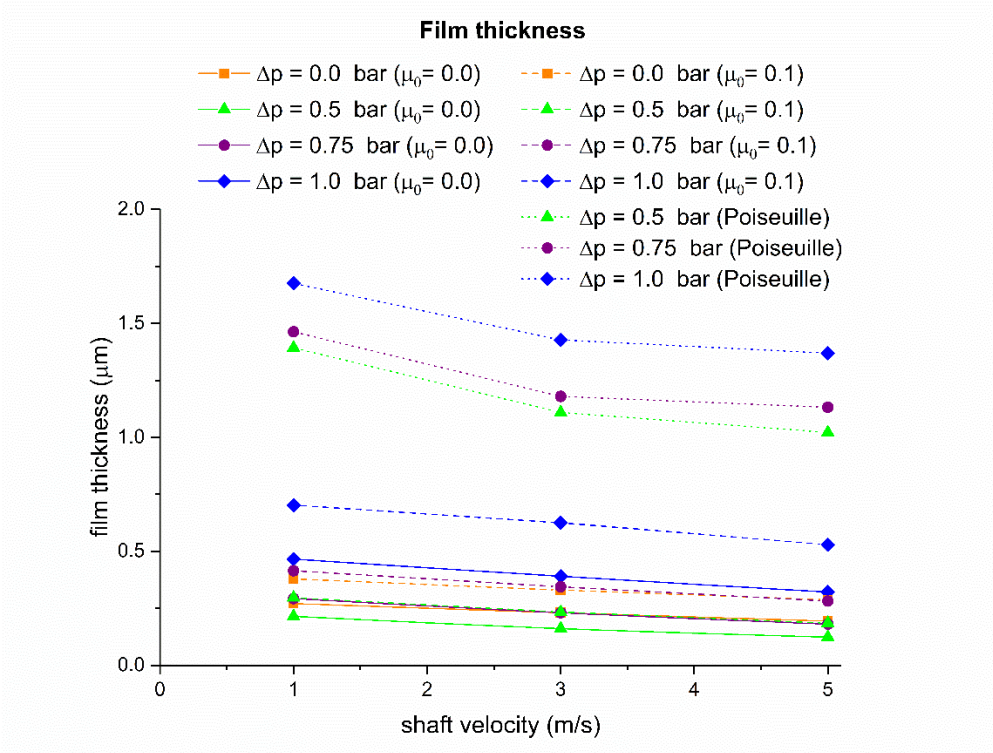

Figure 17. *Film thickness prediction.*

Alternatively, given that the liquid migration observed follows the natural flow direction, the gap required assuming a fully pressure-driven flow can be estimated, leading to reasonable results (see Figure 17). Note that some lubricant is driven across the seal even when there is no pressure difference, hence Poiseuille's expression alone cannot explain it. The film thicknesses shown in Figure 17 follow the central film thickness expression for soft-EHL $h \propto (u\eta)^{0.66}$ [16].

4. Discussion

The frictional torque measurements revealed that the stern tube seal analysed operates at the right side of the minimum of the Stribeck

curve. Notice that the separation between the seal and the shaft decreases as the velocity increases. That is inconvenient as it is a self-induced mechanism: the greater the shaft velocity, the higher the contact temperature, further decreasing the film thickness and leading to an even higher temperature. The film thickness predictions allow the lambda ratio to be estimated at each operation point. The lambda ratio ranges from 0.1 to 2 for all the estimated film thicknesses shown in Figure 17 ($\sigma = 1.23\ \mu m$). The elastomeric seal material deforms, leading to new surface roughness characteristics and therefore the denominator of the lambda ratio becomes debatable [13]. The challenge consists typically in dividing the torque in a dry and a viscous component. By applying a linear fit to the log G - log μ plot the slopes indicate that the operating points tested belong to the right hand side of the transition between the mixed and full film lubrication regimes [14], i.e. between 0.25 and 0.3. It is important to point out that the traditional Stribeck curve may only partially capture the operation of rotary lip seals [20]. The question remains, how much of the measured frictional torque belongs to direct asperity contact and how much to the shear of the lubricant? As stated by Van Leeuwen, the lubrication condition cannot be determined by the friction behaviour alone [15].

Reverse pumping typically ensures the flow of lubricant from the back side to the spring side even when pressurized [29], i.e. upstream pumping. The results show a flow rate from the spring side to the back side instead. This occurs even when there is no pressure difference. No lubricant migration was observed when the shaft was not rotating. The contact pressure profile between the seal and the shaft is almost symmetric when there is no pressure difference and becomes more skewed when the pressure difference increases [21]. Therefore, when the seal is not pressurized neither the reverse pumping nor the pressure-driven flow take place. The shaft liner was manufactured following the same procedure used for the real application, hence a screw thread may be left. The lead of the shaft can explain the oil migration when non-pressurized. Alternatively, the loss of the nominal parallelism between the seal and the shaft [43] or the poor followability of the seal at larger velocities [40] are also plausible explanations. Reverse pumping is expected to be present under pressurized situations, i.e. counteracting the natural flow direction. However, besides a skewed radial pressure profile, the surface roughness or the

stiffness of the seal are also of importance for the generation of the upstream pumping phenomenon.

The fluid film thickness was deduced from the frictional torque and from the flow rate measurements, leading to results between 0.1 μm and 2 μm. The friction torque in Eq. 2 is represented by two terms: one for the direct contact between asperities and the other one for the viscous shear of the lubricant. Notice that the dry friction force term in [27] remains constant when the shaft velocity increases. A larger hydrodynamic pressure build-up usually results from an increase of velocity, leading to a decrease of the load carried by the direct asperity contact. Eq. 2 assumes that hydrodynamics does not play a role as in concentric rotating cylinders. A more accurate approximation of the film thickness may be obtained by setting a non-constant μ_0 as in [16]. Additionally, using the film thickness predicted by Eq. 2 (Figure 17), the pressure-driven flow, i.e. Poiseuille flow, reaches a maximum 0.05 mm^3/s. The Poiseuille flow alone cannot explain the flow rate measurements, hence reinforcing the shaft surface lead pumping hypothesis.

Eq. 4 was shown to accurately capture the temperature at the contact. The formula relies on the $K_{\Delta T}$ parameter relating the heat dissipation density to the temperature increment at the contact. Notice that while the power dissipated increases with an increase in the pressure difference, the power dissipated density decreases with it. This is explained by a larger increase in the contact width with the pressure difference. Note that the $K_{\Delta T}$ values calculated are two to five times larger than the ones obtained for smaller seals [27]. The contact temperature was extrapolated from the temperature measurements at the garter spring groove, hence the predictions may be inaccurate to some extent. A poorer dissipation of the heat produced at the contact or the overheating of the shaft can also explain the larger $K_{\Delta T}$. The amount of heat that can be dissipated by the lubricant flow rate across the seal was estimated to be approximately 0.1% of the total heat dissipated, hence it was neglected. In [21], the fluoroelastomer compound used for this particular stern tube seal was shown to soften between 20 °C and 40 °C when the rubbery plateau is reached. Although the model accounted for the thermal expansion of the components, the constitutive material model was left temperature-independent and therefore the radial force may be overestimated. Note that both the contact width and the radial load are assumed to be the same under static and dynamic conditions. A slight oil temperature

increase was measured at the narrower sections of the setup, i.e. back-up wall and spacers, which may lead to a different oil condition at the seal intake. Ultimately, the actual shaft and sump oil temperatures on a real ship are unknown and will significantly impact the energy balance of the tribo-system.

The models for rotary lip seals found in literature are generally for smaller rotary lip seals with a null pressure difference. The details on the stern tube seals operation are kept within the original equipment manufacturers, so they have not been disclosed. The results presented constitute a first reference to large rotary seals under pressurized conditions. The shear thinning observed in some of the stern tube lubricants [42] would lead to a further decrease in the film thickness at higher velocities. This would reduce the service time of the seals. The results obtained show a migration of lubricant from the spring side to the back side. In that case, seawater would leak to the stern tube increasing the liquid height of the oil tanks. The lubricant spillage in real ships is estimated to be a hundred times larger and in the opposite direction [44]. Although seals operating with a water-oil interface were not tested, the latter suggests that there is an additional oil spillage mechanism in ships which was not captured by the stern tube test setup developed. The transient operation, a large seal-shaft misalignment, or sudden such as the propeller being temporarily out of the water, can explain the large oil consumption values reported. Additionally, differences in the flow rate of each seal results in a different pressure condition from the original one. Monitoring the oil level of the tanks while sailing would contribute to the understanding of the complex stern tube system.

Every rotary lip seal has its own characteristics and what applies to one type of seal does not apply to others. The models presented require the dry friction coefficient or the equivalent film thickness, among other things, to be determined experimentally. When the material of the seal is switched, for example, the radial force, the contact temperature and the seal followability vary, leading to a completely different scenario.

5. Conclusions

A testing setup was developed, allowing an insight into the actual operation conditions of stern tube seals. The rig made it possible to accurately measure the frictional torque, flow rate and operating temperature under a wide range of velocities, oil sump temperatures

and pressure differences. On one hand, the friction torque results revealed that the behaviour of a stern tube seal resembles the operation of smaller rotary lip seals. It is noteworthy that the frictional torque decreased when the shaft velocity increased, leading to narrower film heights. On the other hand, the direction of the flow rate across the seal calls into question whether a reverse pumping mechanism is necessary at all. The existing expressions relating the operational conditions of rotary lip seal are shown to hold for large pressurized rotary lip seals as long as the results at each pressure difference are characterized individually.

References

[1] E.T. Jagger, "Rotary Shaft Seals: The Sealing Mechanism of Synthetic Rubber Seals Running at Atmospheric Pressure," *Proc. Inst. Mech. Eng. Part J J. Eng. Tribol.*, vol. 171, no. 1, pp. 597–616, 1957.

[2] R.F. Salant, "Soft elastohydrodynamic analysis of rotary lip seals," *Proc. Inst. Mech. Eng. Part C*, vol. 224, no. 12, pp. 2637–2647, 2010.

[3] M.J.L. Stakenborg, "On the sealing mechanism of radial lip seals," Ph.D. dissertation, Eindhoven University of Technology, 1988.

[4] D.E. Johnston, "Rotary shaft seals," *Tribol. Int.*, vol. 19, no. 4, pp. 170–174, 1986.

[5] Y. Kawahara, M. Abe, and H. Hirabayashi, "An Analysis of Sealing Characteristics of Oil Seals," *ASLE Trans.*, vol. 23, no. 1, pp. 93–102, 1980.

[6] L.A. Horve, "Understanding The Sealing Mechanism Of The Radial Lip Seal For Rotating Shafts," in *Fluid Mechanics and its Applications*, Dordrecht: Springer Netherlands, 1992, pp. 5–19.

[7] M.O.A. Mokhtar, M.A.A. Mohamed, M.E. El-Giddawy, and S.A.Y. Yassen, "On the effect of misalignment on the performance of U-type lip seal," *Wear*, vol. 223, no. 1–2, pp. 139–142, 1998.

[8] B.S. Nau, *Fluid Sealing*, vol. 8. Dordrecht: Springer

Netherlands, 1992.

[9] L.A. Horve, *Shaft seals for dynamic applications*. New York: Marcel Dekker Inc., 1996.

[10] R.F. Salant, "Theory of lubrication of elastomeric rotary shaft seals," *Proc. Inst. Mech. Eng. Part J J. Eng. Tribol.*, vol. 213, no. 3, pp. 189–201, 1999.

[11] P. Baart, "Grease lubrication in radial lip seals," Luleå University of Technology, 2009.

[12] M. Ogata, T. Fujii, and Y. Shimotsuma, "Study on fundamental characteristics of rotating lip-type oil seals.," *Tribol. Ser.*, vol. 11, no. XVIII(ii), pp. 553–560, 1987.

[13] P. Cann, E. Ioannides, B. Jacobson, and A.A. Lubrecht, "The lambda ratio - a critical re-examination," *Wear*, vol. 175, no. 1–2, pp. 177–188, 1994.

[14] B.J. Hamrock, S.R. Schmid, and B.O. Jacobson, *Fundamentals of Fluid Film Lubrication*, 2nd ed. New York: CRC Press, 2004.

[15] H. van Leeuwen and M. Wolfert, "The sealing and lubrication principles of plain radial lip seals: an experimental study of local tangential deformations and film thickness," in *Elastohydrodynamics*, 1996, pp. 219–232.

[16] M. Organisciak, P. Baart, and A. Paykin, "Theoretical and experimental study of the frictional losses of radial shaft seals for industrial gearbox," *Power Transmission Engineering*, pp. 58–63, 2015.

[17] B. Wennehorst, "On Lubrication and Friction in Soft Rough Conformal Sliding Contacts," Ph.D. dissertation, Leibniz Universität Hannover, 2016.

[18] G. Poll and A. Gabelli, "Formation of Lubricant Film in Rotary Sealing Contacts: Part II—Lubricant Film Modeling."

[19] B. Wennehorst and G.W.G. Poll, "Soft micro-elastohydrodynamic lubrication and friction at rough conformal contacts," *Proc. Inst. Mech. Eng. Part J*, vol. 231, no. 3, pp. 302–315, 2017.

[20] D.E. Johnston and R. Vogt, "Rotary shaft seal friction, the

influence of design, material, oil and shaft surface," *SAE Tech. Pap.*, no. 41 2, 1995.

[21] F.X. Borras, M. Bazrafshan, M. B De Rooij, and D. J Schipper, "Stern tube seals under static condition: A multi-scale contact modeling approach," *Proc. Inst. Mech. Eng. Part J*, May 2020.

[22] D. Frölich, B. Magyar, and B. Sauer, "A comprehensive model of wear, friction and contact temperature in radial shaft seals," *Wear*, vol. 311, no. 1–2, pp. 71–80, 2014.

[23] Y. Arai, "Sealing theory in oil seals - 1," in *JSLE-ASLE International Lubrication Conference*, 1976, pp. 830–839.

[24] C. Burkhart, K. Peter, S. Thielen, and B. Sauer, "Online determination of reverse pumping values of radial shaft seals and their tribologically equivalent system," in *22nd International Colloquium Tribology*, 2020, pp. 1–2.

[25] W. Sinzara, I. Sherrington, E.H. Smith, H. Brooks, and A. Onsy, "Effects of Eccentric Loading on Lip Seal Performance," in *6th European Conference on Lubrication Management and Technology*, 2018.

[26] A. Maoui, M. Hajjam, and D. Fribourg, "An experimental study on the temperature and the friction torque of rotary lip seal," in *8th EDF & LMS Workshop: "Dynamic Sealing in severe operating conditions,"* 2009, pp. 1–7.

[27] T. Engelke, "Einfluss der Elastomer-Schmierstoff-Kombination auf das Betriebsverhalten von Radialwellendichtringen (in German)," Ph.D. dissertation, Leibniz Universität Hannover, 2011.

[28] X. Jia, S. Jung, W. Haas, and R.F. Salant, "Numerical simulation and experimental study of shaft pumping by plunge ground shafts with rotary lip seals," *Tribol. Int.*, vol. 48, pp. 155–161, 2012.

[29] R. Flitney, "Rotary Seals," in *Seals and Sealing Handbook*, 6th ed., Waltham: Butterworth-Heinemann, 2014, pp. 105–288.

[30] M. Baumann, F. Bauer, H.W. Haas, and G. Baitinger, "How to measure lead in sealing technology?," *Seal. Technol.*, vol. 2013, no. 7, pp. 8–12, 2013.

[31] T. Kunstfeld and W. Haas, "Shaft surface manufacturing methods for rotary shaft lip seals," *Seal. Technol.*, no. 7, pp. 5–9, 2005.

[32] M. Organisciak, J. Jordan, and S. Barbera, "A new approach to predict rotating lip seal friction application to industrial seals," in *17th International Sealing Conference*, 2012, pp. 130–141.

[33] F. Hirano and H. Ishiwata, "The Lubricating Condition of a Lip Seal," *Proc. Inst. Mech. Eng.*, vol. 180, no. 3B, pp. 187–196, 1965.

[34] A. Gabelli, "Micro-elastohydrodynamic lubricant film formation in rotary lip seal contacts," *Tribol. Ser.*, vol. 14, pp. 57–68, 1989.

[35] A. Gabelli and G. Poll, "Formation of Lubricant Film in Rotary Sealing Contacts: Part I—Lubricant Film Modeling," *J. Tribol.*, vol. 114, no. 2, pp. 280–287, 1992.

[36] R.F. Salant and A.L. Flaherty, "Elastohydrodynamic analysis of reverse pumping in rotary lip seals with microundulations," *J. Tribol.*, vol. 116, no. 1, pp. 56–62, 1994.

[37] P.G.M. Van Bavel, T.A.M. Ruijl, H.J. Van Leeuwen, and E.A. Muijderman, "Upstream Pumping of Radial Lip Seals by Tangentially Deforming, Rough Seal Surfaces," *J. Tribol.*, vol. 118, no. 2, pp. 266–275, 1996.

[38] M. Hajjam and B. Dominique, "Non-Newtonian effects on elastohydrodynamic behaviour of rotary lip seals," *Proc. Inst. Mech. Eng. Part J*, vol. 220, no. 2, pp. 79–85, 2006.

[39] D. Shen and R.F. Salant, "A transient mixed lubrication model of a rotary lip seal with a rough shaft," *Tribol. Trans.*, vol. 49, no. 4, pp. 621–634, 2006.

[40] H. van Leeuwen and M.J.L. Stakenborg, "Visco-Elastohydrodynamic (VEHD) Lubrication in Radial Lip Seals: Part 2 - Fluid film formation," *Trans. ASME*, vol. 112, pp. 584–591, 1990.

[41] R.F. Salant, "Rotary lip seal operation with an ingested meniscus," *J. Tribol.*, vol. 119, no. 4, p. 887, 1997.

[42] F.X. Borras, M.B. de Rooij, and D.J. Schipper, "Rheological and Wetting Properties of Environmentally Acceptable Lubricants

(EALs) for Application in Stern Tube Seals," *Lubricants*, vol. 6, no. 4, p. 100, Nov. 2018.

[43] F.X. Borras, M.B. de Rooij, and D.J. Schipper, "Misalignment-Induced Micro-Elastohydrodynamic Lubrication in Rotary Lip Seals," *Lubricants*, vol. 8, no. 2, p. 19, Feb. 2020.

[44] D.S. Etkin, "Worldwide analysis of in-port vessel operational lubricant discharges and leakages." Cortlandt Manor, pp. 2–9, 2008.

[45] H.K. Müller and B.S. Nau, "Rotary Lip Seals," in *Fluid Sealing Technology: Principles and Applications*, New York: Marcel Dekker Inc., 1998, pp. 73–110.

[46] Parker, *Rotary Seal Design Guide*. 2006.

[47] M. El Gadari, A. Fatu, and M. Hajjam, "Shaft roughness effect on elasto-hydrodynamic lubrication of rotary lip seals: Experimentation and numerical simulation," *Tribol. Int.*, vol. 88, pp. 218–227, 2015.